8-2018

Numerical study of the electron-phonon interaction in multiorbital materials

Shaozhi Li
University of Tennessee, sli43@vols.utk.edu

To the Graduate Council:

I am submitting herewith a dissertation written by Shaozhi Li entitled "Numerical study of the electron-phonon interaction in multiorbital materials." I have examined the final electronic copy of this dissertation for form and content and recommend that it be accepted in partial fulfillment of the requirements for the degree of Doctor of Philosophy, with a major in Physics.

Steven S. Johnston, Major Professor

We have read this dissertation and recommend its acceptance:

Elbio R. Dagotto, Takeshi Egami, Thomas A. Maier, Hanno Weitering

Accepted for the Council:

Dixie L. Thompson

Vice Provost and Dean of the Graduate School

(Original signatures are on file with official student records.)

Numerical study of the electron-phonon interaction in multiorbital materials

A Dissertation Presented for the

Doctor of Philosophy

Degree

The University of Tennessee, Knoxville

Shaozhi Li

August 2018

This theise is dedicated to my family for their patience, support and understanding.

Acknowledgements

I first would like to thank my supervisor Steven Johnston for his patient, supporting, and guidance over the past four years. He is a very patient and good teacher. I still remember the time when I just joined our group, he spent a lot of time to teach me Green's functions and never complained my ignorant. Also, I would like to thank him to improve my English very much.

Next, I would like to thank members of my committee, Dr. Hanno Weitering, Dr. Elbio Dagotto, Dr. Thomas A. Maier, and Dr. Takeshi Egami for their time and helpful suggestions in general. I am also very grateful to my collaborates, Dr. Beth Nowadnick, Dr. Guangkun Liu, Dr. Ehsan Khatami, Dr. Yan Wang, Yanfei Tang, and Nitin Kaushal. At last, I would like to thank my labmates Umesh Kumar, Ken Nakatsukasa, and Phillip Dee.

At this time, I would like to say thank you to my fiancee, Wanwan Liang, who brings me happiness and serene to my life. Sometimes, doing research jobs makes my life painful. But she is a kind of medicine to cure this painful and gives me the courage to go on. I also thank my parents for their endless and unconditional care and love. I love them so much, and I would not have made it this far without them.

Abstract

This thesis examines the electron-phonon (e-ph) interaction in multiorbital correlated systems using various numerical techniques, including determinant quantum Monte Carlo and dynamical mean field theory. First, I studied the non-linear e-ph coupling in a one band model and found that even a weak non-linear e-ph couplings can significantly shape both electronic and phononic properties. Second, I study the interplay between the e-ph and electron-electron (e-e) interactions in a multiorbital Hubbard-Holstein model in both one- and infinite-dimension. In both cases, I found that a weak e-ph interaction is enough to induce a phase transition from the Mott phase to the charge-density-wave phase. Moreover, I find that not only the e-e correlation but also the e-ph interaction can induce an orbital-selective phase. Our results imply that the e-ph interaction is significant in the multiorbital correlated materials, such as the iron-based superconductors. Last, I studied the offdiagonal e-ph interaction in a two-dimensional three-orbital model defined on a Lieb lattice. I consider an sp-type model, which is like a 2D analog of the barium bismuthate high temperature superconductors. I found a metal-to-insulator (MI) transition as decreasing temperature at half filling and identified a dimerized structure in the insulating phase. With hole doping, the ordered polarons and bipolarons correlations disappear but the short-range correlations are present, implying that polarons and bipolarons preform in the matellic phase and freeze into a periodic array in the insulating state. In sum, this thesis reveals the importance of the e-ph interaction in the multiorbital materials and gives an alarm to people when study these multiorbital materials.

Table of Contents

List of Figures

Chapter 1

Introduction

1.1 Superconductors

A superconductor is a material that has zero electric resistance below a critical temperature T_c and zero internal magnetic field below a critical field H_c [Meissner effect [181]]. Superconductivity was first discovered in mercury in 1911 [59]. After that, numerous studies have been done in looking for new superconducting materials. Although hundreds of superconducting materials have been discovered, in general, there are only two different classes of superconductors. The first one is called the conventional superconductor, which can be explained by the BCS theory [9]. The BCS theory claims that attractive potential between two electrons is given by the electron-phonon (e-ph) interaction. In experiments, the highest recorded conventional superconducting temperature before 1980 was 23.2 K discovered in the film Nb_3Ge [197]. Later, a higher conventional superconducting temperature $T_c = 40$ K was found in MgB_2, due to anharmonic phonons [189].

The second class of superconductor is the unconventional superconductor, which can not be explained by the BCS theory. Some unconventional superconductors can have a very high critical transition temperature compared to the conventional superconductors. For example, the $BiSrCaCu_2O_x$ has T_c of about 105 K [164]. Usually, we refer to those superconductors, which has a critical transition temperature $T_c > 77$ K (boiling point of liquid N_2), as "high T_C" superconductors. The mechanism of the unconventional superconductivity is unclear, although the majority of physicsts believe that it is driven by the electronic or

magnetic interactions between electrons [228, 229]. The first sample of high-temperature superconductivity is $La_{1-x}Ba_xCuO_4$ discovered in 1986 with $T_c = 30$ K [17]. Further research found the highest critical temperature of cuprates is around $T_c = 133$ K, discovered in $HgBa_2Ca_2Cu_3O_8$ [232]. In addition, another widely studied group of superconductors are the iron-based superconductors (FeSCs), which was first discovered in F-doped LaFeAsO in 2008 [117]. The symmetry of the superconducting order of the FeSCs is suggested as an extended s-wave with sign reversal [174, 132, 162], while it is d-wave symmetry in cuprates. Hence, the unconventional superconductor has abundant physical phenomena, which makes understanding its mechanism more difficult. In the following, I will discuss some details about these two groups of materials.

1.1.1 The High T_c cuprates

Cuprate superconductors have a common feature in the crystal structure, that the crystal is divided into CuO_2 planes and blocking layers [see Fig. 1.1 (a)]. Superconductivity occurs only in CuO_2 planes and the blocking layers supply charge carriers to the CuO_2 plane [214]. In different cuprate compounds, the blocking layers are different. Fig. 1.1 shows the unit cells of four cuprates: $HgBa_2CuO_{4+\delta}$ (Hg1201), $YBa_2Cu_3O_{6+\delta}$ (YBCO), $La_{2-x}Sr_xCuO_4$ (LSCO), and $Tl_2Ba_2CuO_{6+\delta}$ (Tl2201). These four cuprates show completely different structures in the blocking layers, but that doesn't change the electronic properties near the fermi surface very much because those properties are determined by the CuO_2 planes (Fig. 1.1 (c)) [205].

In the cuprates, the Cu atom is partially filled with a $3d^9$ shell and the oxygen atom is fully filled with a $2p^6$ shell. In Hg1201, the Cu^{2+} ions are surrounded by four oxygen atoms in the plane and two oxygen atoms outside of the plane. The six oxygen atoms form an octahedron and generate a crystal field, which lifts the five-fold degeneracy of the 3d orbitals and separates them into the e_g doublet and t_{2g} triplet, as shown in Fig. 1.2. The elongation of the octahedron along the c-axis lifts the remaining degeneracy of the e_g and t_{2g} orbitals leaving the $3d_{x^2-y^2}$ orbital lying highest in energy. At the same time, the tetragonal structure of the unit cells in Fig. 1.1 (b) breaks the degeneracy of the three O 2p orbitals, as shown in Fig 1.2. Because of the similar energy of the Cu d orbitals and the O 2p-orbitals, there is
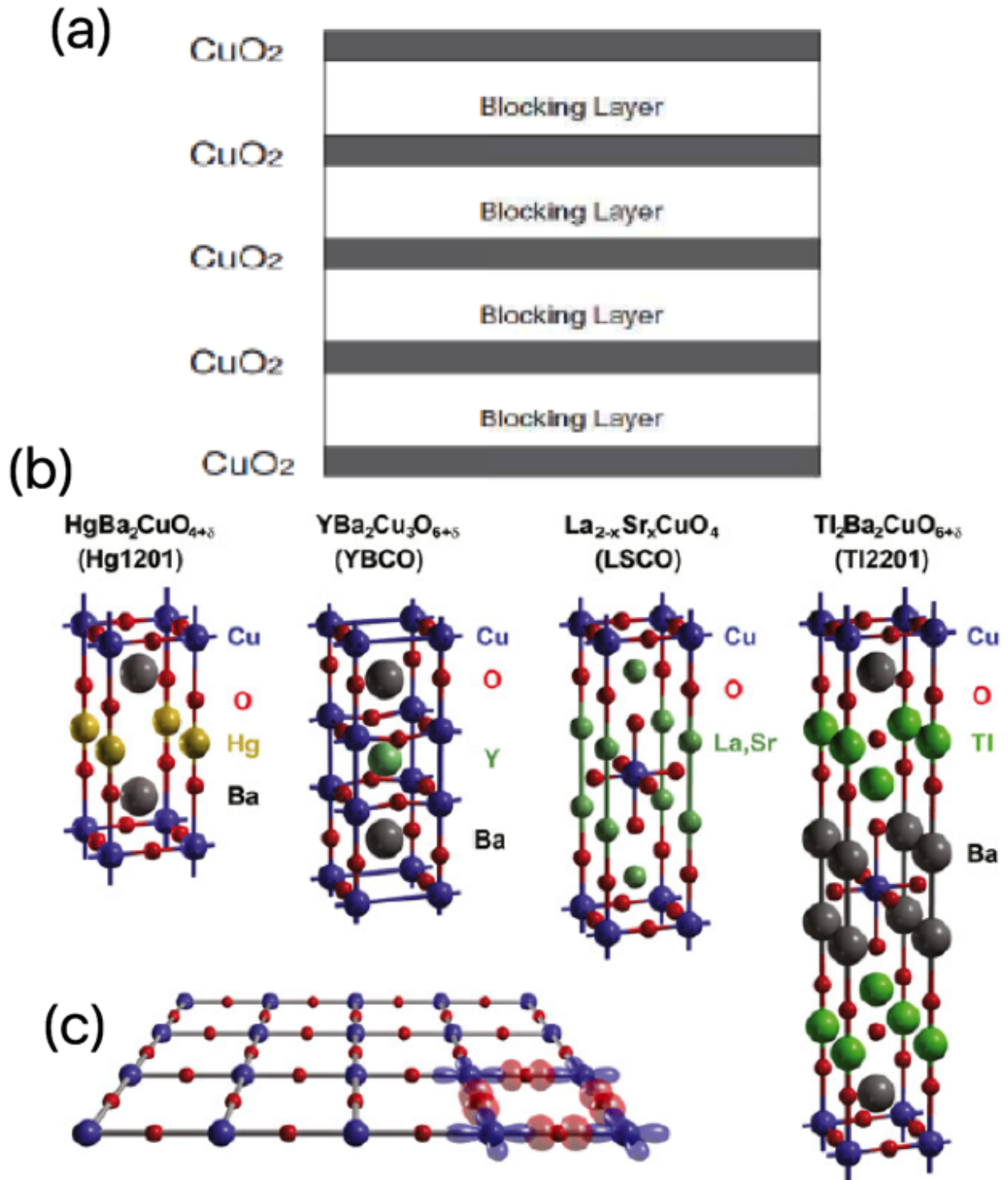
Figure 1.1: (a) Schematic structure of high-temperature superconductors. (b) Crystal structure of four cuprates: Hg1201, YBCO, LSCO, and TI2201. (c) The CuO_2 sheet is presented and the most important electronic orbitals, Cu $d_{x^2-y^2}$ and O p_σ are shown. This diagram comes from Ref. [10].
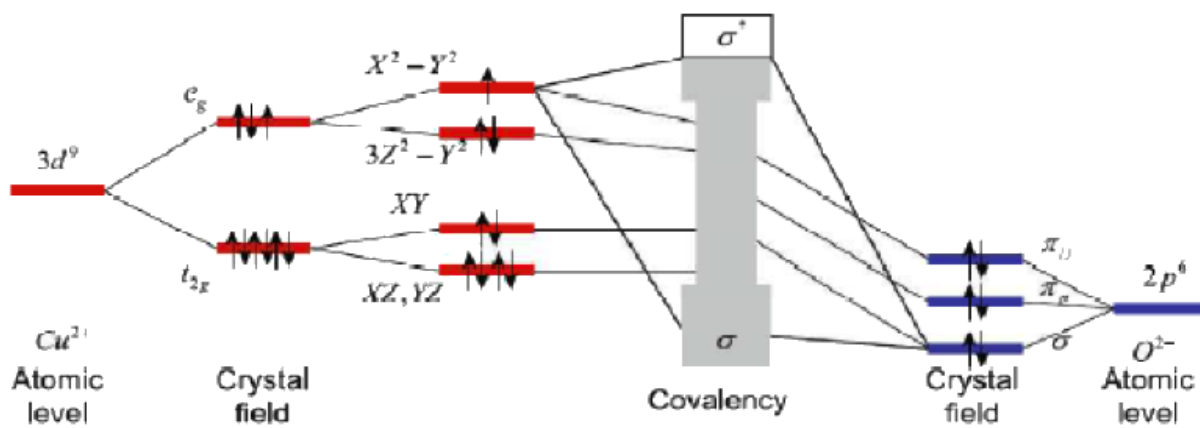
Figure 1.2: A schematic of the orbital energy levels and covalent bonding in the CuO_2 plane.This diagram comes from Ref. [214].

a strong hybridization between them. The topmost partially filled band is the $pd - \sigma^*$ band composed of the Cu $3d_{x^2-y^2}$ and O $2p_{x,y}$ orbitals.

A typical phase diagram of cuprate high-temperature superconductor is shown in the left part of Fig. 1.3, in which the phase of zero dopant concentration is an antiferromagnetic insulator (AF, the blue region), and the doped carriers destroy AF and lead to a superconducting phase (red region). With increasing hole doping, the pseudogap appears, in which conventional Fermi-Landu liquid theory fails to work and a superconducting gap is opened. The pseudogap is not found in conventional superconductors. The optimal hole concentration x is about 0.16, where T_c is maximum. In the overdoped region when $x > 0.16$, the superconducting phase disappears and a "Normal" metallic phase appears. On the electron doping side, there is no pseudogap and the superconducting phase penetrates into the AF region. The phase diagram is not symmetric about $x = 0$.

1.1.2 Iron-based Superconductors

The iron-based superconductors mainly have five classes according to their structure: "1111" type (LaFeAsO) [161],"122" type (AFe_2As_2) [222], "111" type (MFeAs) [257], "11" type (FeSe) [102] and "32522" type ($Sr_3Sc_2O_5Fe_2As_2$) [238](Fig. 1.4 (a)). Similar to the cuprates, the iron-based superconductors have Fe-As layers and blocking layers alternatively stacking along the c-axis. The blocking layers usually act as the insulating charge reservoir and the Fe_2As_2 layer acts as the active conducting block. The Fe_2As_2 plane structure is shown in Fig. 1.4 (b), where As atoms reside above and below this plane. The magnetic structure of the Fe_2As_2 plane consists of ferromagnetic chains that are coupled antiferromagnetically in the orthogonal direction [198].

Although the crystal structure of cuprates and FeSCs are similar that both are layer structures, their electronic properties are very different. Most of the cuprates are octahedral, while most of the FeSCs are tetrahedral at room temperature. Fig. 1.5 (b) shows that the t_{2g} orbitals (d_{xy}, d_{xz}, and d_{yz} orbitals) have higher energy in the tetrahedral crystal structure and are relevant to the conduction in FeSCs, while the higher energy orbitals e_g ($d_{x^2-y^2}$ and d_{z^2} orbitals) are associated with conduction in cuprates. Also comparing the superconducting phase diagrams of cuprates and iron pnictides (Fig. 1.3), two different things can be easily
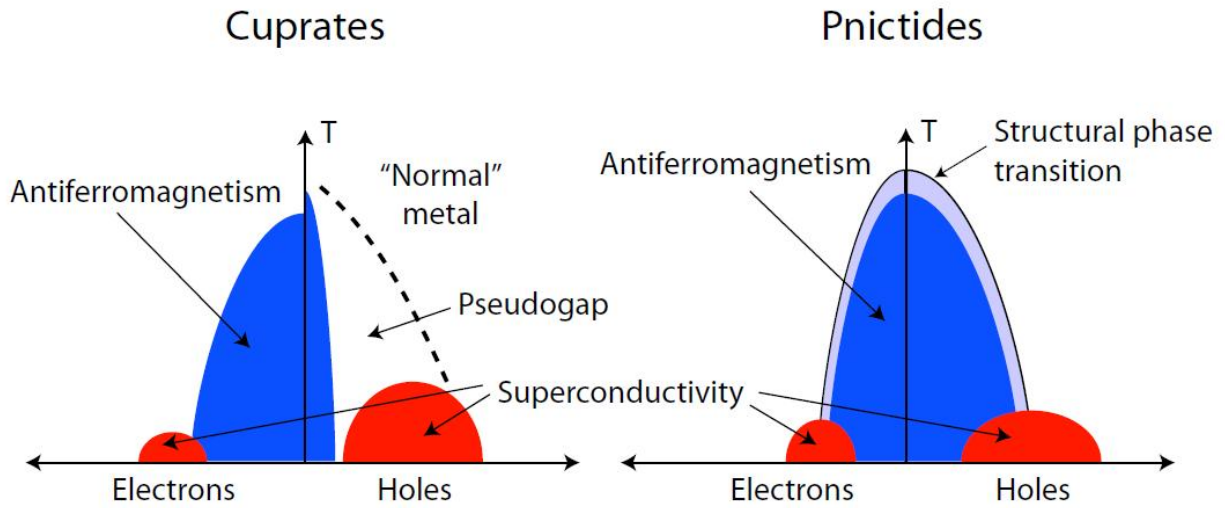
Figure 1.3: The generalized temperature-filling phase diagram of the high-T_c cuprates (left) and iron-based superconductors (right). This diagram comes from Ref. [135].
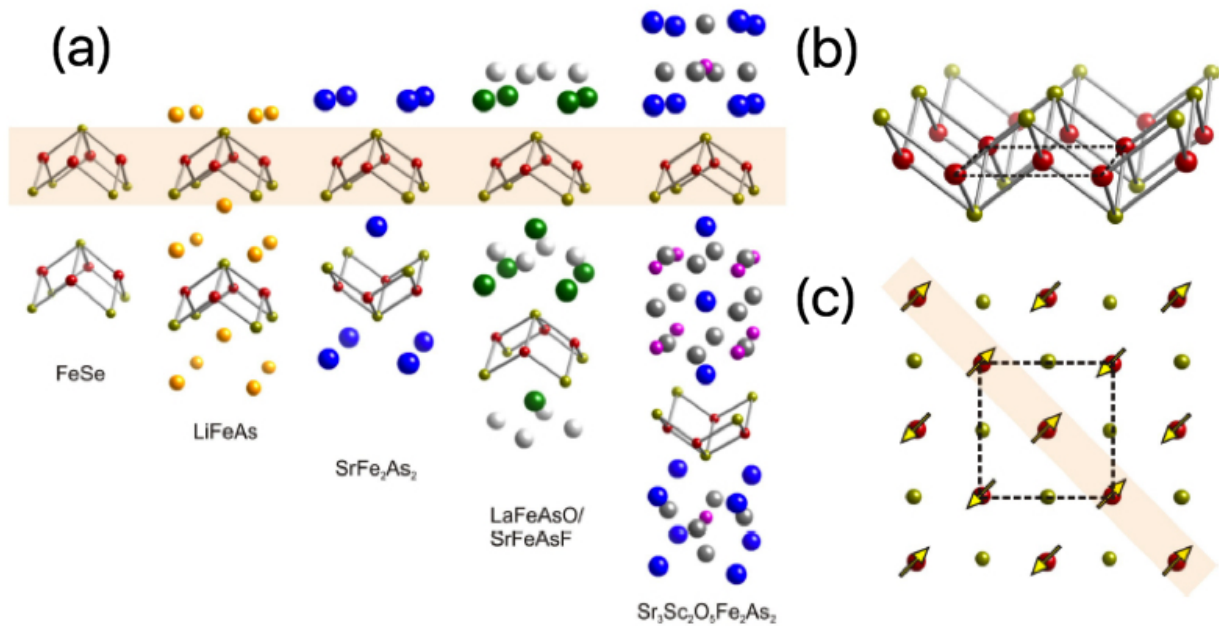
Figure 1.4: Crystallographic and magnetic structures of the iron-based superocnductors. (a) The five tetragonal structures known to support supercoductivity. (b) Iron layer structure. Iron ions are shown in red and pnictogen.chalcogen anions are shown in gold. (c) The magnetic structure in the iron layer. This diagram comes from Ref. [198].
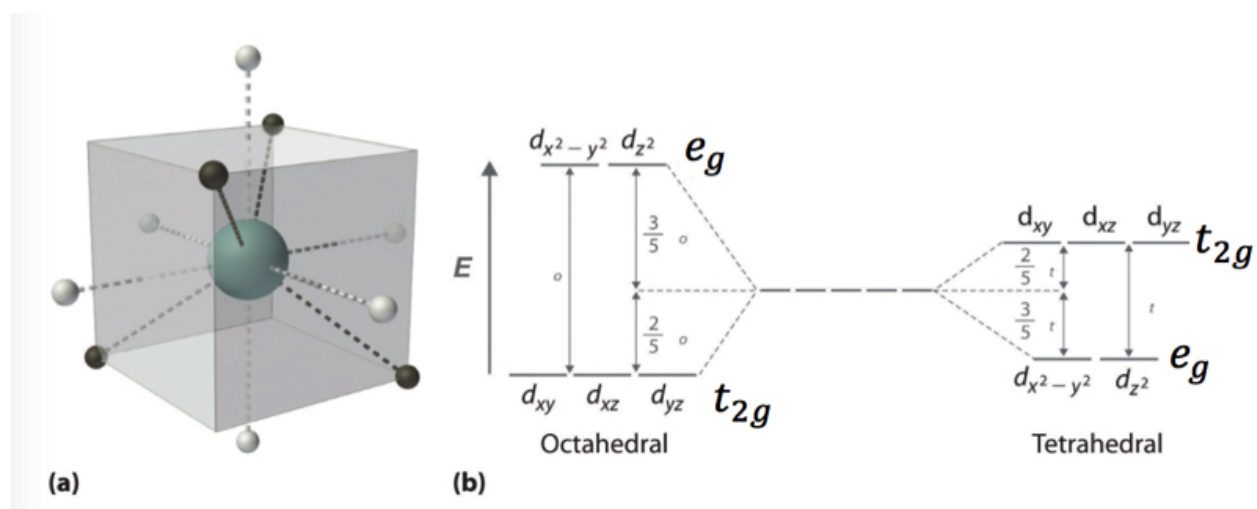
Figure 1.5: (a) Tetraheral ligand field surrounding a central transition metal (green sphere). (b) Splitting of the degenerate d-orbitals (withoud a ligand field) due to an oactahedral ligand field (left) and the tetraheral field (tight). This diagram comes from [8].

identified. There is no pseudogap in the iron pnictides and one additional phase, the nematic phase [190, 255], is presented. The nematic phase sits below the structure phase transition and above the antiferromagnetism transition. The nematic phase has been reported in the 1111 [118] and 11 system [261], but in the 122 system, the structure phase transition temperature coincides with the magnetic transition temperature. Although it was recently reported that the nematic phase in $BaFe_2(As_{1-x}P_x)_2$ appears at a temperatures higher than the structural/magnetic transition [119], it is still unknown whether the existence of nematic phase is universal for each FeSCs.

Different from the cuprate, there are five d orbitals near the fermi surface in iron pnictides. Fig. 1.6 shows the five 3d orbitals distribution near the Fermi surface, which is calculated via a two-dimensional band model [81]. Around the Γ point, the $3d_z^2$ orbital contributes to the two band ζ_{z^2} and ω_{z^2} well below E_F. There are two hole pockets at the Γ point, formed from $3d_{xz}$ and $3d_{yz}$ orbitals. The $3d_{xy}$ orbital contributes to the electron pocket at the M point. This electron pocket is also associated with $3d_{yz}$ orbital along the x-axis and the $3d_{xz}$ orbital along the y-axis, respectively. The $3d_{x^2-y^2}$ orbital was found to be irrelevant to the low-energy electronic structure. These results also consist with an angle-resolved photoemission spectroscopy (ARPES) study in $BaFe_{1.85}Co_{0.15}As_2$ [290] and generally true across the FeSCs.

1.1.3 $Ba_{1-x}K_xBiO_3$ and $BaPb_{1-x}BiO_3$ superconductors

Pure $BaBiO_3$ is insulating to well above 800 K and has a perovskite structure. At room temperature, its crystal structure is a cubic lattice with Bi atoms siting at each corner and O atoms linking each Bi pair (see Fig. 1.7). In the insulating state, the uniform crystal structure is distorted and the BiO_6 unit cell is tilted and consisted by two octahedron that one is expanded and the other one is collapsed. Earlier, it was recognized that this insulating phase comes from the charge order state comprised of Bi^{3+} and Bi^{5+} sites [50, 51, 204], and the two octahedron correspond to the Bi^{3+} and Bi^{5+} oxidation states [110]. But experiments have not observed distinct bismuth valences in $BaBiO_3$ [89, 31, 267]. Some theories have proposed the insulating state is induced by the attractive on-site interaction [217, 251] or the negative charge transfer energy that holes reside on the oxygen ligands [182]. The origin of the insulating state is still not clear now. A recent DFT calculation showed that the
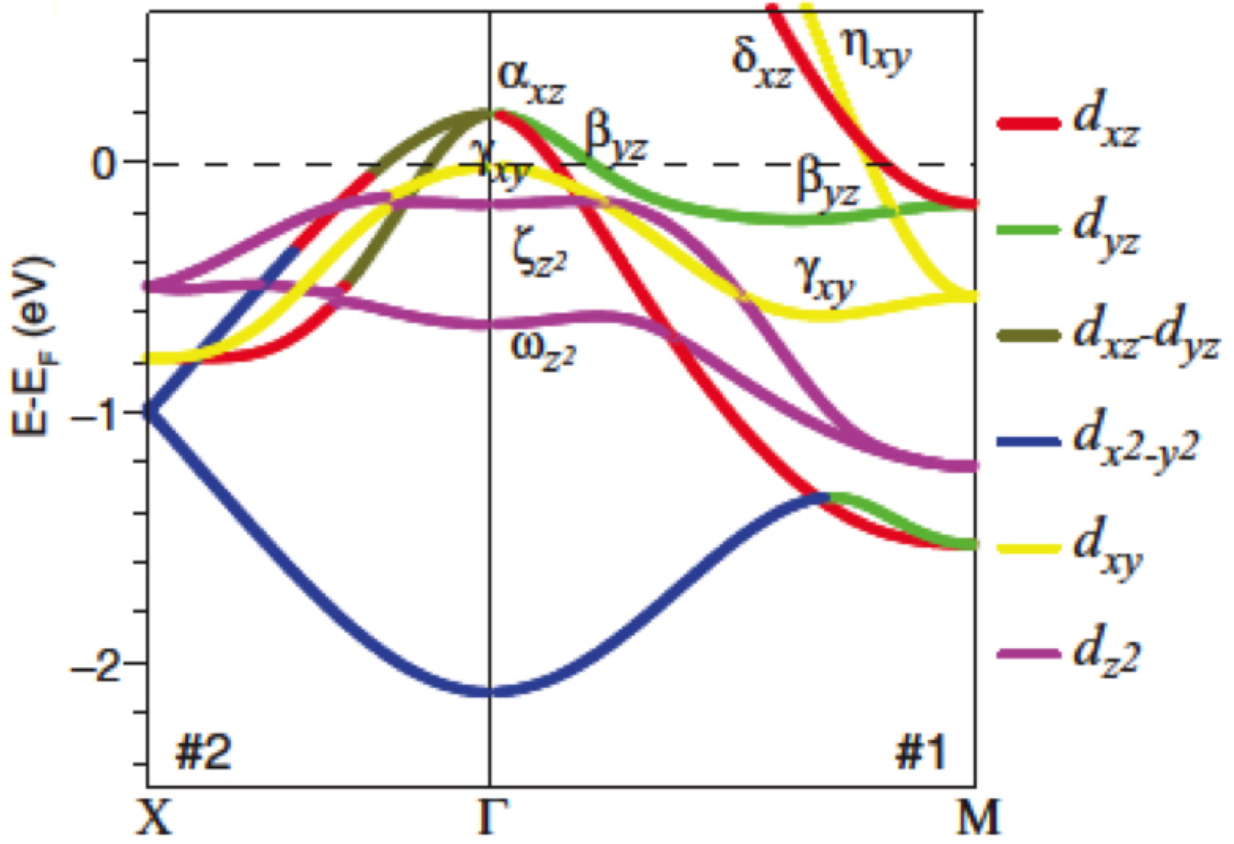
Figure 1.6: A typical orbital assignment of bands of iron pnictide as calculated in Ref. [290]
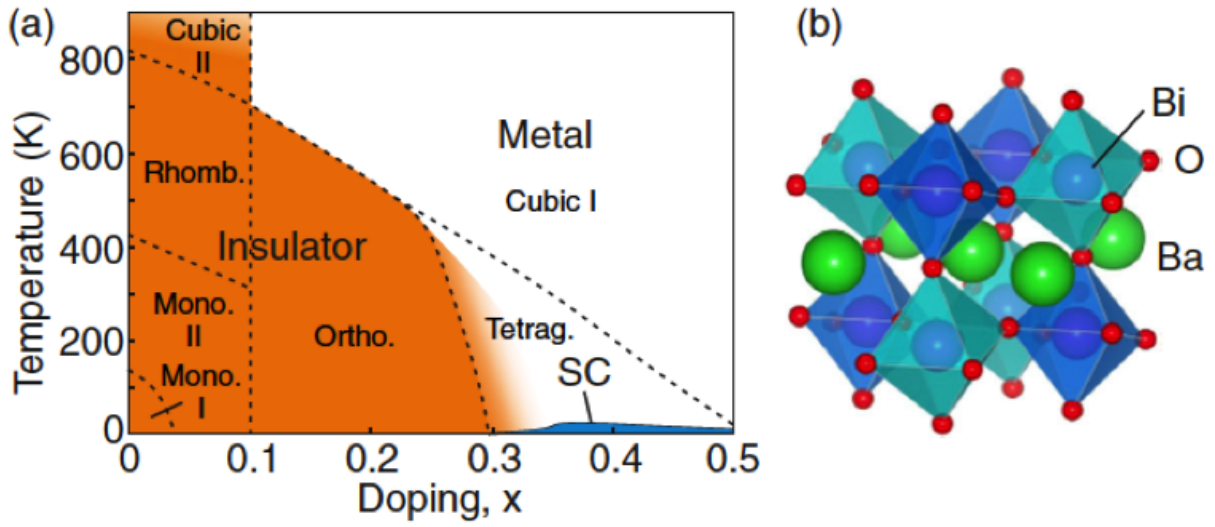
Figure 1.7: (a) Sketch of the x-T phase diagram of $Ba_{1-x}K_xBiO_3$. The space groups are: Mono. I=$P2_1/n$; Mono. II=$I2/m$; Rhomb.=$R\bar{3}$; Cubic II=$Fm\bar{3}m$. (b) Depiction of the insulating ground state ($x = 0$) exhibiting breathing and tilting distortions. The collapsed and expanded BiO_6 octahedra are shown in dark and light blue (gray), respectively. [207]

electronic band structure of $BaBiO_3$ near the Fermi surface is dominated by the Bi $6s$ and O $2p$ states (see Fig. 1.8[207]). It was found that most of Bi $6s$ states contribute to dispersive bands roughly 8 to 13 eV below the Fermi surface, while the O $2p$ states are located from 4 to 7 eV below the Fermi surface. This result consistent with the ARPES results [207] and suggests that when hole doping (i. e. K doping), most of holes occupy the O $2p$ orbitals within the sublattice of collapsed BiO_6 octahedra [73]. This result does not favor the $Bi^{3+}Bi^{5+}$ charge order state, in which holes should reside on the Bi atom to destroy the charge order.

In Pb or K-doped $BaBiO_3$ with high values of superconducting transition temperature are observed, which extended up to 13 K for Pb-doped alloys [11] and up to 30 K for K alloys [173]. The superconductivity of $Ba_{1-x}K_xBiO_3$ is observed with x values from about 0.30 to 0.45. The maximum T_c is 34 K occurs at $x \approx 0.35$. The crystal structure in the superconducting phase is tetragonal. The cubic-to-tetragonal transition is continuous. In $Ba_{1-x}K_xBiO_3$, with increasing x, holes are added to the parent system but without modifying the underlying BiO lattice. While in $BaPb_{1-x}Bi_xO_3$, the case is different. With increasing x, not only are holes introduced but also Bi atoms are replaced by Pb atoms. Superconductivity with narrow transition temperature is observed only close to $x = 0.25$ in $BaPb_{1-x}Bi_xO_3$.

1.2 Correlations in High T_c superconductors

1.2.1 Cuprates

Electrons on $3d$ orbitals have a strong local Coulomb interaction U that prevents two electrons to reside on a single site. Typically, the insulator driven by a strong local Coulomb interaction ($U \gg t$, t is the hopping integral) is called a Mott insulator. And the phase related to the Mott insulator is called a Mott phase, which can be described by the Hubbard model. It was found that the Mott transition in a single band Hubbard model is related to the lattice geometry, dimension, and U. For example, on a one-dimensional chain, the ground state for a half-filled band is insulating for any nonzero U [152]. On two-dimensional square lattices the critical value for the Mott phase transition at half filling is $U_c \sim 4t$[268];
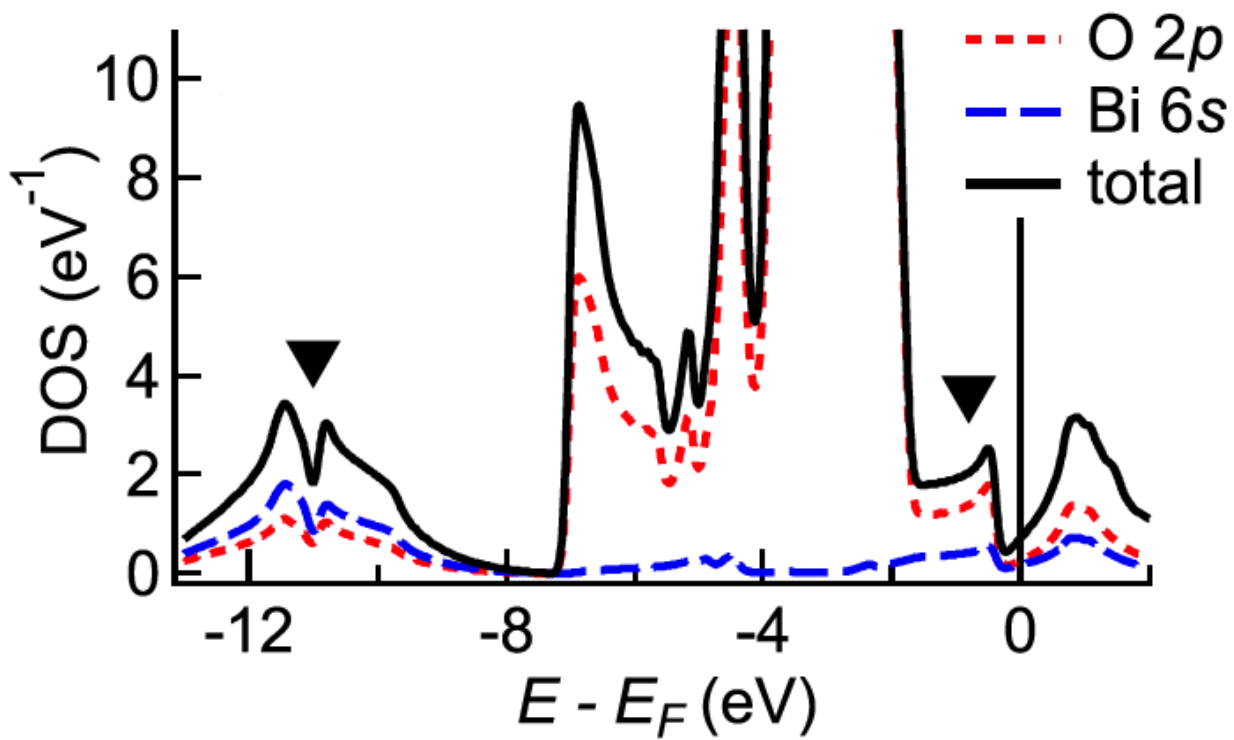
Figure 1.8: Calculated total DOS (solid line), as well as the O $2p$ and bi $6s$ orbital-projected DOS (short and long dashed lines, respectively.)[207]

but on two dimensional triangular lattices the phase transition boundary at hall filling is at $12t$ [7].

For the cuprates, the case is a little more complex. The hybridization between the Cu $3d_{x^2-y^2}$ and O $2p_{x(y)}$ electrons forms a bonding (B), nonbonding (NB), and antibonding (AB) bands near the Fermi surface (see fig. 1.9 (a)). The bonding and nonbonding bands are fully occupied and the antibonding band is half occupied. At half filling, the Hubbard interaction splits the antibonding band into two bands (see fig. 1.9(b)): the upper Hubbard band (UHB) and the lower Hubbard band (LHB). In the cuprates, the charge transfer energy Δ of moving one electron from oxygen atoms to the copper atom is smaller than the onsite Coulomb repulsion U, which characterizes these compounds more precisely as charge-transfer insulators (see fig. 1.9(c)) [284]. In the undoped cuprates, both the inverse photoemission spectroscopy [77, 274] and optical conductivity [250, 49] measurements found the charge transfer gap Δ is about 1.5 eV. Also, an extended photoemission spectroscopy study found that local Coulomb repulsion on the copper is about 12 eV in $La_{2-x}Sr_xCuO_4$ [237] and $Bi_2Sr_2CaCu_2O_8$ [286]. All these results support that the cuprates are charge-transfer insulators.

Therefore the cuprates should be described in terms of the three-band Hubbard model, in which Cu $3d_{x^2-y^2}$ as well as O $2p_x$ and $2p_y$ orbitals are included [67, 251]. However, because of the hybridization between the correlated Cu and the O orbitals, the first hole occupied state correspond to the O-derived Zhang-Rice singlet band (see fig. 1.9(d)) [288]. It was suggested that one can use an effective single-band Hubbard model to describe the cuprates. In the effective single-band Hubbard model, the Zhang-Rice singlet band corresponds to the lower Hubbard band, and the in-plane Cu-derived band is treated as the the upper Hubbard band. These two bands are separated by an effective Mott gap Δ. The Hamiltonian is written as

$$H = -t \sum_{\langle i,j \rangle, \sigma} \left(c_{i,\sigma}^\dagger c_{j,\sigma} + h.c. \right) + U \sum_i \hat{n}_{i,\uparrow} \hat{n}_{i,\downarrow}, \tag{1.1}$$
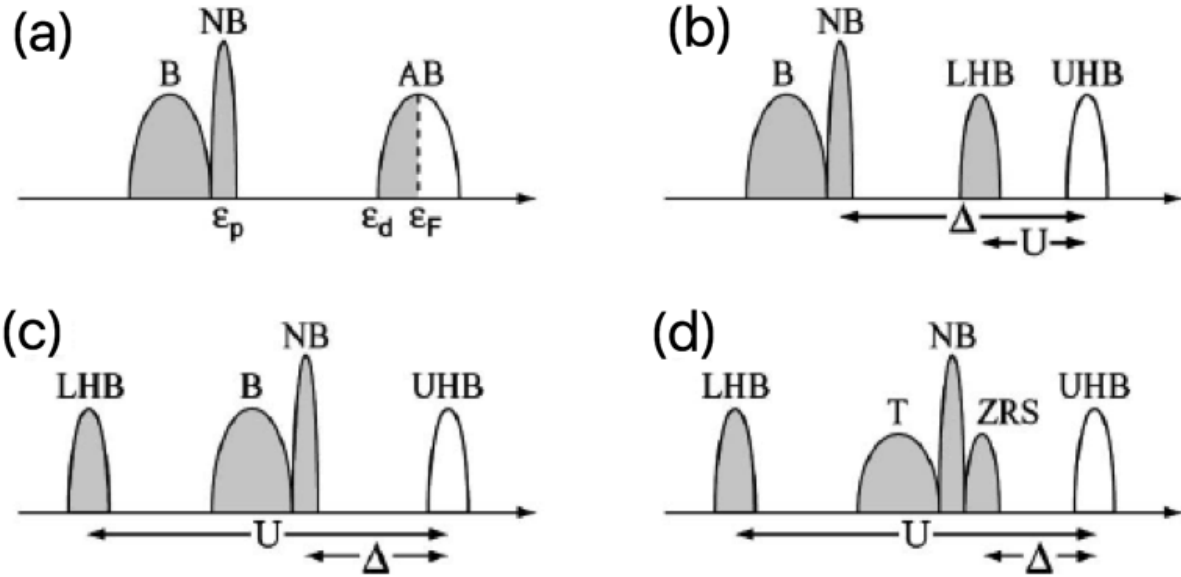
Figure 1.9: Density of states for opening a correlated gap. (a) the system is metallic in the absence of electronic correlations, and becomes (b) a Mott insulator or (c) a charge-transfer insulator, respectively, for $\Delta > W$ and $U > \Delta > W$. (f) due to the hybridization with the upper Hubbard band, the nonbonding band further splits into triplet and Zhang-Rice single states. In the graph, B, AB, and NB represent bonding, antibonding, and nonbonding bands, respectively. This graphs comes from Ref. [58]

.

in which $c_{i,\sigma}^{\dagger}\left(c_{i,\sigma}\right)$ creates (annihilates) an electron or hole on site i with spin σ, $\langle i,j \rangle$ represnets nearest-neighbor pairs, t is the hopping integral, and $\hat{n}_{i,\sigma} = c_{i,\sigma}^{\dagger}c_{i,\sigma}$ is the number operator.

In the strong-coupling limit $(U \gg t)$, the Hubbard Hamiltonian can simplify into the $t - J$ Hamiltonian [56], which is more commonly used in studying the low-lying excitations of the half filled antiferromagnetic insulator

$$H = -t \sum_{\langle i,j \rangle, \sigma} \left(\tilde{c}_{i,\sigma}^{\dagger}\tilde{c}_{j,\sigma} + h.c. \right) + J \sum_{\langle i,j \rangle} \left(\mathbf{S}_i \cdot \mathbf{S}_j - \frac{\hat{n}_i \hat{n}_j}{4} \right), \tag{1.2}$$

where the operator $\tilde{c}_{i,\sigma} = c_{i,\sigma}(1 - \hat{n}_{i,-\sigma})$ excludes double occupancy, $J = 4t^2/U$ is the antiferromagnetic exchange coupling constant, and $\mathbf{S}_i$ is the spin operator for site i.

1.2.2 Iron-based superconductors

Many theoretical and experimental studies have shown that the electronic correlations in the iron-based materials are not as strong as in the cuprates[273, 211]. A simple indication of this is the absence of any Mott physics in the FeSCs: the parent compounds are all metallic and there is no indication of nearby insulating behavior. Also x-ray absorption and inelastic scattering measurements on $SmFeAsO_{0.8}$, $BaFe_2As_2$, and $LaFe_2P_2$ show that their spectra closely resemble that of elemental metallic Fe, suggesting Hubbard $U \lesssim 2$ eV and Hund's coupling strength $J \sim 0.8$ eV [273].

Another key difference is that all 3d orbitals rather than a single $3d_{x^2-y^2}$ play essential roles in electronic properties in FeSCs, which requires us to consider a multiorbital hubbard model. The details of the multiorbital Hubbard model will be discussed in chapter 5. Multiple d orbitals in FeSCs produces more diverse phenomena than that in cuprates, such as Hund's metals [79] and spin-freezing behavior [265]. Also, it was found that different 3d orbitals in iron chalcogenides have different properties, which is called the orbital-selective property [275, 282]. For example, the d_{xy} orbital at Γ point is renormalized by a factor of ~ 16, while d_{xz} and d_{yz} orbitals are only renormalized by a factor of ~ 4 in $FeTe_{0.56}Fe_{1.72}Se_2$ [275]. Moreover, an ARPES study showed that the spectral weight of the d_{xy} orbital near the Fermi surface disappears when warming $FeTe_{0.56}Se_{0.44}$, $K_{0.76}Fe_{1.72}Se_2$, and FeSe film

grown on $SrTiO_3$, which suggests that the orbital-selective Mott phase (OSMP) transition occurs in iron chalcogenides as well [275, 276]. The OSMP refers to a phase in which a part of orbitals is Mott insulating while the other orbitals are metallic. Fig. 1.10 shows a theoretical simulation of the OSMP transition with different quasiparticle weight and orbital filling on five 3d orbitals for the regular and 1/5-depleted iron selenides square lattices, respectively [282]. The orbital-selective properties could be easily captured in fig. 1.10 and the Mott phase transition firstly occurred on the d_{xy} orbital, which coincides with experimental results. In sum, the physics picture in the FeSCs is more complex than that in the cuprates and many people argued that those multiple degrees of freedom, including orbital, charge, and spin, play a significant role in high-temperature superconductors [65].

1.2.3 $Ba_{1-x}K_xBiO_3$ and $BaPb_{1-x}BiO_3$ superconductors

$Ba_{1-x}K_xBiO_3$ is nonmagnetic and a transition-metal-free superconductor. Due to the fact that CDW and SC phases are presented in the phase diagram, a negative-U extended Hubbard model is proposed to explain the pairing mechanism [217, 251, 183]. But the issue is where does the negative U come from. Rice and his co-workers claimed the negative U arises from the electron-phonon interactions [217]; however, Varma proposed that the negative U occurs due to the nonlinear screening and the polarization of interatomic repulsion [251]. The nonlinear screening is that the energy of the $6s^0$ configuration is screened by the charge transfer from the oxygen octahedra to the 6p shell, which prefers double occupations on a Bi site. If the negative U has an electronic origin, the semiconducting phase of these materials is unique, because charge $\pm 2e$ bosonic bound states of two electrons or two holes dominate its transport properties. The electronic origin explains the two different gaps observed in the optical and transport experiments (2 and 0.24 eV, respectively) that in the optical experiments the excitation is two-particle excitation, while in the transport experiments the excitation is single particle excitation [246, 247]. But the superconducting transition temperature and the coherence length produced by the electronic origin are much higher and lower than results from experiments, respectively. Instead, if the phonon mechanism is employed, it is easy to get a reasonable numbers for the transition temperatures [246]. Later, photoemission and x-ray absorption experiments showed that the two gaps 2 eV and 0.24
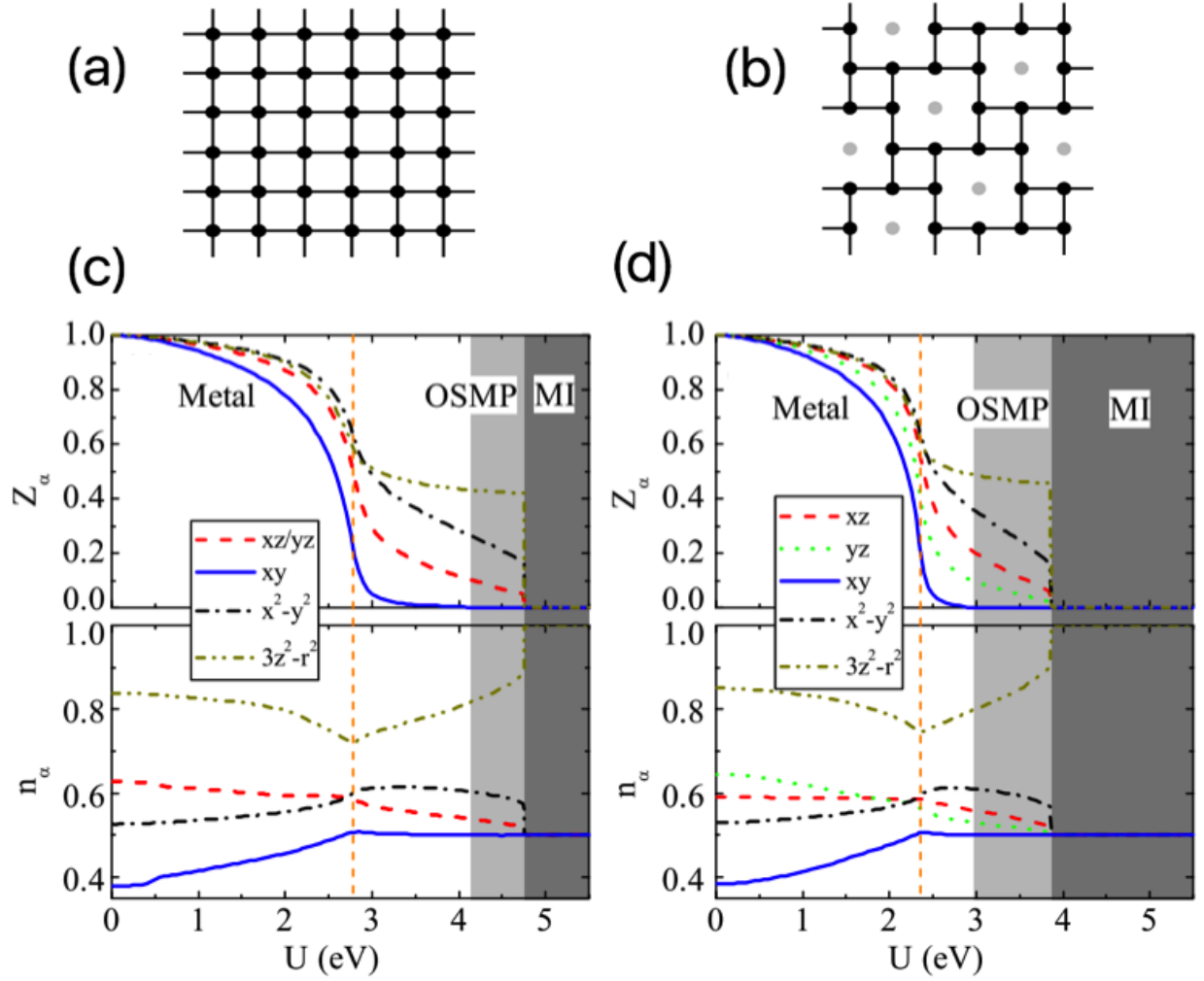
Figure 1.10: (a), (b) The regular and 1/5-depleted square lattices, respectively, corresponding to the alkaline iron selenides with disordered and $\sqrt{5} \times \sqrt{5}$ ordered iron vacancies. (c) and (d) shows the evolution of orbital resolved quasiparticle spectral weight Z_α and orbital filling factor (per iron site per spin) with U for the multiorbital model on lattices (a) and (b), respectively. This graphs is cited from Ref. [282]

.

eV in fact correspond to the direct and indirect energy gaps [124, 191]. This result is against the electronic origin. However, the problem of the phonon mechanism is that the electron-phonon coupling calculated by the standard DFT, LDA, or GGA approach is insufficient to account for the high T_c in $Ba_{1-x}K_xBiO_3$. This issue is addressed by introducing correlation effects in the standard DFT [74, 279]. It is found that the strong electronic correlations can enhance the e-ph coupling and estimated the realistic e-ph coupling $\lambda \sim 1.0$ for optimal hole doped $BaBiO_3$, which is large enough to explain the high Tc in K-doped $BaBiO_3$ [279]. However, Plumb *et. al.* compared band structures of $BaBiO_3$ from the standard DFT calculation and the angle-resolved photoemission spectroscopy (ARPES) experiment, and found that both band structures are consistent with each other [207]. This result indicates the electron correlations in $BaBiO_3$ is weak. If this conclution is correct, to support the phonon mechanism, the community needs to figure out to answer a question that how a small e-ph coupling can lead to a high T_c.

1.3 Evidence for the Electron-Phonon Interactions in high-T_C superconductors

1.3.1 the Cuprates

Many people believe the e-e interaction plays a key role in superconductivity in the cuprates and the e-ph interaction is negligible [12, 30, 87]. But this idea seems too premature in light of several experimental studies. For example, in different hole-doped cuprate materials, two kinks are observed in the electronic dispersion along the nodal and antinodal directions, respectively, using ARPES [136, 54]. A common sense is that these kinks are induced by the electron-boson coupling, but the question is whether the boson is the magnon or the phonon. This issue can be addressed considering that both kinks exist above and below T_c [54], suggesting the boson should not be the spin response mode, which only observed in certain materials and only below T_c. Moreover, it is suggested the nodal kink is induced by the half-breathing mode based on neutron experiments [206] and the antinodal kink is induced by the 40 meV B_{1g} oxygen "bond-buckling" phonon [54, 60, 142]. Both kinks are also observed in electron-doped cuprate superconductors and are likely induced by the half-

and full breathing mode phonons, respectively [201]. The evidence to support phonon is that in the electron-doped cuprate superconductors, neutron experiments showed that the energy of the spin resonance mode is at most 10 meV [270], which is much smaller than the energies of the nodal and antinodal kinks and the spin resonance mode could not be responsible for both kinks.

The importance of the phonon is also corroborated in inelastic neutron-scattering experiments and inelastic X-ray scattering, which showed the bond-stretching phonon anomaly in $La_{2-x}Sr_xCuO_4$ and $YBa_2Cu_3O_{0.95}$. [215, 216, 245]. This anomaly occurs at a wave vector corresponding to the charge order and is associated with charge inhomogeneity in cuprate superconductors.

Many people argue that the e-ph coupling cannot support the d-wave symmetry pairing in the cuprate superconductors, but the aforementioned facts imply that the e-ph coupling may be important to our understanding of superconductivity, although its contribution is likely to be indirect [114]. This indicates the e-ph coupling remains necessary to be studied in the correlated system.

Usually, there are two types of the e-ph couplings. The first one is via a deformation coupling where the atomic vibration modulates the overlap of the atomic orbitals of neighboring atoms. One famous theoretical model to capture this coupling is the Su-Shrieff-Heeger model [243], which has been widely used to study in organic materials [146]. This type of coupling is relevant to the half- and full breathing modes in the cuprates [60], which will be discussed in detail in chapter 6. The second one is the electrostatic coupling. This occurs when the lattice site oscillates through a local crystal field arising from an asymmetry in the local crystal environment. In this case, the e-ph coupling modulates the onsite energy of the atomic orbitals and can be described by the Holstein model, which is written as

$$H = -t \sum_{\langle i,j \rangle, \sigma} \left(c_{i,\sigma}^{\dagger} c_{j,\sigma} + h.c. \right) + \sum_i \left(\frac{\hat{p}_i^2}{2M} + \frac{K\hat{x}_i^2}{2} \right) + g \sum_{i,\sigma} \hat{x}_i \hat{n}_{i,\sigma}. \tag{1.3}$$

Here, $c_{i,\sigma}^{\dagger}$ $(c_{i,\sigma})$ is the electron creation operator, and $\hat{x}_i$ and $\hat{p}_i$ are the atoms' displacement and momentum operators, respectively. The last term of the Hamiltonian describes the

charge transfer e-ph coupling. In the cuprates, the coupling to the c-axis modes is largely of this type [61].

1.3.2   the FeSCs

Similar to the cuprates, the electron-phonon (e-ph) interaction was considered as a secondary interaction in FeSCs since a first principle study found the e-ph coupling constant in LaFeAsO is only $\lambda = 0.21$, which is not enough to produce high T_c [26]. This calculation is based on the paramagnetic phase, which is not the case for the parent compounds of FeSCs. It is suggested that the e-ph coupling through the spin channel is relevant in Fe pnictides, since the lattice is intimately involved in magnetism such as the Invar effect [66]. Later, DFT studies showed that the e-ph interaction is enhanced by the magnetism up to $\lambda \lesssim 0.35$ [280, 25, 48], which is still not enough to explain the high superconducting critical temperature but is strong enough to have a non-negligible effect on superconductivity and other properties. In experiments, infrared spectroscopy studies find an unusual redshift of the E_u mode in the K-doped $BaFe_2As_2$ [271] as well as the asymmetry line shape of the optical conductivity near the E_u mode [271, 101], suggesting the coupling between lattice vibrations and other channels, such as charge or spin. Recently, femtosecond time- and angle-resolved photoemission spectroscopy (trAPRES) and time-resolved x-ray diffraction (trXRD) measurements were performed to record the deformation energy induced by the A_{1g} phonon in FeSe [224]. It is found that the e-ph coupling strength is about ten times as estimated in Ref. [26], which could be captured in DMFT+LDA calculations. All these results highlight that phonons play an important role in shaping electronic properties in bulk FeSCs materials.

In addition, phonons become more pronounced at interfaces. Recently, it was discovered a dramatic enhancement of the superconducting transition temperature in FeSe, from 8 K in bulk [102] to nearly 70 K [141] when grown as a single unit cell layer on $SrTiO_3$ substrates. One suggested that this enhancement comes from the forward phonon scattering between the FeSe film and the substrate [141, 138, 258, 259, 213]. Also, some studies claimed that the substrate allows an antiferromagnetic ground state of FeSe and opens e-ph coupling channels within the monolayer[47]. In sum, the e-ph interaction cannot be neglected a priori in FeSCs.

1.3.3 $Ba_{1-x}K_xBiO_3$ and $BaPb_xBiO_3$ superconductors

The importance of e-ph interactions in $Ba_{1-x}K_xBiO_3$ has been revealed by many experiment studies and has been postulated in many theoretical works. For example, the oxygen-isotope effect is prominent in $Ba_{1-x}K_xBiO_3$ [13, 158, 94]. For a BCS superconductors, isotopic substitution of a particular atomic species will affect the superconducting transition temperature as well as the phonon spectrum. By measuring T_c between a 100% ^{16}O sample and a 65% ^{18}O exchanged sample of $Ba_{0.6}K_{0.4}BiO_3$, it was found the T_c obeys $T_c \sim M_O^{-\alpha_O}$, where M_O is the mass of the oxygen isotope and $\alpha_O = 0.22 \pm 0.03$ [13]. Also, the e-ph coupling is confirmed in the Tunneling spectroscopy measurements and it was found clear evidence of phonon images in tunneling conductance up to 60 meV [287, 103] and the e-ph coupling constant $\lambda \sim 1$ [94]. This large e-ph coupling constant is confirmed by specific heat experiments as well [130].

Although it was proposed that the nonlinear screening can induce the negative-U in the Hubbard model, the detailed numerical calculations are not available. Moreover, it was found the effective Hubbard U is always positive in the five-orbital model, including Bi s and p, and O p_σ orbitals, in the four-orbital model, including Bi s and O p_σ orbitals, and in an effective one band model using the constrained density-functional theory [253]. There is no indication of a negative U arising from the electronic origin.

1.3.4 Nonlinear electron-phonon coupling

The electron-phonon coupling is one of the factors determining the stability of cooperative order in solids, such as the superconductivity, charge, and spin density waves. In the pump-probe experiments, the transient lattice displacement driven by the optical photons could be large, implicating the nonlinear e-ph coupling needed to be considered. Therefore, the ability of controlling the e-ph coupling strength by optical driving may open up new possibilities to steer materials' functionalities. For example, the nonlinear e-ph coupling of Raman-active modes has been widely studied in MgB_2 and is treated as a key factor to explain the observed high T_C and boron isotope effect in MgB_2 [277]. Also, both terahertz time-domain spectroscopy (THZ TDS) and time- and angle-resolved photoemission spectroscopy

(tr-ARPES) experiments showed a transient threefold enhancement of the e-ph coupling constant in SiC [208], which is likely due to the nonlinear e-ph coupling [235]. But another tr-ARPES experiment showed the transient electron-boson interaction is reduced in a cuprate superconductor [289]. The suppression of the electron-boson coupling may be due to the interplay between the nonlinear e-ph interaction and the Coulomb interaction. However, it remains unclear how the nonlinear e-ph coupling corporate/compete with the linear e-ph coupling and the Coulomb interaction in solid materials [120]. In the chapter 3, I will answer a part of this question and explain the interplay between the nonlinear and linear e-ph couplings and study its effect on the superconductivity and the CDW phase.

1.4 Scope and Organization

The goal of this thesis is to examine the role of e-ph interactions in multiorbital strongly correlated systems using numerical techniques. The overall organization is as follows. Chapter 1 (this chapter) focus on introducing e-e correlations and e-ph interactions in high-temperature superconductors, including cuprates, FeSCs, and $Ba_{1-x}K_xBiO_3$. The effective Hubbard model for the cuprates and the Holstein model, in which the onsite energy of the atomic orbitals is modulated by the lattice vibration, are introduced as well in this chapter.

Chapter 2 introduces two numerical techniques used to solve the Hamiltonian relevance to phonons and correlated electrons. The first one is the determinant quantum monte carlo (DQMC) and the second one is the dynamical mean field theory (DMFT). I will use the Hubbard model to illustrate how these two techniques work.

In chapter 3 I will study the role of the nonlinear e-ph coupling in an modified Holstein model. Here, the e-e interaction is not included in this model. My starting point is to understand the interplay between the nonlinear and linear e-ph couplings absence of the Coulomb interaction. The influence of the Coulomb interaction will be considered in my future research.

In chapter 4 I will examine the momentum dependence of the orbital-selective behavior in a three-orbital Hubbard model. It will be shown that itinerant electrons in the OSMP have strong momentum dependence while the localized electrons are almost momentum

independent. This study also paves a way to further examine the role of the e-ph interaction in the OSMP.

In chapters 5 I will study the influence of the e-ph interaction on the orbital-selective behavior in a multiorbital Hubbard-Holstein model. This work will be done in both infinite- and one-dimensions using DMFT and DQMC, respectively. It will show that a weak to intermediate e-ph coupling can strongly modified the phase diagram both in a 1D system and an infinite dimension system. It is hopefully to extend my conclusion to two and three dimensions, where the cuprates and FeSCs is relevant.

In chapter 6 I will study the breathing phonon in superconductors $Ba_{1-x}K_xBiO_3$. I will show how the nonlocal e-ph coupling produces a dimerized structure and how this structure disappears as doping. Also, I will study the localization of polarons and bipolarons in the metal-to-insulator transition. The superconducting state induced by the breathing phonon will examined as well.

Finally, in chapter 7, conclusions will be presented as well as discussion of possible extensions of this work in the future.

Chapter 2

Methodology

Most of the strongly correlated many body problems cannot be solved in analytically. One simple model for the correlated systems is the Hubbard model. In this chapter, I will present two numerical methods to solve the Hubbard model. The first method is the determinant quantum Monte Carlo, which allows to treat e-e and e-ph interactions exactly. The second one is the dynamical mean field theory, which neglects spatial correlations. The application of the determinant quantum Monte Carlo to the Holstein model is also discussed in this chapter.

2.1 Hubbard model

The Hubbard model was originally proposed to describe the ferromagnetism in transition metals [104]. The Hamiltonian includes the electron hopping and onsite electron-electron interaction terms and is written as

$$H = - \sum_{\langle i,j \rangle, \sigma} t_{i,j} c_{i,\sigma}^{\dagger} c_{j,\sigma} + \sum_{i} U \hat{n}_{i,\uparrow} \hat{n}_{i,\downarrow} - \mu \sum_{i} \hat{n}_{i,\uparrow} \hat{n}_{i,\downarrow}, \tag{2.1}$$

in which $c_{i,\sigma}^{\dagger}$ creates an electron with spin σ on site i, t_{ij} is the hopping integral, U is the onsite Coulomb repulsion strength, and μ is the chemical potential used to fix the charge density. The Hubbard model describes an interacting many-body system which cannot be solved analytically, except in dimension $d = 1$ with nearest-neighbor hopping [152]. To study

correlation phenomena such as the Mott transition in higher dimensions, both dynamical mean field theory (DMFT) [78, 166] and Quantum Monte Carlo (QMC) methods have been widely applied.

To better understand the Hubbard model, I will discuss the solution of the single site case, which is the simplest case. In the single site limit, the electron Green's function at the imaginary time τ is

$$
\begin{aligned}
G(\tau) &= -\langle T_\tau c_\uparrow(\tau) c_\downarrow^\dagger(0) \rangle \\
&= -\frac{e^{\mu\tau} + e^{\beta\mu} e^{\tau(\mu-U)}}{1 + 2e^{\beta\mu} + e^{\beta(2\mu-U)}},
\end{aligned}
\tag{2.2}
$$

where β is the reciprocal of the thermodynamic temperature. The Green's function in the Matsubara frequency space is

$$
\begin{aligned}
G(\mathrm{i}\omega_n) &= \int_0^\beta d\tau G(\tau) e^{\mathrm{i}\omega_n \tau} \\
&= \frac{1}{1 + 2e^{\beta\mu} + e^{\beta(2\mu-U)}} \left[\frac{e^{\mu\beta} + 1}{\mu + \mathrm{i}\omega_n} + \frac{e^{(2\mu-U)\beta} + e^{\mu\beta}}{\mu - U + \mathrm{i}\omega_n} \right].
\end{aligned}
\tag{2.3}
$$

The spectral function is obtained via

$$
-G(\tau) = \int_{-\infty}^{\infty} A(\omega) \frac{e^{-\omega\tau}}{1 + e^{-\beta\omega}} d\omega,
\tag{2.4}
$$

in which

$$
A(\omega) = \frac{1 + e^{\beta\mu}}{1 + 2e^{\beta\mu} + e^{\beta(2\mu-U)}} \delta\left(\omega + \mu\right) + \frac{e^{\beta\mu} + e^{\beta(2\mu-U)}}{1 + 2e^{\beta\mu} + e^{\beta(2\mu-U)}} \delta\left(\omega + \mu - U\right).
\tag{2.5}
$$

Equation 2.5 shows that there are two δ functions in the spectral functions. These two δ functions are separated by a Mott gap with a scale of U. On the cluster, these two δ functions are expanded to continuous functions.

2.2 Determinant Quantum Monte Carlo Method

Solving the Hubbard model on the cluster remains a big challenge to date. Determinant quantum Monte Carlo is one of the ways to solve the Hubbard model exactly. DQMC is an auxiliary field imaginary-time Monte Carlo method for simulating interacting systems of particles in the grand canonical ensemble [24, 231, 269]. In the following, I will discuss the application of DQMC in solving the Hubbard model.

2.2.1 The General Methodology

First I divide the Hubbard model into two parts, $H = K + V$, where

$$
K = -t \sum_{i,\sigma}(c_{i,\sigma}^{\dagger}c_{i+1,\sigma} + h.c.) - \mu \sum_{i}(n_{i,\uparrow} + n_{i\downarrow}), \tag{2.6}
$$

$$
V = U \sum_{i} n_{i\uparrow}n_{i\downarrow} \tag{2.7}
$$

Here, K is the non-interacting Hamiltonian and V is the Hubbard interaction. In DQMC, the major task is to calculate the partition function $Z \equiv \mathrm{Tr}e^{-\beta H}$. One way to obtain the partition function is dividing the inverse temperature interval $[0, \beta]$ into many small imaginary time slices $\Delta\tau = \beta/L$ (L is the number of time slices). Then the partition function can be written as

$$
\begin{aligned}
Z &\equiv \mathrm{Tr}e^{-\beta H} \\
&= \mathrm{Tr}e^{-\Delta\tau LH} \\
&= \mathrm{Tr}\left[e^{-\Delta\tau V}e^{-\Delta\tau K}\right]^{L} + \mathcal{O}\left(\Delta\tau^{2}\right) \\
&\approx \mathrm{Tr}\prod_{l}\left[e^{-\Delta\tau V}e^{-\Delta\tau K}\right].
\end{aligned} \tag{2.8}
$$

In the Eq. (2.8) the Trotter approximation is applied [269, 76]. $\Delta\tau$ is a controllable error, and when $\Delta\tau$ is small enough, this approximation is reasonable. The Hubbard interaction term can be reduced into quadratic terms by introducing an auxiliary field $s_{i,l} = \pm 1$ at each

site and time slice and applying a discrete Hubbard-Stratonovich transformation [95]

$$
e^{-\alpha n_{i,\uparrow} n_{i,\downarrow}} =
\begin{cases}
\frac{1}{2} e^{\alpha/2(n_{i,\uparrow}+n_{i,\downarrow})} \sum_{s_{i,l}=\pm 1} e^{-\lambda s_{i,l}(n_{i,\uparrow}-n_{i,\downarrow})} & (\alpha > 0) \\
\frac{1}{2} e^{\alpha/2(n_{i,\uparrow}+n_{i,\downarrow})} \sum_{s_{i,l}=\pm 1} e^{-\lambda s_{i,l}(n_{i,\uparrow}+n_{i,\downarrow}-1)+\frac{\alpha}{2}} & (\alpha < 0)
\end{cases},
\tag{2.9}
$$

where $\lambda = \ln(e^{|\alpha|/2} + \sqrt{e^{|\alpha|}-1})$. In the single band Hubbard model $\alpha = \Delta\tau U > 0$. Then the partition function can be written as

$$
\begin{aligned}
Z &= \text{Tr} \prod_l \left[e^{-\Delta\tau V(l)} e^{-\Delta\tau K} \right] \\
&= \text{Tr} \prod_l \left\{ \left[\prod_i \frac{1}{2} e^{\alpha/2(n_{i,\uparrow}+n_{i,\downarrow})} \sum_{s_{i,l}=\pm 1} e^{-\lambda s_{i,l}(n_{i,\uparrow}-n_{i,\downarrow})} \right] e^{-\Delta\tau K} \right\}.
\end{aligned}
\tag{2.10}
$$

The term $e^{\alpha/2(n_{i,\uparrow}+n_{i,\downarrow})}$ can be absorbed into the chemical potential by changing K to $K' = K + \sum_i \frac{U}{2}(n_{i,\uparrow} + n_{i,\downarrow})$. If I define matrices

$$
B_l^{\uparrow(\downarrow)} = e^{-(+)\sum_i \lambda s_{i,l} n_{i,\uparrow(\downarrow)}} e^{-\Delta\tau K'},
\tag{2.11}
$$

the partition function becomes

$$
\begin{aligned}
Z &= \text{Tr} \prod_l (\sum_{s_{i,l}} B_l^{\uparrow} B_l^{\downarrow}) \\
&= \sum_{s_{i,l}\pm 1} \text{Tr}(B_L^{\uparrow} B_{L-1}^{\uparrow} ... B_1^{\uparrow}) \text{Tr}(B_L^{\downarrow} B_{L-1}^{\downarrow} ... B_1^{\downarrow}).
\end{aligned}
\tag{2.12}
$$

In order to calculate the partition function, I use the following relationship [24]

$$
\text{Tr} \left(e^{c^\dagger T_1 c} \ e^{c^\dagger T_2 c} \ ... e^{c^\dagger T_n c} \right) = \det \left(I + e^{T_1} e^{T_2} ... e^{T_n} \right),
\tag{2.13}
$$

where $c^\dagger = \left[c_1^\dagger, c_2^\dagger, \ldots, c_N^\dagger \right]$ is a row vector and I is a $N \times N$ identity matrix (N is the size of the system). T_m is an arbitrary symmetric matrix. Then the partition function is

$$
Z = \sum_{s_{i,l}=\pm 1} \det \left(I + B_L^{\uparrow} B_{L-1}^{\uparrow} ... B_1^{\uparrow} \right) \det \left(I + B_L^{\downarrow} B_{L-1}^{\downarrow} ... B_1^{\downarrow} \right)
$$

$$= \sum_{s_{i,l}=\pm 1} \det\left(M^{\uparrow}\right)\det\left(M^{\downarrow}\right), \tag{2.14}$$

in which $M^{\uparrow(\downarrow)} = I + B_L^{\uparrow(\downarrow)}B_{L-1}^{\uparrow(\downarrow)}...B_1^{\uparrow(\downarrow)}$.

The thermodynamic expectation value of any observable $\hat{O}$ at finite temperature is defined by

$$\langle\hat{O}\rangle = \frac{\mathrm{Tr}\left(\hat{O}e^{-\beta H}\right)}{Z}. \tag{2.15}$$

Most observables can be expressed in terms of the single particle Green's function. The equal time Green's function $G_{ij}^{\sigma}(l)$ at a discrete time $\tau = l\Delta\tau$ and at a displacement $\mathbf{d} = \mathbf{r}_i - \mathbf{r}_j$ for an electron propagating through the field produced by the $s_{i,l}$ is given by [269]

$$
\begin{aligned}
G_{ij}^{\sigma}(l) &= \langle \mathrm{T}_\tau[c_{i,\sigma}(\tau)c_{j,\sigma}^\dagger(\tau)]\rangle \\
&= [I + B_l^\sigma...B_1^\sigma B_L^\sigma...B_{l+1}^\sigma]_{ij}^{-1} \\
&= M_{i,j}^{-1}.
\end{aligned} \tag{2.16}
$$

To evaluate $\langle\hat{O}\rangle$, Eqs. 2.14 and 2.15 show that I need to do a summation over all $\{s_{i,l}\}$ configurations. However, it is impossible to go through all $\{s_{i,l}\}$ configurations in numerical calculations. To overcome this issue, I use the importance sampling method in the Monte Carlo. Here, the importance sampling generates a sequence of Hubbard-Stratonovich (HS) configurations $\{s_{i,l}\}$, with a distribution probability $p\left(\{s_{i,l}\}\right) = \frac{\det M^{\uparrow}\det M^{\downarrow}}{Z}$. In the Monte Carlo, the transition probability $W\left(\{s_{i,l}\} \to \{s'_{i,l}\}\right)$ decides how to accept an update. The relationship between the transition probability and the distribution probability is given by a detailed balance condition

$$W\left(\{s_{i,l}\} \to \{s'_{i,l}\}\right) \times p\left(\{s_{i,l}\}\right) = W\left(\{s'_{i,l}\} \to \{s_{i,l}\}\right) \times p\left(\{s'_{i,l}\}\right). \tag{2.17}$$

Then I have

$$\frac{W\left(\{s_{i,l}\} \to \{s'_{i,l}\}\right)}{W\left(\{s'_{i,l}\} \to \{s_{i,l}\}\right)} = \frac{p\left(\{s'_{i,l}\}\right)}{p\left(\{s_{i,l}\}\right)} \equiv R. \tag{2.18}$$

In the Monte Carlo, I can only obtain R rather than $W\left(\{s_{i,l}\} \to \{s'_{i,l}\}\right)$ and $W\left(\{s'_{i,l}\} \to \{s_{i,l}\}\right)$. The specified value of $W\left(\{s_{i,l}\} \to \{s'_{i,l}\}\right)$ is not given in Eq. (2.18). But I can choose any $W\left(\{s_{i,l}\} \to \{s'_{i,l}\}\right)$ once it satisfy Eq. (2.18). One typical solution is the Metropolis-Hastings algorithm [91, 18]. Here, I use the heat bath method [53], which is given by

$$W\left(\{s_{i,l}\} \to \{s'_{i,l}\}\right) = \begin{cases} \frac{R}{R+c} & R > 1 \\ \frac{R}{1+c\times R} & R \leq 1 \end{cases}, \tag{2.19}$$

where c is adjusted in our code to maintain a certain acceptance rate.

In the determinant quantum Monte Carlo, I first set the initial HS field for each time slice and site and then flip the HS field at one site and time slice. The ratio of determinants after and before flipping is

$$R = R^{\uparrow}R^{\downarrow} = \frac{\det M'^{\uparrow}\det M'^{\downarrow}}{\det M^{\uparrow}\det M^{\downarrow}}. \tag{2.20}$$

in which M'^{σ} is a new M matrix after flipping a field $s_{i,l} \to -s_{i,l}$. There is an efficient algorithm for calculating R^{σ} [269, 115], that is

$$R^{\sigma} = \frac{\det M'^{\sigma}}{\det M^{\sigma}} = 1 + [1 - G_{ii}^{\sigma}(l)]\Delta_{ii}^{\sigma}(i,l), \tag{2.21}$$

in which $\Delta_{jk}^{\uparrow,\downarrow}(i,l) = \delta_{ji}\delta_{ki}[e^{\pm 2\Delta\tau s_{i,l}} - 1]$. For each flip, the transition probability is calculated via Eq. (2.19) and compared to a random number r. Once $W\left(\{s_{i,l}\} \to \{s'_{i,l}\}\right) > r$ I accept this field flipping with a new Green's function

$$G'^{\sigma}(l) = G^{\sigma}(l) - \frac{G^{\sigma}(l)\Delta^{\sigma}(i,l)[1 - G^{\sigma}(l)]}{1 + [1 - G_{ii}^{\sigma}(l)]\Delta_{ii}^{\sigma}(i,l)}. \tag{2.22}$$

After all sites on a given time slice have been updated, I advance to the next time slice. The Green's function for the next slice is given by

$$G^{\sigma}(l+1) = B_{l+1}^{\sigma}G^{\sigma}(l)[B_{l+1}^{\sigma}]^{-1}. \tag{2.23}$$

In DQMC I first set a large number of updating steps for warming up in that the HS fields should be updated close to the thermal equilibrium configurations before any measurement is applied.

2.2.2 Unequal Time Green's Function

Green's function $G(\mathbf{r}_i, \tau_l; \mathbf{r}_j, \tau_{l'})$ is a function of $\mathbf{r}_i - \mathbf{r}_j$ and $\tau_l - \tau_{l'}$. When $\tau_l = \tau_{l'} = l\Delta\tau$, Green's function $G(\mathbf{r}_i, \tau_l; \mathbf{r}_j, \tau_{l'})$ becomes equal time Green's function $G_{ij}(l)$. The equal time Green's function can be calculated via Eq. (2.16). However, in order to measure dynamic quantities, one needs to measure the unequal time Green's function ($\tau_l \neq \tau_{l'}$), which can be obtained by [115]

$$G(\tau_l, \tau_{l'}) = \begin{cases} G(l') \left[B(l-1) \cdots B(l') \right] & (\tau_l > \tau_{l'}) \\ -G(l') \left[B(l-1) \cdots B(1) B(L) \cdots B(l') \right] & (\tau_l < \tau_{l'}) \end{cases} \tag{2.24}$$

2.2.3 Measurements and Error Estimates

The average value of an observable $\hat{O}$ defined in Eq. (2.15) is obtained by

$$\langle \hat{O} \rangle = \frac{1}{M} \sum_{k=1}^{M} \langle O \rangle_k, \tag{2.25}$$

where M is the number of measurements, $\langle O \rangle_k$ is the result at a given field configuration $\{s_{i,l}\}$. The sample variance is defined by

$$s^2 = \frac{1}{M-1} \sum_{k=1}^{M} [\langle O \rangle_k - \langle \hat{O} \rangle]^2, \tag{2.26}$$

Many physical observables can be evaluated by the Green's function. For example, the charge density $n_{i,\sigma}$ of spin σ on the site i is obtained by

$$\langle n_{\sigma,i} \rangle = \frac{1}{L} \sum_{l=0}^{L-1} [1 - G_{ii}^{\sigma}(l)]. \tag{2.27}$$

The double occupancy on site i is given by

$$\langle n_{i,\uparrow} n_{i,\downarrow} \rangle = \frac{1}{L} \sum_{l=0}^{L-1} \left(1 - G_{ii}^{\uparrow}(l)\right) \left(1 - G_{ii}^{\downarrow}(l)\right), \tag{2.28}$$

and the local moment on site i is

$$\langle (n_{i,\uparrow} - n_{i,\downarrow})^2 \rangle = \langle n_{i,\uparrow} + n_{i,\downarrow} \rangle - 2\langle n_{i,\uparrow} n_{i,\downarrow} \rangle$$
$$= \frac{1}{L} \sum_{l=0}^{L-1} \left[\left(2 - G_{ii}^{\uparrow}(l) - G_{ii}^{\downarrow}(l)\right) - 2\left(1 - G_{ii}^{\uparrow}(l)\right)\left(1 - G_{ii}^{\downarrow}(l)\right) \right]. \tag{2.29}$$

Correlation functions can be expressed in terms of $G^{\sigma}(\tau)$ through application of the Wick theorem as well [165]. For example, the charge-density-correlation function χ_{CDW} is defined as [230, 172]

$$\chi_{\text{CDW}}(\mathbf{q}) = \frac{1}{N} \int_0^{\beta} d\tau \langle \rho_{\mathbf{q}}(\tau) \rho_{\mathbf{q}}^{\dagger}(0) \rangle$$
$$= \frac{1}{N} \sum_{\mathbf{r}_i, \mathbf{r}_j, \sigma, \sigma'} e^{-i\mathbf{q} \cdot (\mathbf{r}_i - \mathbf{r}_j)} \int_0^{\beta} d\tau \langle n_{\mathbf{r}_i, \sigma}(\tau) n_{\mathbf{r}_j, \sigma'}(0) \rangle \tag{2.30}$$

in which $\rho_{\mathbf{q}}(\tau) = \sum_{\mathbf{r}_i, \sigma} e^{-i\mathbf{q} \cdot \mathbf{r}_i} n_{\mathbf{r}_i, \sigma}(\tau)$, $n_{\mathbf{r}_i, \sigma} = c_{\mathbf{r}_i, \sigma}^{\dagger}(\tau) c_{\mathbf{r}_i, \sigma}(\tau)$, and N is the total cluster size. Following Wick theorem, $\langle n_{\mathbf{r}_i, \sigma}(\tau) n_{\mathbf{r}_j, \sigma'}(0) \rangle$ is calculated by

$$\langle n_{\mathbf{r}_i, \sigma}(\tau) n_{\mathbf{r}_j, \sigma'}(0) \rangle = \begin{cases} \langle n_{\mathbf{r}_i, \sigma}(0) \rangle & \mathbf{r}_i = \mathbf{r}_j, \sigma = \sigma', \tau = 0 \\ \langle n_{\mathbf{r}_i, \sigma}(\tau) \rangle \langle n_{\mathbf{r}_j, \sigma'}(0) \rangle & \sigma \neq \sigma' \\ \langle n_{\mathbf{r}_i, \sigma}(\tau) \rangle \langle n_{\mathbf{r}_j, \sigma}(0) \rangle - \\ G^{\sigma}(\mathbf{r}_j - \mathbf{r}_i, -\tau) G^{\sigma}(\mathbf{r}_i - \mathbf{r}_j, \tau) & \sigma = \sigma' \end{cases}.$$

The magnetic correlations $\chi_{\text{S}}(\mathbf{q})$ is given by [269, 95]

$$\chi_{\text{S}}(\mathbf{q}) = \frac{1}{N} \sum_{\mathbf{r}_i, \mathbf{r}_j} e^{i\mathbf{q} \cdot (\mathbf{r}_i - \mathbf{r}_j)} \int_0^{\beta} d\tau \left\langle \left[n_{\mathbf{r}_i, \uparrow}(\tau) - n_{\mathbf{r}_i, \downarrow}(\tau) \right] \left[n_{\mathbf{r}_j, \uparrow}(0) - n_{\mathbf{r}_j, \downarrow}(0) \right] \right\rangle. \tag{2.31}$$

For conventional superconductors, the gap has s-wave symmetry; while for cuprates, the gap has d-wave symmetry. The different gap symmetries lead to different formulas for pair-field or superconducting susceptibilities. For completeness, a general formula for these two kinds of gaps with only onsite and nearest neighbor correlations is [269, 230, 172]

$$\chi_{\text{SC}} = \frac{1}{N} \int_0^\beta d\tau \langle \Delta\ (\tau)\Delta^\dagger(0) \rangle, \tag{2.32}$$

where

$$\Delta^\dagger(\tau) = \begin{cases} \sum_i c_{i,\uparrow}^\dagger c_{i,\downarrow}^\dagger & s-\text{wave} \\ \frac{1}{2} \sum_{i,\delta} P_\delta c_{i,\uparrow}^\dagger c_{i+\delta,\downarrow}^\dagger & d-\text{wave} \end{cases}. \tag{2.33}$$

Here, δ is an index that runs over nearest neighbors of the site i and the phase factor P_δ alternates in sign with $P_{\pm\hat{x}} = 1 = -P_{\pm\hat{y}}$. To distinguish the two gap symmetries, the pair-field susceptibilities will be denoted χ_s and χ_d for the s- and d- wave case, respectively.

2.2.4 The Fermion Sign Problem

In general, the factor $\det(M^\uparrow)\det(M^\downarrow)$ is not positive due to Fermi statistics. When I apply an operator $c_{j,\sigma}^\dagger$ to a many-body wave function $|\psi\rangle$, a phase factor ± 1 is determined by the order of the creation operators $c_{i,\sigma}^\dagger$ applied to the vacuum state to produce $|\psi\rangle$. But I don't know this order in my DQMC calculations, which results in a negative value of $\det(M^\uparrow)\det(M^\downarrow)$ for some configurations. This negative problem is called the Fermion sign problem. To overcome it the absolute value of the product $|\det(M^\uparrow)\det(M^\downarrow)|$ is used and the expectation value of an observable must be augmented by

$$\langle \hat{O} \rangle = \frac{\langle OP_s \rangle}{\langle P_s \rangle}, \tag{2.34}$$

where P_s denotes the sign of the product $\det(M^\uparrow)\det(M^\downarrow)$. The average sign depends on a number of factors including the size of the system, the overall filling, the strength of the interaction U, and inverse temperature β [157, 105]. At low temperature, the sign problem becomes terrible and the average sign value tends toward zero for the Hubbard model at

non-half fillings due to particle-hole asymmetry. When the average sign value close zero, the observable obtained from Eq. 2.34 becomes a meaningless large value.

2.3 Dynamical Mean Field Theory

2.3.1 Fermions in infinite dimensions

The DMFT maps a lattice problem with many degrees of freedom onto an effective single-site problem with fewer degrees of freedom. More specifically, instead of studying the lattice problem, DMFT extracts a local site on the cluster and using bath levels to effective describte the hybridization on the cluster. At the same time, DMFT keeps all local interaction on this local site. Results from DMFT are quanlitive correct for high dimensions and become exact in the limit of infinite dimensions ($d \to \infty$) [78, 84].

Before talking about the DMFT technique, it is necessaty to rescale the Hubbard Hamiltonian to ensure that in the $d \to \infty$ limit the energy per lattice site does not diverge. The on-site Coulomb interaction term is not sensitive to the dimensionality and U can be the same. The total kinetic energy in the mean field approximation with nearest-neighbour hopping t is $H_{\mathrm{KE}} = \int d\varepsilon \rho(\varepsilon) t$, and the density of states for the hyper-cubic lattice is $\rho(\varepsilon) = \int \frac{d^d k}{(2\pi)^d} \delta(\varepsilon - \varepsilon_{\mathbf{k}})$, in which $\varepsilon_{\mathbf{k}} = -2t \sum_{i=1}^{d} \cos(k_i)$. In the infinity dimension ($d \to \infty$), the bandwidth diverges and so do the density of states and kinetic energy. The proper scaling is determined from the density of states for $d \to \infty$. One way to obtain the density of states for $d \to \infty$ uses the Fourier transform of $\rho(\varepsilon)$, which factorizes:

$$
\begin{aligned}
\Phi(s) &= \int_{-\infty}^{\infty} d\varepsilon e^{is\varepsilon} \rho(\varepsilon) = \int \frac{d^d k}{(2\pi)^d} e^{is\varepsilon_k} \\
&= \left[\int_{-\pi}^{\pi} \frac{dk}{2\pi} \exp\left(-\frac{2ist_*}{\sqrt{sd}} \cos(k) \right) \right]^d = J_0 \left(\frac{2t_*}{\sqrt{2d}} \right)^d \\
&= \left[1 - \frac{t_*^2 s^2}{2d} + O\left(\frac{1}{d^2} \right) \right]^2 = \exp\left[-\frac{t_*^2 s^2}{2} + O\left(\frac{1}{d} \right) \right],
\end{aligned} \tag{2.35}
$$

where $J_0(z)$ is a Bessel function and $t = t_*/\sqrt{2d}$. Then the density of states is

$$
\rho(\varepsilon) = \int_{-\infty}^{\infty} \frac{d\varepsilon}{2\pi} e^{-is\varepsilon} \Phi(s) = \frac{1}{2\pi \mid t_* \mid} \exp\left[-\frac{\varepsilon^2}{2t_*^2} \right]. \tag{2.36}
$$

When t_* is constant, the kinetic energy becomes finite. Hence, on the hypercubic lattice, the nearest-neighbor hopping t must be scaled proportional to $1/\sqrt{2d}$ to obtain a meaningful finite limit. In general, the n-th nearest neighbor hopping amplitude t_n must be scaled proportional to $1/\sqrt{Z_n}$, where Z_n is the number of sites connected by t_n. On the Bethe lattice with infinite nearest neighbors Z ($Z \to \infty$), the nearest-neighbor hopping $t = t_*/\sqrt{Z}$ and the density of states has a semi-elliptic form $\rho(\varepsilon) = \frac{\sqrt{4t_*^2 - \varepsilon^2}}{2\pi t_*^2}$ [64].

2.3.2 Detailed procedures

DMFT extracts one local site in the Hubbard model and treats it as an impurity site in the Anderson impurity model (see Fig, 2.1). Here, the interaction bewteen the impurity site and energy baths is effectively equal the interaction between this site and other sites in a lattice model.

The Hamiltonian of the Anderson model is read as

$$H_{\mathrm{AIM}} = \sum_{p\sigma} \epsilon_p a_{p\sigma}^\dagger a_{p\sigma} + \sum_{p\sigma} (V_p c_\sigma^\dagger a_{p\sigma} + h.c.) + U\hat{n}_\uparrow \hat{n}_\downarrow - \mu(\hat{n}_\uparrow + \hat{n}_\downarrow), \tag{2.37}$$

where $a_{p\sigma}^\dagger$ creates an electron with spin σ on the bath p, $c_\sigma^\dagger$ creates an electron with spin σ on the impurity site, and $\hat{n} = c_\sigma^\dagger c_\sigma$. The last term of Eq. (2.37) is introduced since this Hamiltonian will be solved in the canonical ensemble and the chemical potential is used to fixe the particle filling.

The Green's function of the impurity site is defined as

$$G(i\omega_n) = \frac{1}{i\omega_n + \mu - \Gamma(i\omega_n) - \Sigma(i\omega_n)}, \tag{2.38}$$

where ω_n is the Mastubara frequency $\omega_n = 2(n+1)\pi/\beta$, β is the inverse of the temperature, $\Sigma(i\omega_n)$ is the self-energy, and $\Gamma(i\omega_n)$ is the hybridization function and is defined as

$$\Gamma(i\omega_n) = \sum_p \frac{|V_p|^2}{i\omega_n - \epsilon_p}. \tag{2.39}$$
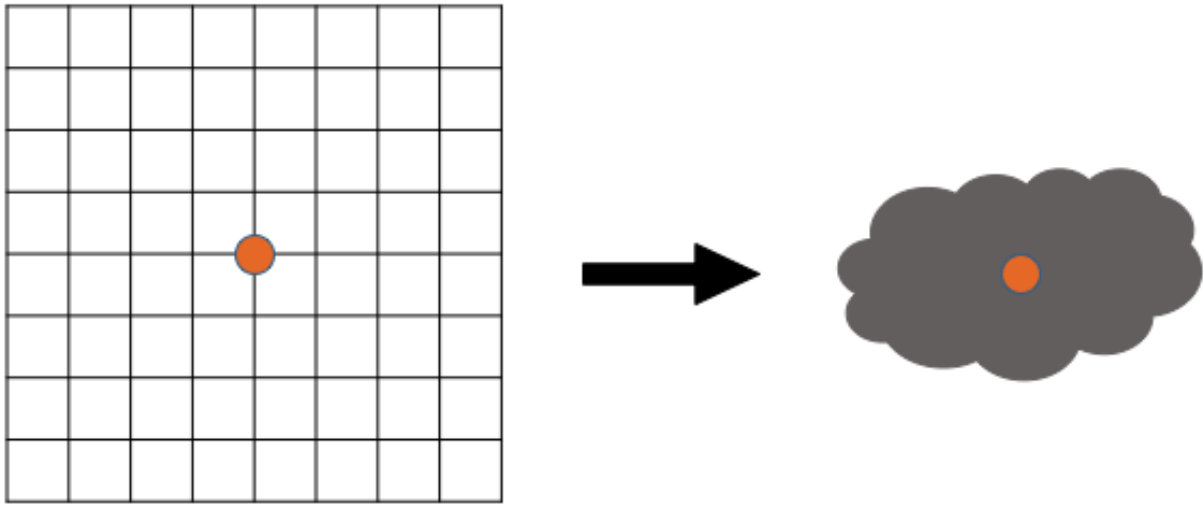
Figure 2.1: DMFT extracts one site from lattices and keeps local interactions on this site. At the same time, this site is coupled to energy baths.

The local Green's function of the Hubbard model is written as

$$G_{\mathrm{loc}}(i\omega_n) = \frac{1}{N} \sum_k \frac{1}{i\omega_n - \xi_k - \mu - \Sigma(k, i\omega_n)}, \tag{2.40}$$

where ξ_k is the eigenenergy of the kinetic energy of Eq. (2.1) and k is the momentum. In the dynamical mean field approximation, I assume the self-energy $\Sigma(k, i\omega_n)$ is mometum independent and labelled as $\Sigma_{\mathrm{loc}}(i\omega_n)$. The local hybridization function of the Hubbard model is obtained by

$$\Gamma_{\mathrm{loc}}(i\omega_n) = i\omega_n + \mu + \Sigma_{\mathrm{loc}}(i\omega_n) - G_{\mathrm{loc}}^{-1}(i\omega_n). \tag{2.41}$$

In the DMFT, I first give an initial value to $\Sigma_{\mathrm{loc}}(i\omega_n)$ and calculate the local hybridization function $\Gamma_{\mathrm{loc}}(i\omega_n)$ via Eq. (2.41). This local hybridizarion function should equal $\Gamma(i\omega_n)$ in that the hybridization to the bath is used to describe the hybridization between a local site and other sites in the Hubbard model. The parameters V_p and ξ_p in Eq. (2.37) are determined via Eq. (2.39) using the least squares minimization. Here, this fitting process is done using the open-source *MINPACK* library. Solving the Anderson Impurity Hamiltonian, I can get the impurity Green's function $G(i\omega_n)$ and self-energy $\Sigma(i\omega_n)$. The DMFT requires the impurity self-energy $\Sigma(i\omega_n)$ equal the local self-energy $\Sigma_{\mathrm{loc}}(i\omega_n)$. For clarity, the whole DMFT procedure is shown in Fig. 2.2. The iteration continues until a self-consistent solution (Σ) is reached.

2.3.3 Impurity solver: Exact Diagonalization

In this thesis, I use the exact diagonalization to solve the Anderson impurity Hamiltonian [155]. Assuming that I study the Anderson impurity Hamiltonian on a cluster with $N - 1$ bath sites and one impurity site, I have two possible states for each site: spin up and spin down. Thus the system has 2^N states, and this is the dimension of the Hamiltonian matrix. The basis states in the charge number representations are $|n_1, n_2, n_3, \cdots, n_N\rangle_\uparrow \otimes |m_1, m_2, m_3, \cdots, m_N\rangle_\downarrow$, where n_i is the charge number on site i with spin up and m_i is the charge number on site i with spin down. For fermions, n_i and m_i can only be 0 or 1. The
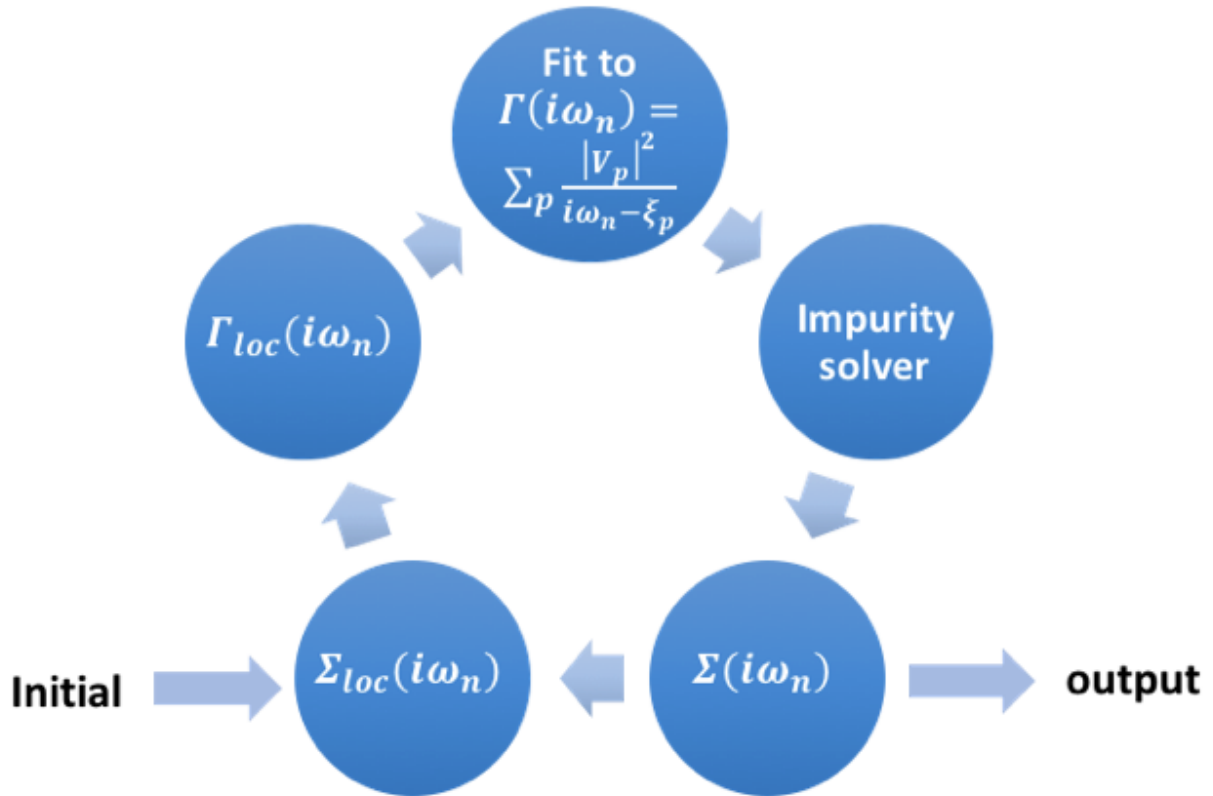
Figure 2.2: DMFT self-consistent loop.

2^N states can be enumerated as

$$\begin{aligned}
|\phi_1\rangle &= |0,0,0,\cdots,0,0\rangle_\uparrow \otimes |0,0,0,\cdots,0\rangle_\downarrow, \\
|\phi_2\rangle &= |1,0,0,\cdots,0,0\rangle_\uparrow \otimes |0,0,0,\cdots,0\rangle_\downarrow, \\
|\phi_3\rangle &= |0,1,0,\cdots,0,0\rangle_\uparrow \otimes |0,0,0,\cdots,0\rangle_\downarrow, \\
&\vdots \\
|\phi_{2^N}\rangle &= |1,1,1,\cdots,1,1\rangle_\uparrow \otimes |1,1,1,\cdots,1,\rangle_\downarrow.
\end{aligned} \tag{2.42}$$

The Anderson impurity Hamiltonian matrix is computed via

$$H_{ij} = \langle \psi_i | H | \psi_j \rangle. \tag{2.43}$$

For example, assume there are one impurity site and two bath levels. In the basis, I set the first site as the impurity site and the other two sites corresponding to the bath 1 and bath 2. Here, I take the two basis states as

$$\begin{aligned}
|\phi_i\rangle &= |1,1,0\rangle_\uparrow \otimes |1,0,0\rangle_\downarrow, \\
|\phi_j\rangle &= |1,1,0\rangle_\uparrow \otimes |1,0,0\rangle_\downarrow.
\end{aligned}$$

Calculating H_{ij} one term by one term, I have

$$\begin{aligned}
\langle \phi_i | \sum_{p=1}^{2} \sum_\sigma \epsilon_p a_{p\sigma}^\dagger a_{p\sigma} | \phi_j \rangle &= \epsilon_1, \\
\langle \phi_i | \sum_{p=1}^{2} \sum_\sigma \left(V_p c_{p\sigma}^\dagger a_{p\sigma} + h.c. \right) | \phi_j \rangle &= 0, \\
\langle \phi_i | U \hat{n}_\uparrow \hat{n}_\downarrow | \phi_j \rangle &= U, \\
\langle \phi_i | -\mu \left(\hat{n}_\uparrow + \hat{n}_\downarrow \right) | \phi_j \rangle &= -2\mu.
\end{aligned}$$

Then the Hamiltonian matrix element is $\epsilon_1 + U - 2\mu$.

A big issue of the exact diagonalization is that the Hamiltonian matrix size grows exponentially with increasing N, making even small lattices of typically 10 sites difficult

to handle with standard diagonalization techniques. To make the Hamiltonian matrix size accessible to the available computing power, I can reduce the matrix size by using

$$[H, \mathbf{S}^2] = [H, S^z] = [\hat{N}, H] = 0, \tag{2.44}$$

where H is the Hamiltonian, $\mathbf{S}^2$ is the total spin number, S^z is the total spin in the z direction, and $\hat{N}$ is number operator. This equation tells that $\mathbf{S}^2$, S^z, $\hat{N}$ are good quantum numbers, and I can divide the 2^N states into $(N+1)^2$ subspaces with each subspace has a fixed number of particles and a fixed number of S^z. For example, in the subspace (n, m), there are $\begin{pmatrix} N \\ n \end{pmatrix} \times \begin{pmatrix} N \\ m \end{pmatrix}$ basis elements. For $N = 10$, the size of the largest subspace is 63,504, which is much smaller than $2^{20} = 1,048,576$. Hence, when the Hamiltonian matrix is constructed in the subspace, it is much easier to diagonalize this small matrix.

2.3.4 Green's function

After doing the exact diagonalization, I can get the eigenenergy E_n and eigenstate $|\phi_n\rangle$. The Green's function is calculated using these eigenvalues via

$$
\begin{aligned}
G(\mathbf{r}_i, \mathbf{r}_j, i\omega_n) &= \frac{1}{Z} \sum_{n,m} \frac{e^{-\beta E_n} + e^{-\beta E_m}}{i\omega_n + E_m - E_n} \langle \phi_m | c_i | \phi_n \rangle \langle \phi_n | c_j^\dagger | \phi_m \rangle \\
&= \frac{1}{Z} \sum_m e^{-\beta E_m} \sum_n \left[\frac{\langle \phi_m | c_i | \phi_n \rangle \langle \phi_n | c_j^\dagger | \phi_m \rangle}{i\omega_n + E_m - E_n} + \frac{\langle \phi_m | c_j^\dagger | \phi_n \rangle \langle \phi_n | c_i | \phi_m \rangle}{i\omega_n + E_n - E_m} \right].
\end{aligned}
\tag{2.45}
$$

There are two summations appearing in the expansion for the Green's function, and if the space of the basis is large, it will take a long time to calculate this Green's function. To reduce the time, I use a Lanczos vector procedure rather than doing summations directly [202]. The summations in the bracket in Eq. (2.45) can be written as

$$\sum_n \frac{\langle \phi_m | c_i | \phi_n \rangle \langle \phi_n | c_j^\dagger | \phi_m \rangle}{i\omega_n + E_m - E_n} = \langle \phi_m | c_i \frac{1}{i\omega_n + E_m - H} c_j^\dagger | \phi_m \rangle \tag{2.46}$$

$$\sum_n \frac{\langle \phi_m | c_j^\dagger | \phi_n \rangle \langle \phi_n | c_i | \phi_m \rangle}{i\omega_n + E_n - E_m} \quad = \quad \langle \phi_m | c_j^\dagger \frac{1}{i\omega_n + H - E_m} c_i | \phi_m \rangle. \tag{2.47}$$

First, let me focus on $\mathbf{r}_i = \mathbf{r}_j$. Then Eq. (2.46) and Eq. (2.47) become

$$\sum_n \frac{\langle \phi_m | c_i | \phi_n \rangle \langle \phi_n | c_i^\dagger | \phi_m \rangle}{i\omega_n + E_m - E_n} \quad = \quad \langle \phi_m | c_i \frac{1}{i\omega_n + E_m - H} c_i^\dagger | \phi_m \rangle \tag{2.48}$$

$$\sum_n \frac{\langle \phi_m | c_i^\dagger | \phi_n \rangle \langle \phi_n | c_i | \phi_m \rangle}{i\omega_n + E_n - E_m} \quad = \quad \langle \phi_m | c_i^\dagger \frac{1}{i\omega_n + H - E_m} c_i | \phi_m \rangle. \tag{2.49}$$

Then I need to evaluate $\langle \phi_m | A^\dagger \frac{1}{z-H} A | \phi_m \rangle$ or $\langle \phi_m | A^\dagger \frac{1}{z+H} A | \phi_m \rangle$, in which z is a complex value, A and $A^\dagger$ are particle operators, and H is the Hamiltonian operator. The first step of the Lanczos vector procedure is constructing a basis, on which the projection of the Hamiltonian is a tridiagonal matrix. I construct the first basis element via

$$|\tilde{f}_0\rangle = A|\phi_m\rangle,$$

and normalize $|\tilde{f}_0\rangle$ as

$$|f_0\rangle = \frac{|\tilde{f}_0\rangle}{\sqrt{\langle \tilde{f}_0 | \tilde{f}_0 \rangle}}.$$

Then I construct the second basis element $|f_1\rangle$ through

$$|\tilde{f}_1\rangle \quad = \quad H|f_0\rangle - \alpha_0|f_0\rangle,$$
$$|f_1\rangle \quad = \quad \frac{|\tilde{f}_1\rangle}{b_0},$$

where $\alpha_0 = \langle f_0 | H | f_0 \rangle$ and $b_0 = \sqrt{\langle \tilde{f}_1 | \tilde{f}_1 \rangle}$. Similary, the third basis element is constructed by

$$|\tilde{f}_2\rangle \quad = \quad H|f_1\rangle - \alpha_1|f_1\rangle - b_0|f_0\rangle,$$
$$|f_2\rangle \quad = \quad \frac{|\tilde{f}_2\rangle}{b_1},$$

where $\alpha_1 = \langle f_1|H|f_1\rangle$ and $b_1 = \sqrt{\langle \tilde{f}_2|\tilde{f}_2\rangle}$. The fourth basis element is given by

$$
\begin{aligned}
|\tilde{f}_3\rangle &= H|f_2\rangle - \alpha_2|f_2\rangle - b_1|f_1\rangle, \\
|f_3\rangle &= \frac{|\tilde{f}_3\rangle}{b_2},
\end{aligned}
$$

where $\alpha_2 = \langle f_2|H|f_2\rangle$ and $b_2 = \sqrt{\langle \tilde{f}_3|\tilde{f}_3\rangle}$. In general, the lth basis element is defined as

$$
\begin{aligned}
|\tilde{f}_l\rangle &= H|f_{l-1}\rangle - \alpha_{l-1}|f_{l-1}\rangle - b_{l-2}|f_{l-2}\rangle, \\
|f_l\rangle &= \frac{|\tilde{f}_l\rangle}{b_{l-1}},
\end{aligned}
$$

where $\alpha_{l-1} = \langle f_{l-1}|H|f_{l-1}\rangle$ and $b_{l-2} = \sqrt{\langle \tilde{f}_{l-2}|\tilde{f}_{l-2}\rangle}$.

After constructing M basis elements, I construct the Hamiltonian matrix in the $|f_i\rangle$ basis. The Hamiltonian matrix then is

$$
H = \begin{bmatrix}
\alpha_0 & b_0 & 0 & 0 & \cdots & 0 & 0 \\
b_0 & \alpha_1 & b_1 & 0 & \cdots & 0 & 0 \\
0 & b_1 & \alpha_2 & b_2 & \cdots & 0 & 0 \\
\vdots & \vdots & \vdots & \vdots & \ddots & \vdots & \vdots \\
0 & 0 & 0 & 0 & \cdots & b_{M-1} & \alpha_M
\end{bmatrix}
\tag{2.50}
$$

Next, I evaluate $\langle \phi_m|A^\dagger \frac{1}{z-H}A\,|\phi_m\rangle$.

$$
\begin{aligned}
\langle \phi_m|A^\dagger \frac{1}{z-H}A\,|\phi_m\rangle &= \langle \tilde{f}_0|\frac{1}{z-H}|\tilde{f}_0\rangle \\
&= \sum_{s,t} \langle \tilde{f}_0|\phi_s\rangle\langle \phi_s|\frac{1}{z-H}|\phi_t\rangle\langle \phi_t|\tilde{f}_0\rangle \\
&= \sum_s \frac{|\langle \tilde{f}_0|\phi_s\rangle|^2}{z-E_s} \\
&= \sum_s \frac{|\langle f_0|\phi_s\rangle|^2}{z-E_s}\langle \tilde{f}_0|\tilde{f}_0\rangle \\
&= \sum_s \frac{|\langle f_0|\phi_s\rangle|^2}{z-E_s}\langle \phi_m|A^\dagger A\,|\phi_m\rangle.
\end{aligned}
\tag{2.51}
$$

The summation $\sum_s \frac{|\langle f_0|\phi_s\rangle|^2}{z-E_s}$ is the first element of the matrix $\frac{1}{z-H}$. Since the matix $z-H$ is a tridiagonal matrix, it is easily to obtain

$$\left[\frac{1}{z-H}\right]_{1,1} = \frac{1}{z-\alpha_0 - \cfrac{b_0^2}{z-\alpha_1 - \cfrac{b_1^2}{z-\alpha_2 - \cfrac{\cdots}{z-\alpha_M}}}}. \tag{2.52}$$

Similarly,

$$\langle\phi_m|A^\dagger\frac{1}{z+H}A\,|\phi_m\rangle = \sum_s \frac{|\langle f_0|\phi_s\rangle|^2}{z+E_s}\langle\phi_m|A^\dagger A\,|\phi_m\rangle$$

$$= \left[\frac{1}{z+H}\right]_{1,1}\langle\phi_m|A^\dagger A\,|\phi_m\rangle, \tag{2.53}$$

$$\left[\frac{1}{z+H}\right]_{1,1} = \frac{1}{z+\alpha_0 + \cfrac{b_0^2}{z+\alpha_1 + \cfrac{b_1^2}{z+\alpha_2 + \cfrac{\cdots}{z+\alpha_M}}}}. \tag{2.54}$$

Then $\langle\phi_m|c_i\frac{1}{i\omega_n+E_m-H}c_i^\dagger|\phi_m\rangle$ and $\langle\phi_m|c_i^\dagger\frac{1}{i\omega_n-E_m+H}c_i|\phi_m\rangle$ are calculated by using Eq. (2.51), Eq. (2.52), Eq. (2.53), and Eq. (2.54).

If $\mathbf{r}_i \neq \mathbf{r}_j$, I need to construct another two operators to obtain $\langle\phi_m|c_j^\dagger\frac{1}{z+H}c_i|\phi_m\rangle$. I define

$$U = c_i + c_j,$$
$$V = c_i + ic_j,$$

and note that

$$W = \langle\phi_m|U^\dagger\frac{1}{z+H}U\,|\phi_m\rangle,$$
$$R = \langle\phi_m|V^\dagger\frac{1}{z+H}V\,|\phi_m\rangle,$$
$$Q_1 = \langle\phi_m|c_i^\dagger\frac{1}{z+H}c_i|\phi_m\rangle$$
$$Q_2 = \langle\phi_m|c_j^\dagger\frac{1}{z+H}c_j|\phi_m\rangle.$$

W, R, Q_1, and Q_2 are easily calculated via Eq. (2.51) and Eq. (2.52). Then I have

$$\langle\phi_m|c_j^\dagger\frac{1}{z+H}c_i|\phi_m\rangle = \frac{W-Q_1-Q_2}{2} + i\frac{R-Q_1-Q_2}{2}. \tag{2.55}$$

$\langle\phi_m|c_i\frac{1}{z-H}c_j^\dagger|\phi_m\rangle$ can be obtained using the same method.

The number of the basis elements M used in the Lanczos vector procedure must be large enough to let $\langle\phi_m|A^\dagger\frac{1}{z\pm H}A\,|\phi_m\rangle$ converge. At low temperature, the Boltzmann factor $\frac{e^{-\beta E_m}}{Z}$ decreases to zero for the high energy excited state. That means I don't need to include all eigenstates for the first summation over m in Eq. (2.45). Keeping the lowest 100 states is usually enough to obtain an accurate result for $\beta = 100/t$.

2.4 Holstein model

The goal of this thesis is to study electron-phonon (e-ph) coupling in the presence of strong e-e interactions. To this end, the application of DQMC to the Holstein model is examined. In the Holstein model, phonons are included as independent harmonic oscillators, characterized by a frequency Ω, on each site. The e-ph interaction is included as a local coupling. The Hamiltonian is given by

$$H = K + H_{\text{lat}} + H_{\text{e}-\text{ph}}, \tag{2.56}$$

where K is the same as in Eq. 2.6,

$$\begin{aligned} H_{\text{lat}} &= \Omega\sum_i(b_i^\dagger b_i + \frac{1}{2}) \\ &= \sum_i \frac{1}{2}M\Omega^2\hat{X}_i^2 + \frac{1}{2M}\hat{P}_i^2, \end{aligned} \tag{2.57}$$

and

$$\begin{aligned} H_{\text{e}-\text{ph}} &= g\sum_{i,\sigma}\hat{n}_{i,\sigma}(b_i^\dagger + b_i) \\ &= \sum_{i,\sigma}\alpha\hat{n}_{i,\sigma}\hat{X}_{i,\sigma}. \end{aligned} \tag{2.58}$$

Here, $b_i^\dagger$ creates a phonon on lattice site, M is the ion mass, $\hat{X}_i$ and $\hat{P}_i$ are the lattice position and momentum operators, respectively, and $g = \alpha/\sqrt{2M\Omega}$ is the strength of the e-ph coupling.

The partition function is given by

$$
\begin{aligned}
Z &= \mathrm{Tr}\left[e^{-\beta H}\right] = \mathrm{Tr}\left[e^{-\beta(H_{\mathrm{e-ph}}+K+H_{\mathrm{lat}})}\right] \\
&= \int D\underline{X}(0)\langle\underline{X}(0)|e^{-\beta(H_{\mathrm{e-ph}}+K+H_{\mathrm{lat}})}|\underline{X}(0)\rangle \\
&= \int D\underline{X}(0)D\underline{X}(1)\cdots D\underline{X}(L-1)\langle\underline{X}(0)|e^{-\Delta\tau(H_{\mathrm{e-ph}}+K+H_{\mathrm{lat}})}|\underline{X}(1)\rangle \\
&\quad \langle\underline{X}(1)|e^{-\Delta\tau(H_{\mathrm{e-ph}}+K+H_{\mathrm{lat}})}|\underline{X}(2)\rangle\cdots\langle\underline{X}(L-1)|e^{-\Delta\tau(H_{\mathrm{e-ph}}+K+H_{\mathrm{lat}})}|\underline{X}(0)\rangle,
\end{aligned}
$$

$$(2.59)$$

in which $\underline{X}(l) = \{X_1(l), X_2(l), X_3(l), \cdots, X_N(l)\}$ is a set of displacement configuration on the cluster at an imaginary time $l\Delta\tau$. Considering that

$$
\begin{aligned}
z\left(\underline{X}(l),\underline{X}(l+1)\right) &= \langle\underline{X}(l)|e^{-\Delta\tau(H_{\mathrm{e-ph}}+K+H_{\mathrm{lat}})}|\underline{X}(l+1)\rangle \\
&= \int D\underline{P}(l)\langle\underline{X}(l)|\underline{P}(l)\rangle\langle\underline{P}(l)|e^{-\Delta\tau(H_{\mathrm{e-ph}}+K+H_{\mathrm{lat}})}|\underline{X}(l+1)\rangle \\
&\approx \int D\underline{P}(l)\langle\underline{X}(l)|\underline{P}(l)\rangle\langle\underline{P}(l)|e^{-\Delta\tau H_{\mathrm{e-ph}}}e^{-\Delta\tau K}e^{-\Delta\tau\frac{M\Omega^2}{2}\sum_i \hat{X}_i^2}e^{-\Delta\tau\frac{1}{2M}\sum_i \hat{P}_i^2}|\underline{X}(l+1)\rangle \\
&= \int D\underline{P}(l)\langle\underline{X}(l)|\underline{P}(l)\rangle\langle\underline{P}(l)|e^{-\Delta\tau\frac{1}{2M}\sum_i \hat{P}_i^2}|\underline{X}(l+1)\rangle \\
&\quad \times e^{-\Delta\tau\frac{M\Omega^2}{2}\sum_i X_i(l)-\Delta\tau H_{\mathrm{e-ph}}[\underline{X}(l)]-\Delta\tau K} \\
&= \left(\frac{1}{2\pi\hbar}\right)^{\frac{Nd}{2}}\int D\underline{P}(l)e^{\frac{i}{\hbar}\sum_i P_i(l)X_i(l)}e^{-\frac{i}{\hbar}\sum_i P_i(l)X_i(l+1)}e^{-\frac{\Delta\tau}{2M}\sum_i P_i^2(l)} \\
&\quad \times e^{-\Delta\tau\frac{M\Omega^2}{2}\sum_i X_i(l)-\Delta\tau H_{\mathrm{e-ph}}[\underline{X}(l)]-\Delta\tau K} \\
&= \left(\frac{M}{\Delta\tau\hbar}\right)^{\frac{Nd}{2}}e^{-\Delta\tau\sum_i\left[\frac{M}{2}\left(\frac{X_i(l)-X_i(l+1)}{\Delta\tau\hbar}\right)^2+\frac{M\Omega^2}{2}X_i^2(l)\right]}e^{-\Delta\tau H_{\mathrm{e-ph}}[\underline{X}(l)]-\Delta\tau K},
\end{aligned}
$$

$$(2.60)$$

$z\left(\underline{X}(l),\underline{X}(l+1)\right)$ is a function of $\underline{X}(l)$ and $\underline{X}(l+1)$, and all phonon operator has been integrated out. The position operator $\hat{X}_i$ is replaced with a set of continuous variable $X_i(l)$ defined on the same discrete imaginary-time grid as the Hubbard-Stratonovich fields. The momentum operator is replaced with a finite difference $P_i(l) = M\frac{X_i(l+1)-X_i(l)}{\Delta\tau\hbar}$. The partition

function is

$$
\begin{aligned}
Z \;=\; & \int D\underline{X}(0) D\underline{X}(1)\cdots D\underline{X}(L-1) z\left(\underline{X}(0), \underline{X}(1)\right) z\left(\underline{X}(1), \underline{X}(2)\right)\cdots \\
& z\left(\underline{X}(L-1), \underline{X}(L-0)\right)
\end{aligned}
\tag{2.61}
$$

Then the B_l^σ matrix defined in Eq. (2.11) is modified as

$$
B_l^\sigma = e^{-\Delta\tau\alpha X(l)} e^{-\Delta\tau K}.
\tag{2.62}
$$

The matrix $X(l)$ is a diagonal matrix, whose ith diagonal element is $X_i(l)$.

Similar with the update in the Hubbard model, the single-site update in the Holstein model is performed by $X_i(l) \to X_i'(l) = X_i(l) + \Delta X_i(l)$. The proposed update is accepted with probability $R = R^\uparrow R^\downarrow e^{-\Delta\tau\Delta E_{ph}}$, where ΔE_{ph} is the total change in bare phonon energy associated with the update and

$$
\begin{aligned}
\Delta E_{ph} \;=\; & \frac{M\Omega^2}{2}\left(X_i'^2(l) - X_i^2(l)\right) + \frac{M}{2}\left(\frac{X_i(l+1) - X_i'(l)}{\Delta\tau}\right)^2 + \frac{M}{2}\left(\frac{X_i'(l) - X_i(l-1)}{\Delta\tau}\right)^2 \\
& -\frac{M}{2}\left(\frac{X_i(l+1) - X_i(l)}{\Delta\tau}\right)^2 - \frac{M}{2}\left(\frac{X_i(l) - X_i(l-1)}{\Delta\tau}\right)^2
\end{aligned}
\tag{2.63}
$$

R^σ is the same as defined in Eq. (2.21) with $\Delta^\sigma(i,l)$ replaced by

$$
\Delta_{jk}^\sigma(i,l) = \delta_{ik}\delta_{jk}\left[\exp\left(-\Delta\tau\Delta X_i(l)\right) - 1\right].
\tag{2.64}
$$

In addition to the single-site update, I have to perform a block update at low temperature, where the rate of acceptance of single-site updates is slow. For large β the total expectation value of the phonon momentum is small and a large change of $X_i(l)$ leads to a large change of phonon momentum and will be rejected in the DQMC algorithm. As a result, phonon configurations can be frozen and a large number of small phonon updates are needed to move such a configuration to another statistically independent configuration. The introduced block update allows large changes in $X_i(l)$ with a small change in phonon kinetic energy. Therefore,

the block update helps to efficiently move the phonon configurations out of false minima at lower temperatures.

The block update is performed by $X_i(l) \rightarrow X_i(l) + \Delta X$ for all $l \in [0, L)$. There is no fast updating formula for the block update and the equal time Green's function is required to be recomputed from Eq. (2.16). Then the block update takes a lot of time in DQMC calculations, and scales as $O(N^3)$.

2.5 Analytical Continuation

The DQMC calculation provides M samples of the electron Green's function $G(\mathbf{q}, \tau) = \langle T_\tau \left[\mathbf{c_q}(\tau) \mathbf{c_q^\dagger}(0) \right] \rangle$ and the phonon Green's function $D(\mathbf{q}, \tau) = \langle T_\tau [\hat{X}_\mathbf{q}(\tau) \hat{X}_{-\mathbf{q}}(0)] \rangle$ measured on the imaginary time axis τ. In the analytical continuation calculation, I regroup these samples into m bins by averaging M/m samples for each bin. The Green's function is related to its spectral function on the real axis by

$$G(\mathbf{q}, \tau) = \int_{-\infty}^{\infty} d\omega \frac{e^{-\tau\omega}}{1 + e^{-\beta\omega}} A(\mathbf{q}, \omega), \tag{2.65}$$

$$D(\mathbf{q}, \tau) = \int_{-\infty}^{\infty} d\omega \frac{\omega e^{-\tau\omega}}{1 - e^{-\beta\omega}} \frac{B(\mathbf{q}, \omega)}{\omega}, \tag{2.66}$$

in which $A(\mathbf{q}, \omega)$ and $B(\mathbf{q}, \omega)$ are the electron and phonon spectral functions, respectively. $A(\mathbf{q}, \omega)$ is always positive and can be interpreted as a probability function. While $B(\mathbf{q}, \omega)$ is negative for $\omega < 0$. $B(\mathbf{q}, \omega)$ is not the probability function and not normalized. In order to normalize the phonon spectral function, Eq. (2.66) is divided by a factor $D(\mathbf{q}, T) = \int_0^\beta D(\mathbf{q}, \tau) d\tau$. Generally, I can use a single equation to indicate the relationship between the Green's function and the spectral function,

$$O(\tau) = \int_{-\infty}^{\infty} d\omega K(\omega, \tau) f(\omega), \tag{2.67}$$

where $O(\tau)$ is $G(\omega)$ for fermions and $\frac{D(\tau)}{D(T)}$ for bosons and $f(\omega)$ is $A(\mathbf{q}, \omega)$ for fermions and $\frac{B(\mathbf{q}, \omega)}{\omega D(\mathbf{q}, T)}$ for bosons. The kernel function $K(\omega, \tau)$ is $\frac{e^{-\tau\omega}}{1 + e^{-\beta\omega}}$ for fermions and $\frac{\omega e^{-\tau\omega}}{1 - e^{\beta\omega}}$ for bosons.

The spectral function $f(\omega)$ is obtained by the Maximum Entropy method (MEM) [108, 32], which requires one to maximize

$$Q = 2\alpha S - Y, \tag{2.68}$$

where Y is given by

$$Y = \sum_{i,j}^{L} [\tilde{O}(\tau_i) - \bar{O}(\tau_i)][C^{-1}]_{i,j}[\tilde{O}(\tau_j) - \bar{O}(\tau_j)]. \tag{2.69}$$

$\tilde{O}(\tau_i)$ is the Green's function at imaginary time slice τ_i produced from a proposed spectral function by Eq. (2.66), and $\bar{O}(\tau_i)$ is the average Green's function at time slice τ_i from DQMC. The covariance matrix C is defined as

$$C_{i,j} = \frac{1}{M-1} \sum_{k=1}^{M} [O_k(\tau_i) - \bar{O}(\tau_i)][O_k(\tau_j) - \bar{O}(\tau_j)], \tag{2.70}$$

in which $O_k(\tau_i)$ is the Green's function at imaginary time slice τ_i from the kth bin in the DQMC. The entropy S is obtained from

$$S = \int d\omega \left[f(\omega) - m(\omega) - f(\omega) \ln \frac{f(\omega)}{m(\omega)} \right], \tag{2.71}$$

in which $m(\omega)$ is a default model and there I use the Gaussian model $m(\omega) = \frac{1}{\sqrt{2\pi}\sigma} e^{-\frac{(\omega-\mu_0)^2}{2\sigma^2}}$. Here, μ_0 is the median and σ^2 is the variance. Any information that is known about the spectrum beforehand, can be encoded in the default model. The entropy has a maximum value of zero when $f(\omega) = m(\omega)$. When $f(\omega) \neq m(\omega)$, S is negative. How negative is a measure of how much $f(\omega)$ differs from $m(\omega)$.

The solution of the spectral function $f(\omega)$ should minimize Y. Meanwhile, the principle of maximum entropy says that the values of a spectral function $f(\omega)$ are to be assigned by maximizing the entropy expression. α is introduced as a weight factor to denote which one is more likely to be fitted. If $\alpha = 0$ the solution just minimizes Y. If $\alpha \to \infty$ the solution just

maximizes entropy and is the default model $m(\omega)$. A good solution requires $a \sim 1$, which leads to both conditions being satisfied.

To maximize Q, one has to solve this equation

$$\alpha \nabla S - \nabla Y = 0, \tag{2.72}$$

with

$$\nabla S = -\ln \frac{f(\omega_i)}{m(\omega_i)}, \tag{2.73}$$

$$\nabla Y(\tilde{O}, \bar{O}) = \frac{\partial \tilde{O}}{\partial f} \frac{\partial Y(\tilde{O}, \bar{O})}{\partial \tilde{O}} = K^T(\omega, \tau) \frac{\partial Y(\tilde{O}, \bar{O})}{\partial \tilde{O}}. \tag{2.74}$$

The matrix $K(\omega, \tau)$ can be decomposed as $K = V \Sigma U^T$, where V and U are orthogonal matrices. The solution could therefore be represented in terms of a new variable u, where $\ln f/m = Uu$. Then Eq. (2.72) can be written as

$$-\alpha u = \Sigma V^T \frac{\partial Y(\tilde{O}, \bar{O})}{\partial f} = g. \tag{2.75}$$

A Newton method can be applied to Eq. (2.75) by starting some trial value of u and increasing at each iteration being given by $J\delta u = -\alpha u - g$, where $J = \alpha I + \partial g/\partial u$ is the Jacobian of the system.

The solution of Eq. (2.75) depends on α, so the next step is to calculate the posterior probability $p(\alpha|\bar{O}, m)$ of α, which could be found in Ref. [108] and Ref. [32]. The expression for the posterior probability α derived by Gull [86],

$$p(\alpha|\bar{O}, m) = p_r(\alpha) \times \sqrt{\prod_i \frac{\alpha}{\alpha + \lambda_i}} \times e^Q, \tag{2.76}$$

where $p_r(\alpha) = \frac{1}{\alpha}$ and λ_i is the ith eigenvalue of a matrix Λ. The matrix Λ is defined by

$$\Lambda_{ij} = \sqrt{f(\omega_i)} \frac{\partial^2 Y}{\partial f(\omega_i) \partial f(\omega_j)} \sqrt{f(\omega_j)}, \tag{2.77}$$

and

$$\frac{\partial^2 Y}{\partial f(\omega_i)\partial f(\omega_j)} = \left[K^{\mathrm{T}}C^{-1}K\right]_{i,j} \tag{2.78}$$

Once the posterior probability is obtained, the spectral function is evaluated by

$$\bar{f} = \int fp(\alpha|\bar{O},m)d\alpha. \tag{2.79}$$

Chapter 3

The effects of non-linear electron-phonon interactions

In this chapter, determinant quantum Monte Carlo (DQMC) simulations are used to study non-linear electron-phonon (e-ph) interactions in a two-dimensional Holstein-like model on a square lattice. The key result presented in this chapter have appeared in Ref. [147, 148]

Electron-phonon coupling is an important interaction in many molecular systems and solids, which dresses carriers to form quasiparticles (called polarons) with increased effective masses and modified dispersion relations [68, 62]. Nearly all treatments of this interaction make use of linear models, where an electronic degree of freedom is coupled to the first-order displacement of the ions. Theorists typically justify this by expanding the e-ph interaction Hamiltonian in powers of the lattice displacement and then truncating the expansion under the assumption that the net displacements from equilibrium are small. For example, the motion of an atom in an external potential $\Psi_{ext}(X)$ established by the remainder of the crystal introduces an on-site electrostatic coupling between the lattice displacement X and the carrier density $n_{i,\sigma}$, given by

$$H_{site} = -e \sum_{i,\sigma} n_{i,\sigma} \Phi_{ext}(X). \tag{3.1}$$

Typically Φ_{ext} is a non-linear function which scales like an inverse power of X. Thus, an expansion of $\Phi_{ext}(X)$ yields $H_{site} = H_0 + H_{e-ph} + O(X^2)$, where H_0 is the on-site Hamiltonian

in the absence of atomic motion and H_{e-ph} is the usual (linear) e-ph coupling. The higher-order terms are typically dropped assuming that X is small; however, large displacements are expected in a number of situations. For example, in the limit of a strong e-ph coupling, linear models predict large lattice distortions surrounding carriers as small polarons are formed [62, 80, 1, 3]. This result violates the assumptions underlying the linear models and indicates the necessity of including higher-order terms in the expansion [1, 3].

Non-linear e-ph interactions have a dramatic effect on polaron properties in the single-carrier limit. This was first demonstrated in Ref. [1], which examined the problem using the non-perturbative "momentum average" approximation and found that small higher-order interactions lead to a dramatic undressing of the polaron. This result is of potential relevance to many systems where strong e-ph interactions have been inferred from experiments [137, 143, 170, 277, 43]; however, it is not clear whether the single-polaron result will generalize straightforwardly to the finite carrier concentrations relevant for these materials. Calculations at finite carrier concentrations are also needed in order to understand the impact of non-linearity on broken symmetry states like superconductivity [9] and charge density waves (CDW) [83].

In this chapter, I examine non-linear interactions in the many body limit by studying the non-linear single-band Holstein model in two dimensions using DQMC. DQMC has previously been applied to linear Holstein models [231, 52, 113], but to the best of my knowledge, it has not been applied to any e-ph models with non-linear interactions. First I focus on the competition between Peierls CDW correlations and s-wave superconductivity that is known to occur in the linear model [231, 172]. As with the single-carrier limit, I find that inclusion of a nonlinear interaction renormalizes both the effective frequency of the Holstein phonon and the effective e-ph coupling strength, resulting in significant changes in both the electronic and phononic properties of the model. While this allows superconductivity to emerge from behind the competing CDW order, I conclude that a non-linear interaction is ultimately detrimental to superconductivity in the Holstein model due to a renormalization of the effective linear e-ph coupling.

3.1 The non-linear Holstein model

The modified single-band Holstein Hamiltonian is

$$H = H_{\text{el}} + H_{\text{lat}} + H_{\text{int}}, \tag{3.2}$$

where

$$H_{\text{el}} = -t \sum_{\langle i,j \rangle,\sigma} c_{i,\sigma}^\dagger c_{j,\sigma} - \mu \sum_{i,\sigma} \hat{n}_{i,\sigma}, \tag{3.3}$$

contains the non-interacting electronic terms,

$$H_{\text{lat}} = \sum_i \left[\frac{\hat{P}_i^2}{2M} + \frac{M\Omega}{2} \hat{X}_i^2 \right] = \sum_i \Omega \left[b_i^\dagger b_i + \frac{1}{2} \right], \tag{3.4}$$

contains the non-interacting lattice terms, and

$$H_{\text{int}} = \sum_{i,k,\sigma} \alpha_k \hat{n}_{i,\sigma} \hat{X}_i^k = \sum_{i,k,\sigma} g_k \hat{n}_{i,\sigma} \left(b_i^\dagger + b_i \right)^k, \tag{3.5}$$

contains the interaction terms to k^{th} order in the atomic displacement. Here, $c_{i,\sigma}^\dagger$ ($c_{i,\sigma}$) creates (annihilates) an electron of spin σ on lattice site i; $b_i^\dagger$ (b_i) creates (annihilates) a phonon on lattice site i; $\hat{n}_{i,\sigma} = c_{i,\sigma}^\dagger c_{i,\sigma}$ is the number operator; μ is the chemical potential; t is the nearest-neighbor hopping integral; M is the ion mass; Ω is the phonon frequency; $\hat{X}_i$ and $\hat{P}_i$ are the lattice position and momentum operators, respectively; and $g_k = \alpha_k (2M\Omega)^{-\frac{k}{2}}$ is the strength of the e-ph coupling to k^{th} order in displacement.

The non-linear Holstein model is characterized by several dimensionless parameters, and the specific choice in parametrization is not unique. Here, I follow the convention used in previous works, where the usual dimensionless parameter $\lambda = \alpha_1^2/(M\Omega^2 W) = g_1^2/(4t\Omega)$ parametrizes the linear coupling strength and $\xi_k = g_k/g_{k-1}$ parametrizes the non-linear interaction terms. This choice provides a convenient interpretation with large λ implying a strong linear interaction and large ξ_k implying strong non-linear effects. In the linear model ($\xi_k = 0$) $\lambda > 1$ implies the formation of small polarons. Thus, this choice of parametrization

is also useful for making comparisons to my expectations gained from studying the linear model.

In my calculations I keep $g_1 > 0$ without loss of generality. Furthermore, Ref. [1] examined terms to 4th order in the interaction and found that the largest effect was produced by the 2nd order terms. I expect a similar result here and restrict myself to $k = 2$ while defining $\xi = \frac{g_2}{g_1}$. Furthermore, I neglect the anharmonic terms in the lattice potential, which are not expected to significantly alter my results when $\xi > 0$ [1]. (Such terms are needed, however, when ξ is large and negative, see section 3.1.2.5.) I examine two-dimensional square lattices with a linear dimension N (a total of $N \times N$ sites) and set $a = t = M = 1$ as the units of distance, energy, and mass, respectively. I typically work on lattice sizes ranging from $N = 4$ to 8 in size. In general I do not observe significant finite size effects [147], which is likely due to the local nature of the interaction in the model.

The Holstein model and its non-linear extension do not suffer from a fermion sign problem due to particle-hole symmetry [269, 157]. I am therefore able to perform simulations to arbitrarily low temperatures [147]; however, I find that most of the physical properties I am interested in can be examined for $\beta = 4/t$. I use this temperature for all plots in this work unless stated otherwise and present results for an imaginary time discretization of $\Delta\tau = 0.1/t$. In all of my simulations, I have not observed any significant $\Delta\tau$ errors introduced by this choice.

3.2   Results and Discussion

3.2.1   Charge-density-wave and superconductivity correlations

I first examine CDW and superconducting correlations. A measure of the CDW correlations is obtained from the charge susceptibility

$$\chi_C(\mathbf{q}) = \frac{1}{N} \int_0^\beta d\tau \langle \rho(\mathbf{q}, \tau) \rho^\dagger(\mathbf{q}, 0) \rangle, \tag{3.6}$$

where $\rho(\mathbf{q}) = \sum_{i,\sigma} e^{i\mathbf{q}\cdot\mathbf{R}_i}\hat{n}_{i,\sigma}$. Similarly, a measure of the s-wave superconducting correlations is obtained from the pair-field susceptibility

$$\chi_{SC} = \frac{1}{N}\int_0^\beta d\tau \langle \Delta(\tau)\Delta^\dagger(0)\rangle, \tag{3.7}$$

where $\Delta^\dagger = \sum_k c_{k,\uparrow}^\dagger c_{-k,\downarrow}^\dagger = \sum_i c_{i,\uparrow}c_{i,\downarrow}$.

Figure 3.1 shows the CDW and superconducting correlations as a function of the band filling in the linear and non-linear models at an inverse temperature $\beta = 5/t$. Here the linear coupling has been fixed to $\lambda = 0.25$. The results for the linear model ($\xi = 0$) agree well with previous work [230], where $\mathbf{q} = (\pi,\pi)$ CDW correlations are dominant due to a strong $\mathbf{q} = (\pi,\pi)$ nesting condition on the Fermi surface near half filling ($\langle n \rangle \sim 1$) [231, 172]. The non-linear interaction dramatically alters these results. The initial effect is rapid and I find that $\chi_C(\pi,\pi)$ is suppressed near $\langle n \rangle \sim 1$ by an order of magnitude for a relatively small value of the non-linear coupling $\xi = 0.05$. This suppression continues for increasing values of ξ, but it is less dramatic after the initial decrease.

The ξ dependence of $\chi_C(\pi,\pi)$ and χ_{SC} is examined further in Fig. 3.2. Results are shown for $N = 8$ cluster with a fixed filling of $\langle n \rangle = 1$ and $\lambda = 0.25$. The behavior matches the expectations from Fig. 3.1 and the rapid initial suppression of the CDW correlations for small non-zero values of ξ is evident. Similar results were obtained in the single-polaron limit, where a small value of ξ produced large changes in the polaron's effective mass and quasiparticle weight, but gave way to more gradual changes in these properties for further increases in the value of ξ [1].

In the linear model, CDW correlations directly compete with s-wave superconductivity and the former dominate at low temperatures, particularly for fillings near $\langle n \rangle \approx 1$ [231, 52, 113, 172]. Thus, there is a concomitant enhancement in the pair-field susceptibility once the CDW correlations are suppressed by the non-linear interaction, which is evident in Figs. 3.1 and 3.2. After its initial rise, however, χ_{SC} is relatively independent of the value of ξ for all values of the band filling examined, apart from a slight suppression of χ_{SC} in the vicinity of $\langle n \rangle \approx 0.65$. Thus, the non-linear coupling does not significantly enhance or suppress
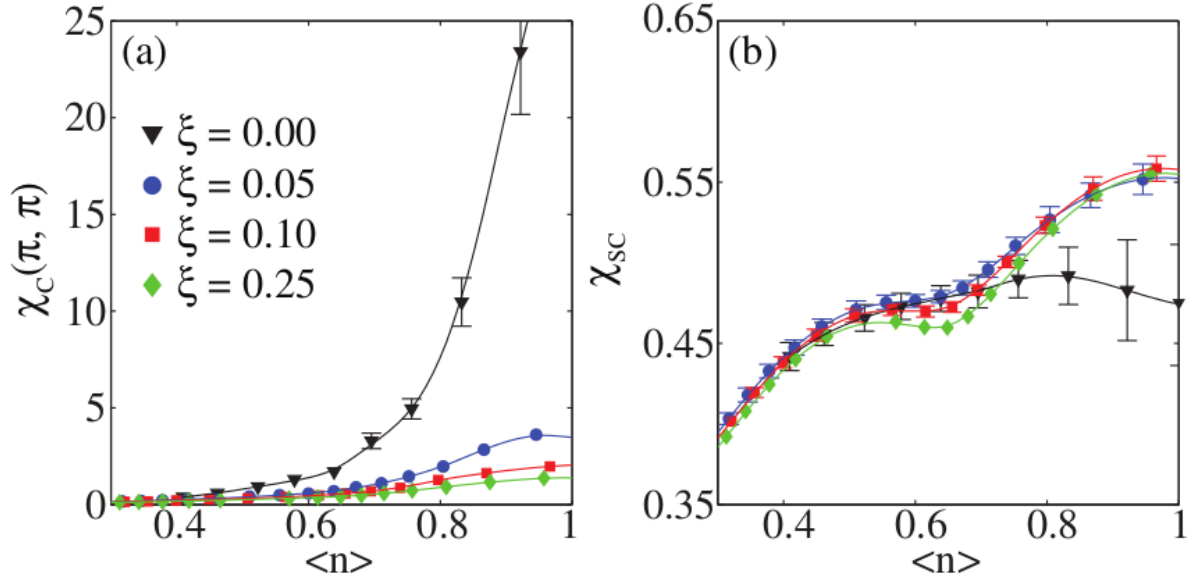
Figure 3.1: (color online) (a) $\mathbf{q} = (\pi, \pi)$ charge and (b) pair-field susceptibilities as a function of filling for the linear ($\xi = 0$, black downward triangle) and non-linear ($\xi = 0.05$, blue circle; $\xi = 0.10$, red square; and $\xi = 0.25$, green diamond) Holstein models with $\Omega = t$ and $\lambda = 0.25$. The remaining parameters are $N = 8$, $\beta = 5/t$, and $\Delta\tau = 0.1/t$. Error bars smaller than the marker size have been suppressed for clarity.
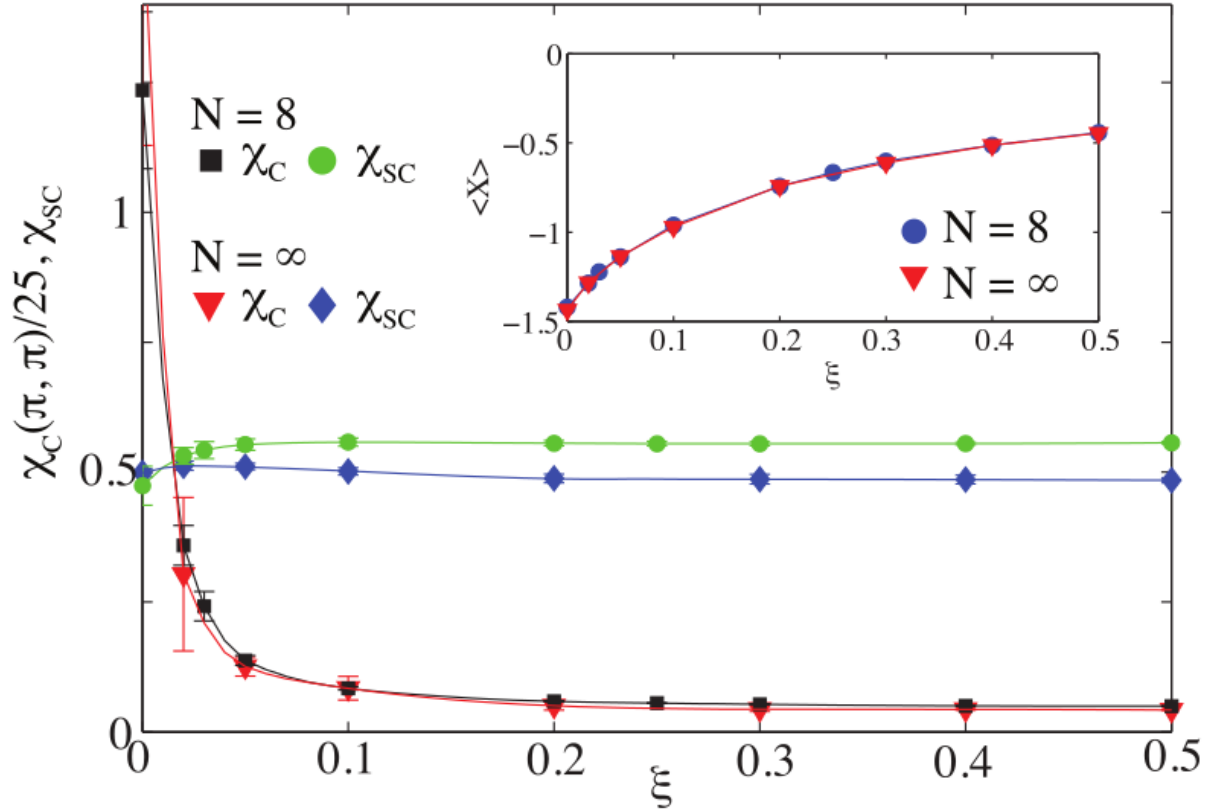
Figure 3.2: (color online) The charge $\chi_C(\pi, \pi)$ (black square and red downward triangle) and pair-field χ_{SC} (green circle and blue diamond) susceptibilities as a function of ξ at half filling $\langle n \rangle = 1$. Results are shown for a $N = 8$ cluster and in the thermodynamic limit $N \to \infty$, which is obtained from a finite-size scaling analysis. The remaining parameters are identical to those used in Fig. 3.1. The charge susceptibility has been rescaled by a factor of 25. Inset: the average value of the lattice displacement as a function of ξ. Error bars smaller than the marker size have been suppressed for clarity.

superconductivity at this temperature once the competition with the CDW correlations has been suppressed or eliminated.

The inset of Fig. 3.2 plots the average lattice displacement $\langle X \rangle = \frac{1}{N} \sum_i X_i$ as a function of ξ. This quantity serves as a proxy for the average number of phonon quanta (which is not directly accessible in the DQMC formalism) as larger lattice distortions are described by coherent states with increasing numbers of phonon quanta. For increasing values of ξ, the average lattice displacement is reduced, and thus, so is the number of phonon quanta on each site. This is fully consistent with the single-carrier limit where the number of phonon quanta in the polaron cloud dropped dramatically for non-zero values of ξ [1]. This relaxation of the lattice displacement shown here thus reflects the undressing of the lattice bipolarons that from the $\mathbf{q} = (\pi, \pi)$ CDW state.

Finite-size effects are also examined in Fig. 3.2, where results in the thermodynamic limit $N \to \infty$ obtained from a finite-size scaling analysis are also shown. The behavior of the CDW susceptibility is nearly identical to the finite cluster results, while the pair-field susceptibility is slightly suppressed in the thermodynamic limit. This indicates that suppression of the CDW correlations for increasing ξ is well captured by the $N = 8$ clusters while the pair-field susceptibility is slightly overestimated. I conclude that finite-size effects associated with determining the susceptibilities on the $N = 8$ cluster are small and have little bearing on my conclusions.

If the non-linear coupling results in a undressing of the polarons, one might expect the system to relax back to a metallic state for large values of ξ. I therefore examine the spectral weight at the Fermi level in order to confirm this expectation. A measure of the spectral weight at the Fermi level ($\omega = 0$) can be obtained from the imaginary time Green's function via the relationship [248]

$$\beta G(\mathbf{k}, \tau = \beta/2) = \frac{\beta}{2} \int d\omega A(\mathbf{k}, \omega) g(\omega, \beta), \tag{3.8}$$

where $g(\omega, \beta) = \cosh^{-1}(\beta\omega/2)$ and $A(\mathbf{k}, \omega) = -\frac{1}{\pi} \text{Im} G(\mathbf{k}, \omega)$ is the spectral function. At low temperatures $g(\omega, \beta)$ is peaked at $\omega = 0$ and therefore weights the spectral weight at the Fermi level. The local propagator $G(\mathbf{r} - \mathbf{r}' = 0, \tau = \beta/2) \propto \sum_{\mathbf{k}} G(\mathbf{k}, \beta/2)$ is then

a measure of the total spectral weight at the Fermi level. For simplicity I introduce the notation $\beta G(\mathbf{r} = \mathbf{r}', \tau = \beta/2) = \beta G_{\beta/2}$.

Figure 3.3(a) shows $\beta G_{\beta/2}$ as a function of ξ. Results are shown at half filling for a number of cluster sizes, as well as the thermodynamic limit. The behavior is similar for all cases examined. For $\xi = 0$ the CDW correlations dominate, resulting in the formation of a CDW gap that reduces the spectral weight at $\omega = 0$. The spectral weight is restored for increasing values of ξ, which is consistent with the closing of the CDW gap. For large ξ the value of $\beta G_{\beta/2}$ approaches the non-interacting value, which is indicated by the dashed lines. Therefore, at $\beta = 5/t$, the system is metallic but with a slightly reduced ξ-dependent spectral weight. The metallicity of the system is further evidenced by the temperature dependence of $\beta G_{\beta/2}$, shown in Fig. 3.3(b) for the $\xi = 0.25$, $N = 8$ case. Here, $\beta G_{\beta/2}$ increases for decreasing temperatures as expected for a Fermi liquid where the quasiparticle scattering rate scales as T^2. The full DQMC result, however, deviates from the non-interacting limit, indicating that the quasiparticles remain slightly dressed by the e-ph interaction. This picture is consistent with the one obtained from the single-carrier limit, where the small polaron relaxes to a large polaron with a renormalization factor Z only slightly reduced from 1 at large values of ξ [1].

I have demonstrated that the system re-enters a metallic phase as the value of ξ is increased and the effective linear coupling is decreased. I would therefore like to access if superconductivity emerges as the ground state if the temperature is lowered further. To examine this, Fig. 3.4(a) plots the temperature dependence of several relevant susceptibilities for the half filling (Fig. 3.4(a)) and approximately quarter-filled models (Fig. 3.4(b)). At half filling the $\mathbf{q} = (\pi, \pi)$ CDW correlations are weakened; however, they remain as the dominate correlations in the system for all values of ξ examined (for reference, $\chi_C(\pi, \pi)/\chi_{SC} \sim 2.2$ for $\xi = 0.5$ and $\beta = 5/t$). This remains true upon further cooling and thus the ground state of the system with $\xi = 0.2$ remains a $\mathbf{q} = (\pi, \pi)$ CDW insulator albeit with a drastically reduced transition temperature.

Away from half filling $\chi_C(\pi, \pi)$ is reduced by a combination of the non-linear interaction and the loss of the Fermi surface nesting at this wave vector. For example, in the vicinity of a quarter filling I find $\chi_{SC} > \chi_C(\pi, \pi)$. But other ordering vectors become relevant at
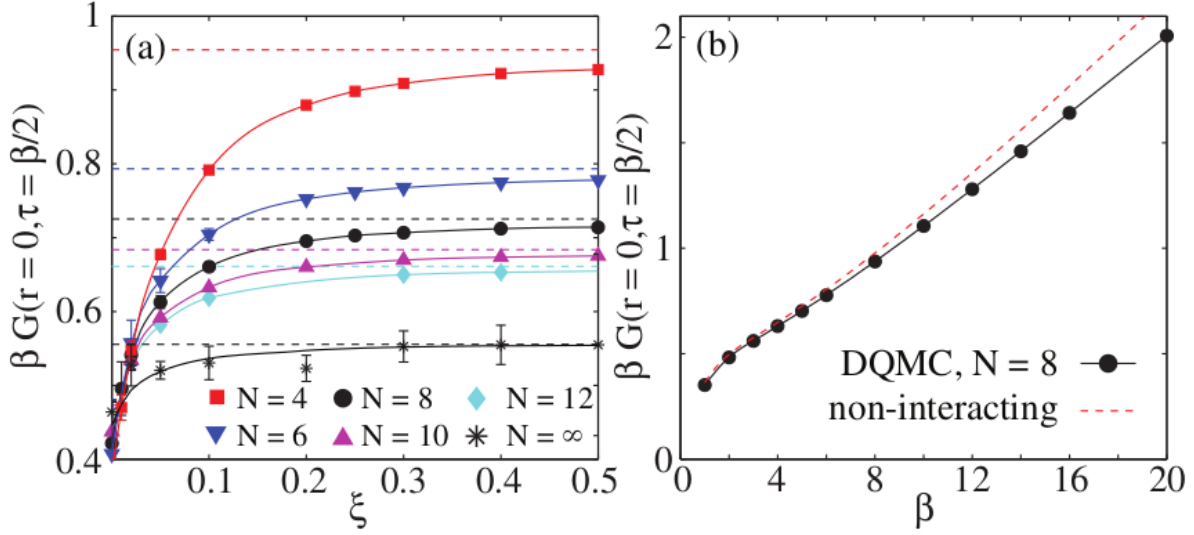
Figure 3.3: (color online) (a) The spectral weight at the Fermi level given by $\beta G(\mathbf{r} = \mathbf{r}', \tau = \beta/2) \equiv \beta G_{\beta/2}$ (see main text) as a function of the non-linear coupling ξ for various cluster sizes and $\Omega = t$ and $\lambda = 0.25$. Results are also shown in the thermodynamic limit $N \to \infty$, which was obtained from a finite-size scaling analysis. The inverse temperature is $\beta = 5/t$. The dashed lines indicae the value for the non-interacting ($\lambda = \xi = 0$) case $\beta G_{\beta/2}^{(0)}$. (b) The temperature dependence of $\beta G_{\beta/2}$ for the $N = 8$ cluster and $\xi = 0.25$. The red dashed line is the result for the non-interacting case. Error bars smaller than the marker size have been suppressed for clarity.
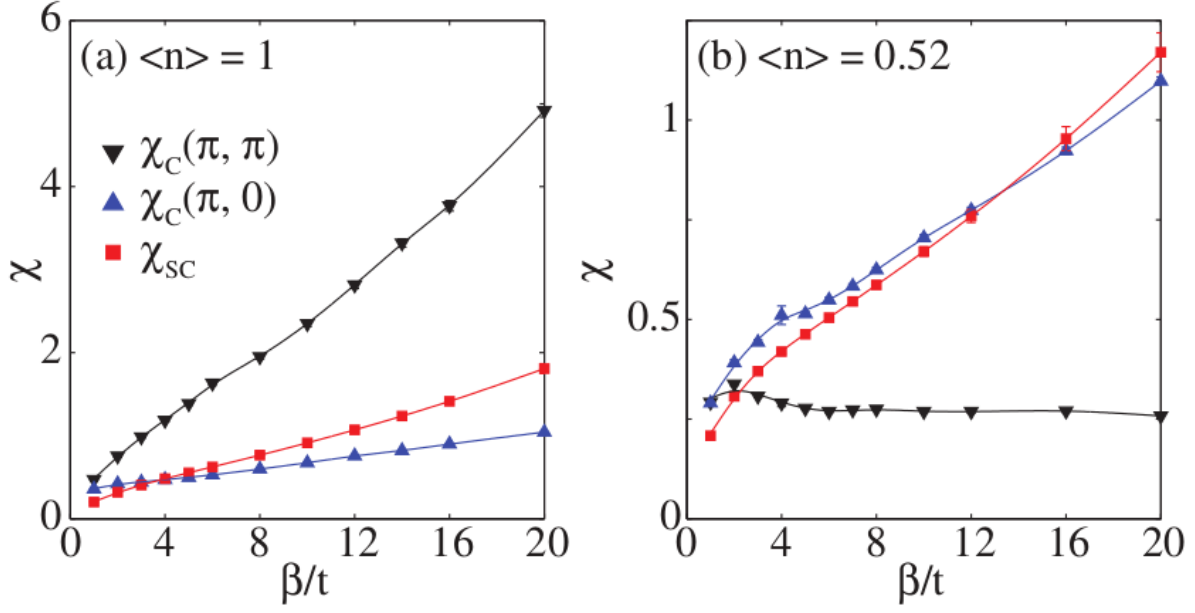
Figure 3.4: (color online) The charge $\chi_C(\mathbf{q})$ and pair-field χ_{SC} susceptibilities as a function of temperature for the non-linear model ($\xi = 0.25$) at fillings (a) $\langle n \rangle = 1$ and (b) $\langle n \rangle = 0.52$. The charge susceptibilities at wave vectors $\mathbf{q} = (\pi, \pi)$ (black downward triangle) and $\mathbf{q} = (\pi, 0)$ (blue upward triangle) are shown. The remaining parameters were $\lambda = 0.25$, $\Omega = t$, and $\Delta\tau = 0.1/t$, and the results were obtained on an $N = 8$ cluster. The red dashed line is the result for the non-interacting case. Error bars smaller than the marker size have been suppressed for clarity.

these fillings, and for $\langle n \rangle \sim 0.52$ the $\mathbf{q} = (\pi, 0)$ ordering vector becomes the dominate vector. Moreover, for $\beta = 5/t$, $\chi_C(\pi, 0) \sim \chi_{SC}$ suggesting that superconductivity could emerge as the ground state at this filling. For decreasing temperatures $\chi_C(\pi, 0)$ and χ_{SC} increase concurrently, but the superconducting pair-field susceptibility overtakes the charge susceptibility at $\beta \sim 14/t$. This signals a superconducting ground state at low temperature but with a reduced T_c owing to the renormalized effective linear coupling. (see section 3.1.2.4)

Finally, in Fig.3.5 I examine the dependence of my results at half-filling on the linear coupling strength λ and the phonon frequency Ω. Figures 3.5(a) and (b) show $\chi_C(\pi, \pi)$ and χ_{SC}, respectively, for $\Omega = t, 3t/2$, and $3t$ and $\lambda = 0.5$. The results follow the trends I have discussed. For $\xi = 0$ the CDW correlations increase with increasing linear coupling or with decreasing phonon frequency, consistently with prior work [230]. In all cases, however, the CDW correlations are suppressed for increasing non-linear interaction strengths. The weakening of the effective linear coupling and suppression of the CDW ordered phase by the non-linear interaction is therefore a generic result, and I expect that this result will hold into the adiabatic regime $\Omega \ll t$.

3.2.2 The quasiparticle residue

In this section, I examine the carrier's quasiparticle reside $Z(\mathbf{k})$ as a function of the non-linear coupling strength and doping. This quantity is related to the effective mass via $Z^{-1} \propto \frac{m^*}{m}$. It can be obtained from the imaginary axis self-energy $\Sigma(\mathbf{k}, i\omega_n)$ using the relationship $Z(\mathbf{k}) = \frac{1}{1+b(\mathbf{k})}$ [6], where

$$b(\mathbf{k}) = \lim_{\omega_n \to 0} -\frac{\partial \mathrm{Re}\Sigma(\mathbf{k}, i\omega_n)}{\partial \omega_n} = \lim_{\omega_n \to 0} -\frac{\mathrm{Im}\Sigma(\mathbf{k}, i\omega_n)}{\omega_n}. \tag{3.9}$$

Here, I approximate $b(\mathbf{k})$ by evaluating Eq. (3.9) for the lowest Matsubara frequency $\omega_n = \pi/\beta$.

Fig. 3.6 shows $Z(\mathbf{k})$ as a function of carrier concentration for several values of the non-linear coupling ξ. These results were obtained on an $N = 4$ cluster, using a linear coupling strength $\lambda = 0.25$ and $\Omega = t$. In the linear model ($\xi = 0$, red dots) the quasiparticle residue decreases as the filling approaches $\langle n \rangle = 1$, where the $\mathbf{Q} = (\pi, \pi)$ CDW correlations begin
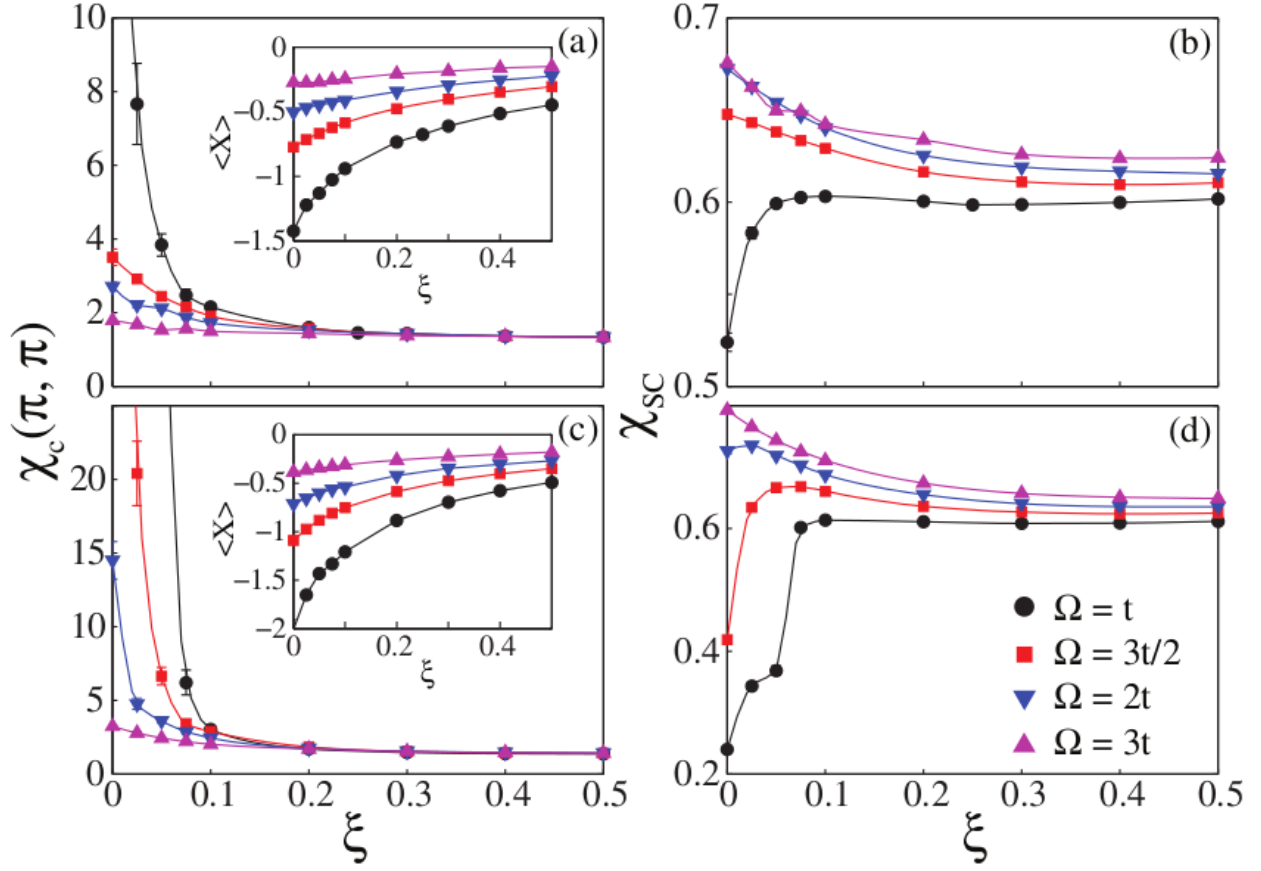
Figure 3.5: (color online) The Ω-dependence of the (a), (c) charge $\chi_C(\pi, \pi)$ and (b), (d) superconducting pair field χ_{SC} susceptibilities for the half-filling model. The linear couplings are $\lambda = 0.25$ for the top panels and 0.5 for the bottom panels. Results are shown for an $N = 8$ cluster. Error bars smaller than the marker size have been suppressed for clarity.
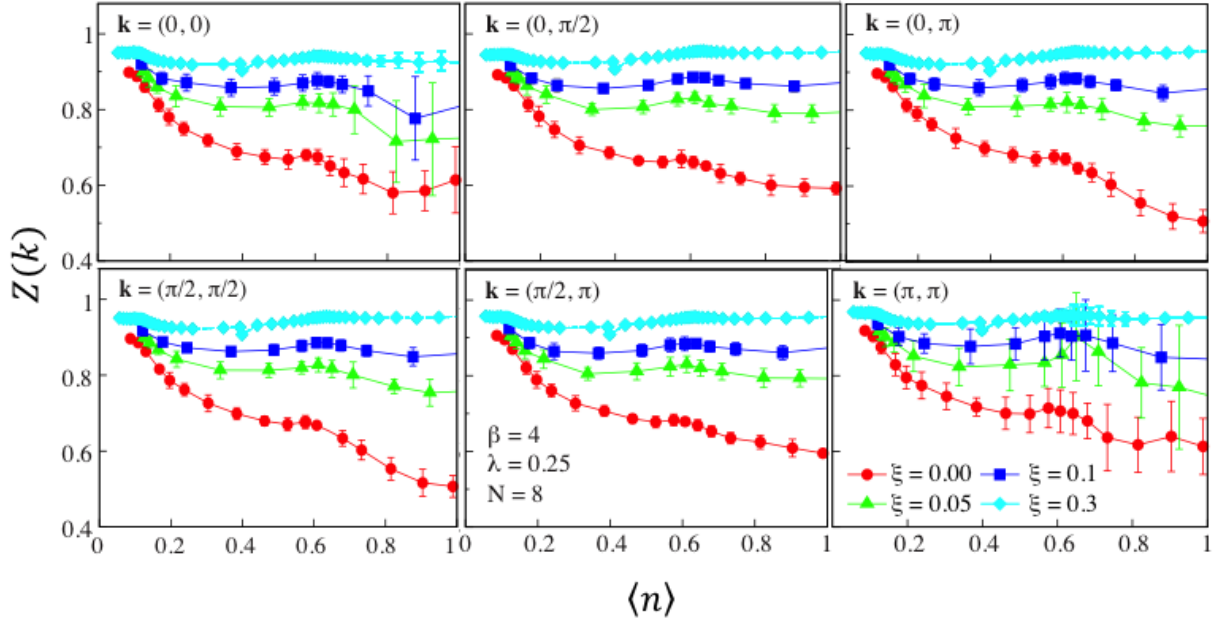
Figure 3.6: (color online) The quasiparticle residue $Z(\mathbf{k})$ as a function of band filling $\langle n \rangle$ for (a) $\mathbf{k} = (0,0)$, (b) $(0, \pi/2)$, (c) $(0, \pi)$, (d) $(\pi/2, \pi2)$, (e) $(\pi/2, \pi)$, and (f) (π, π). Results are shown for various values of the non-linear interaction strength ξ, as indicated in panel (f), and are obtained using an $N = 4 \times 4$ cluster with a linear coupling $\lambda = 0.25$ and an inverse temperature $\beta = 4/t$. Error bars smaller than the marker size have been suppressed for clarity.

to dominate the system. Note that strong CDW correlations are observed, even for the small value of the linear coupling used here, due to a perfect (π, π) nesting condition in the two-dimensional Fermi surface. (For reference, this choice of parameters predicts a CDW transition temperature $\beta_c \sim 5.2/t$ on an $N = 8$ cluster for the linear model, obtained from extrapolating $1/\chi_C(\mathbf{q})$ to zero as a function of β.) This nesting condition also results in large lattice displacements in the linear model. As a result, the inclusion of the non-linear terms has a significant effect on the quasiparticle residue where, for $\xi > 0$, a significant undressing of the quasiparticles occurs and the quasiparticle residues at all momenta begin to rise. This occurs at all doping, however, the effect is more pronounced near half-filling. (My $\xi = 0$ results are in good agreement with Ref. [185], which examined larger system sizes using a complementary diagrammatic Monte Carlo method.)

The formation and suppression of the CDW gap is also reflected in the spectral weight at the Fermi level. Fig. 3.7a plots $G_{\beta/2}$ as a function of filling $\langle n \rangle$ for the same parameters used in Fig. 3.6. Fig. 3.7b plots similar results obtained on a larger cluster and at lower temperature, where the qualitative behavior is the same. The spectral weight in the linear model initially grows with increasing carrier concentration, but saturates as the concentration approaches half-filling and CDW correlations begin to dominate. When a non-linear interaction is introduced, however, $G_{\beta/2}$ increases at most fillings, which is most pronounced near $\langle n \rangle \sim 1$. (The dip around $\langle n \rangle = 0.6$ is a finite size effect due to the smaller number of momentum points in the $N = 4$ cluster. It is much less pronounced on the larger $N = 8$ cluster.) This spectral weight increase directly reflects the increase in the quasiparticle residue and the suppression of the CDW correlations. Previously I showed that a large non-linear coupling drives the system into a metallic state at half-filling, with the value of $\beta G_{\beta/2}$ approaching the non-interacting value [147]. The results in Fig. 3.7 indicate that this also occurs for carrier concentrations away from half-filling.

The results presented in Figs. 3.6 and 3.7a are obtained on a $N = 4$ cluster; however, they are qualitatively representative of the results obtained for all examined cluster sizes, as hinted at by comparing Figs. 3.7a and 3.7b. To confirm this, in Fig. 3.8 I perform a finite size scaling analysis for $Z(0, \pi)$ at half-filling, where the reduction in Z by CDW correlations is most pronounced. From this analysis it is clear that the qualitative behavior
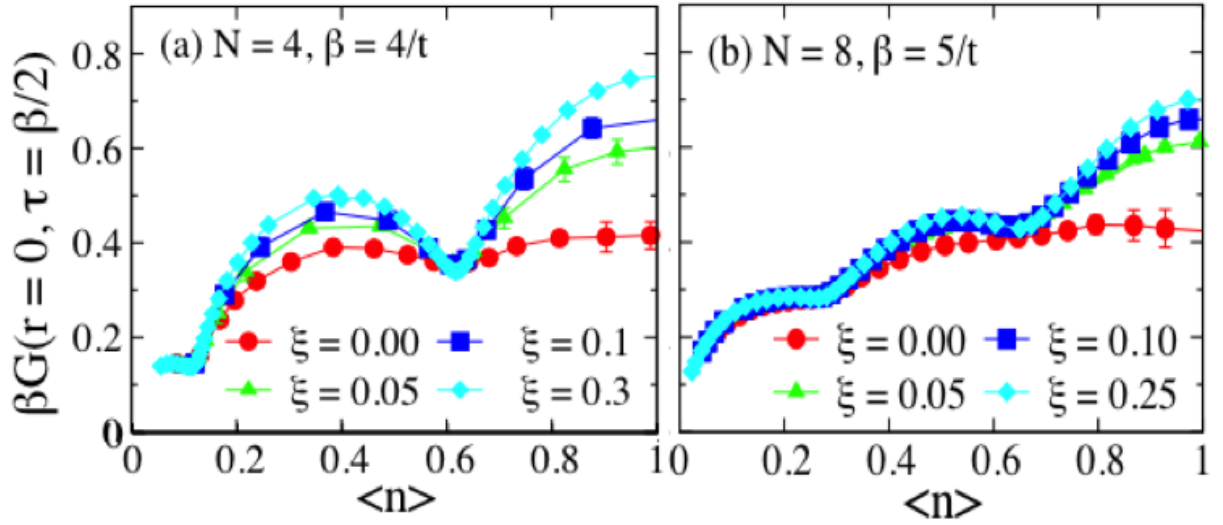
Figure 3.7: The spectral weight at the Fermi level given by $\beta G(r = 0, \tau = \beta/2) \equiv \beta G_{\beta/2}$ as a function of band filling $\langle n \rangle$ for various values of the non-linear coupling strength ξ. (a) Results for a $N = 4$ cluster and an inverse temperature $\beta = 4/t$. (b) Results for a larger $N = 8$ cluster and a lower temperature $\beta = 5/t$. All results are obtained for a linear coupling $\lambda = 0.25$ and a frequency of $\Omega = t$. Error bars smaller than the markers have been suppressed for clarity.
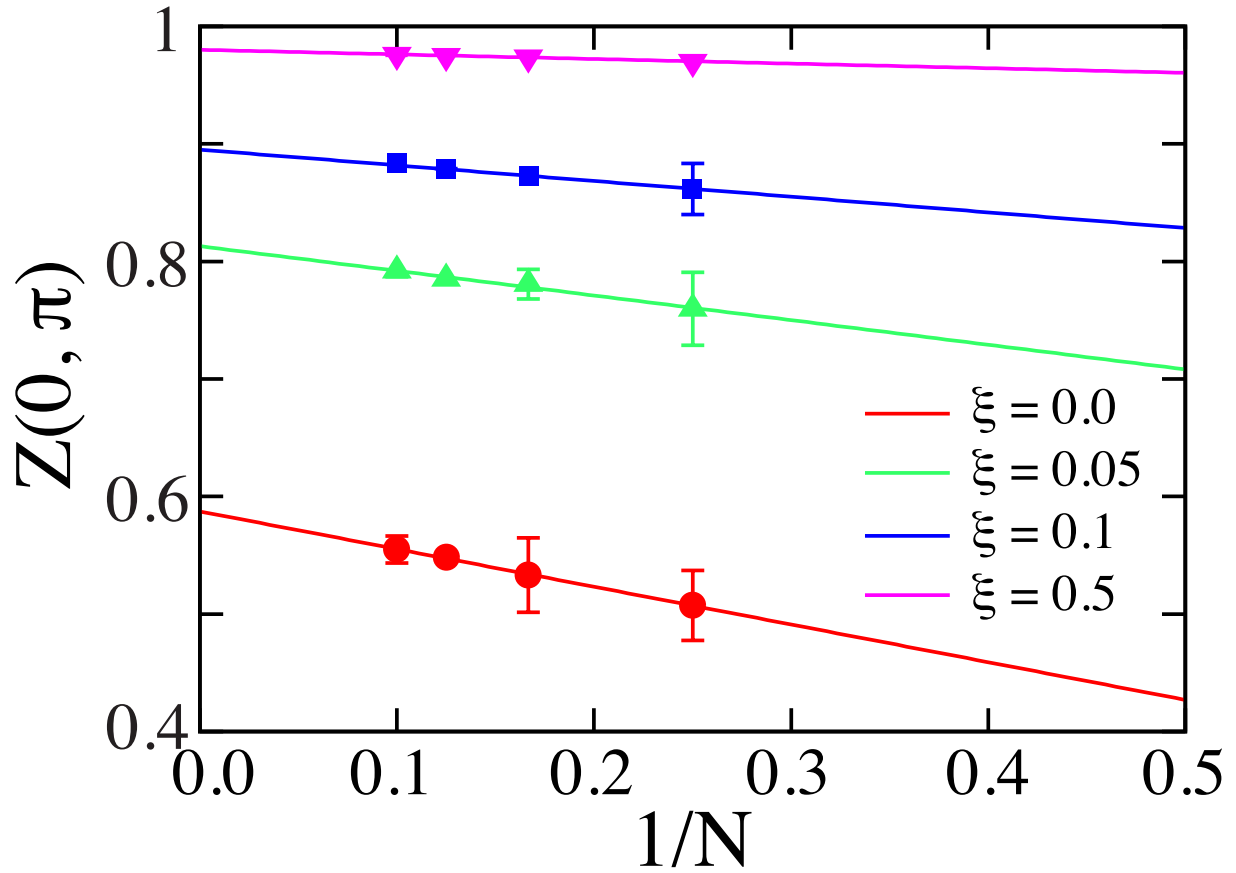
Figure 3.8: (color online) A finite size scaling analysis of $Z(0, \pi)$ as a function of $1/N$ where N is the linear dimension of the cluster. The parameters for the calculations are $\beta = 4/t$, $\Omega = t$, and $\lambda = 0.25$. Error bars smaller than the marker size have been suppressed for clarity.

is not affected by finite size effects and survives in the thermodynamic limit. Moreover, the more pronounced finite size effects occur when the non-linear interaction is weak. As similar scaling results were obtained for both the charge susceptibility and the electron spectral weight in my previous work [147], I conclude that the qualitative physics of the non-linear model can be obtained on an $N = 4$ cluster.

In Fig. 3.9a I consider the temperature dependence of $Z(\mathbf{k})$ and average displacement of the lattice $\langle X \rangle = \frac{1}{N^2 L} \sum_{i=1}^{N} \sum_{l=1}^{L} X_{i,l}$ for the half-filled model. Here, results for $Z(0, \pi)$ only are shown, since similar trends were found at all momenta. Focusing first on the linear model, I find that $Z(0, \pi)$ decreases with temperature as the CDW correlations begin to set in. The average lattice displacement, however, does not exhibit the same temperature dependence (see inset of Fig. 3.9a). As the non-linear interaction strength grows, however, the quasiparticle residue increases back towards its non-interacting value. For small ξ this rise is somewhat rapid, but it gives way to a more gradual increase for $\xi \gtrsim 0.1$. The increase is also accompanied by a decrease in the average lattice displacement (inset of Fig. 3.9). This behavior mirrors the observed ξ-dependence of the CDW susceptibility [147], and is consistent with the conclusion that a finite $\xi > 0$ undresses the carriers and relaxes the lattice distortions normally present in the linear model.

The Ω-dependence of $Z(\pi, 0)$ and $\langle X \rangle$ for the same model are shown in Fig. 3.9b. Here, the $\xi = 0$ results are consistent with those obtained for the 1D Holstein model, where the tendency to form a CDW grows with decreasing phonon frequencies [98]. Consequently, both the quasiparticle residue and average lattice displacement decrease as the value of Ω increases. The introduction of $\xi > 0$ results in the further decrease in these quantities.

From this section I conclude that the non-linear interaction with $\xi > 0$ acts to undress the quasiparticles and that this is a generic result, regardless of the values of Ω and β. The undressing, however, is much more pronounced at low temperatures, for smaller values of the phonon frequency, and near half-filling, where the CDW correlations (and subsequently the local lattice displacements) are largest in the linear model.
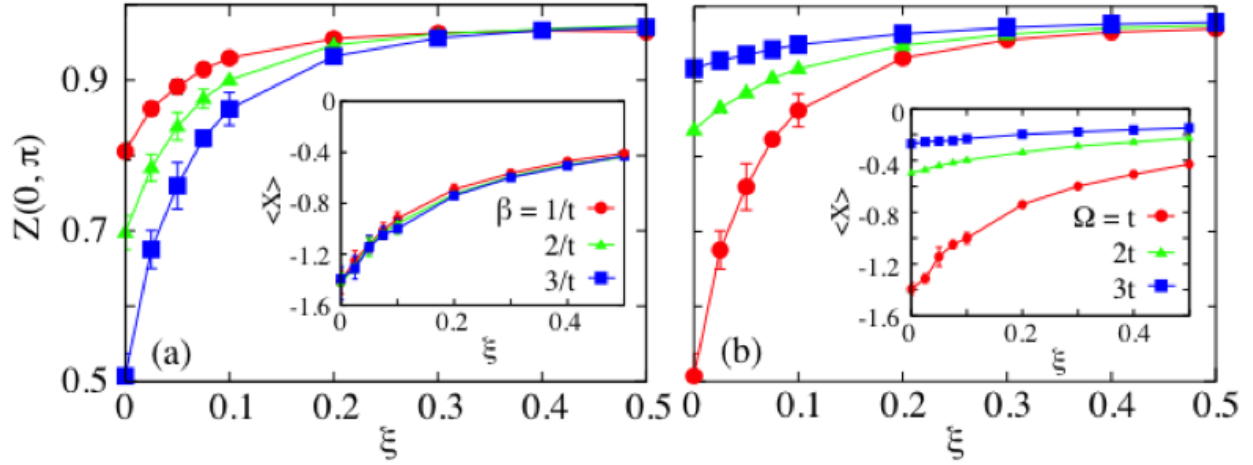
Figure 3.9: The (a) temperature and (b) Ω dependence of the quasiparticle residue in the half-filled model as a function of non-linear coupling strength ξ. The insets show the corresponding expectation value of the lattice displacement. All results are obtained on an $N = 4$ cluster and with a linear coupling $\lambda = 0.25$. Error bars smaller than the marker size have been suppressed for clarity.

3.2.3 Electron and Phonon energetics

The average kinetic energy of the electronic subsystem $\langle \text{KE} \rangle_{\text{el}} = -t \sum_{\langle i,j \rangle, \sigma} \langle c_{i,\sigma}^{\dagger} c_{j,\sigma} \rangle$ at $\beta = 4/t$ is shown in Fig. 3.10. Results are shown as a function of band filling $\langle n \rangle$ for various ξ and for a linear coupling $\lambda = 0.25$. For $\xi = 0$ the total kinetic energy $-\langle \text{KE} \rangle_e$ increases as a function of $\langle n \rangle$ as higher momentum states are populated in the Fermi sea, however, the total kinetic energy saturates as the filling increases beyond $\langle n \rangle > 0.6$. This is due to the saddle point in the band dispersion at $(0, \pi)$ and is also present in the non-interacting model (indicated by the dashed line). When the non-linear interaction is added I see an overall increase in the total kinetic energy, which tends towards the non-interacting value at all fillings for large ξ. This again reflects the undressing of the quasiparticles and the subsequent increase in mobility of the electronic subsystem.

Fig. 3.10b shows the corresponding e-ph interaction energy, defined as $\langle \text{E} \rangle_{\text{e-ph}} = \sum_i \langle g_1 \hat{n}_i \hat{X}_i + g_2 \hat{n}_i \hat{X}_i^2 \rangle$. Unsurprisingly, the total e-ph interaction energy increases with band filling as both the average number of electrons per site and the average lattice displacement increase. This is most evident in the linear model ($\xi = 0$). Increasing the value of ξ naturally leads to smaller lattice displacements and a significant decrease in $\langle \text{E} \rangle_{\text{e-ph}}$.

The average kinetic $\langle \text{KE} \rangle_{\text{ph}}$ and potential $\langle \text{PE} \rangle_{\text{ph}}$ energies of the lattice are shown in Figs. 3.11a and 3.11b, respectively. They are given by

$$\langle \text{KE} \rangle_{\text{ph}} = \frac{1}{2\Delta\tau} - \frac{M}{2} \Big\langle \sum_{i,l} \Big(\frac{X_{i,l+1} - X_{i,l}}{\Delta\tau} \Big)^2 \Big\rangle \tag{3.10}$$

$$\langle \text{PE} \rangle_{\text{ph}} = \frac{M\Omega^2}{2} \Big\langle \sum_{i,l} X_{i,l}^2 \Big\rangle. \tag{3.11}$$

(The factor of $\frac{1}{2\Delta\tau}$ appearing in Eq. (10) is a Euclidean correction introduced by the Wick rotation to the imaginary-time axis [113].)

In the linear model I see a very weak variation in the phonon kinetic energy as a function of filling, with a slight decrease observed near half-filling when the CDW correlations increase. This is consistent with prior observations of the lattice kinetic energy in the vicinity of a CDW transition in the Hubbard- Holstein model [113]. The average potential energy of the lattice grows as the average number of carriers per site increases. When the non-linearity
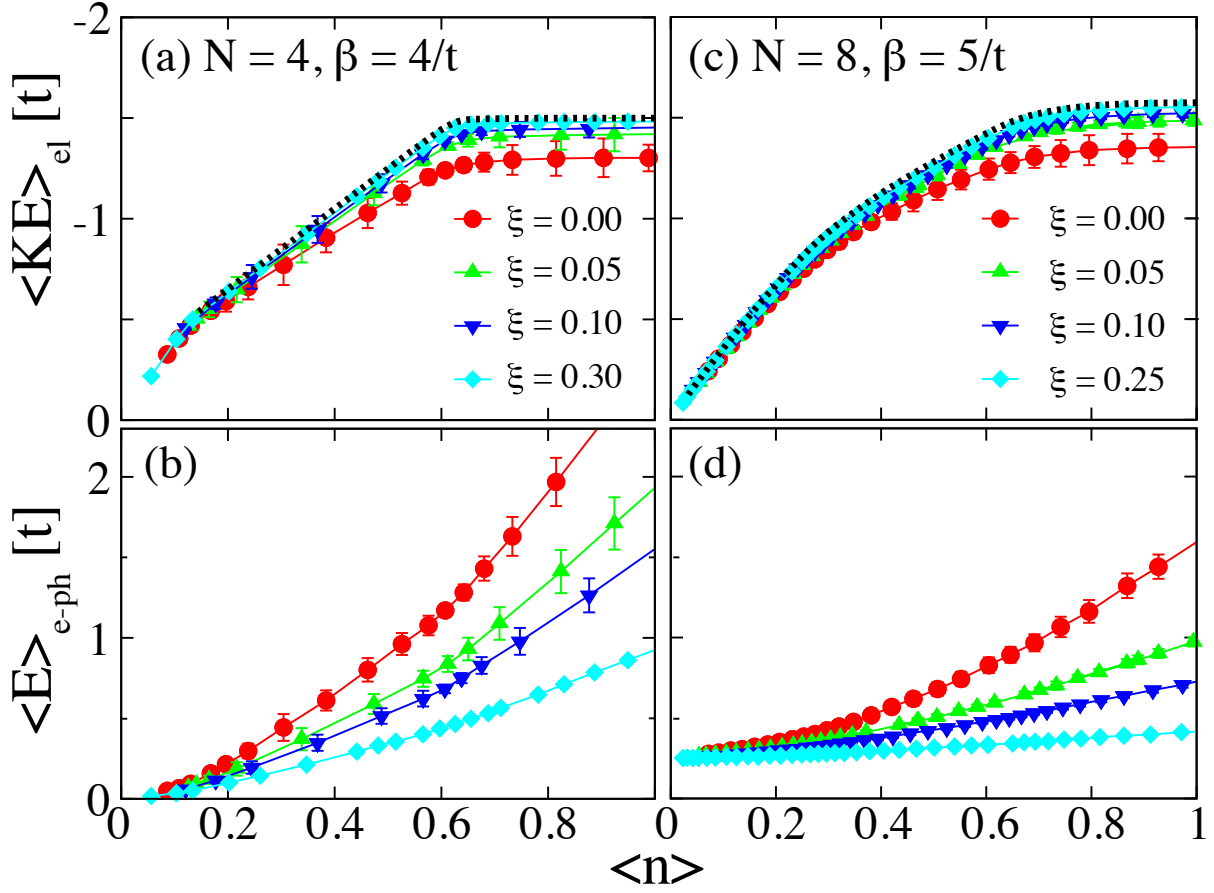
Figure 3.10: (color online) (a) The electron kinetic energy $\langle KE \rangle_{\text{el}}$ and (b) the e-ph energy $\langle E \rangle_{\text{e-ph}}$ as a function of band filling $\langle n \rangle$ for various non-linear interaction strengths ξ, as indicated. Results are obtained on an $N = 4$ cluster and with a linear coupling $\lambda = 0.25$, phonon frequency $\Omega = t$, and an inverse temperature $\beta = 4/t$. The dashed lines in panels (a) and (c) indicate the non-interacting result. (c) and (d) show corresponding results for a larger $N = 8$ cluster and $\beta = 5/t$. The remaining parameters are the same as in (a) and (b). Error bars smaller than the marker size have been suppressed for clarity.
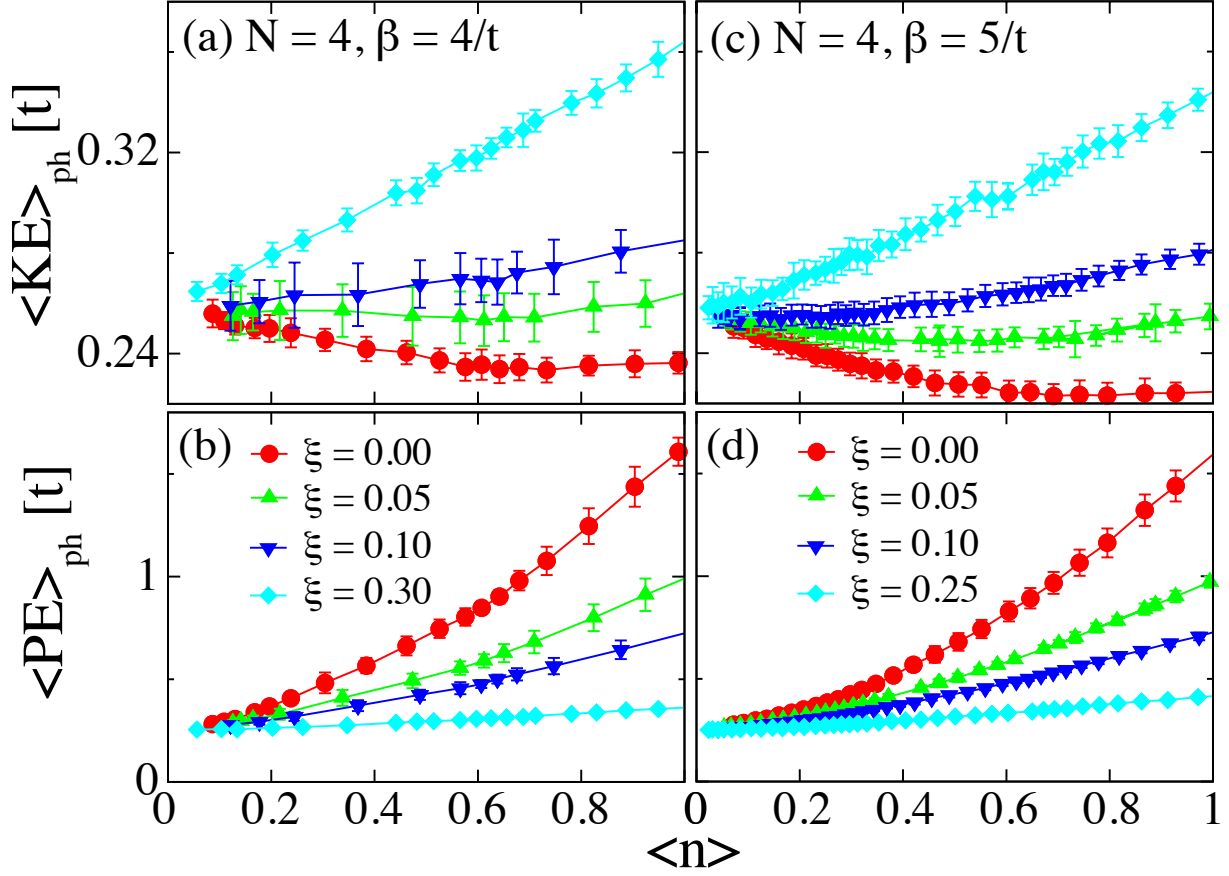
Figure 3.11: (color online) The phonon (a) kinetic energy $\langle KE \rangle_{ph}$ and (b) potential energy $\langle PE \rangle_{ph}$ as a function of band filling $\langle n \rangle$ for various of the non-linear interaction strength ξ, as indicated in panel (b). Results are obtained on an $N = 4$ cluster and with a linear coupling $\lambda = 0.25$, $\Omega = 1$, and $\beta = 4/t$. (c) and (d) show similar results obtained on a larger $N = 8$ cluster with $\beta = 5/t$. Error bars smaller than the marker size have been suppressed for clarity.

is introduced and the lattice distortions diminish (see 3.9b, inset), and I see an increase in the lattice kinetic energy, which is attributed to the hardening of the phonon dispersion. At the same time, I see a decrease in the total lattice potential energy. Here, the non-linear interaction has two opposing effects: the increase in the phonon frequency increases the lattice potential energy while the decrease in the effective linear coupling decrease the net lattice distortions and subsequently lowers the potential energy. My results indicate that the latter effect has the stronger impact.

The energetics reported here are completely consistent with the conclusion that the non-linear interaction acts to harden the phonon frequency and weaken the effective linear interaction, which results in an undressing of the quasiparticles for $\xi > 0$.

3.2.4 Phonon Spectral Properties

In the linear Holstein model the formation of the CDW phase is accompanied by a softening of the phonon dispersion to zero energy at the nesting wavevector $\mathbf{Q} = 2\mathbf{k}_F = (\pi, \pi)$ [195, 172, 252, 262]. This softening is generated by the strong nesting condition of the non-interacting Fermi surface. The inclusion of the non-linear e-ph interaction is therefore expected to modify the phonon dispersion in two important ways: first, it will undo the softening at $\mathbf{Q}$ as the CDW correlations are suppressed. Second, it will result in an overall renormalization of the phonon frequency, as showed in the Ref. [1]. I confirm these expectations in this section by examining the phonon spectral function $B(\mathbf{q}, \nu)$ and the phonon density of states (DOS) $N_{\mathrm{ph}}(\nu) = \frac{1}{N^2} \sum_{\mathbf{q}} B(\mathbf{q}, \nu)$.

In the non-interacting limit, $B(\mathbf{q}, \nu)$ and $N_{\mathrm{ph}}(\nu)$ are delta functions centered at the bare phonon frequency Ω. In the presence of a non-zero linear interaction only, this distribution shifts to lower energy and broadens. This is illustrated in Figs. 3.12 and 3.13a, which plot $N_{ph}(\nu)$ and the momentum-resolved phonon spectral function $B(\mathbf{q}, \nu)$, respectively, for the half-filled model. These results were obtained on $N = 8$ clusters, with a linear coupling $\lambda = 0.25$, $\Omega = t$, and at an inverse temperature of $\beta = 4/t$. Due to the finite value of λ, the phonon frequency softens from its non-interacting value and $N_{ph}(\nu)$ for the linear model consists of a broad, asymmetric distribution centered at $\sim 0.60t$. The asymmetry in $N_{ph}(\nu)$ reflects the momentum dependence of the softening and the low-energy spectral weight in
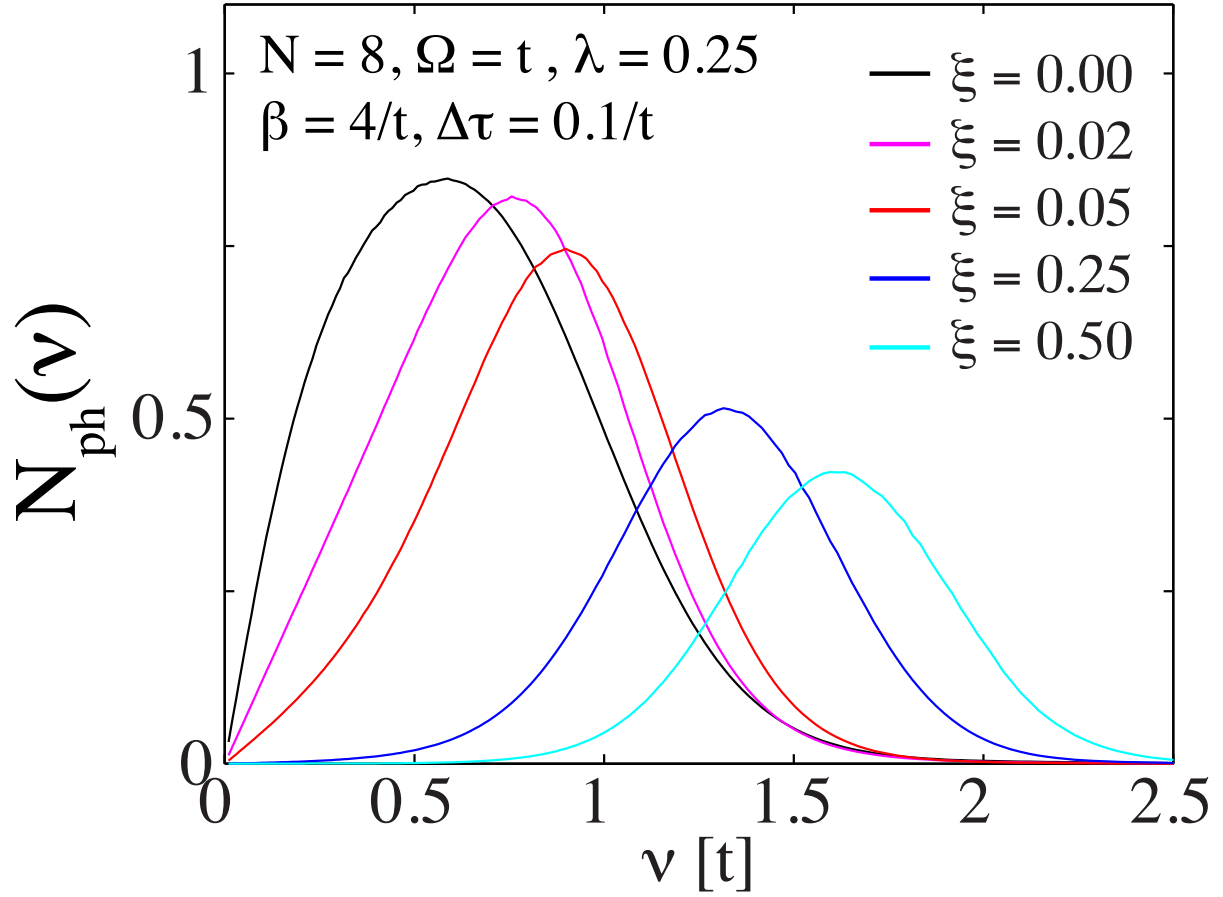
Figure 3.12: (color online) The phonon density of states $N_{\mathrm{ph}}(\nu) = \frac{1}{N}\sum_{\mathbf{q}} B(\mathbf{q},\nu)$ for the half-filled model as a function of the non-linear interaction strength. The remaining calculation parameters are as indicated.
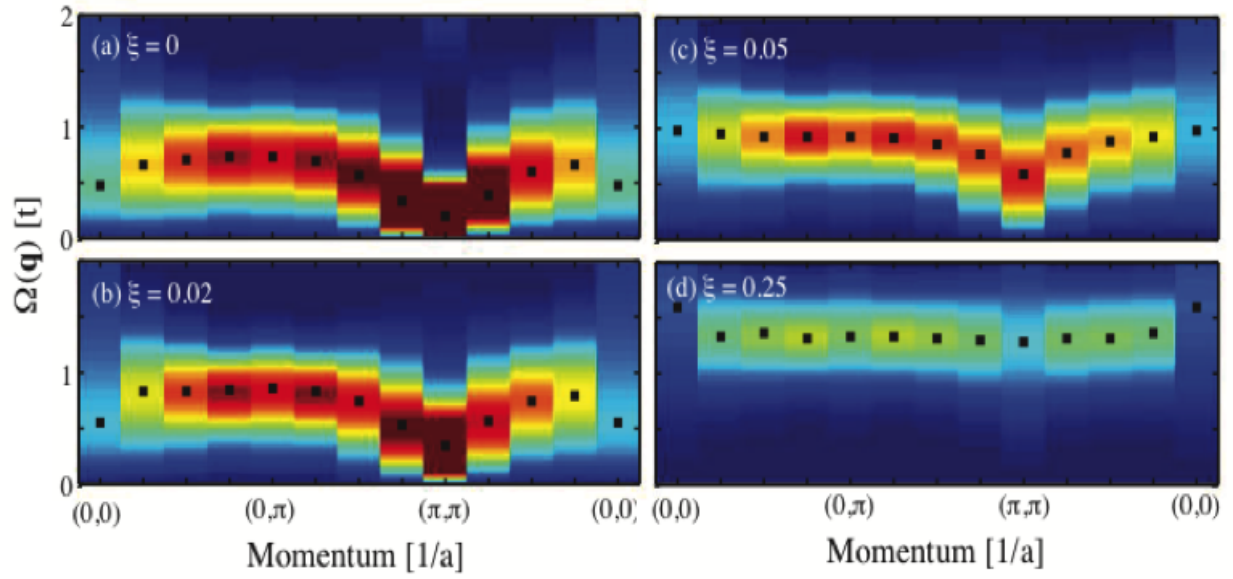
Figure 3.13: (color online) The momentum resolved phonon spectral function $B(\mathbf{q}, \nu)$ for the half-filled model and for various values of the non-linear interaction strength, as indicated in each panel. Results were obtained on an $N = 8$ cluster with $\lambda = 0.25$, $\Omega = t$, $\beta = 4/t$ and $\Delta\tau = 0.1/t$. The black squares indicate the position of the peak in the phonon spectral function.

$B(\mathbf{Q},\nu)$, coupled with the requirement that $B(0) = 0$ for bosons. This is more easily seen in the momentum-resolved spectral function (Fig. 3.13a), which has a clear Kohn anomaly at $\mathbf{Q} = (\pi, \pi)$.

Two prominent changes occur when $\xi \neq 0$. First, the peak in the DOS shifts to higher energies, which verifies the hardening of the effective phonon frequency. This behavior is also clearly seen in the momentum resolved spectral functions, shown in Fig. 3.13. Second, the pronounced Kohn anomaly begins to disappear as the CDW correlations are suppressed with increasing values of ξ. Both of these results confirm my expectations.

3.2.5 Mean-field Treatment of the quadratic e-ph interaction

As I have repeatedly seen, the non-linear e-ph interaction acts to renormalize both the bare linear interaction strength λ and the bare phonon frequency Ω. Both of these effects can be *qualitatively* understood at the mean-field (MF) level for the quadratic model, where an effective linear Hamiltonian is obtained by performing a MF decoupling of the interaction terms proportional to $b_i^\dagger b_i^\dagger$ and $b_i b_i$ [1]. The resulting effective MF Hamiltonian is

$$H_{MF} = H_{el} + \sum_i \Omega_{MF} \left(b_i^\dagger b_i + \frac{1}{2} \right) + \sum_{i,\sigma} g_{MF} \hat{n}_{i,\sigma} \left(b_i^\dagger + b_i \right),$$

where $\Omega_{MF} = \Omega + 2g_2$ and $g_{MF} = g_1(1 - \frac{2g_2}{\Omega + 4g_2})$ are the renormalized phonon frequency and e-ph coupling constants, respectively. One immediately sees that the quadratic e-ph interaction leads to a softening (hardening) of the phonon frequency and an increase (decrease) in the effective linear interaction strength g_1 for $\xi < 0$ ($\xi > 0$). These two effects combine to produce an overall increase (decrease) in the strength of the effective dimensionless coupling $\lambda_{eff} \propto \frac{g_{MF}^2}{\Omega_{MF}}$.

The MF treatment of the non-linear interaction is consistent with the general trends reported here and in Refs. [147] and [1]. I stress, however, that the MF description only provides a qualitative picture of the non-linear effects. To illustrate this, I compare my DQMC results for the full non-linear Hamiltonian against the predictions obtained from two sets of effective linear models. The first is the MF-derived model defined by Eq. (3.12). The

second is the set of effective linear models whose parameters are obtained by tuning the Ω_{eff} and g_{eff} to reproduce the electronic properties of the system.

I consider the MF-derived model first. Fig. 3.14 compares the results for the quasiparticle residue, $\chi_C(\pi, \pi)$, and the pair-field susceptibility χ_{SC} calculated using the full non-linear model [Eq. (3.2)] to results obtained from a DQMC simulation of the corresponding MF-derived linear model [Eq. (3.12)] at half-filling. I find that the MF model does a poor job in quantitatively capturing the electronic properties; it underestimates both the quasiparticle residue $Z(0, \pi)$ and the tendency towards the formation of a CDW when compared to the full non-linear model. The MF model also over-predicts the magnitude of the superconducting pair-field susceptibility when ξ is large and under-predicts it when ξ is small.

The results shown in Fig. 3.14 demonstrate that the MF treatment of the quadratic interaction can only provide a qualitative picture of the physics of the non-linear model; however, another choice in effective model might do a better job. I explored this possibility by adjusting the effective coupling strength in the linear model such that the linear model reproduced the electronic properties of the full non-linear model. This procedure was performed for two choices in the phonon frequency. First, I set the phonon frequency equal to the bare value and adjusted the value of the coupling strength to reproduce the quasiparticle residue, as shown Fig. 3.15a. The value of the linear coupling strength g_{eff} needed to produce this agreement is shown in the inset (black solid $\triangle$), where it is compared against the corresponding value of $g_{MF} = g_1 + 2g_2$. By tuning the value of g_{eff} I am able to accurately capture the quasiparticle residue. The charge and superconducting pair-field susceptibilities are also well reproduced, indicating that this effective model is capable of capturing the electronic properties of the system. But when I examine the phonon properties (Figs. 3.15c & 3.15d) I find some disagreement, particularity with respect to the predicted kinetic energy of the lattice, where the linear model systematically under-predicts the correct results.

The comparison between the two models can be improved somewhat if I set the phonon frequency to be equal to Ω_{MF} and again readjust the value of g_{eff}. This case is shown in Fig. 3.15e-h. Using this choice I am again able to accurately capture the electronic properties and improve the comparison between the kinetic energy. But this comes at the expense of the level of agreement between the average lattice potential energy and the average lattice
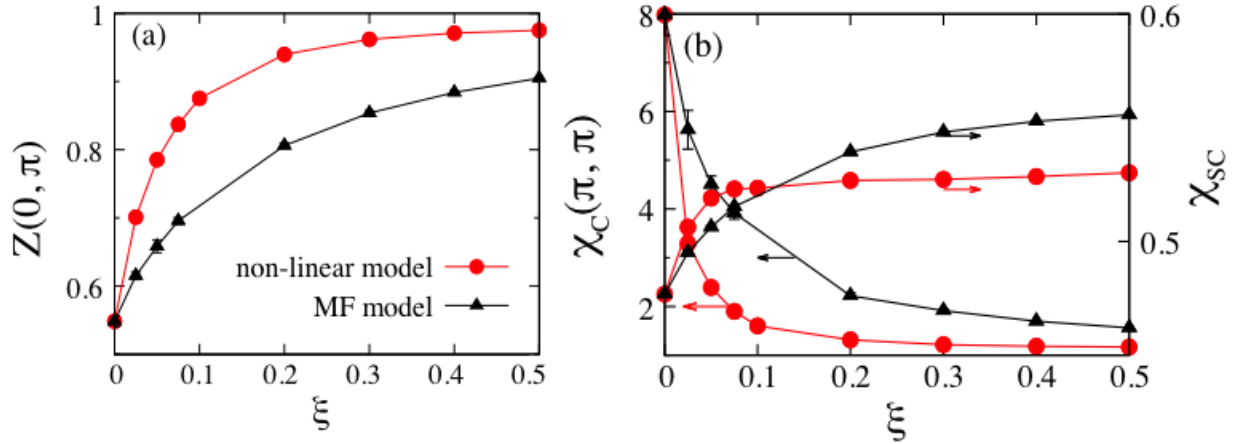
Figure 3.14: (color online) A comparison of (a) the quasiparticle residue and (b) CDW $\chi_C(\pi, \pi)$ and pair field susceptibilities χ_{SC} obtained from the non-linear model and its effective linear model, as defined in the main text. The bare linear coupling and phonon frequency are $\lambda = 0.25$ and $\Omega = t$, respectively. In both cases results are obtained on an $N = 8$ cluster and at an inverse temperature of $\beta = 4/t$. Error bars smaller than the marker size have been suppressed for clarity.
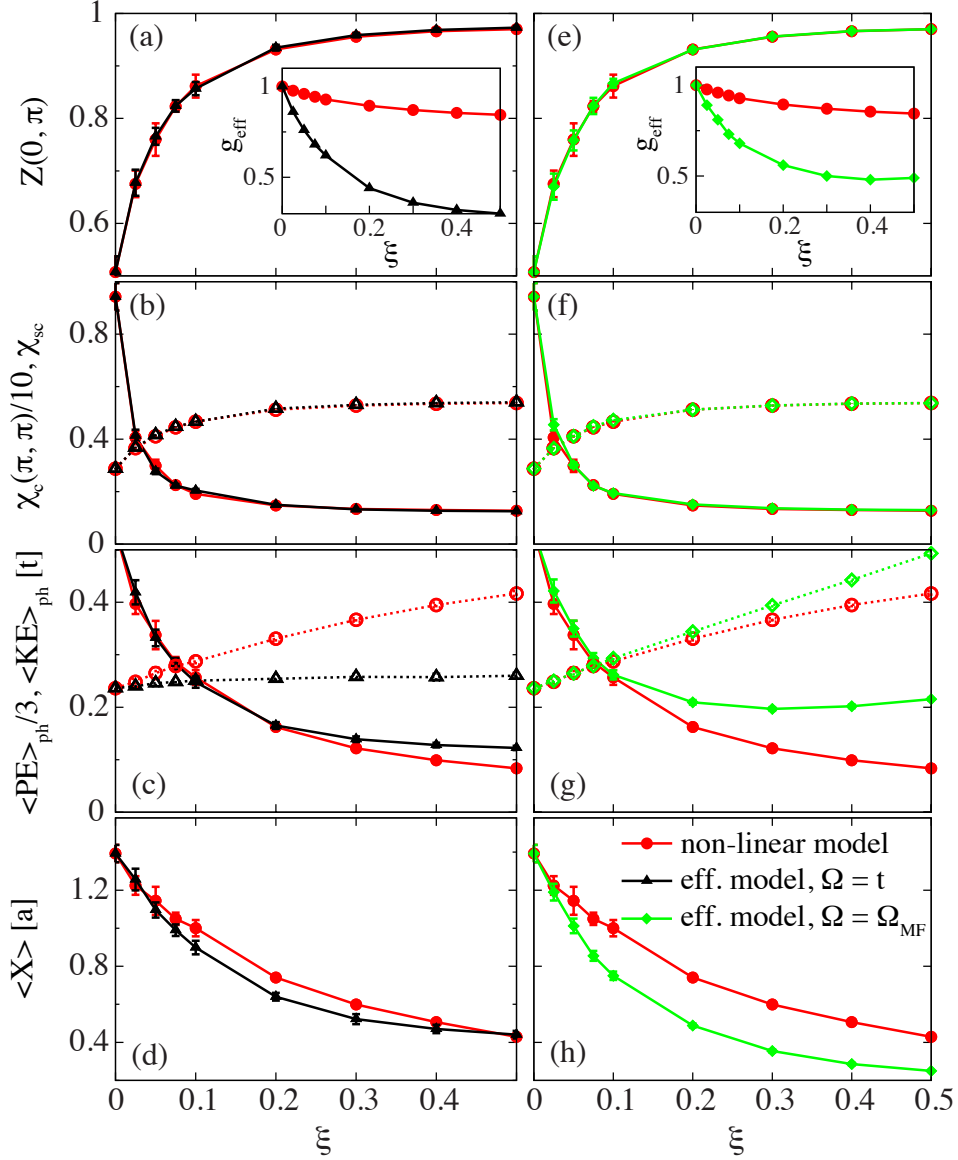
Figure 3.15: (color online) A comparison of the results obtained for the full non-linear model and an effective linear model where the value of the *e*-ph coupling constant has been adjusted to reproduce the electronic properties of the non-linear model. Panels (a)-(d) show a comparison for an effective linear model with $\Omega = t$, equal to the bare phonon frequency. Panels (e)-(f) show a comparison for an effective linear model with $\Omega = \Omega_{MF}$. The top row [panels (a) & (e)] compares the quasiparticle residues obtained with both models. The second row [panels (b) & (f)] shows the resulting charge (solid lines) and pair-field (dashed lines) susceptibilities. The third row [panels (c) & (g)] show the resulting phonon potential and kinetic energies. The potential energy has been divided by a factor of three and is indicated by the solid lines while the kinetic energy is indicated by the dashed lines. Finally, the bottom row [panels (d) & (h)] show the average value of the lattice displacement. The remaining parameters of the simulation are $\beta = 4/t$ and $N = 8$.

displacement. From this I conclude that an effective linear model cannot capture both the electronic and phononic properties of the non-linear model, for a fixed value of the phonon frequency. These results show that while the *qualitative effects* can be understood using an effective linear model, the full non-linear interaction should be retained if one wishes to accurately capture the effects of the non-linear interaction on both the phononic and electronic properties of the system. A similar conclusion was reached in Ref. [1] in the single carrier limit.

3.2.6   Negative values of ξ

I have shown that a positive ($\xi > 0$) non-linear coupling results in a hardening of the phonon frequency and a renormalization of the effective linear e-ph coupling to weaker values. But what about the case when $\xi < 0$, where the MF model predicts an enhanced effective linear coupling? Before examining this case, one should note that a large negative ξ necessarily requires the inclusion of additional anharmonic terms in the lattice potential [2]. For $\xi < 0$ ($g_2 < 0$) the phonon frequency given by $\Omega_{eff} = \Omega + 2g_2$ can become negative for sufficiently large values of g_2, indicating an instability in the lattice. In this event the anharmonic terms of the lattice potential are required to maintain stability. At present, my codes do not contain such terms and I am unable to examine this case in great detail. I therefore restrict ourselves to a larger value of $\Omega = 2t$ and small values of $|g_2|$ in order to get a feel for the $g_2 < 0$ regime while ensuring the stability of the lattice.

Fig. 3.16a shows the quasiparticle residue, $\chi_C(\pi, \pi)$, and χ_{SC} as a function of band filling for various values of $\xi < 0$. These results were obtained for a linear coupling of $\lambda = 0.25$ and on an $N = 8$ cluster. I find that the quasiparticles are more effectively dressed when $\xi < 0$, and the quasiparticle residue is much smaller for all fillings when increasing negative quadratic interactions are included. The CDW correlations are also significantly enhanced, as reflected in the charge susceptibility shown in Fig. 3.16b. Both of these observations are in line with the expected increase in the effective linear coupling. Furthermore, since the CDW phase directly competes with s-wave superconductivity, the pair-field susceptibility is suppressed at filling values where the CDW correlations dominate. In addition, I also see a noticeable decrease in the pair-field susceptibility at band fillings where the CDW
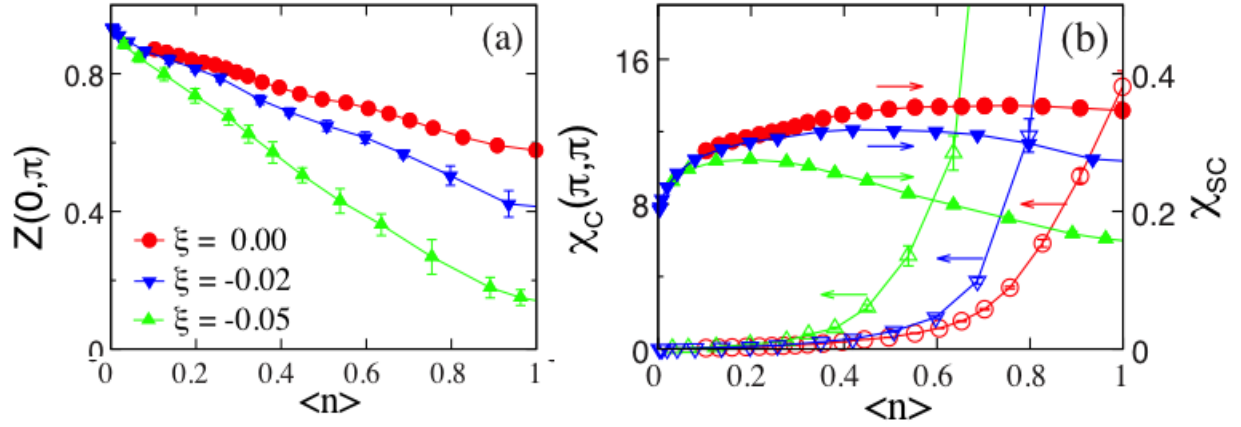
Figure 3.16: (color online) (a) the quasiparticle residue and (b) CDW $\chi_C(\pi, \pi)$ (open symbols) and pair field susceptibilities χ_{SC} (solid symbols) as a function of band filling. The parameters are set as: $\lambda = 0.25$, $\Omega = 2t$, $\beta = 4$. The results are obtained on an $N = 8$ cluster. Error bars smaller than the marker size have been suppressed for clarity.

does not dominate. This suggests that the negative non-linear interaction has a detrimental effect on the superconducting transition temperature, which stems from the decrease in the quasiparticle residue. Fig. 3.17 plots the momentum dependence of the charge susceptibility $\chi(\mathbf{q})$ as a function of negative ξ at half filling, where it is clear that the dominant CDW correlations are still being set by the Fermi surface nesting condition.

3.3   Conclusion

We have examined a non-linear Holstein model on a two-dimensional square lattice and at finite temperatures and carrier concentrations using determinant quantum Monte Carlo. The competition between CDW and superconducting correlations was re-examined as a function of the non-linear e-ph interaction strength. The primary effect of the positive non-linear e-ph interaction is a dramatic suppression of the CDW correlations that dominate the linear model. A less pronounced effect was observed for the superconducting correlations. These effects are attributed to a combined hardening of the phonon mode and renormalization of the effective linear coupling by the non-linear terms. The net result is an overall reduction in the e-ph interaction strength. This assumption is corroborated by checking quasiparticle properties. It found that a positive nonlinear interaction term serves to undress the quasiparticles leading to carriers with lighter effective masses. This leads to changes in the energetics of both the electrons and phonons, as well as the relaxation of the local lattice distortions surrounding each carrier. I have also examined the case when the quadratic e-ph interaction has the opposite sign as the linear interaction, although this case cannot be explored in detail without the inclusion of additional anharmonic terms in the lattice potential. Nevertheless, in my limited range of accessible parameters, I found that a quadratic interaction results in an increased dressing of the carriers and an enhanced tendency towards the formation of a $Q = (\pi, \pi)$ CDW ordered phase.

While many of the effects we have discussed can be understood qualitatively at the mean-field level, we have demonstrated that the quantitative effects can only be captured by the full non-linear model. Specifically, the effective linear models fail to simultaneously capture the electronic and phononic properties. Therefore the full non-linear model must be retained
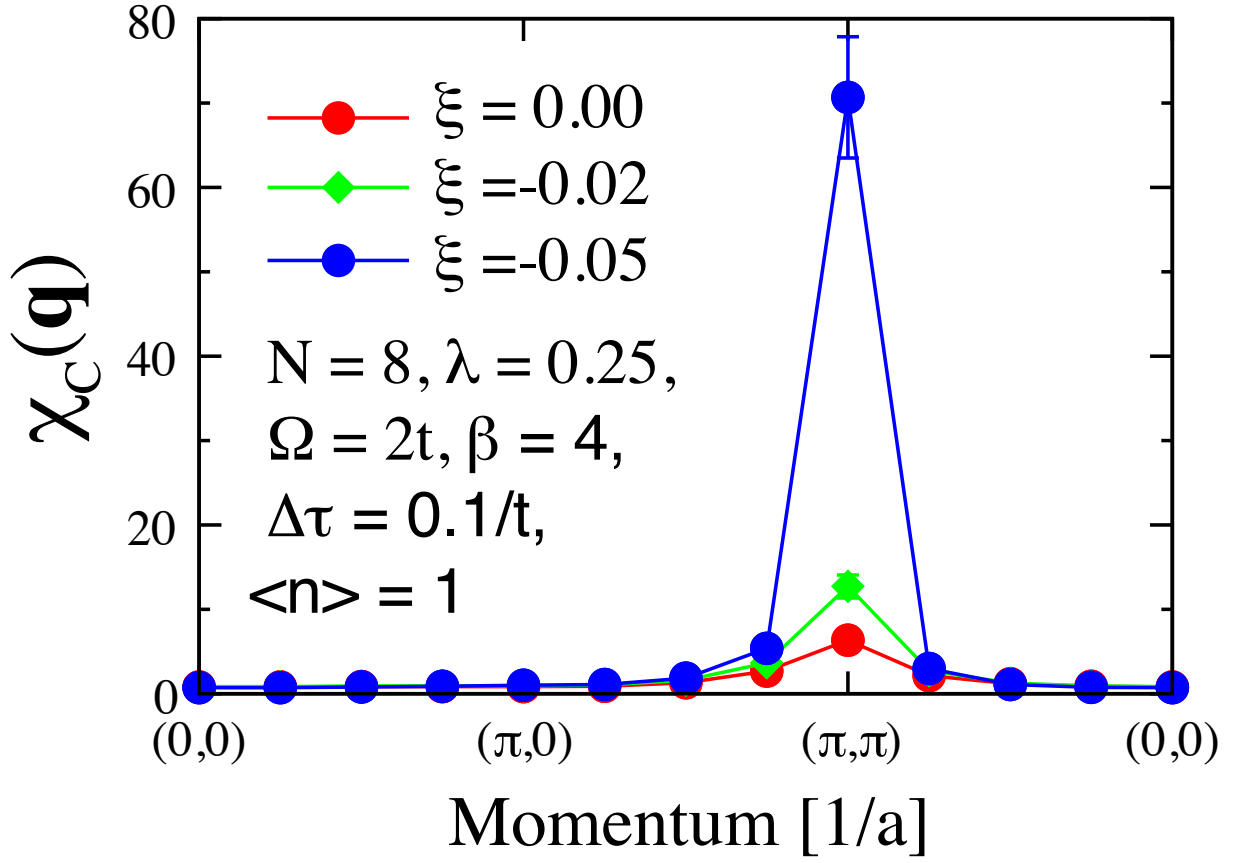
Figure 3.17: (color online) The momentum dependence of the charge susceptibility $\chi(\mathbf{q})$ as a function of non-linear interaction strength $\xi < 0$ at half filling. The parameters are set as: $\lambda = 0.25$, $\Omega = 2t$, $\beta = 4$. The results are obtained on an $N = 8$ cluster. Error bars smaller than the marker size have been suppressed for clarity.

if one wishes to accurately capture the properties of the electrons and the phonons. Our results are in good agreement with the results obtained in the single particle limit,[1] and show that non-linearities are relevant at finite carrier concentrations.

My results also have implications for pump-probe experiments aimed at studying the strength of the e-ph interaction. For example, the higher-order interaction terms can become important in such experiments if the external field drives the lattice to large displacements, even if the electron-lattice coupling at equilibrium is weak. Therefore, if the lattice is pumped too strongly, there is a danger that the non-linearity will enter and renormalize the effective coupling to smaller values. In doing so, one could drive the system hard enough that they extinguish the interactions they are trying to probe. Obviously, this will be less of an issue if the pump pulses are weak and the lattice is only slightly perturbed; however, these effects may become extremely important if the lattice is strongly pumped as our results show that even a small non-linear contribution can have an order-of-magnitude impact. Moving forward it will be important to study the role of non-linear electron-lattice coupling and anharmonic lattice potentials as the community continues to study systems driven far from equilibrium.

Finally, these results call for a re-evaluation of claims of high-T_c superconductivity mediated by non-linear e-ph coupling [192]. I stress, however, that physics arising from the non-linear coupling is different from anharmonic effects due to the lattice potential, which are thought to play key role in MgB_2 [277] and KOs_2O_6 [39].

Chapter 4

The orbital-selective Mott phase

In this chapter, I study non-local correlations in a three-orbital Hubbard model defined on an extended one-dimensional chain using determinant quantum Monte Carlo. Besides, some DMRG calculations have been done to support my DQMC results by Nitin Kaushal. I focus on a parameter regime with robust Hund's coupling, which produces an orbital-selective Mott phase (OSMP) at intermediate values of the Hubbard U. The OSMP has been widely studied using dynamical mean field theory, which neglects non-local correlations. In this chapter, I will show the momentum dependence of the OSMP and discuss the importance of the non-local correlations. The results presented in this chapter have appeared in Ref. [148].

In recent years the scientific community renewed its interest in understanding the properties of multi-orbital Hubbard models, and this has been intensified by the discovery of the iron-based superconductors [111, 240, 57, 220]. On a theoretical front, this is a challenging problem due to a lack of non-perturbative methods for treating multi-orbital Hubbard models at intermediate or strong couplings and on extended systems. Nevertheless, considerable progress has been made using mean-field-based approaches [220, 282, 71, 79, 291, 126, 266, 154, 180, 178, 187, 233, 72, 153], resulting in new concepts such as that of a Hund's metal [291, 278, 79, 133] and the orbital-selective Mott phase (OSMP) [5, 79]. These concepts are central to understanding the paradoxical appearance of both localized and itinerant characteristics in many multi-orbital systems [179, 169] and bad metallic behavior in the presence of sizable electronic correlations [179].

The most widely used numerical approach in this context is single-site multi-orbital dynamical mean-field theory (DMFT) [78, 220]. Generally speaking, DMFT maps the full lattice problem onto an impurity problem embedded in an effective medium, which approximates the electron dynamics on a larger length scale as a local renormalization [78]. While this technique has had considerable success in addressing many aspects of the OSMP and other physics related to the multi-orbital problem [126, 154, 38, 153, 21, 180, 178, 266, 106, 82], it is unable to capture spatial fluctuations and non-local correlations encoded in the k-dependent self-energy $\Sigma(\mathbf{k}, \omega)$. This is a potential short coming as non-local correlations are known to have an impact in the case of the single-band Hubbard model [85, 199]. It is therefore important to assess the importance of such non-local effects on multi-orbital properties such as the OSMP.

To date, most non-perturbative studies of non-local effects have used cluster DMFT or the dynamical cluster approximation (DCA) [194, 139, 140, 16, 144, 233]; however, these techniques are typically limited to a handful of sites when multiple orbitals are included in the basis. This is due to technical issues related to each choice in impurity solver, such as the Fermion sign problem in the case of quantum Monte Carlo or the exponential growth of the Hilbert space in the case of exact diagonalization. As a result, these studies have only addressed short-range spatial fluctuations. One study of the OSMP has been carried out on a larger two-dimensional cluster using determinant quantum Monte Carlo (DQMC). In that case, however, the OSMP was imposed by the model by assuming that electrons in a subset of orbitals were localized as Ising spins [29]. In light of these limitations it is desirable to find situations where multi-orbital physics can be modeled on extended clusters that support long-range spatial fluctuations and where the properties under study emerge from the underlying many-body physics of the model.

In this regard, one dimensional (1D) models are quite promising. For example, two recent density matrix renormalization group (DMRG) studies have been carried out for an effective 1D three-orbital model representative of the iron-based superconductors [218, 219]. More recently, it was demonstrated that DQMC simulations for a simplified version of the same model can also be carried out to low temperatures due to a surprisingly mild Fermion sign problem [156]. These observations open the doorway to non-perturbative studies of this

model on extended clusters, thus granting access to the momentum-resolved self-energies and non-local correlations. 1D studies along these lines are also directly relevant for the recently-discovered quasi-1D selenide $Ba_{1-x}K_xFe_2Se_3$ [35, 34, 203, 63, 160, 159]. In this context, it is important to note that DMFT becomes more accurate in higher dimensions and therefore one expects its ability to describe multi-orbital Mott physics in 1D to be diminished.

Motivated by these considerations, I examine the properties of a three-orbital Hubbard Hamiltonian on an extended 1D cluster using DQMC and DMRG, with a particular focus on its k-resolved self-energies and spectral properties. I thus gain explicit access to non-local correlations occurring on longer length scales than those addressed in previous non-perturbative studies. In general, I find that the OSMP leads to a mixture of localized and itinerant bands, where the former are characterized by a localized (momentum-independent) self-energy while the latter exhibits significant non-local (momentum-dependent) correlations. This also leads to a band-dependent relative shift of the underlying electron- and hole-like bands. I also identify an insulating state driven by orbital ordering in a region of parameter space previously associated with an OSMP [218, 219].

Before proceeding, I clarify my definition for the OSMP region and its critical temperature. This region is defined here by the situation where the population of a particular orbital (orbital three) converges to $\langle n_3 \rangle = 1$ while a gap simultaneously opens in the density of states for this orbital. While this is a sound operative definition of my purpose, there are subtleties that must be addressed as a warning to the reader. In the context of DMFT, investigations of multiorbital models [199, 153] in the plane defined by temperature T and coupling strength U/W (W is the bandwidth) show that there is an analytic connection between the Mott insulating side of a line of first order transitions and the weak coupling metallic side. The line of first-order transitions survives the introduction of temperature, but it has an end point at a finite T in analogy to the gas/liquid transition. For example, in the analysis of the localized orbital reported in Ref. [153], the quasiparticle weight Z is claimed to be nonzero at finite T on the insulating side (although it is extremely small at low temperatures). I believe that Z being zero or very small is similar to the condition that my localized orbital's population is equal to or very close to one. As a consequence, what I have defined as a transition towards an OSMP may in fact be a region where $\langle n_3 \rangle \approx 1$

but not exactly 1. If this is the case, then my critical temperature is in reality a very sharp crossover towards a region that only reaches true OSMP characteristics at $T = 0$ (or at the much lower temperature where magnetic block correlations develop). Note that DMFT is valid in infinite dimension, while my problem is in the opposite limit, so these arguments are all qualitative at best. In spite of these subtleties, I will refer to the region below my critical temperature defined by $\langle n_3 \rangle$ converging to 1 as an OSMP for simplicity, with the caveat that exact OSMP characteristics may be reachable only at lower T.

4.1 One-dimensional three-orbital Hubbard model

I study a simplified three-orbital model defined on a 1D chain as introduced in Ref. [218]. This model displays a rich variety of phases including block ferromagnetism, antiferromagnetism, Mott insulting phases, metallic and band insulating phases, and several distinct OSMPs [218, 219, 156]. The Hamiltonian is $H = H_0 + H_{\text{int}}$, where

$$H_0 = -\sum_{\substack{\langle i,j \rangle \\ \sigma, \gamma, \gamma'}} t_{\gamma\gamma'} c^\dagger_{i,\gamma,\sigma} c_{j,\gamma',\sigma} + \sum_{i,\sigma,\gamma} (\Delta_\gamma - \mu) \hat{n}_{i,\gamma,\sigma} \tag{4.1}$$

contains the non-interacting terms of H, and

$$\begin{aligned} H_{\text{int}} &= U \sum_{i,\gamma} \hat{n}_{i,\gamma,\uparrow} \hat{n}_{i,\gamma,\downarrow} + \left(U' - \frac{J}{2}\right) \sum_{\substack{i,\sigma,\sigma' \\ \gamma<\gamma'}} \hat{n}_{i,\gamma,\sigma} \hat{n}_{i,\gamma,\sigma'} \\ &+ J \sum_{i,\gamma<\gamma'} S^{\text{z}}_{i,\gamma} S^{\text{z}}_{i,\gamma'} \end{aligned} \tag{4.2}$$

contains the on-site Hubbard and Hund's interaction terms. Here, $\langle \dots \rangle$ denotes a sum over nearest-neighbors, $c^\dagger_{i,\gamma,\sigma}$ ($c_{i,\gamma,\sigma}$) creates (annihilates) a spin σ electron in orbital $\gamma = 1, 2, 3$ on site i, Δ_γ are the on-site energies for each orbital, $S^{\text{z}}_{i,\gamma}$ is the z-component of the spin operator $\mathbf{S}_{i,\gamma}$, and $\hat{n}_{i,\gamma,\sigma} = c^\dagger_{i,\gamma,\sigma} c_{i,\gamma,\sigma}$ is the particle number operator.

Note that in Eq. (4.2) I have neglected the pair-hopping and spin-flip terms of the interaction. These terms can have an important influence on the details of the OSMP in higher dimensions. In the context of the current model, however, a previous DMRG [156]

study found that these terms only alter the location of the phase boundaries and do not qualitatively change the nature of the underlying phases. Since my focus here is on the non-local correlations associated with these phases, rather than subtle issues regarding their boundaries, I neglect the spin-flip and pair hopping terms in order to manage the Fermion sign problem in the DQMC calculations.

Following Ref. [218], I set $t_{11} = t_{22} = -0.5$, $t_{33} = -0.15$, $t_{13} = t_{23} = 0.1$, $t_{12} = 0$, $\Delta_1 = -0.1$, $\Delta_2 = 0$, and $\Delta_3 = 0.8$ in units of eV while the chemical potential μ is adjusted to obtain the desired filling. These parameters produce a non-interacting band structure analogous to the iron-based superconductors, with two hole-like bands centered at $k = 0$ and an electron-like band centered at $k = \pi/a$, where a is the lattice constant, as shown in Fig. 4.1. Due to the weak inter-orbital hopping, each of the bands is primarily derived from a single orbital, as indicated by the line thickness and colors in Fig. 4.1. One can therefore (loosely) regard the orbital character as an indicator of the band in this model. For example, the top most band is primarily composed of orbital $\gamma = 3$. The total bandwidth of the non-interacting model is $W = 4.9|t_{11}| = 2.45$ eV. This will serve as the unit of energy. I further set $a = 1$ as the unit of length. The interaction parameters are fixed to $U' = U - 2J$, $J = U/4$, while U is varied. This parameter regime results in a robust OSMP for intermediate values of U [156, 219, 218], which is my focus here.

The model is studied using non-perturbative DQMC method. The primary drawback to DQMC is the Fermion sign problem [157, 105], which typically limits the range of accessible temperatures for many models. Indeed, when the spin-flip and pair hopping terms of the Hund's interaction are included in the Hamiltonian, I find that the model has a prohibitive sign problem. But when these terms are neglected the corresponding sign problem becomes very mild [156], even in comparison to similar simplified multi-orbital models in 2D [212, 28]. Given that these terms do not qualitatively affect the phase diagram [156] for current model, I have neglected them here. Unless otherwise stated, all of my DQMC results were obtained on an $L = 24$ site cluster with periodic boundary conditions and for an average filling of $\langle n \rangle = 4$ electrons, which corresponds to 2/3 filling.
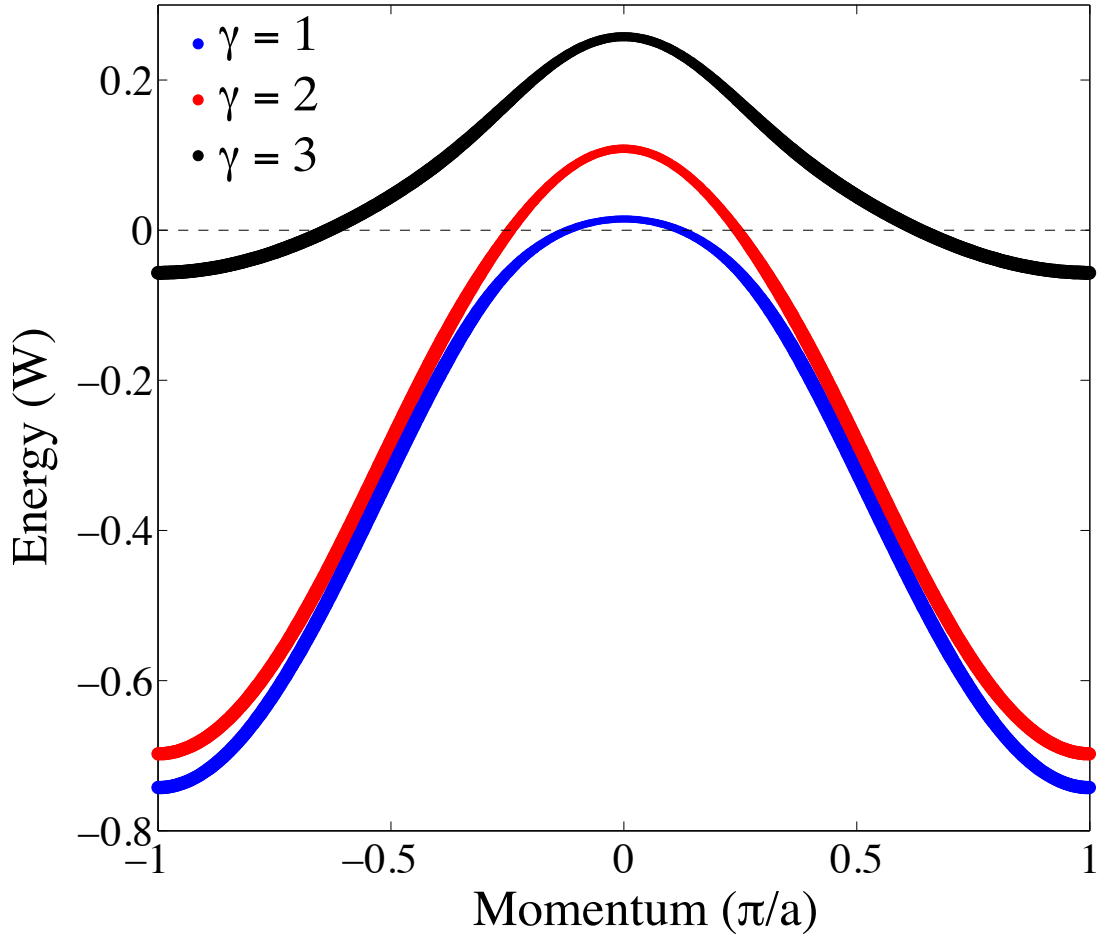
Figure 4.1: (color online) A fat band plot of the non-interacting band structure at a total filling of $\langle \hat{n} \rangle = 4$, where the thickness of the lines indicates the majority orbital content of the band. The top most band has the narrowest bandwidth and is primarily of orbital 3 character. The lower two bands disperse over a much larger energy range and are primarily composed of orbitals 1 and 2, respectively.

4.2 Results

4.2.1 Low temperature properties

I first focus on the low temperature $\beta = 73.5/W$, where I can identify the ground state properties. Here, I set the chain length $L = 16$. Fig. 4.2a plots the average sign value as a function of U. The average value of the sign is quite high for most values of U, indicating the low-temperature properties can be accessed. It is interesting to observe that the sign problem is at its worst when $U/W \sim 0.4$, which is near the phase boundary between the metallic and orbital-selective Mott phases for this model. This phase transition between the metallic and OSMP can be easily identified in Fig. 4.2b, which plots the U dependence of orbital occupations. As increasing U, n_3 increases and finally is locked at 1, which implying that a Mott gap is opened on the orbital 3. While, n_1 and n_2 are still fractional in that orbital 1 and orbital 2 are metallic phases. The OSMP sits in $U/W \in [0.4, 1]$. Fig. 4.2 c shows the magnetic structure factor on the orbital 3 at $U/W = 0.01$ and $U/W = 0.8$, respectively. The magnetic structure factor is defined as $S_f(q) = 1/L \sum_{j,m} e^{iq(r_j - r_m)} \mathbf{S}_{j,\gamma=3} \cdot \mathbf{S}_{m,\gamma=3}$. In the metallic phase ($U/W = 0.01$), the orbital 3 is paramagnetic, while in the OSMP, the magnetic structure on the orbital 3 has a peak around $q = 0.5\pi/a$, implying the magnetic structure on the chain is the block spin state [156, 219, 218]. As increasing the temperature to $\beta = 19.6/W$, the block spin state disappears (see Fig. 4.2d) and the magnetic structure on the orbital 3 becomes disordered. In the following, I will show the Mott gap is still there at this elevated temperature. This result shows that the insulating state on the orbital 3 is a Mott insulator rather than slater insulator.

4.2.2 Self-energies in the OSMP

I then study some of the standard metrics for the formation of an OSMP as a function of temperature, namely the average filling per orbital and the quasiparticle residue $Z_\gamma(k, i\omega_n)$. DQMC results for $\langle n \rangle = 4$ and $U/W = 0.8$ are summarized in Fig. 4.3. The temperature dependence of the individual orbital occupations $\langle n_\gamma \rangle$, plotted in Fig. 4.3a, has the standard indications of the formation of an OSMP: At high temperature (small β) I see noninteger fillings for all three orbitals. As the temperature is lowered (large β), however, orbitals one
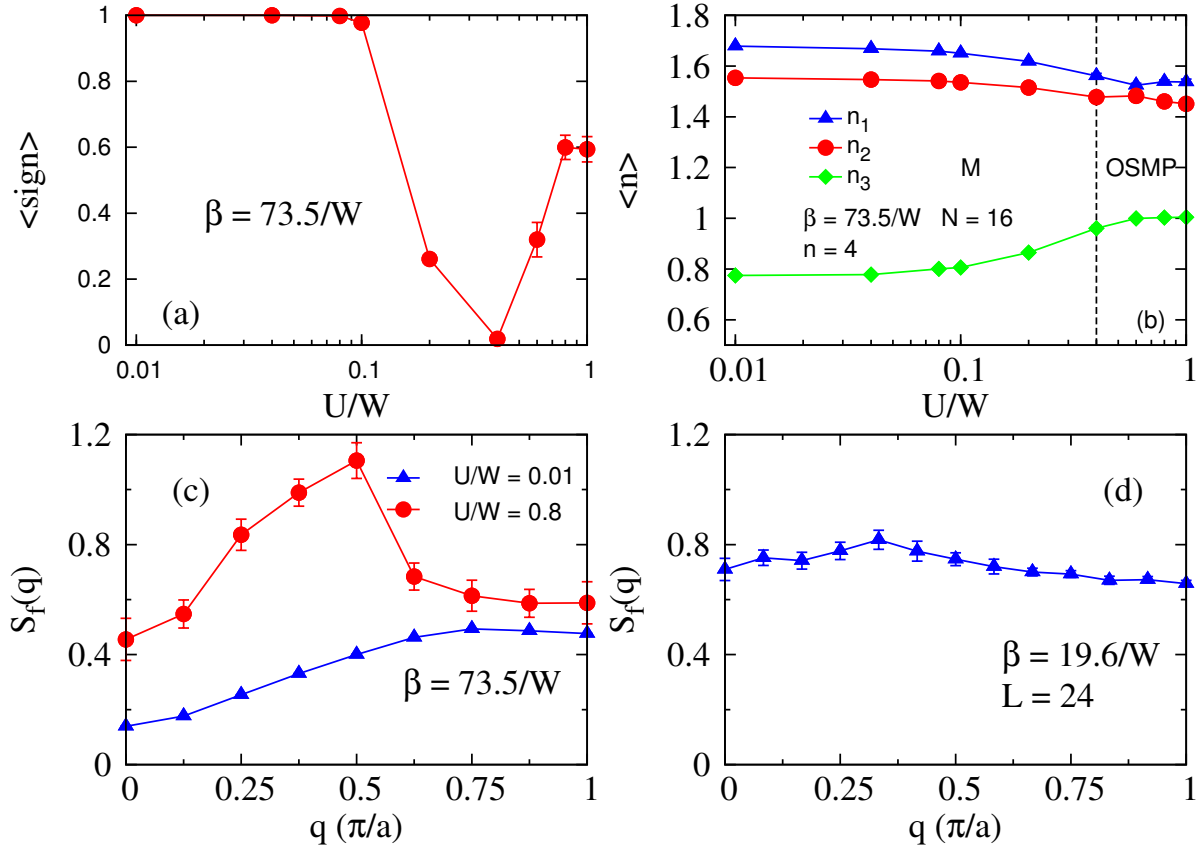
Figure 4.2: (color online) (a) the average sign value as a function of the Hubbard U. (b) The U dependence of orbital occupations. (c) The magnetic structure factor of the orbital 3 at $U/W = 0.8$. In (a)-(c), the temperature is $\beta = 73.5/W$. (d) The magnetic structure factor of the orbital 3 at $U/W = 0.8$ and $\beta = 19.6/W$. In each panel, error bars smaller than the marker size have been suppressed for clarity.
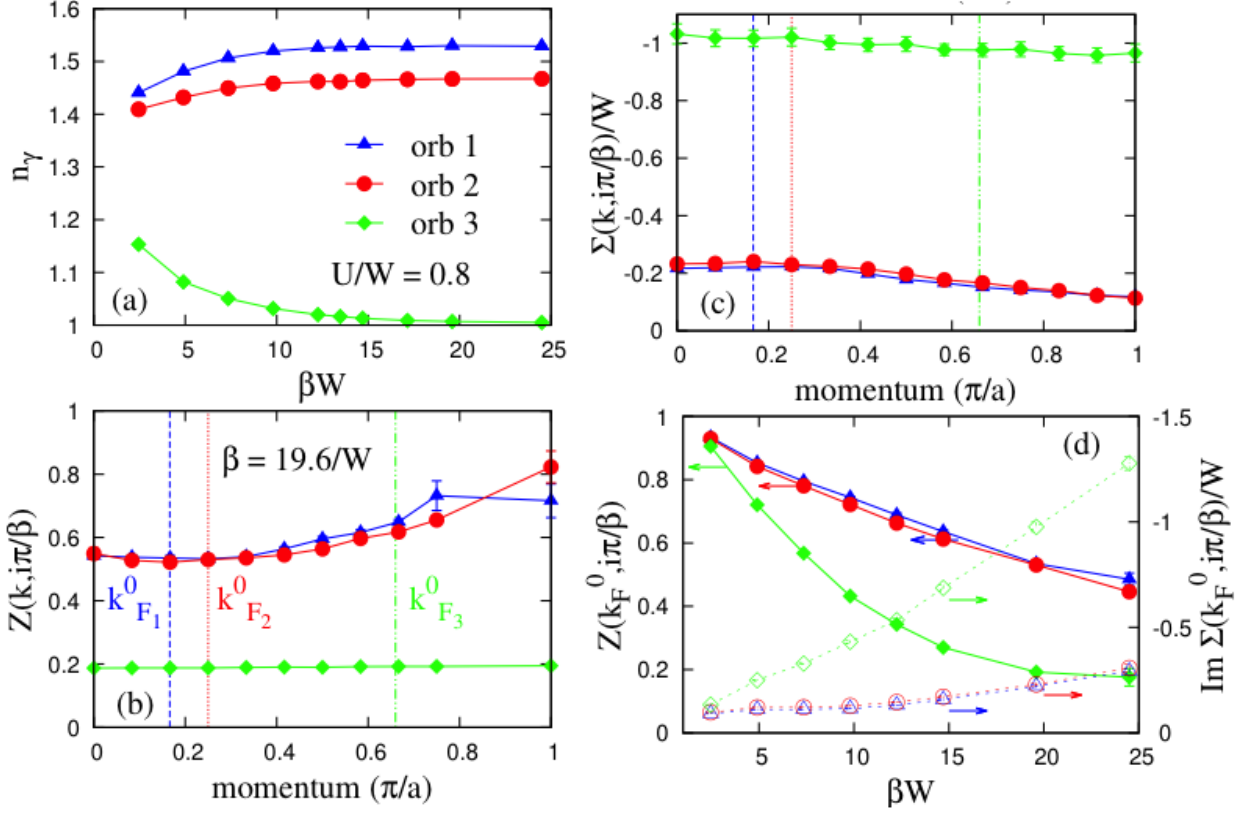
Figure 4.3: (color online) Orbitally resolved electronic properties for $U/W = 0.8$ ($W = 2.45$ eV) at different temperatures. (a) The temperature dependence of orbital occupations. (b) The orbital resolved quasiparticle residue $Z_\gamma(k, i\pi/\beta)$ at an inverse temperature $\beta = 19.6/W$. (c) The normalized electron self energies $\mathrm{Im}\Sigma_\gamma(k, i\pi/\beta)$ at $\omega_n = \pi/\beta$ as a function of momentum. Each curve is normalized by its $k = 0$ value to highlight the overall momentum dependence. The scale is determined by $\mathrm{Im}\Sigma_\gamma(0, i\pi/\beta) = -0.53$, -0.57, and -2.53 for $\gamma = 1, 2, 3$, respectively, and in units of the bandwidth W. The blue, red, and green dash lines in (b) and (c) correspond to the bare Fermi momentum of the non-interacting bands. Panel (d) shows orbitally resolved quasiparticle residues $Z_\gamma(k_{\mathrm{F}}^0, i\pi/\beta)$ and self energies $\mathrm{Im}\Sigma_\gamma(k_{\mathrm{F}}^0, i\pi/\beta)$ at Fermi momentum as a function of temperature. In each panel, error bars smaller than the marker size have been suppressed for clarity.

and two smoothly approach fillings of ~ 1.53 and ~ 1.47, respectively, while orbital three locks into an integer value of exactly 1. In many studies the "stiffness" of orbital three's integer occupation is taken as an indication of an OSMP [218, 219], where this orbital has undergone a transition to a Mott insulating state while remaining orbitals host itinerant electrons. Indeed, for $U/W = 0.8$ and at low temperature, the integer filling observed in orbital three is robust against changes in the chemical potential and interaction strength U (see Refs. [156, 218, 219]). This indicates that this integer filling is indeed driven by the interaction and is not a simple coincidence of the non-interacting band parameters. However, as I will show, this does not always correspond to an OSMP. For $U/W = 0.8$ the two fractionally filled orbitals are in fact itinerant, but for larger values of U/W these same orbitals retain a fractional filling but are driven into an insulating state by the onset of orbital ordering in these two orbitals.

The mixed itinerant/localized nature of the OSMP at $U/W = 0.8$ is reflected in the momentum dependence of quasi-particle residue $Z_\gamma(k, \mathrm{i}\pi/\beta)$ and the orbitally resolved normalized self-energies $R(k) = \mathrm{Im}\Sigma_\gamma(k, \mathrm{i}\pi/\beta)/\mathrm{Im}\Sigma_\gamma(0, \mathrm{i}\pi/\beta)$, plotted in Figs. 4.3c and 4.3d, respectively, for $\omega_n = \pi/\beta$. The self-energy is extracted from the dressed Green's function using Dyson's equation

$$\hat{G}^{-1}(k, \mathrm{i}\omega_n) = \hat{G}_0^{-1}(k, \mathrm{i}\omega_n) - \hat{\Sigma}(k, \mathrm{i}\omega_n), \tag{4.3}$$

where the $\hat{G}$ notation denotes a matrix in orbital space, $\hat{G}_0(k, \mathrm{i}\omega_n) = [\mathrm{i}\omega_n\hat{I} - \hat{H}_0(k)]^{-1}$ is the non-interacting Green's function, and $\hat{H}_0(k)$ is the Fourier transform of the non-interacting Hamiltonian defined in orbital space. The quasi-particle residue is obtained from the diagonal part of the self-energy using the identity

$$\hat{Z}(k, \mathrm{i}\pi/\beta) = \left(\hat{I} - \frac{\mathrm{Im}\hat{\Sigma}(k, \mathrm{i}\pi/\beta)}{\pi/\beta}\right)^{-1}, \tag{4.4}$$

where $\hat{I}$ is a 3×3 unit matrix.

As can be seen from Fig. 4.3c, the self-energies for each orbital have a sizable k-dependence at this temperature. (In this case I have normalized the self-energy by its

value at $k = 0$ in order to highlight the overall momentum dependence. The magnitude of $\text{Im}\Sigma_\gamma(0, i\pi/\beta)$ is given in the figure caption.) In the case of orbitals one and two, the magnitude of the self-energy varies by nearly 50% throughout the Brillouin zone. In contrast, the momentum dependence of $\Sigma_3(k, i\pi/\beta)$ for orbital three is much weaker, varying by only 5-10% and reflecting the localized nature of the carriers in these orbitals. Similarly, the quasi-particle residue for the orbital three is essentially momentum independent, while it increases for the two itinerant orbitals as k tracks towards the zone boundary. The k dependence at the remaining Matsubara frequencies accessible to my simulations (not shown) exhibits a similar trend, with orbitals one and two having a strong k-dependence while orbital three is nearly momentum independent at each ω_n.

The momentum dependence shown in Fig. 4.3 indicates that the local self-energy approximation introduced by DMFT may miss quantitative aspects of the electronic correlations in the OSMP with mixed itinerant and local characteristics. It should be noted that my results have been obtained in 1D, which is the worst case situation for DMFT [4]. It is expected that the local approximation will perform better in higher dimensions, since DMFT becomes exact in the limit of infinite dimensions; however, it is unclear how well the method will capture similar non-local correlations in two dimensions relevant for the Fe-based superconductors. A recent study [233] has argued that the local approximation is quite accurate for parameters relevant to the iron-based superconductors, however, it remains to be seen if this will remain true for all parameter regimes or when longer range fluctuations are included. My results further highlight the need for the continued development of numerical methods capable of handling the strong Hubbard and Hund's interactions in intermediate dimensions and on extended clusters.

Figure 4.3d examines the temperature dependence of $Z(k_\text{F}^0, \frac{i\pi}{\beta})$ and $\text{Im}\Sigma(k_\text{F}^0, \frac{i\pi}{\beta})$ at the Fermi momenta k_F^0 of the non-interacting system. (These are indicated by the dashed lines in 4.3b and 4.3c.) Here, I find indications of anomalous behavior for the itinerant electrons, where the quasiparticle residues of all three orbitals decrease with temperature. This is accompanied by an increase in $\text{Im}\Sigma(k_\text{F}, \frac{i\pi}{\beta})$ as T is lowered. This is perhaps expected for orbital three, as Z ($\text{Im}\Sigma$) for the localized orbitals should decrease (increase) as this orbital becomes more localized. For the itinerant orbitals, however, one would naively expect the

self-energy to decrease as temperature is lowered, which is opposite to what is observed. I believe that this is due to the Hund's interaction between the itinerant electrons and the localized spins on orbital three. At this temperature I find no evidence of a magnetic ordering in my model [156], despite the fact that a local moment has clearly formed in the OSMP. This means that the orientation of the local moment is random and fluctuating at these temperatures. This produces a fluctuating potential acting on the itinerant electrons via the Hund's coupling, thus generating a residual scattering mechanism at low temperatures that reduces the quasiparticle residue and increases the self-energy.

4.2.3 Momentum and Temperature Dependence of the Spectral Weight

Next, I turn to the momentum dependence of the spectral weight for the three orbitals in the vicinity of the Fermi level. This can be estimated directly from the imaginary time Green's function using the relationship [248]

$$\beta G(k, \tau = \beta/2) = \frac{\beta}{2} \int d\omega \frac{A(k, \omega)}{\cosh\left(\frac{\beta\omega}{2}\right)},$$

where $A(k, \omega)$ is the single-particle spectral function. At low temperature, the function $\frac{\beta}{2} \cosh^{-1}\left(\frac{\beta\omega}{2}\right)$ is sharply peaked around $\omega = E_F = 0$. The quantitiy $\beta G(k, \tau = \beta/2)$ therefore provides a measure of the spectral weight at momentum k, integrated within a window of a few β^{-1} of the Fermi level. Using this relationship I do not have to perform the extra step of analytically continuing the data to the real frequency axis.

Figures 4.4a-4.4c summarize $\beta G(k, \beta/2)$ for $U/W = 0.1$, $U/W = 0.8$, and $U/W = 2$, respectively. The results in the weak coupling limit ($U/W = 0.1$, Fig. 4.4a) are consistent with that of a fully itinerant system: all three orbitals have a maximal spectral weight at a momentum point very close to the Fermi momenta of the non-interacting system (indicated by the dashed lines). This is exactly the behavior one expects for a well-defined quasiparticle band dispersing through E_F, where the peak in the spectral weight occurs at k_F. The proximity of the peaks in $\beta G(k, \beta/2)$ to the non-interacting values of k_F indicates that
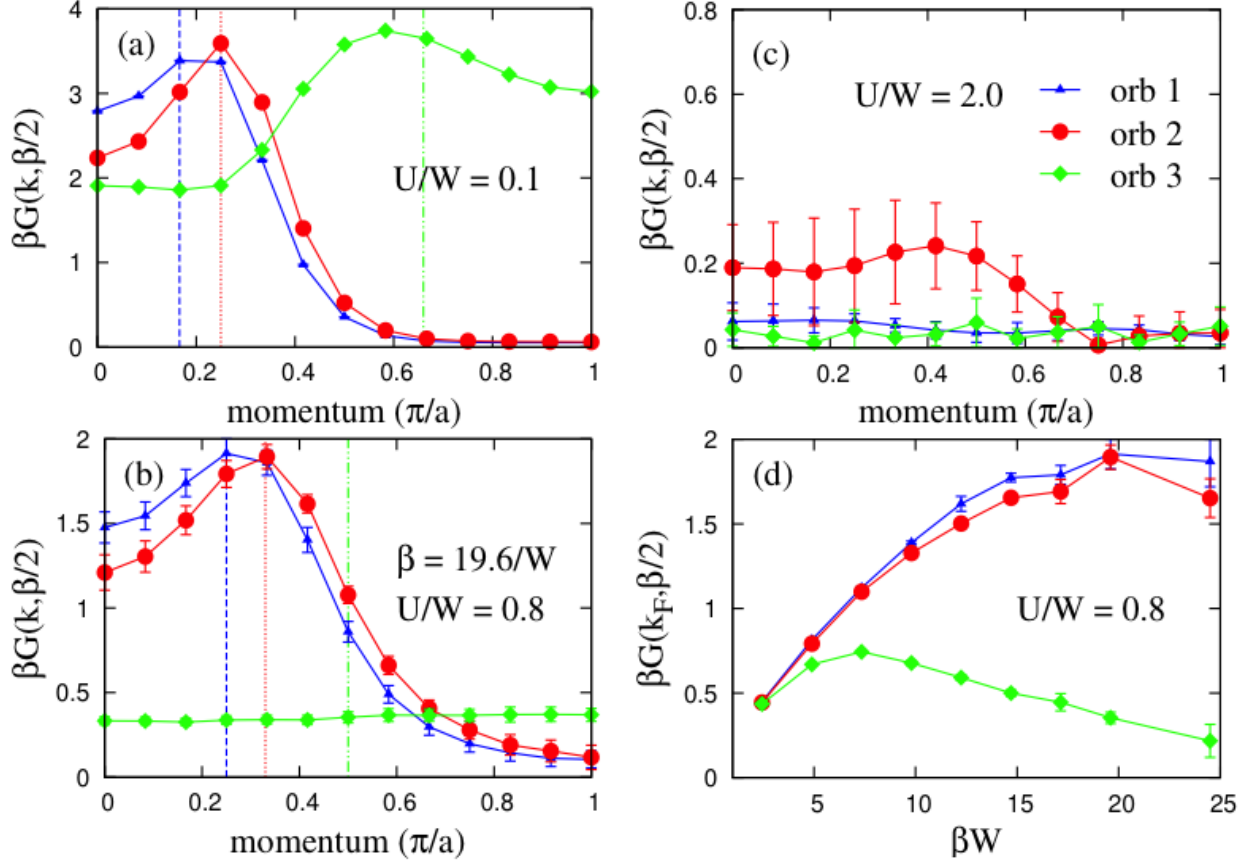
Figure 4.4: (color online) The momentum dependence of Green functions $G(k, \tau = \beta/2)$ for a) $U/W = 0.1$, b) 0.8, and c) 2.0. The inverse temperature in all three cases is $\beta = 19.6/W$. The blue, red, and green dash lines in each panel indicate the Fermi momentum of the three non-interacting bands. (d) $G(k_{\mathrm{F}}, \tau = \beta/2)$ as a function of inverse temperatures β for the OSMP $U/W = 0.8$. Error bars smaller than the marker size have been suppressed for clarity.

the Fermi surface is only weakly shifted for this value of the interaction parameters. However, as I will show in Sec. 4.2.4, these shifts are band dependent.

In the intermediate coupling regime ($U/W = 0.8$, Fig. 4.4b), where the OSMP has formed, I again see both localized and itinerant characteristics. The spectral weight of the localized orbital is small and independent of momentum, as expected for the formation of a localized Mott state. Conversely, the spectral weight of the remaining orbitals still exhibits a momentum dependence characteristic of dispersive bands. Despite this, the total spectral weight is decreased, indicating that spectral weight has been transferred to higher binding energies by the Hubbard and Hund's interactions. This is also reflected in the position of the maximum spectral weight, which has shifted to a slightly larger k value due to a renormalization of the Fermi surface by the interactions. I also observe that the spectral weight at the zone boundary increases relative to the zone center, consistent with a flattening of the bands and a broadening of the spectral function with increasing U. (This will be confirmed shortly when I examine the spectral functions directly.) A similar transfer of spectral weight was observed in a two-dimensional cluster DMFT study [194].

The temperature evolution of spectral weight $\beta G(k_{\mathrm{F}}, \beta/2)$ at the Fermi momentum for the OSMP ($U/W = 0.8$) is shown in Figure 4.4d. In a metallic system one generally expects the spectral weight at the Fermi level to increase as the temperature is decreased. Initially, this is what is observed for all three orbitals, however, the spectral weight for orbital three reaches a maximum around $\beta = 7.5/W$ before decreasing as the temperature is lowered further and the OSMP gap forms on this orbital. Conversely, the spectral weight of the itinerant orbitals continues to rise until saturating at $\beta/W \approx 15$. This saturation is again due to the presence of a residual scattering channel, which I associate with the fluctuating localized spins present on the localized orbital three.

The $U/W = 0.8$ results confirm the mixed itinerant/local character of the model at intermediate coupling. When the value of U is further increased, I find that all three bands become localized while maintaining partial occupancies for each band. To demonstrate this, Fig. 4.4c shows results for $U/W = 2$. In this case, the orbital occupations for the three orbitals are $\langle n_1 \rangle = 1.55$, $\langle n_2 \rangle = 1.44$, $\langle n_3 \rangle = 1$, which are similar to those obtained at $U/W = 0.8$. At face value one might therefore conclude that the system is in an OSMP

[218, 156], however, an examination of the spectral weight reveals that the system is in fact insulating. As can be seen in Fig. 4.4c, at $U/W = 2$ and $\beta = 19.6/W$, $\beta G(k, \beta/2)$ is nearly momentum independent and the total spectral weight of all three orbitals has significantly decreased (note the change in scale of the y-axis). This behavior is indicative of the formation of a charge gap throughout the Brillouin zone. The ultimate origin of this insulating behavior is the formation of a long-range orbital ordering, as I will show in Sec. 4.2.5.

4.2.4   Band-dependent Fermi surface renormalization

It is now well known that *ab initio* band structure calculations based on density functional theory (DFT) do not describe the electronic structure of the iron based superconductors as measured in ARPES experiments. (For a recent review, see Ref. [220].) Generally speaking, the calculated band structure usually needs to be rescaled by an overall factor, which is attributed to reduction in bandwidth driven by electronic correlations. In addition, the size of the Fermi surfaces is often overestimated by DFT in comparison to measurements. A prominent example of this is LiFeAs [41], where the inner most hole pocket realized in nature is substantially smaller than the one predicted by DFT [134, 69]. In order to correct this, the electron- and hole-bands need to be shifted apart [220], which requires a momentum-dependent self-energy correction.

I examine this issue within my model in Fig. 4.5, which plots the expectation value of the orbitally-resolved number operator in momentum space $n_\gamma(k) = \frac{1}{2} \sum_\sigma \langle c^\dagger_{\mathbf{k}, \gamma, \sigma} c_{\mathbf{k}, \gamma, \sigma} \rangle$ for various values of the interaction strength. In the non-interacting limit, and in a single-band case, this quantity is equal to the Fermi-Dirac distribution and the location of the leading edge corresponds to k_F. In a multi-band system the mixing of the orbital character complicates this picture; however, in my model the leading edge still corresponds to k_F due to the weak hybridization between orbitals. In the weak coupling case ($U/W = 0.1$) I observe a small shift in the position of the leading edge. Within error bars, the curve $n_1(k)$ and $n_2(k)$ shift to slightly larger momenta while $n_3(k)$ shifts towards smaller momenta. This indicates that the size of the Fermi surfaces are increasing and the electron-like and hole-like bands are shifted towards one another by the interactions. This trend continues as U/W is increased
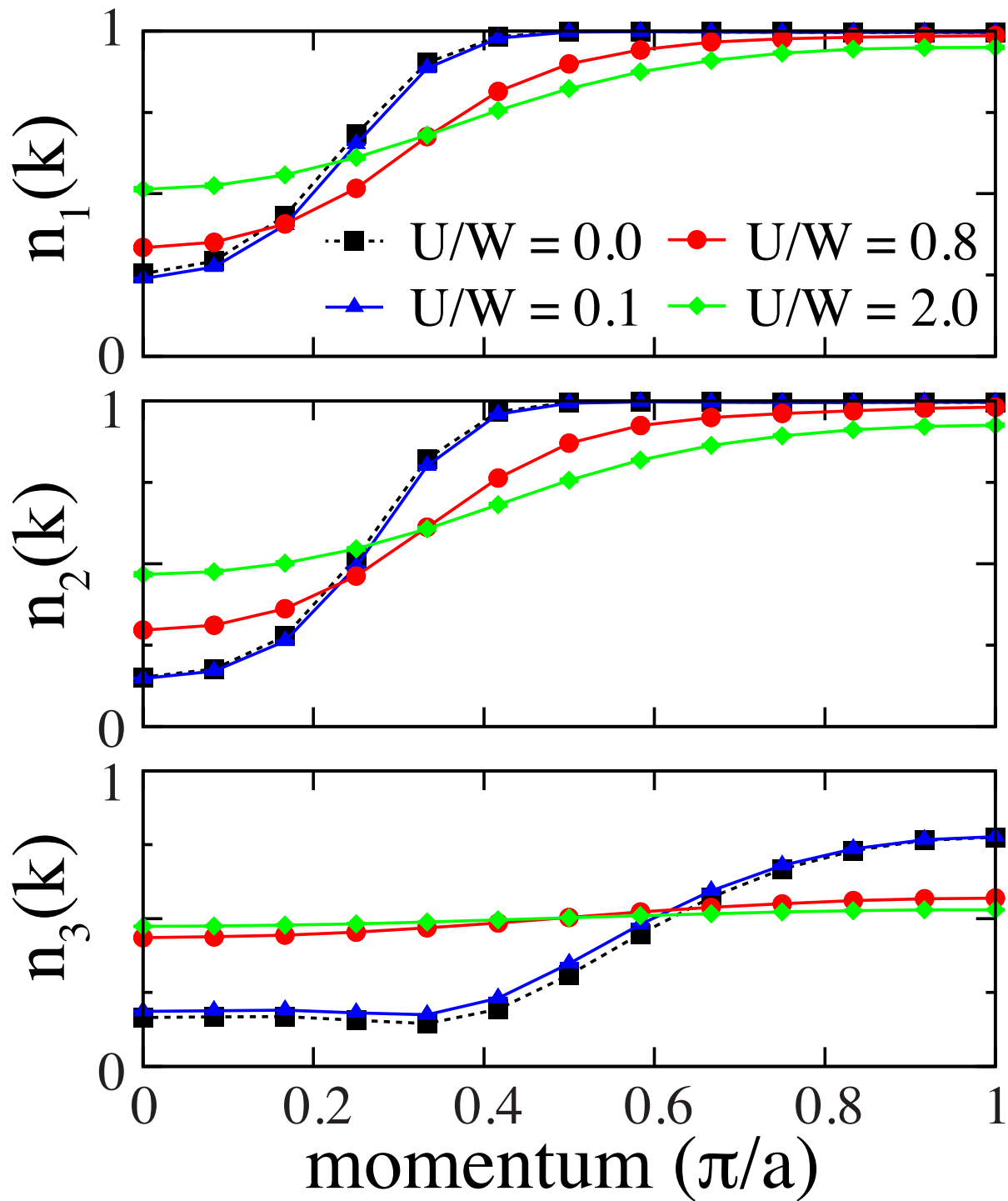
Figure 4.5: (color online) The momentum dependence of the number operator $n_\gamma(k) = \frac{1}{2}\sum_\sigma \langle c^\dagger_{\mathbf{k},\gamma,\sigma} c_{\mathbf{k},\gamma,\sigma}\rangle$ for each band. Results are shown for the non-interacting case $U = 0$ (black dashed, $\square$), $U/W = 0.1$ (blue solid, $\triangle$), $U/W = 0.8$ (red solid $\circ$), and $U/W = 2$ (green solid $\diamond$) and at an inverse temperature of $\beta = 19.6/W$.

to 0.8; however, in this case the electron-like band is significantly smeared out due to the formation of the OSMP.

I note that the direction of the band shifts is reversed from what is generally required for the two-dimensional iron-based superconductors, where the calculated hole-like Fermi surfaces generally need to be shrunk relative to the electron-like Fermi surfaces. I attribute this to differences in the underlying tight-binding model and differences in dimensionality. In this light, it would be interesting to compare the ARPES observed band structures in the quasi-one-dimensional pnictides against the predictions of my model and DFT calculations [203]. Nevertheless, my results do show that non-local correlations arising from a local interaction can produce relative shifts of the electron-like and hole-like bands in a multi-orbital system.

4.2.5 Spectral Properties

4.2.5.1 Intermediate Coupling $U/W = 0.8$

I now examine the spectral properties of the model, beginning with the OSMP. Figure 4.6a shows the temperature evolution of the total density of states (DOS) at $U/W = 0.8$, which is obtained from the trace of the orbital-resolved spectral function $N(\omega) = \sum_{k,\gamma} -\frac{1}{\pi} \mathrm{Im}\hat{G}_{\gamma\gamma}(k, \omega + i\delta)$. In the non-interacting limit (the long-dashed (blue) curve), the DOS has a double peak structure, where the lower (upper) peak corresponds to the bands derived from orbitals one and two (orbital three). The overall structure of the DOS in the interacting case is similar at high temperatures, but some spectral weight is transferred to a broad incoherent tail extending to lower energies. As the temperature is decreased, the peak on the occupied side shifts towards the Fermi level and sharpens. At the same time, a small amount of spectral weight is transferred from the vicinity of the Fermi level into this peak. The appearance of this apparent "pseudogap" is a direct consequence of the OSMP forming on orbital three, which is easily confirmed by examining the orbital-resolved DOS $N_\gamma(\omega) = -\frac{1}{\pi} \sum_k \mathrm{Im}\hat{G}_{\gamma,\gamma}(k, \omega)$ shown in Fig. 4.6b. As can be clearly seen, orbitals one and two have a finite DOS at $\omega = 0$, while orbital three is fully gapped at low-temperature.
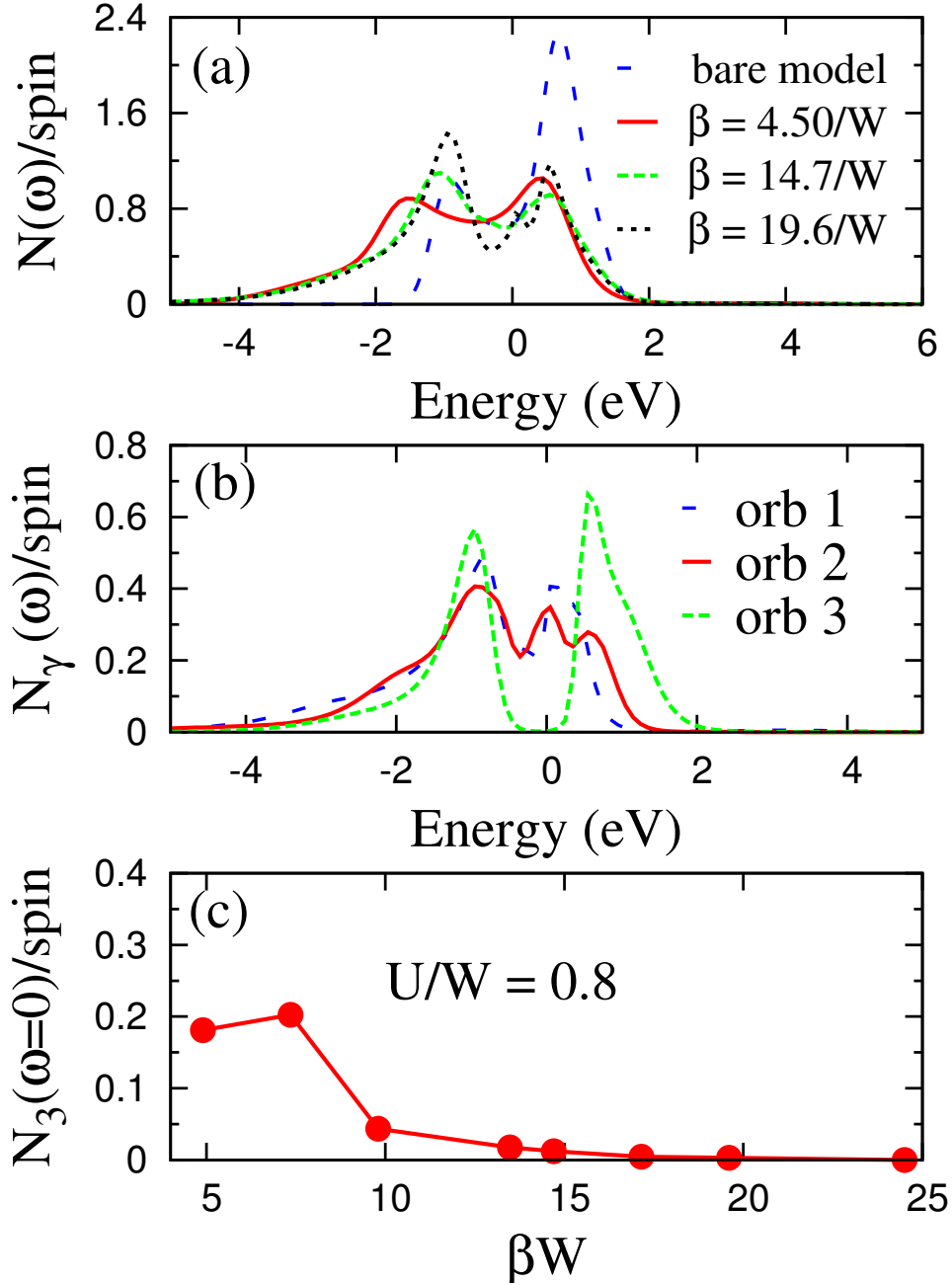
Figure 4.6: (color online) (a) The density of states at different temperatures. (b) The orbitally-resolved density of states for each orbital at an inverse temperature $\beta = 19.6/W$. (c) The density of states at the Fermi surface of the orbital 3 as a function of inverse temperatures β. The Coulomb interaction strength is $U/W = 0.8$ in all three graphs.

I also begin to see the formation of an additional peak near the Fermi level at the lowest temperature I examined ($\beta = 19.6/W$). This feature is more clearly seen in the orbital-resolved DOS (Fig. 4.6b), where it is found to originate from the itinerant orbitals. This peak is due to a hybridization between the itinerant and localized orbitals, which is observable in the k-resolved spectral functions (see Fig. 4.7).

The relevant temperature scale for the formation of the OSMP can be estimated by tracking $N_3(0)$ as a function of temperature, as shown in Fig. 4.6c. Here, a continuous suppression of $N_3(0)$ is observed, with the value reaching zero at $\beta \approx 20/W$. The rate at which $N_3(0)$ decreases also undergoes a distinct change at $\beta \approx 7.5/W$, which coincides with the temperature at which the spectral weight for this orbital at k_{F} is largest (see Fig. 4.4d). I interpret this to mean that the Mott gap on orbital three has formed at $\beta W \approx 10$ (on the $L = 24$ site lattice), growing continuously from zero as the temperature is lowered. In this case, the finite spectral weight between $\beta W = 10 - 20$ is due to thermal broadening across this gap. Since I have observed similar behavior on smaller clusters with DQMC and at zero temperature using DMRG, I believe that the transition to the OSMP will survive in the thermodynamic limit, however, the gap magnitude has some finite size dependence.

The extended length of my 1D cluster grants us access to the momentum dependence of the spectral function, which is shown in Fig. 4.7. The top row of Fig. 4.7 shows the results in the OSMP with $U/W = 0.8$ and $\beta = 19.6/W$, which is the same parameter set used in Fig. 4.6. The total spectral function $A(k,\omega) = -\frac{1}{\pi}\mathrm{Tr}\left[\mathrm{Im}\hat{G}(k,\omega)\right]$ is shown in Fig. 4.7a and the orbital-resolved components $A_\gamma(k,\omega) = -\frac{1}{\pi}\mathrm{Im}\hat{G}_{\gamma\gamma}(k,\omega)$ are shown in Figs. 4.7b-d, as indicated. The lower row of Fig. 4.7 shows similar results obtained for $U/W = 2$ and $L = 8$. (In this case a smaller cluster is sufficient due to the non-dispersing nature of the band dispersions.)

The results in the OSMP with $U/W = 0.8$ reveal localized and itinerant characteristics that are consistent with the spectral weight analysis presented earlier. The itinerant orbitals primarily contribute to dispersing bands that track through the E_{F} ($\omega = 0$), while orbital three has split into two relatively dispersionless upper and lower Hubbard bands above and below E_{F}. At first glance, these Hubbard bands appear to be sharper than the corresponding Hubbard bands in the single-band Hubbard model; however, an examination of the DOS
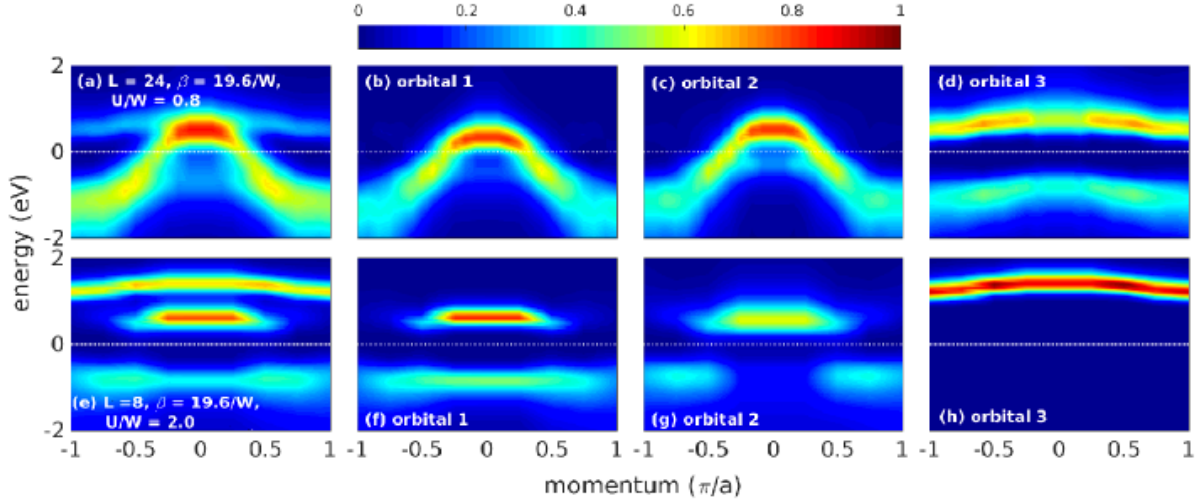
Figure 4.7: (color online) (a) The spectral function for $U/W = 0.8$. (b), (c), and (e) are the orbital 1, 2, and 3 parts of the spectral function in (a), respectively. (e) The spectral function for $U/W = 2$. (f), (g), and (h) are the orbital 1, 2, and 3 parts of the spectral function in (e), respectively. The dash white line labels the Fermi surface. The inverse temperature is set as $\beta = 19.6/W$. Results where obtained with Maximum Entropy DQMC.

104

(Fig. 4.6b) reveals that they are spread out over an energy interval that is larger than the non-interacting bandwidth of the top most band ($W_3 \sim 0.3W \sim 0.735$ eV). In addition to the formation of the Hubbard bands for orbital 3, I also observe two additional effects. The first is an expected narrowing of the bandwidth of the itinerant bands. For this parameter set I obtain $W_1 \sim 1.7$ and $W_2 \sim 1.65$ eV for orbitals one and two, respectively, which should be compared to the non-interacting values of 1.88 and 1.97 eV. The second is the aforementioned hybridization and level repulsion between the itinerant and localized orbitals. This is manifest in the spectral function as a slight "buckling" of orbital three's upper Hubbard band near $k = 0$, and the tracking orbital one's spectral weight along E_{F} near $k = \pm\pi/2a$. It is this trailing intensity that forms the peak observed in the DOS just above the Fermi level at low temperatures.

4.2.5.2 Strong Coupling $U/W = 2$

The spectral properties of the model are very different when the Hubbard interaction is increased to $U/W = 2$. In this case, the total spectral function (Fig. 4.7e) and its orbitally-resolved components (Fig. 4.7f-4.7h) all split into relatively flat Hubbard-like bands above and below E_{F}. (In the case of orbital three, the lower band below E_{F} has been pushed outside of the energy range shown in the figure.) For this value of the interaction strength there is no spectral weight at the Fermi level, and the system is insulating even though orbitals one and two have on average 1.55 and 1.44 electrons/orbital, respectively. (These values are obtained both from the measured equal time orbital occupancies, and from integrating the total spectral weight above and below E_{F}.)

The imaginary axis spectral weight analysis (Fig. 4.4c) and the spectral function analysis (Fig. 4.7) both indicate that for $U/W = 2$ the model is an insulator. The origin of this behavior is the combined action of the Hund's coupling and the onset of an orbital ordering of the itinerant orbitals. All indications show that orbital three has already undergone an orbital selective Mott phase transition (OSMT) when $U/W = 2$. This has the effect of localizing one electron per site within this subset of orbitals while leaving three additional electrons to be distributed among the remaining two itinerant orbitals. A sizable Hund's coupling will decouple the individual orbitals when the crystal field splittings are smaller

than the bandwidth of the material [179]. This is precisely the situation at hand, and thus the remaining nominally itinerant orbitals are decoupled from the localized orbital by the large $J = U/4$. This results in an effective nearly-degenerate two-band system with (nearly) three-quarters filling. This is special case for the two-orbital Hubbard model, which is prone to orbital ordering in one and two-dimensions [93, 38, 226].

The situation is sketched in Fig. 4.8. Assuming ferromagnetic nearest neighbor correlations for orbital three, I have a low-energy ground state configuration as shown in the left side of 4.8a. Here, orbitals one and two adopt alternating double occupations in order to maximize their delocalization energy through virtual hopping processes. This results in near-neighbor orbital correlations. Subsequent charge fluctuations such as the one shown in the right side of the Fig. 4.8a cost a potential energy $PE \sim U' - J = W/2$. This is compensated for by a kinetic energy gain $KE \sim 4t_{11} \sim 4W/4.9$. The ratio between these competing energy scales is $\sim 5/8$, suggesting that charge fluctuations are strongly suppressed by the strong electronic correlations in this subsystem. Note that the situation is worse for antiferromagnetic nearest neighbor correlations in orbital three. The energy cost in this case increases to $\sim U'$, as shown in Fig. 4.8b. Thus both ferro- and antiferromagnetic correlations in orbital three will suppress charge fluctuations and promote orbital ordering. Since the type of magnetic correlations does not matter, such orbital ordering tendencies can be expected in the paramagnetic phases, provided the localized moments have formed in orbital three. This picture is then consistent with insulating behavior (and short-range orbital ordering tendencies, see below) at high temperatures, where no magnetic correlations are observed.

I verify this picture explicitly in Fig. 4.9, which plots the equal-time orbital correlation function $\langle \hat{\tau}_{i+d}\hat{\tau}_i \rangle$, with $\hat{\tau}_i = (\hat{n}_{i,2} - \hat{n}_{i,1})$. Here, results are shown for finite temperature DQMC calculations (Fig. 4.9a) and zero temperature DMRG calculations (Fig. 4.9b) and with $U/W = 2$ in both cases. The "long-range" (with respect to the cluster size) anti-ferro-orbital correlation is clear in the zero temperature results obtained on $L = 8$ and $L = 16$ chains. At finite temperatures ($\beta = 19.6/W$) I find that the orbital correlations are suppressed at long distances, but local anti-ferro-orbital correlation remains on shorter length scales. These combined results demonstrate the presence of short-range orbital correlations at higher
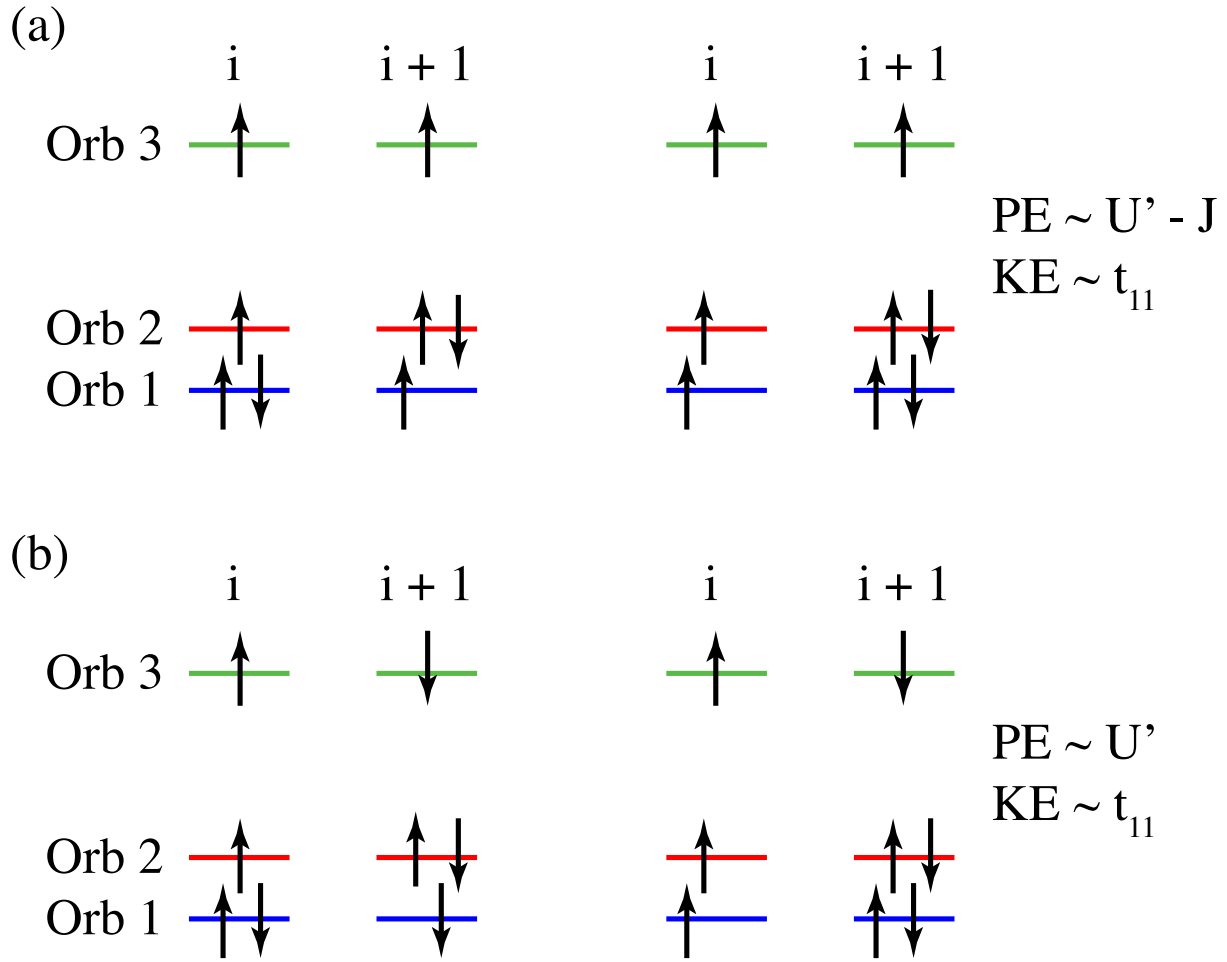
Figure 4.8: A cartoon sketch of the relevant charge fluctuation processes leading to the insulating state when $U/W = 2$ assuming (a) ferromagnetic and (b) antiferromagnetic nearest neighbor correlations within the orbital that has undergone the orbital selective Mott transition (orbital three).
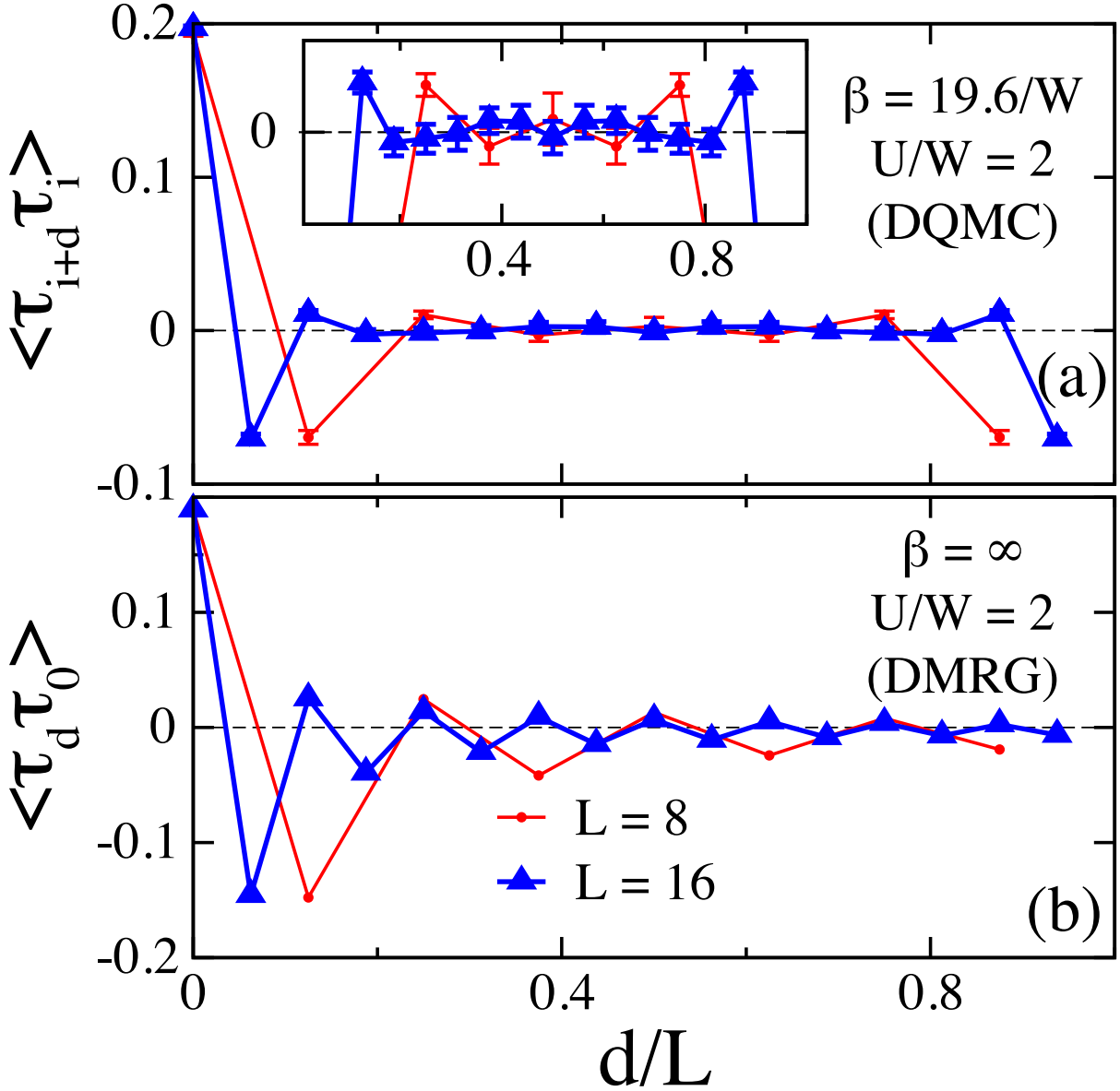
Figure 4.9: Results for the orbital correlation function for the system in the strong coupling case $U/W = 2$. Results are obtained at (a) finite temperature using DQMC and (b) $T = 0$ ($\beta = \infty$) using DMRG. In both cases, results are shown on $L = 8$ (red dots) and $L = 16$ (blue triangles) chains. The DQMC results were obtained on a chain with periodic boundary conditions. The DMRG results were obtained on a chain with open boundary conditions.

temperatures, which grow in length as the temperature is decreased. The corresponding orbitally resolved DOS are plotted in Fig. 4.10 for both cases. Both methods predict that the system is insulating, with a charge gap width on orbitals one and two of about 0.5 eV (estimated from half the peak-to-peak distance in the DOS). The presence of a gap at finite temperature also confirms that the short range orbital correlations are sufficient to open a gap in the spectral function. Finally, I stress these results will survive in the thermodynamic limit $L \to \infty$. This is confirmed in the inset in Fig. 4.10b, which plots the $T = 0$ gap Δ as a function of chain length L, as obtained from DMRG. In this case, computing the DOS for the longer chains is impractical. Therefore, I defined an alternative measure of the gap as $\Delta = E(N + 1) + E(N - 1) - 2E(N)$, where $E(N)$ is the ground state energy of the system with $N = 4L$ electrons. This definition agrees with the gap size obtained directly from the DOS that was explicilty computed for the shorter chains. Using this, I find that the DMRG gap size Δ decreases with increasing chain lengths, until leveling off at a value of ~ 0.2 eV in the $L \to \infty$ limit.

4.3 Discussion and Summary

I have performed a momentum-resolved study of a multi-orbital model defined on extended 1D chains using non-perturbative DQMC and DMRG. This has allowed me to compute the several properties of an OSMP in a momentum resolved manner without resorting to approximate methods. I find that several properties do indeed exhibit significant momentum dependencies, not be captured by local approximations introduced by DMFT; however, the 1D case I have considered represents the worst case for DMFT. In that sense my results complement existing DMFT efforts by providing analysis in a region where the method is expected to perform badly.

My results establish the hierarchy of charge and magnetic orderings in this model. At low temperatures, the DMRG calculations (as well as those in Ref. [218]) demonstrate that orbital three is ferromagnetically ordered at $T = 0$. Contrary to this, my finite temperature DQMC calculations find no indications of any magnetic order for $\beta < 19.6/W$; the magnetic structure factor $S(q)$ is completely featureless as a function of q at these temperatures.
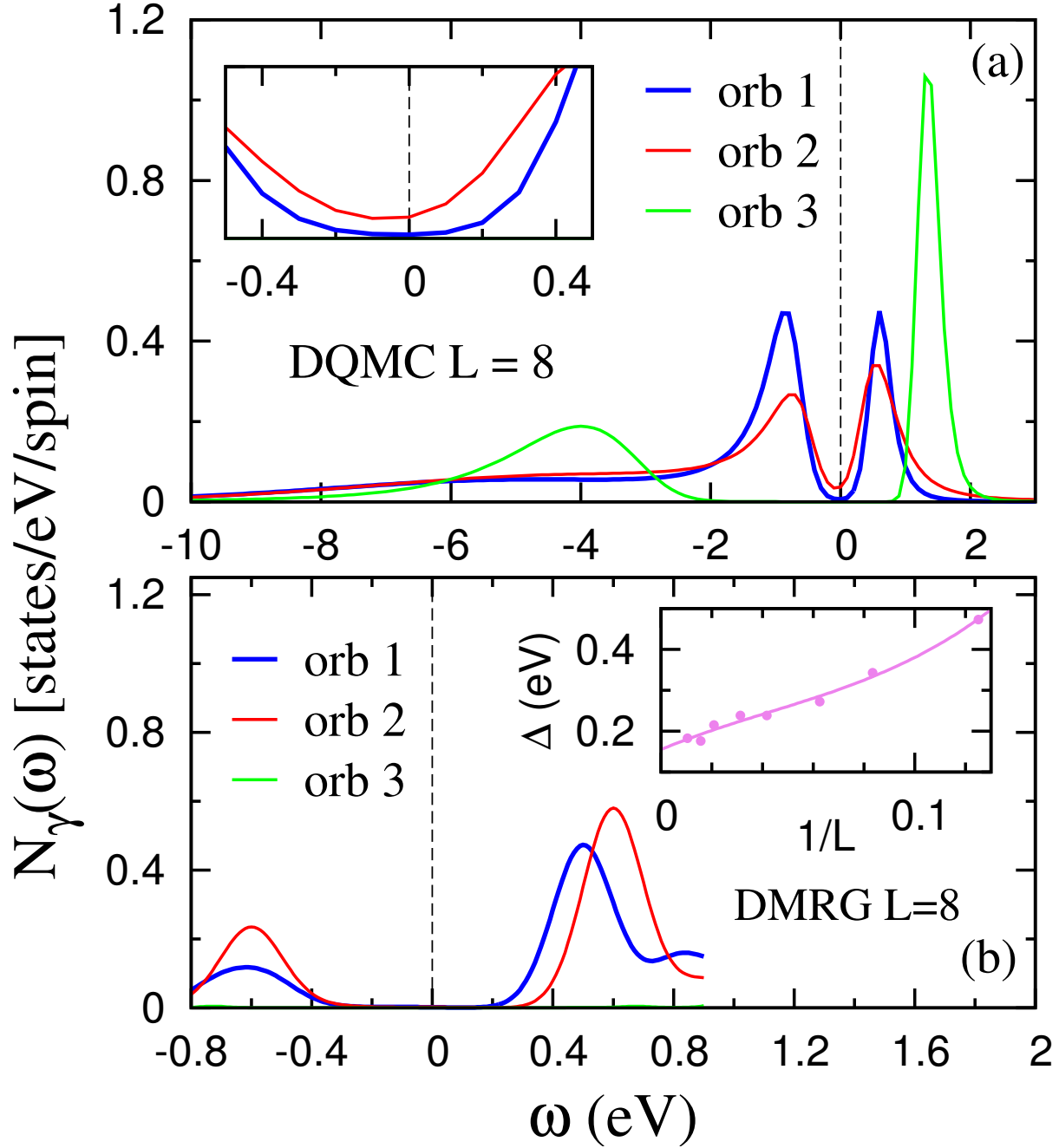
Figure 4.10: Results for the orbitally-resolved density of states for each orbital obtained for $U/W = 2$ and on $L = 8$ site chains. Panel (a) shows DQMC results at $\beta = 19.6/W$ and the inset zooms in to energy around Fermi surface. Panel (b) shows DMRG results for the same conditons but at zero temperature ($\beta = \infty$). The inset plots a finite size scaling analysis of the charge gap obtained within DMRG (see text). The dash line in both panels indicates the Fermi energy.

Despite this, my finite T calculations find an orbital-selective Mott phase, as well as a fully insulating phase arising due to short-range orbital ordering, depending on the strength of the Hubbard interaction U. I therefore conclude that the charge ordering occurs before any magnetic ordering in this model.

The results shown in Fig. 4.3d and 4.4d show that orbital three in my model, which has the narrowest band width, undergoes a transition to a Mott phase at $\beta W \sim 10 - 15$. This in combination with the lack of magnetic signal means that OSMP in this parameter regime is a true Mott phase as opposed to a Slater insulator where the insulating behavior is driven by magnetism. My results also demonstrate that it is insufficient to identify an OSMP using the orbital occupations only in some instances. One should be particularly careful in regions of parameter space where the itinerant bands have average occupations close to special cases known for one and two-orbital Hubbard models. In my case, the average fillings of the itinerant orbitals are $\langle n_1 \rangle \sim 1.53$ and $\langle n_2 \rangle \sim 1.47$, values very close to the special case of $3/4$ filling in a degenerate two-band Hubbard model. At zero temperature, the DMRG results obtain fillings of 1.5 for each orbital.

The orbital correlations in Fig. 4.9 give some indication as to the extend of the cluster one might need to capture these effects using embedded cluster techniques. The $\beta = 19.6/W$ results shown in Fig. 4.9a indicate that the orbital correlations extend over (at least) three lattice sites within the error bars of my data, while at $T = 0$ the correlations (Fig. 4.9b) extend over the length of the cluster. Thus, the low-temperature correlation length can be quite long, even in 1D. Single-site mean-field approaches cannot capture these correlations in either case. However, one might hope that DCA or cluster DMFT extensions may be able to address the short range correlations at elevated temperatures.

Finally, I discuss my results in the context of recent experimental work. ARPES results for AFe_2As_2 have found evidence that the OSMP in these materials disappears as the temperature is lowered [276]. This behavior was explained using a slave-boson approach and attributed to the reduced entropy in the metallic phase in comparison to the OSMP. My results do not show this behavior, and the OSMP is found at low temperature. This difference may be related to the differences in the dimensionality (one vs. two) or number of orbitals (three vs. five) between the models, or the differences between my non-perturbative

approach and other mean-field methods. This highlights the need for continued application of non-perturbative methods to tractable multi-orbital Hubbard models.

Chapter 5

The electron-phonon interaction in correlated multi-orbital systems

In this chapter, I study the interplay between the electron-phonon interaction and the electron-electron interaction in multi-orbital systems. Here, we consider systems both in one dimension and infinite-dimension. In the 1D case, I used the same parameters as I used for the electronic properties in the chapter 4. Holstein phonons are then added into the Hamiltonian to study the phonon effect. This 1D three-orbital Hubbard-Holstein model is studied using DQMC. In infinite-dimension, I use dynamical mean field theory (DMFT) to study a two-orbital Hubbard-Holstein model. The key results presented in this chapter have appeared in Ref. [149] and Ref. [151].

In recent years, many researchers have began studying electron-electron (e-e) interactions in multiorbital systems such as the iron-based superconductors (FeSCs). In doing so, they have discovered numerous new phenomena, including the Hund's metal [92, 79, 71] and the orbital-selective Mott phase (OSMP) [5, 127, 179, 276, 148], which arise from the competing action of the electronic interactions. These concepts have helped shape our understanding of the enigmatic properties of these materials. Despite this success, however, surprisingly little is currently known about how competition/cooperation with other factors such as impurities or the electron-phonon (e-ph) interaction influences these phenomena. This question is important for our microscopic understanding of these materials, as subtle multiorbital correlation effects can produce states that are readily affected by small perturbations.

In the case of the FeSCs, the *e*-ph interaction was ruled out as a possible pairing mediator by early *ab initio* calculations [26] indicating that the total coupling strength was small, with a dimensionless *e*-ph coupling $\lambda \leq 0.2$. Because of this, many researchers have assumed that this interaction plays a secondary role in these materials with regards to other aspects as well. However, there is growing evidence that this outlook may have been premature. For example, more recent calculations find that taking into account the possible magnetism [280, 25, 48, 167] or orbital fluctuations [128, 225] can increase the total *e*-ph coupling strength compared to the original estimates. This finding is consistent with the general notion that electron correlations can enhance *e*-ph interactions [33]. Moreover, the discovery of the FeSe films on oxide substrates [256] has implicated new possible lattice interactions, either across the interface [141, 213] or within the FeSe film [47]. Since bulk FeSe is believed to be in the OSMP regime [260, 70], these experiments naturally raise questions about when and how *e*-ph interactions can influence such multi-orbital phenomena.

Hubbard-Holstein models are the simplest models capturing the interplay between *e*-*e* and *e*-ph interactions. The single-band variant has been extensively studied, particularly at half-filling, where a direct competition occurs between antiferromagnetic Mott insulating (MI) and charge-density-wave (CDW) phases [14, 15, 20, 196, 188, 264, 227, 163, 193, 121]. In comparison, far fewer studies exist for multiband generalizations of the model [272, 128]. Motivated by this, I study the interplay between the *e*-*e* and *e*-ph in the multiorbital Hubbard-Holstein model. In particular, I use DMFT [78] to study the inifinite-dimensional case, since DMFT can give an exact solution in this case. Also, I use DQMC to study the one-dimensional case in that DMFT fails to produce exact solutions in low dimensions.

5.1 The infinite-dimensional case

I first study the interplay between the *e*-*e* and *e*-ph interactions in the degenerate two-orbital Hubbard-Holstein model in infinite-dimension. The Hamiltonian for this model [272] is $H = H_{\mathrm{kin}} + H_{\mathrm{lat}} + H_{\mathrm{e-ph}} + H_{\mathrm{e-e}}$, where

$$H_{\mathrm{kin}} = -\sum_{\langle i,j \rangle, \gamma, \sigma} t_\gamma c_{i,\gamma,\sigma}^\dagger c_{j,\gamma,\sigma} - \mu \sum_{i,\gamma,\sigma} \hat{n}_{i,\gamma,\sigma},$$

$$H_{\text{e}-\text{ph}} + H_{\text{lat}} = g \sum_{i,\gamma,\sigma} \left(b_i^\dagger + b_i \right) \left(\hat{n}_{i,\gamma,\sigma} - \frac{1}{2} \right) + \Omega \sum_i b_i^\dagger b_i,$$

$$H_{\text{e}-\text{e}} = U \sum_{i,\gamma} \hat{n}_{i,\gamma,\uparrow} \hat{n}_{i,\gamma,\downarrow} + U' \sum_{i,\gamma\neq\gamma'} \hat{n}_{i,\gamma\uparrow} \hat{n}_{i,\gamma',\downarrow}$$

$$+ (U' - J) \sum_{i,\gamma<\gamma',\sigma} \hat{n}_{i,\gamma,\sigma} \hat{n}_{i,\gamma',\sigma}$$

$$+ J \sum_{i,\gamma\neq\gamma'} (c_{i,\gamma,\uparrow}^\dagger c_{i,\gamma,\downarrow}^\dagger c_{i,\gamma',\downarrow} c_{i,\gamma',\uparrow} - c_{i,\gamma,\uparrow}^\dagger c_{i,\gamma,\downarrow} c_{i,\gamma',\downarrow}^\dagger c_{i,\gamma',\uparrow})$$

Here, $\langle \cdots \rangle$ denotes a summation over nearest neighbors; $c_{i,\gamma,\sigma}^\dagger$ creates an electron with spin σ in orbital $\gamma = 1, 2$ on site i; $b_i^\dagger$ creates a phonon on site i; $\hat{n}_{i,\gamma,\sigma} = c_{i,\gamma,\sigma}^\dagger c_{i,\gamma,\sigma}$ is the particle number operator; t_γ is the nearest neighbor hopping integral for orbital γ; U and U' are the intra- and inter-orbital Hubbard interactions, respectively. Throughout, I choose $U' = U - 2J$ due to rotational symmetry [78, 36]. J is the Hund's coupling, which is fixed to $J = U/5$ unless otherwise stated; g is the e-ph interaction strength; Ω is the phonon energy; and μ is the chemical potential, which is adjusted to fix the average particle per site to $\langle \hat{n} \rangle = 2$.

I work in infinite dimensions (where DMFT is exact) by adopting a Bethe lattice with a semi-circular density of states $\rho_\gamma(\epsilon) = \frac{8}{\pi W_\gamma^2} \sqrt{(W_\gamma/2)^2 - \epsilon^2}$, where $W_\gamma = 4t_\gamma$ is the bandwidth. Throughout this chapter, I set $W_1 = 5W_2 \equiv W = 2$ eV, fix the temperature at $T = \frac{1}{\beta} = 0.01$ eV, unless otherwise stated, and set the phonon energy to $\Omega = 0.15$ eV. The bandwidth and Hund's coupling J are chosen so that I can obtain a robust OSMP without the e-ph coupling. The dimensionless e-ph coupling constant is defined as $\lambda = \frac{2g^2}{W\Omega}$. The impurity model is solved using the exact diagonalization and the infinite phonon Hilbert space is limited by only allowing up to N_{ph} phonons, where $N_{\text{ph}} \sim 40$ is typical, depending on the parameters used. I have checked that all of my results are well converged for increasing values of N_{ph}.

The convergence of quasiparticle weight with bath size N_{b} is shown in Fig. 5.1, where Fig. 5.1(a) and 5.1(b) are results of $\lambda = 0$ and $U = 0$, respectively. Both Fig. 5.1(a) and 5.1(b) show that phase transition critical values are consistent for $N_{\text{b}} = 4$ and $N_{\text{b}} = 6$. There is a slight difference between $N_{\text{b}} = 4$ and $N_{\text{b}} = 6$ for Z_1, while results of Z_2 are very close. Hence, $N_b = 4$ is enough to produce reliable solutions for the two-orbital model. To reduce the total computational demands, I use $N_{\text{b}} = 4$ in the following calculations.
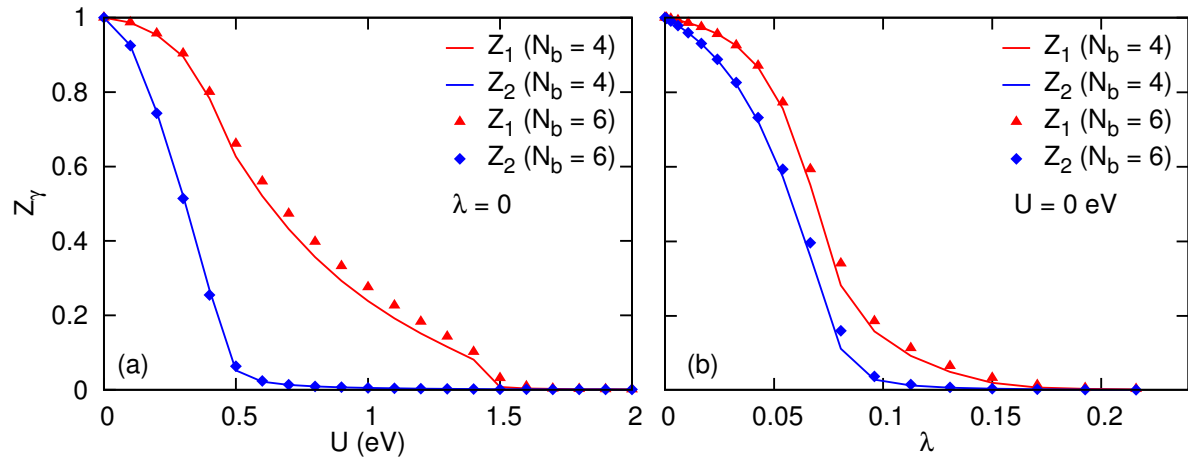
Figure 5.1: (color online) Convergence of quasiparticle weight Z_γ with bath size N_b. Solid lines and points are results of $N_b = 4$ and $N_b = 6$, respectively. In panel (a) $\lambda = 0$ and in panel (b) $U = 0$ eV.

5.1.1 Competition between U and λ

The λ-U phase diagram for the model is shown in Fig. 5.2. Here, I plot the orbitally resolved Matsubara quasiparticle weight $Z_\gamma = \left(1 - \frac{\mathrm{Im}\Sigma(\mathrm{i}\pi T)}{\pi T}\right)^{-1}$ on a logarithmic scale. The quasiparticle weight Z_γ approaches to 1 when it is metallic, while Z_γ approaches to 0 when it is insulating. Five distinct phases can be identified from the values of Z_γ, the local magnetic moment $m_{\gamma z}^2 = \langle(n_{\gamma\uparrow} - n_{\gamma\downarrow})^2\rangle$, and the average number of phonon quanta $N_{\mathrm{ph}} = \langle b^\dagger b\rangle$ (all shown in Fig. 5.3), and their boundaries are indicated by the white lines. Three of these phases are similar to those found in the single-band Hubbard-Holstein model. The first phase is a metallic phase (M) at small (λ, U), where both Z_1 and Z_2 are large. The second is a Mott insulating (MI) phase, which appears at large U. It is identified by a situation where $Z_1 = Z_2 = 0$, the magnetic moments are large $m_{1,z}^2 \approx m_{2,z}^2 \approx 1$, and N_{ph} is nearly zero. The third phase is a CDW insulating phase where $Z_1 = Z_2 = 0$, while N_{ph} is large ($N_{\mathrm{ph}} \gg 1$) and no local moments have formed (i.e. $m_{1,z}^2 \approx m_{2,z}^2 \approx 0$). An examination of the wavefunctions reveals that the CDW phase corresponds to a state where the impurity site is either fully occupied or entirely empty with equal probability, consistent with a checkerboard-type ordering common to the single-band model [196, 15, 14]. This phase is likely to be a $(\pi, \pi, ...)$ CDW order (sometimes referred to as a strong coupling bi-polaronic insulating phase in the single-band case). Alternatively, this phase could also reflect phase separation, although delocalization effects should favor the CDW. Further studies on extended clusters will be needed to address this issue.

In addition to the "standard" phases, I also observe two distinct phases with orbital selective characteristics. The first is the widely studied OSMP, which appears between the M and MI phases. It resembles the same OSMP found in the model without e-ph interactions [177]. Here, the orbital with the narrower bandwidth becomes insulating with $Z_2 = 0$ and $m_{2z}^2 \approx 1$, while the orbital with the wider bandwidth remains itinerant with a non-zero quasiparticle weight. Interestingly, I also observe a second region of orbital selective behavior, located in a small portion of parameter space between the M/OSMP phases and the fully insulating CDW phase, denoted as OSPI in Fig. 1. As with the OSMP, in this region, the narrow band becomes insulating while the wide band remains itinerant with
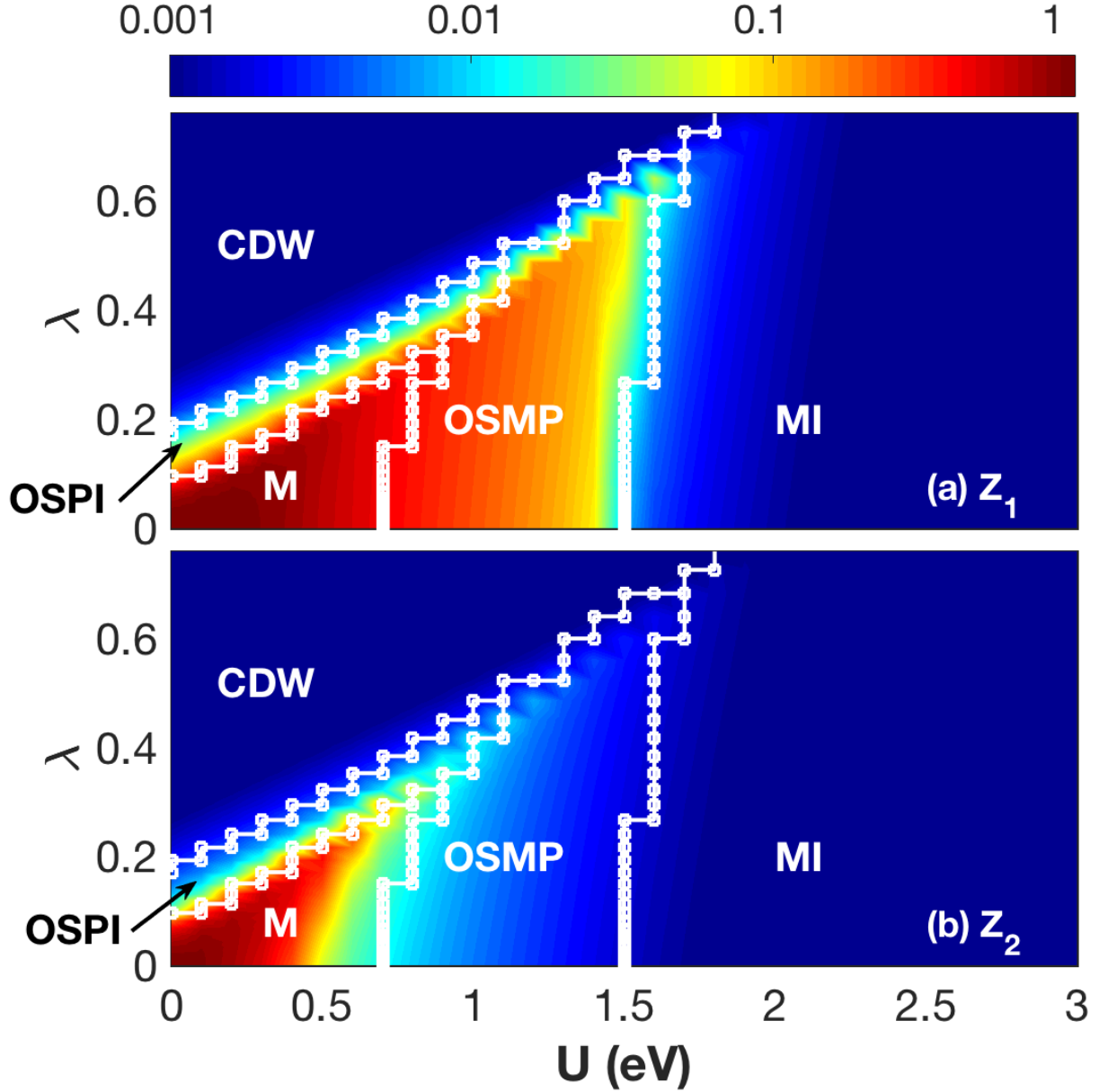
Figure 5.2: (color online) The phase diagram for the two-orbital Hubbard-Holstein model in the e-ph interaction strength (λ) - Hubbard U plane at charge density $n = 2$ and temperature $\beta = 200/W$. (a) and (b) show density plots of quasiparticle weights Z_1 and Z_2 on a logarithmic scale, respectively. The different phases are labeled as follows: metal (M), orbital-selective Mott phase (OSMP), Mott insulater (MI), charge density wave (CDW), and orbital-selective Peierls insulator (OSPI). The white dots indicate points where the calculations were performed, and I plotted them to show phases boundaries. The color scale is plotted using a linear interpolation.
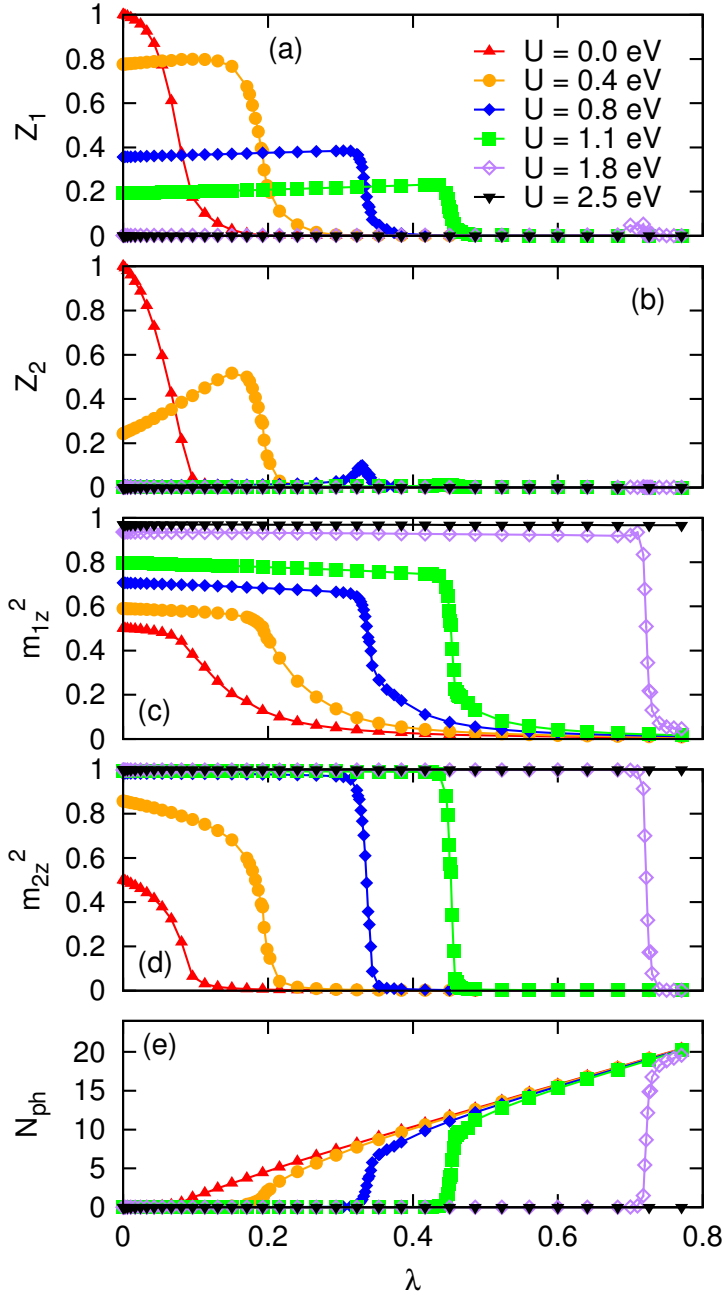
Figure 5.3: (color online) The quasiparticle weights (a) Z_1 and (b) Z_2 as a function of the e-ph interaction strength (λ) at different Hubbard U values. Mean values of the local magnetic moments m_{1z}^2, m_{2z}^2 and phonon numbers (N_{ph}) are shown in (c), (d), and (e), respectively.

$Z_1 \neq 0$ and $Z_2 = 0$. But unlike the OSMP, here I find tiny local moments on orbital 2 with $m_{2z}^2 \leq 0.05$, and a large N_{ph} ($N_{\mathrm{ph}} > 1$). The latter indicates the presence of a sizable lattice distortion. The e-ph interaction drives the orbital-selective insulating properties in this case rather than the Hubbard and Hund's interaction. I label this state an orbital selective Peierls insulator (OSPI), in analogy to the OSMP.

For reference, Fig. 5.3 shows the evolution of the quantities used to identify the five regions of the phase diagram as a function of λ for different values of U. When $U \leq 0.4$ eV, $m_{\gamma z}^2$ and N_{ph} vary smoothly near the phase transition, while for $U > 0.4$ eV, these quantities vary quickly in the transition region, but are nevertheless continuous. This behavior is consistent with a previous DMFT study of the single band Hubbard-Holstein model [15], where a smooth transition occurs at weak coupling that becomes increasingly sharp as U/W increases.

5.1.2 Hysteresis

To study the analogy between the OSMP and the OSPI further, I examine the classification of the phase transitions and their possible hysteresis behavior [153]. Fig. 5.4(a) and 5.4(b) plot the evolution of Z_γ at $T = 0.002$ eV along the $(U, \lambda = 0)$ and $(U = 0, \lambda)$ axes, respectively. Along the $(U, \lambda = 0)$ line, there are two Mott transitions in the two-orbital system, I observe a single hysteresis loop near the OSMP boundary, which indicates a coexistence region, as discussed in Ref. [153]. The critical U values for increasing and decreasing interaction strengths are $U_{c,1} = 0.6$ eV and $U_{c,2} = 0.5$ eV, respectively. Similarly, along the $(U = 0, \lambda)$ line I also find a single coexistence region, consistent with DMFT studies for the single band Holstein model [184, 109]. As with the Mott transition, the hysteresis loop appears close to the first Peierls transition and the critical λ values for increasing and decreasing interactions are $\lambda_{c,1} = 0.08$ and $\lambda_{c,2} = 0.066$, respectively. Thus, the OSMP and OSPI transitions phenomena appear to be analogous to one another. The appearance of hysteresis indicates a first order transition out of the metallic phase while the other transitions are continuous. Finally, I note that the hysteresis behavior disappears at $T = 0.01$ eV, where I performed most of my calculations.
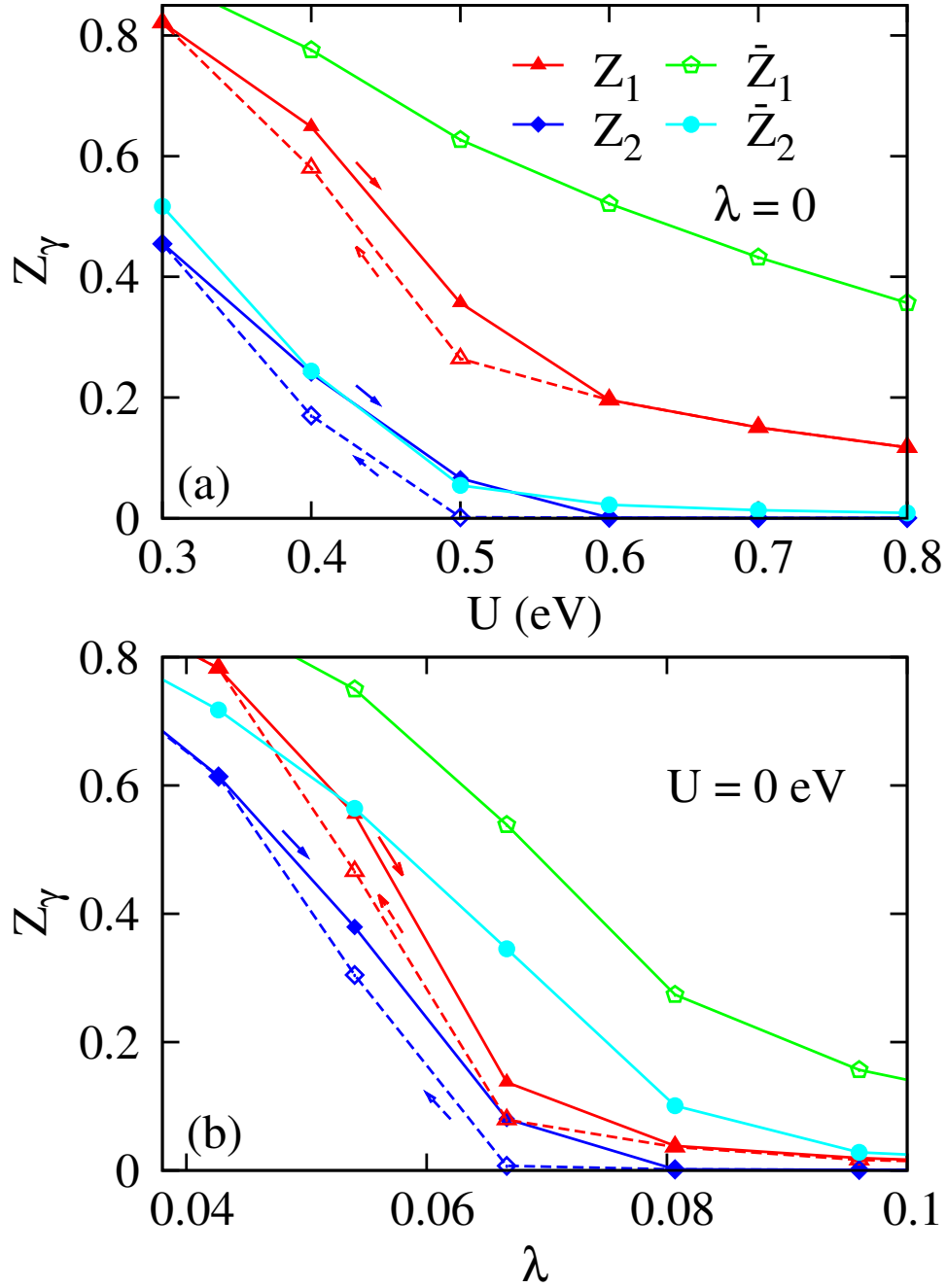
Figure 5.4: (color online) (a) The quasiparticle weight Z_γ as a function of U at a fixed $\lambda = 0$. (b) The quasiparticle weight Z_γ as a function of λ at a fixed $U = 0$. Z_γ are results at $T = 0.002$ eV and $\bar{Z}_\gamma$ are results at $T = 0.01$ eV. The solid lines and the dashed lines are results of increasing and decreasing U or λ, respectively.

5.1.3   Interplay between λ and Hund's coupling

The Hund's coupling plays a major role in establishing the boundaries of the OSMP [127, 180]. Therefore, I explored its role in determining the CDW and OSPI phases observed here. Fig. 5.5 shows the phase diagram in the λ - J/U plane for a fixed $U = 0.8$ eV. For $\lambda < 0.3$, the metallic phase survives to larger values of J/U as λ increases. This result is consistent with the notion that the e-ph interaction mediates an effective attractive interaction that competes with the onsite Hubbard interactions. When $0.3 < \lambda < 0.4$, the OSMP disappears and is replaced by the OSPI and CDW phases and the critical λ value for both phases is decreased as J/U increases. For larger λ, the CDW phase persists for all J/U values. Thus, the Hund's coupling not only favors the OSMP transition but also has a stabilizing effect for the lattice-driven phases.

To gain further insight into the influence of J on the OSPI phase transition, I examined the phase transition from the metallic state to the CDW at a fixed $U = 0.8$ and $\lambda = 0.384$, as shown in Fig. 5.6(a) and 5.6(b). Fig. 5.6 (a) shows quasiparticle weights Z_1 and Z_2 as a function of J/U. The dashed lines are the boundaries of each phase.

On the impurity site, the electronic subspace of the ground state at half-filling can be written as

$$
\begin{aligned}
|\psi\rangle \;=\; & P_1 \left(|0000\rangle + |1111\rangle\right) + \\
& P_2 \left(|1000\rangle + |0100\rangle + |1011\rangle + |0111\rangle\right) + \\
& P_3 \left(|0010\rangle + |0001\rangle + |1101\rangle + |1110\rangle\right) + \\
& P_4 \left(|1100\rangle + |0011\rangle\right) + P_5 \left(|1010\rangle + |0101\rangle\right) + \\
& P_6 \left(|1001\rangle + |0110\rangle\right),
\end{aligned}
$$

in which $|n_{1,\uparrow} n_{1,\downarrow} n_{2,\uparrow} n_{2,\downarrow}\rangle$ are the basis elements for the electronic subspace and $n_{\gamma,\sigma}$ is the electron number for the orbital γ and spin σ. Here, I only need six distinct coefficients P_i due to the particle-hole symmetry of the underlying Hamiltoniain. For example, the weight for the basis states $|0000\rangle$ and $|1111\rangle$ must be the same and equal P_1.
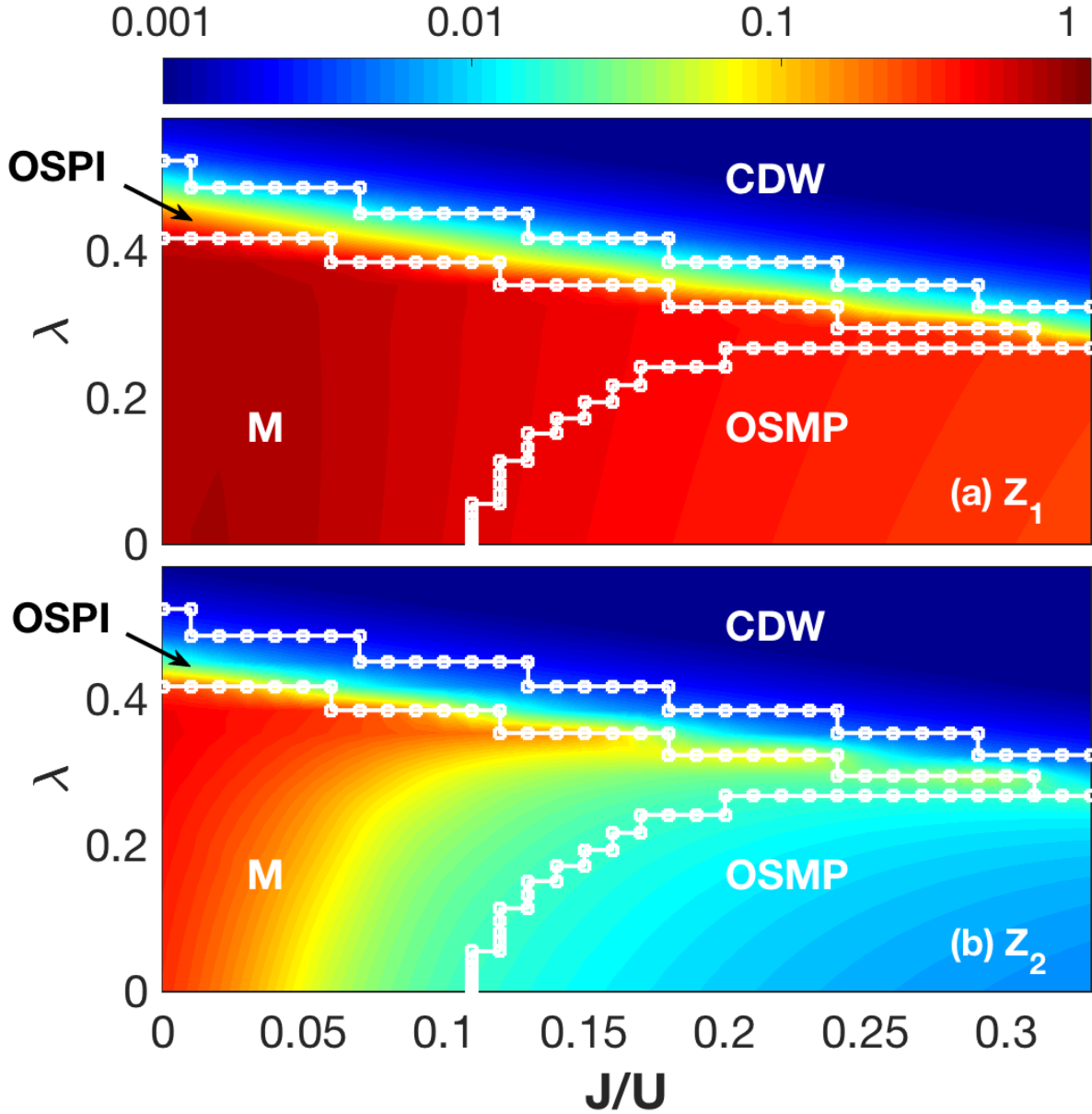
Figure 5.5: (color online) The phase diagram in the λ-J/U plane at filling $n = 2$. (a) and (b) plot quasiparticle weights Z_1 and Z_2, respectively. The labels used in this graph are the same as in Fig. 5.2. The Coulomb interaction is fixed at $U = 0.8$ eV and $U' = U - 2J$. The white dots indicate points where the calculations were performed, and I plotted them to show phases boundaries. The color scale is plotted using a linear interpolation.
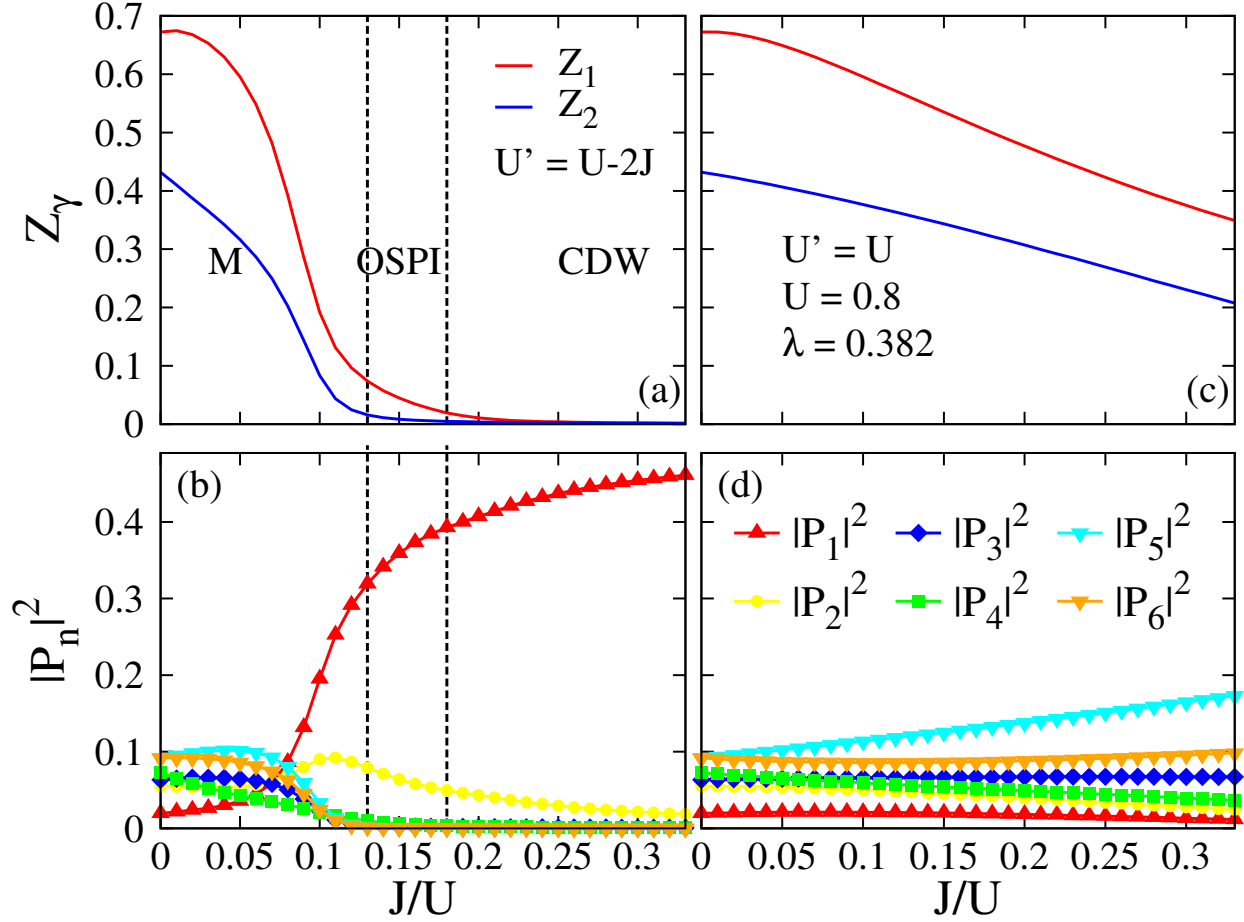
Figure 5.6: (color online) (a) and (c) plot the quasiparticle weights Z_1 and Z_2 vs. J/U. (b) and (d) plot the probabilities $|P_i|^2$ of the eight states mentioned in the text vs. J/U. The interorbital repulsion is fixed to $U' = U - 2J$ in (a) and (b). In (c) and (d) $U' = U$. The Hubbard interaction strength is $U = 0.8$ eV and e-ph interaction strength is $\lambda = 0.384$ in all panels. The dashed lines in (a) and (b) correspond to phase boundaries.

In a pure CDW phase composed of fully occupied and empty sites one has $P_1 = \frac{1}{\sqrt{2}}$ and $P_n = 0$ for $n = 2, ..., 6$. This ground state produces $\langle n_{\gamma,\sigma} n_{\gamma',\sigma'} \rangle = 0.5$, where γ (γ') = 1 or 2 and σ (σ') = $\uparrow$ or $\downarrow$. In a cluster system, the two bases $|0000\rangle$ and $|1111\rangle$ should be arranged on alternating lattice sites to minimize the kinetic energy of the system. This arrangement corresponds to a CDW with ordering vector $Q = \pi$ in 1D, (π, π) in 2D, (π, π, π) in 3D, *etc.*. The value of the six probabilities for each state as a function of J/U is plotted in Fig. 5.6(b). Near the phase transition from the metallic state to the OSPI, P_1 increases quickly, which implies that the state $(|0000\rangle + |1111\rangle)$ has a lower energy and is being preferentially populated. This energy reduction is achieved by decreasing the effective *e-e* interaction via the *e*-ph interaction, such as $U_{\text{eff}} = U + \frac{2\lambda W_\gamma}{\omega^2/\Omega^2 - 1}$. In addition, U' is also renormalized by the *e*-ph interaction via $U'_{\text{eff}} = U' - 2\lambda W$ in the limit of $\Omega \to \infty$. When $U'_{\text{eff}} - J < 0$ and the attraction potential between two orbitals can compensate the energy cost for double occupation on the individual orbitals, thus stabilizing the CDW state. Hence, in the multi-orbital case, the stabilization of the CDW phase with increasing J/U is due to the reduction of the interorbital Hubbard interaction, imposed by the condition that $U' = U - 2J$. In short, increasing J reduces U' and therefore also reduces the total potential energy cost for a double occupation of a given site. The cost for creating a charge ordered phase, where each site alternates between fully occupied and empty, is therefore lowered. To confirm my arguments, I fix $U' = U$ and use the same U and λ values to calculate Z_γ and P_n^2 in Fig. 5.6(c) and 5.6(d), respectively. In this case, neither the CDW nor the OSPI phase are found because the fixed U' prevents $U'_{\text{eff}} - J$ from becoming negative at an intermediate λ. For larger large λ values both the OSPI and CDW phases appear; however, their phase boundaries are largely independent of J/U when $U = U'$.

5.2 The one dimensional case

The prior study was carried out in infinite dimensions, where DMFT is exact; however, given the dependence on dimensionality found for the single-orbital HH model [44, 15, 196], it is essential to study the problem in other dimensions, as a function of doping, and with different techniques. Motivated by this, I present here a complementary study of the three-orbital

HH model defined on an extended 1D chain at an average electron filling $\langle \hat{n} \rangle = 4$. I study the model using DQMC, which is a nonperturbative auxiliary-field technique and capable of handling both the e-e and e-ph interactions on equal footing.

My starting point is a simplified one-dimensional three-orbital Hubbard model as shown in chapter 4. I then add a Holstein-type interaction, where the atomic displacement is coupled to the electron density on each orbital. The full Hamiltonian is $H = H_0 + H_{e-e} + H_{\text{lat}} + H_{e-ph}$, where

$$H_0 = -\sum_{\substack{\langle i,j \rangle \\ \sigma,\gamma,\gamma'}} t_{\gamma\gamma'} c_{i,\gamma,\sigma}^{\dagger} c_{j,\gamma',\sigma} + \sum_{i,\sigma,\gamma} (\Delta_\gamma - \mu) \hat{n}_{i,\gamma,\sigma} \tag{5.1}$$

are the non-interacting electronic terms,

$$H_{\text{lat}} = \sum_i \left[\frac{\hat{P}_i^2}{2M} + \frac{M\Omega^2}{2} \hat{X}_i^2 \right] = \Omega \sum_i \left(b_i^{\dagger} b_i + \frac{1}{2} \right) \tag{5.2}$$

are the noninteracting lattice terms,

$$\begin{aligned} H_{e-e} &= U \sum_{i,\gamma} \hat{n}_{i,\gamma,\uparrow} \hat{n}_{i,\gamma,\downarrow} + \left(U' - \frac{J}{2} \right) \sum_{\substack{i,\sigma,\sigma' \\ \gamma<\gamma'}} \hat{n}_{i,\gamma,\sigma} \hat{n}_{i,\gamma,\sigma'} \\ &+ J \sum_{i,\gamma<\gamma'} S_{i,\gamma}^z S_{i,\gamma'}^z \end{aligned} \tag{5.3}$$

are the on-site Hubbard and Hund's interaction terms, and

$$H_{e-ph} = \alpha \sum_{i,\gamma,\sigma} \hat{X}_i \hat{n}_{i,\gamma,\sigma} = g \sum_{i,\gamma,\sigma} \left(b_i^{\dagger} + b_i \right) \hat{n}_{i,\gamma,\sigma} \tag{5.4}$$

are the e-ph coupling terms. Here, $\langle \ldots \rangle$ denotes a sum over nearest neighbors; $c_{i,\gamma,\sigma}^{\dagger}$ ($c_{i,\gamma,\sigma}$) creates (annihilates) a spin σ electron in orbital $\gamma = 1$, 2, 3 on site i; $b_i^{\dagger}$ (b_i) creates (annihilates) a phonon on lattice site i; $S_{i,\gamma}^z$ is the z-component of the spin operator $\mathbf{S}_{i,\gamma}$; $\hat{n}_{i,\gamma,\sigma} = c_{i,\gamma,\sigma}^{\dagger} c_{i,\gamma,\sigma}$ is the number operator; and $\hat{X}_i$ and $\hat{P}_i$ are the lattice position and momentum operators, respectively. The parameters Δ_γ are the on-site energies for each orbital; $t_{\gamma,\gamma'}$ are the intra- and interorbital hopping integrals; U and U' are the intra- and

interorbital Hubbard interactions, respectively, and J is the Hund's coupling. The parameter $g = \alpha\sqrt{2M\Omega}$ is the strength of the e-ph coupling and Ω is the phonon energy. Finally, μ is the chemical potential, which fixes the average particle number.

In Eq. (5.3) I have neglected the pair-hopping and spin-flip terms of the Hunds interaction, as was done in Ref. [148] for the same model without e-ph interactions. These terms introduce a significant Fermion sign problem [157] for DQMC calculations and are therefore neglected to make the problem tractable. Prior work [156] has shown that these terms only change the location of the various phase boundaries for the model considered here in the absence of the e-ph interaction. I, therefore, proceed assuming that this will also hold true once the phonons are included in calculations.

Throughout this work, I choose $U' = U - 2J$, as is standard for enforcing rotational symmetry [36], although I have neglected the pair hopping and spin-flip terms in Eq. (5.3). I further vary U while holding $J = U/4$ fixed. This choice produces a robust OSMP [218, 156, 148] in the absence the e-ph interaction and is appropriate for the FeSCs. I work at a fixed filling $\langle \hat{n} \rangle = 4$, which is typical for three-orbital Hubbard models used to describe the 2D FeSCs with two hole pockets near the Γ point and one electron pocket near the X (Y) point [55]. I expect that the same filling is needed to describe the quasi-one-dimensional system BaFe$_2$S$_3$. This choice of filling also allows us to make direct comparisons to previous studies in the absence of the e-ph interaction [218, 156, 148], such as the one presented in chapter 4. In this spirit, I also set $t_{11} = t_{22} = -0.5$ eV, $t_{33} = -0.15$ eV, $t_{13} = t_{23} = 0.1$ eV, $t_{12} = 0$ eV, $\Delta_1 = -0.1$ eV, $\Delta_2 = 0$ eV, $\Delta = 0.8$ eV, and $\Omega = 0.5$ eV, again following Refs. [148] and [218]. The total bandwidth of the non-interacting model is $W = 2.45$ eV, which serves as the unit energy in the following calculations. The dimensionless e-ph coupling constant is defined as $\lambda = \alpha^2/(M\Omega^2 W)$. (Note that since this is a multi-band system, different choices of bandwidths are possible. Here, I select the total bandwidth, as was done for the infinite-dimensional case.) Finally, I set $a = M = 1$ as units of distance and mass, respectively, and work at an inverse temperature $\beta = 14.7/W$ unless stated otherwise; this temperature is low enough to identify the ordering tendencies in the model.

I use DQMC to solve the 1D three-orbital HH model. Throughout this work, I use a one-dimensional chain with a chain size $N = 16$ and imaginary time discretization of

$\Delta\tau = 0.245/W$, unless otherwise stated. In all of simulations, I have not observed significant $\Delta\tau$ errors introduced by this choice.

The main results are summarized in Fig. 5.7, which provides a schematic of the phase diagram of the model. I find four distinct regions in the $\lambda - U$ parameter space, including states with metallic (M) characteristics, an OSMP region, a CDW order, and a region with strong orbital correlations (OC) and insulating characteristics. Comparing with the infinite-dimensional case, I find a new phase, namely OC state, but fail to produce the OSPI phase in the one-dimensional case. The details of these four phases will be discussed in the following sections.

5.2.1 Weak Electron-Phonon Coupling

In chapter 4 I presented that the model without phonons showed that an OSMP forms for U values in the range $0.6 < U/W < 2$ for my choice of J. In this state, orbital three becomes insulating while the remaining orbitals host itinerant electrons [218, 156]. The onset of this phase is signaled by the fact that the filling on orbital three $\langle \hat{n}_3 \rangle = 1$. For $U/W > 2$, orbitals 1 and 2 retain a noninteger filling but are driven into an insulating state by the onset of short-range orbital ordering [148]. To avoid this complication, I restrict $U/W < 1$.

I now examine the impact of the e-ph interaction on the OSMP. Figure 5.8 plots the electronic occupations of the three orbitals for different values of U/W and λ. For $\lambda = 0$, Fig. 5.8(c) shows that $\langle \hat{n}_3 \rangle$ converges to 1 as U/W increases, implying that a Mott gap is formed on this orbital for $U/W \geq 0.4$. At the same time, $\langle \hat{n}_1 \rangle$ and $\langle \hat{n}_2 \rangle$ maintain noninteger values, implying that these orbitals remain itinerant [see Fig. 5.8(a) and 5.8(b)]. These results are consistent with previous studies [218, 156]. When I include the e-ph coupling, the orbital occupations are modified significantly. For example, Figs. 5.8(d) - 5.8(f) show that the e-ph coupling tends to make electronic occupations on all three orbitals uniform when $U/W < 0.4$, with the average filling on each orbital approaching $\langle \hat{n}_i \rangle = \frac{4}{3}$ when λ is large. This value of the occupation on each orbital is consistent with a chagre-ordered state where two sites are fully occupied and one site is empty, which is shown in the CDW region of Fig. 5.7. This kind of charge order arises from the attractive interaction mediated by the e-ph interaction. For the fully occupied site, the attractive interaction can be mapped into
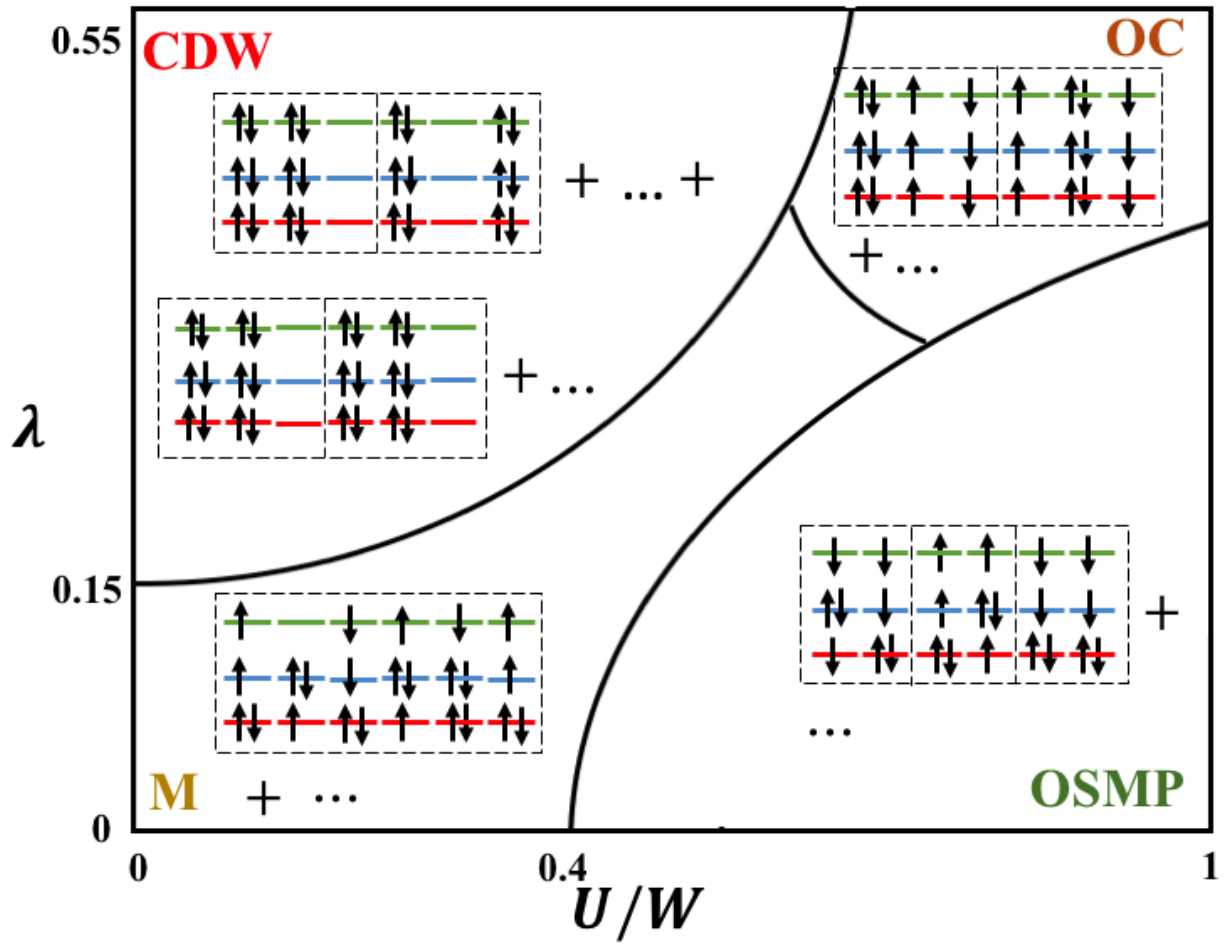
Figure 5.7: (color online) A sketch of the λ-U phase diagram for the model as inferred from DQMC calculations. Four distinct regions are found, which include states with metallic (M) characteristics, an orbital-selective Mott region (OSMP), a charge-density-wave (CDW) order, and a region with strong orbital correlations (OC) and insulating characteristics. The level diagrams sketch the dominant electronic configurations in each region. Here, W denotes the electronic bandwidth.
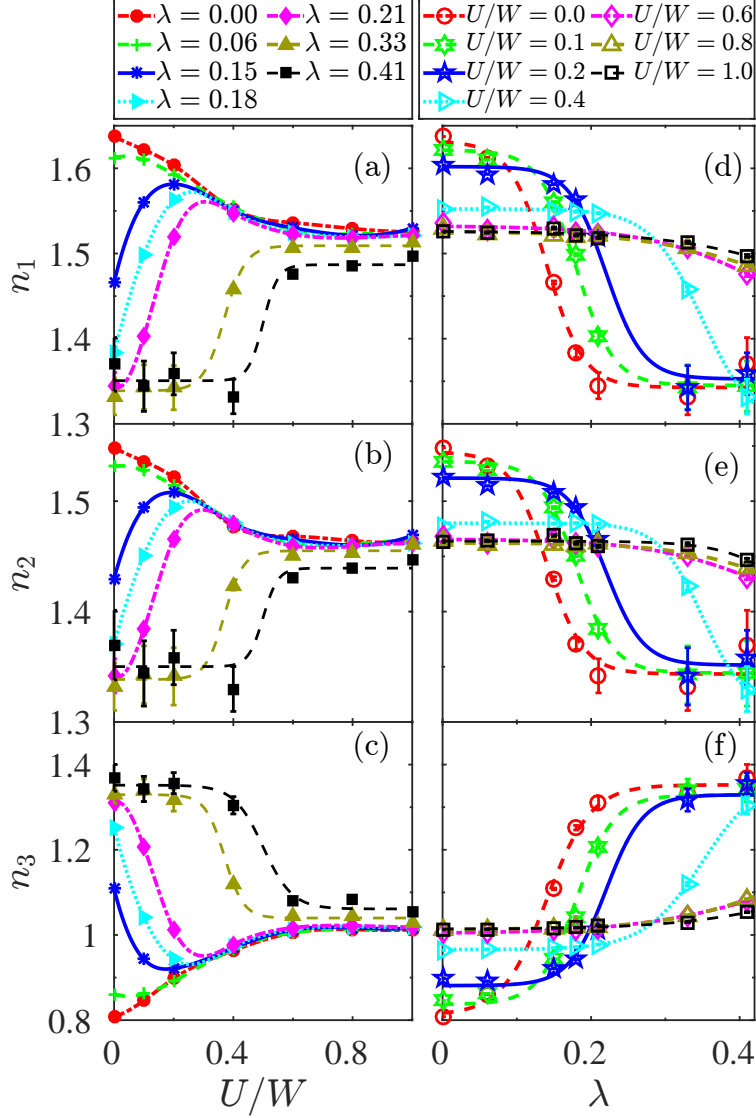
Figure 5.8: (color online) The variation of electronic densities on the three orbitals as a function of the Hubbard U and the e-ph coupling strength λ. Panels (a) - (c) show the variation of electronic densities as a function of the Hubbard U on orbitals $\gamma = 1, 2$, and 3, respectively. Similarly, panels (d) - (f) show the change of electronic densities as a function of λ on the same three orbitals. In each panel, error bars smaller than the marker size have been suppressed for clarity, and a smoothing spline used as a guide to the eye.

a negative effective U for all three orbitals at this site in the large-Ω limit. For an empty site, the effective interaction is not modified by the e-ph coupling. Therefore, the effective Hubbard interaction is not uniform in real space if there is a density modulation. When the e-ph coupling is strong, this nonuniform attractive interaction can produce a charge-ordered state but with a uniform average occupation on each orbital. The transition from a CDW phase to an OSMP can be seen in Fig. 5.8(c), where $\hat{n}_3$ decreases from $\frac{4}{3}$ to 1 at $\lambda = 0.33$. Increasing the e-ph coupling pushes this transition to larger values of U/W; for example, for $\lambda = 0.41$ it occurs at $U/W \sim 0.5$.

The competition between the CDW and OSMP tendencies is also manifest in the behavior of each orbital's double occupation $D_\gamma = \langle \hat{n}_{\gamma,\uparrow} \hat{n}_{\gamma,\downarrow} \rangle - \langle \hat{n}_{\gamma,\uparrow} \rangle \langle \hat{n}_{\gamma,\downarrow} \rangle$, as summarized in Fig. 5.9. When the phonon-mediated effective attraction overcomes the Coulomb repulsion, I expect $D_\gamma > 0$; otherwise, $D_\gamma < 0$. Figures 5.9(a)-5.9(c) present D_γ as a function of U/W for fixed values of λ, where I find that D_γ decreases as U is increased, and D_3 converges to $-\frac{1}{4}$ in the limit of a strong Hubbard interaction, consistent with a Mott insulating state where double occupation is suppressed. Figs. 5.9(d)-5.9(f) alternatively plot the data as a function of λ for fixed values of U/W. Here, I find that for $U/W < 0.4$, D_γ increases as λ increases and converges to $\frac{2}{9}$ on each orbital. This value is consistent with the double occupations expected for the CDW phase shown in Fig. 5.7.

The electronic density and double occupations provide indirect evidence of the CDW phase. To obtain more direct evidence of a CDW order, I calculated the charge susceptibility

$$\chi^c_{\gamma,\gamma'}(q) = \frac{1}{N} \int_0^\beta d\tau \langle \hat{n}_{q,\gamma}(\tau) \hat{n}_{q,\gamma'}(0) \rangle, \tag{5.5}$$

where q is the momentum, τ is the imaginary time, $\hat{n}_{q,\gamma} = \sum_{i,\sigma} e^{iqr_i} \hat{n}_{i,\gamma,\sigma}$, and r_i is the lattice vector.

Figure 5.10 shows the momentum dependence of the three intraorbital charge susceptibilities for $U/W = 0$ and different e-ph coupling strengths. At weak coupling (*i.e.* $\lambda = 0.0$ and $\lambda = 0.06$), $\chi^c_{\gamma,\gamma}(q)$ is small, with no clear peak at any momenta. This observation implies that a finite value of λ is needed for charge correlations to develop at this temperature, and is consistent with the one-dimensional Holstein model [90]. As the value of λ is increased, a clear
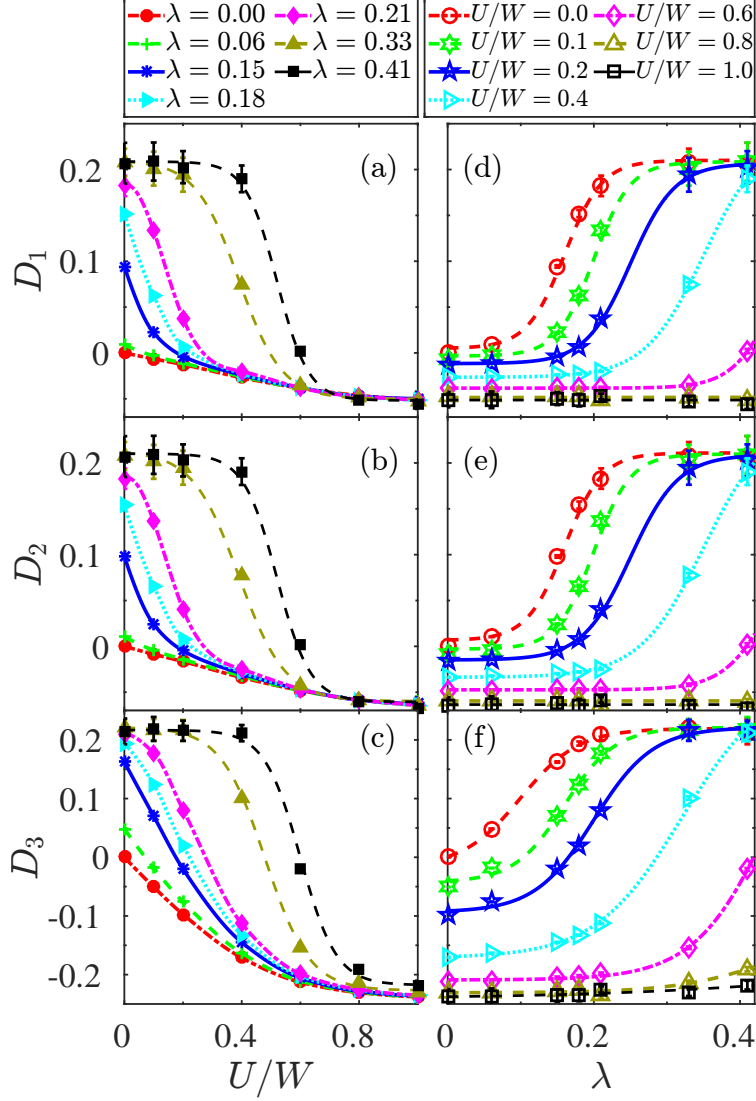
Figure 5.9: (color online) The variation of double occupancies on the three orbitals as a function of the Hubbard U and the e-ph coupling strengths λ. Panel (a) - (c) shows the variation of double occupancies as a function of the Hubbard U on orbitals $\gamma = 1, 2$, and 3, respectively. Similarly, panels (d) - (f) show the change of double occupancies as a function of λ on the same three orbitals. In each panel, error bars smaller than the marker size have been suppressed for clarity, and a smoothing spline is used as a guide to the eye.
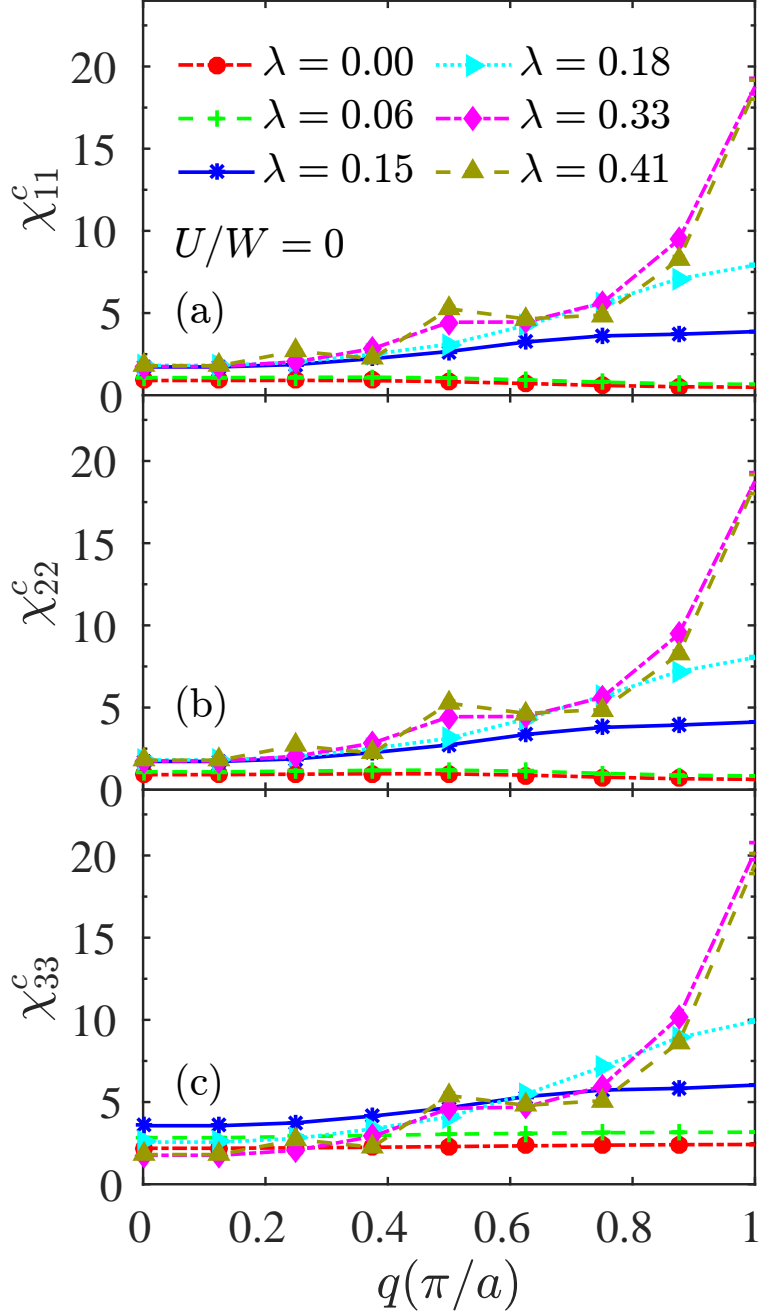
Figure 5.10: (color online) Momentum dependence of the charge correlation function $\chi^c_{\gamma,\gamma}(k)$ for orbtial 1 (a), orbital 2 (b), and orbital 3 (c) at different λ values. The Hubbard $U/W = 0$. In each panel, error bars smaller than the marker size have been suppressed for clarity.

peak structure forms in $\chi^c_{\gamma\gamma}(q)$. For instance, already at $\lambda = 0.18$ I find a peak centered at $q = \pi/a$ for all three orbitals, indicating the formation of a two-sublattice charge correlation at this simulation temperature ($\beta = 14.7/W$). Upon further cooling of the system, I find that additional charge correlations develop at a second q point. For example, Fig. 5.11 compares $\chi^c_{\gamma,\gamma}(q)$ at $\beta = 14.7/W$ and $\beta = 49/W$ for the $\lambda = 0.15$ and $U/W = 0$ case. For temperature $\beta = 14.7/W$, $\chi^c_{\gamma,\gamma}(q)$ has a single peak at $q = \pi/a$; however, as the temperature is decreased to $\beta = 49/W$, $\chi^c_{\gamma,\gamma}(q)$ increases and a second peak forms $q \sim 2\pi/3 - 3\pi/4$, which is evident as a shoulder in $\chi^c_{\gamma,\gamma}(q)$. To better recognize these two peaks, I plot as a guide-to-the-eye the sum of two Lorentzian functions centered at $q = 2\pi/3a$ (dash-dotted line) and $q = \pi/a$ (dotted line).

The two peak structures in $\chi^c_{\gamma,\gamma}(q)$ likely reflect different ordering tendencies. The charge configurations sketched in Fig. 5.7 are consistent with $q_1 \approx 2\pi/3a$ and $q_2 = \pi/a$ orderings. I propose, therefore, that the CDW state is characterized by a superposition of $|\ldots 660660\ldots\rangle$ and $|\ldots 606660\rangle$ configurations along the chain, where the number indicates the number of carriers on each site. These charge configurations are also consistent with the values of the orbitally-resolved single and double occupancies discussed previously. In fact, these two peaks reflect two different values of $2k_F$ that appear in this multiorbital model; The Fermi momentum for orbitals 1 and 2 is $\sim 0.33\pi/a$, while the Fermi momentum for orbital 3 is $\sim 0.5\pi/a$. Thus, these two peak values correspond to $q = 2k_F$ in the weak-coupling limit, where the CDW tendencies are driven primarily by nesting conditions. When I increase the e-ph coupling further, the k_F for orbitals 1 and 2 increases to $0.5\pi/a$. Therefore, I expect that only one peak will be observed in the charge-denstiy-wave susceptibility in the limit of strong e-ph coupling.

I now turn to the spectral weight of the three orbitals in the vicinity of the Fermi level $E_{\rm F}$ to assess whether the various phases I observe are insulating or not. The spectral weight can be estimated directly from the imaginary-time Green's function using the relationship [248]

$$\beta G_\gamma(r = 0, \beta/2) = \beta \sum_k \int d\omega \ \text{sech}(\beta\omega/2) A_\gamma(k, \omega), \qquad (5.6)$$
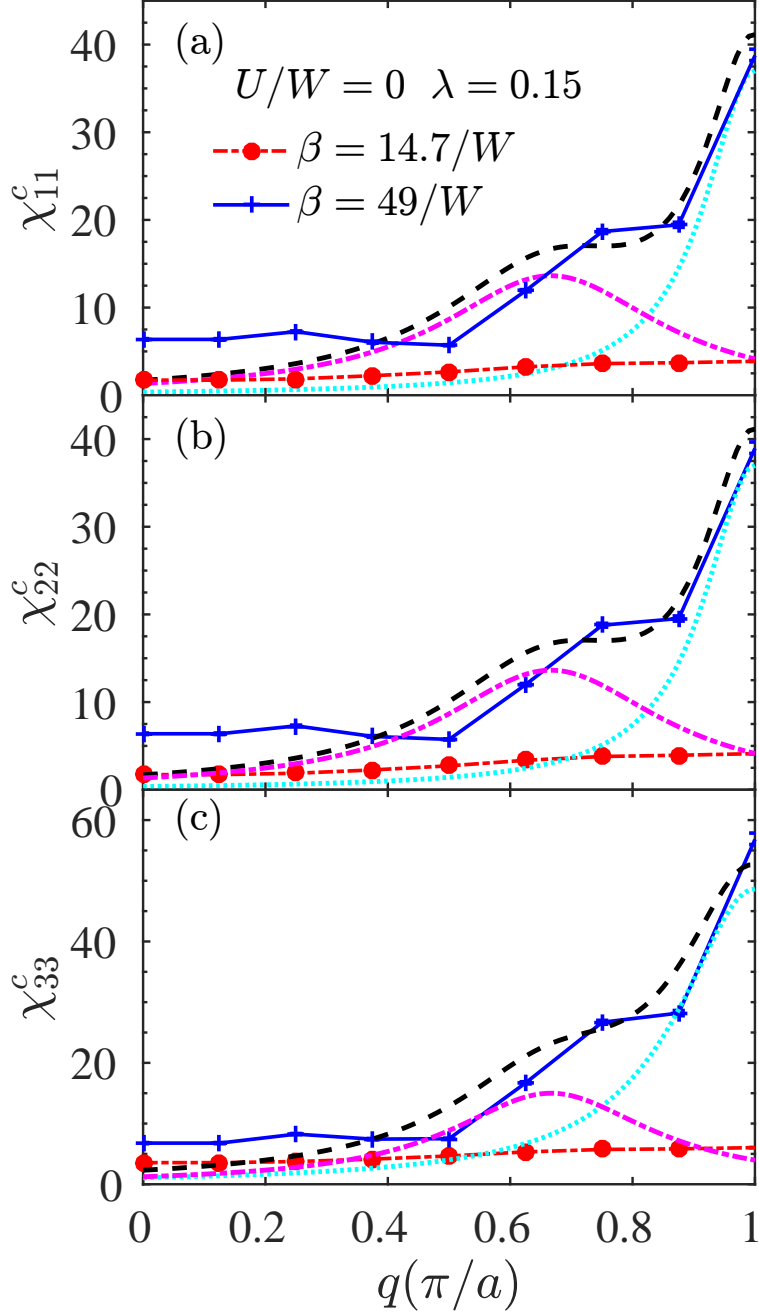
Figure 5.11: (color online) Momentum dependence of the charge correlation function $\chi^c_{\gamma,\gamma}(q)$ for orbtial 1 (a), orbital 2 (b), and orbital 3 (c) at different β values. The Hubbard $U/W = 0$ and $\lambda = 0.15$. The black dashed lines are eye-guided lines for a combination of two Lorentzian functions with different peak positions. The two Lorentzian functions are shown with dotted and dash-dotted lines, respectively. In each panel, error bars smaller than the marker size have been suppressed for clarity.

where $A_\gamma(k, \omega)$ is the orbitally resolved spectral function. At low temperature, the function $\beta \text{sech}(\beta\omega/2)$ is sharply peaked around $\omega = E_\text{F} = 0$ and thus provides a measure of the spectral weight integrated within a window of a few β^{-1} of E_F.

Figure 5.12 plots $\beta G_\gamma(r = 0, \beta/2)$ for the three orbitals for different values of U/W and λ. In Figs. 5.12(a)-5.12(c), the spectral weight of each orbital is plotted as a function of U for fixed λ. In the absence of the e-ph interaction ($\lambda = 0$), the spectral weight of all three orbitals decreases as the Hubbard U is increased. However, the spectral weight on orbital $\gamma = 3$ decreases much more rapidly than the other two orbitals, consistent with the formation of an OSMP [148]. [The small but nonzero value of $\beta G_3(r = 0, \beta/2)$ is due to the elevated temperature of the simulation.] As the value of λ increases, I begin to see the loss of spectral weight in all three orbitals when U/W is small.

Fig. 5.12(d)-5.12(f) plot $\beta G_\gamma(r = 0, \beta/2)$ as a function of λ for fixed U/W. For $U/W = 0$, the spectral weight of all three orbitals is suppressed as the e-ph coupling is increased. I further observe a sudden decrease in the spectral weight of all three orbitals for $\lambda \geq 0.15$, where a prominent peak in $\chi^c_{\gamma,\gamma}(k)$ is observed. Thus, for $\lambda \geq 0.15$ and $U/W = 0$, the system is an insulating state driven by CDW correlations. The behavior of the spectral weight is qualitatively similar for $U/W < 0.2$, however the transition to the CDW phase occurs at larger values of λ as U/W increases. Based on these results, I conclude that the CDW phase appearing at large λ is insulating.

Unlike the OSMP, I do not find any orbital-selective behavior associated with the formation of the CDW phase; the rate at which the spectral weight approaches zero appears to be the same for all three orbitals at this temperature. This result is in contrast to the degenerate two-orbital case with inequivalent bandwidths [149], where orbital-selective CDW behavior was found. This difference could be attributed to changes in the total bandwidth, dimensionality, or model. (For example, the current model has inequivalent bandwidths and crystal-field splittings while the former only had inequivalent bandwidths.) Further studies will be needed to better understand the differences between these two cases.

I now return to the competition between the OSMP and CDW phases. Figures 5.12(a)-(c) reveal that the spectral weight decreases as the strength of the e-ph is increased when U/W is small. For a fixed value of $\lambda \neq 0$, $\beta G_\gamma(r = 0, \beta/2)$ initially increases with U/W,
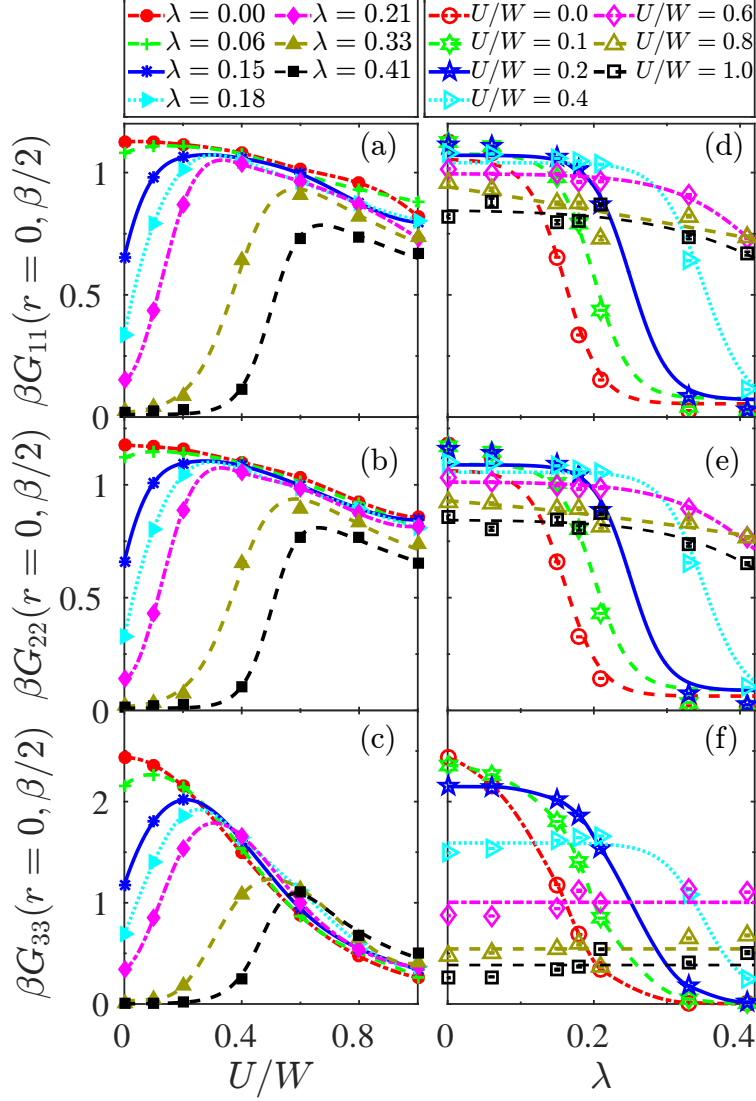
Figure 5.12: (color online) The variation of the spectral weights for the three orbitals as a function of the Hubbard U and the e-ph coupling strength λ. Panels (a) - (c) show the variation of spectral weights as a function of the Hubbard U for three orbitals, respectively. Panels (d) - (f) show the change of spectral weights as a function of λ for three orbitals, respectively. In each panel, error bars smaller than the marker size have been suppressed for clarity, and a smoothing spline is used as a guideline to the eye.

before reaching a maximum value and decreases along the U axis. This behavior reflects the competition between the e-ph and the e-e interactions. At small U/W the CDW correlations dominate, for large U/W the OSMP correlations dominate, and for intermediate values of λ a metallic phase is realized.

5.2.2   Spectral properties of the CDW phase

The spectral function of the OSMP was studied in detail in chapter 4 in the absence of e-ph interactions. I will focus, therefore, on the spectral function of the CDW phase. Figure 5.13 shows the spectral function for $U = 0$ and $\lambda = 0.33$ and the orbitally-resolved components. The system is insulating, with a large CDW gap and broadened spectral features, consistent with the spectral weight analysis. The upper bands of three orbitals have dispersions with a clear folded shape, while the lower bands of orbitals 1 and 2 have a more cosine-like dispersion. This cosinelike shape arises from the combination of an incoherent peak and an additional peak arising from thermally activated transitions to states with additional phonons excited [99]. To better recognize these two peaks, Figs. 5.13(e) - 5.13(l) plot the spectral functions at fixed momentum $k = 0$, π/a, $\pi/4a$, and $3\pi/4a$ for orbitals 1 and 2. The red dashed curve denotes Lorentzian fits of the data allowing for an incoherent peak above and below the Fermi level and an additional thermally excited peak below the Fermi level. The fitting results are consistent with the Maxent results. I find that the thermally excited state is located around $E = -2.5$ eV and is momentum independent, consistent with previous results for the one-dimensional single-band spinless Holstein model [99]. The folded band is observed at $k = 0$ and $k = \pi/a$ and at $k = \pi/4a$ and $k = 3\pi/4a$, respectively. The intensity of the incoherent peak below the Fermi level in the folded band is much weaker than that of the thermally excited peak, leading to a cosine shape observed in the upper panels of Fig. 5.13.

5.2.3   Strong electron-phonon coupling

The previous single-site DMFT study of the two-orbital HH model at a half-filling observed a direct transition between the OSMP and CDW phase in the strong e-ph coupling limit [149], with no intervening metallic phase. In contrast, for the current model, I find evidence for an
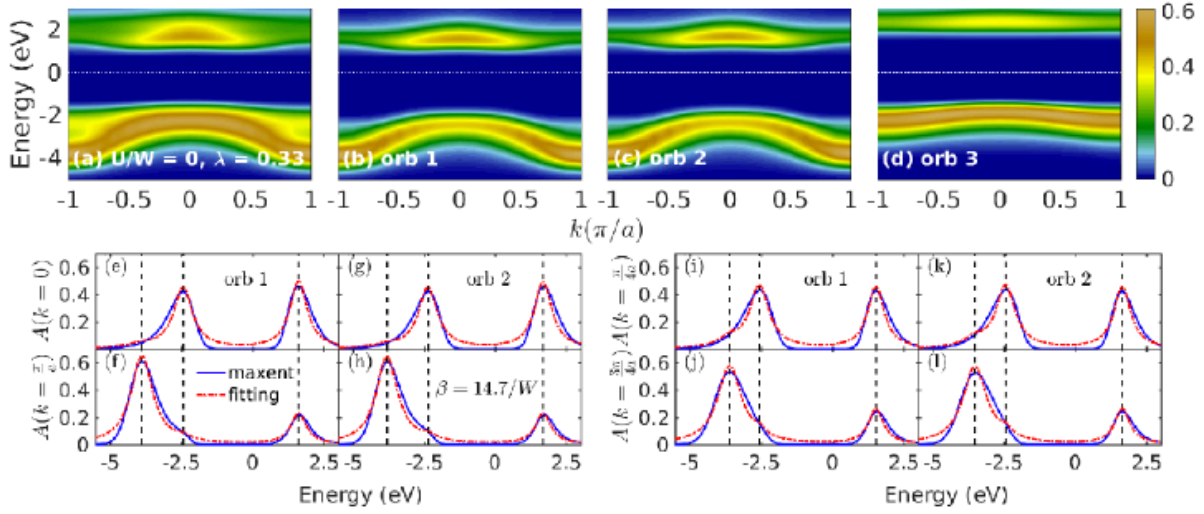
Figure 5.13: (color online) Spectral functions for $U = 0$ and $\lambda = 0.33$. Panels (b),(c), and (d) are the orbital 1, 2, and 3 components of the spectral function in (a), respectively. Panels (e), (f), (i), and (j) are spectral functions of the orbital 1 at momentum $k = 0$, $k = \frac{\pi}{a}$, $k = \frac{\pi}{4a}$, and $\frac{3\pi}{4a}$, respectively. Similarly, (g), (h), (k), and (l) are spectral functions of the orbital 2 at those four momenta. The black dashed lines show three peaks positions in the maximum entropy results. The red dotted lines are Lorentzian fitting results.

orbitally correlated insulating state located between the CDW phase and OSMP at strong couplings. Figure 5.14 shows the spectral function [Fig. 5.14(a)] and its three orbitally resolved components [Figs. 5.14(b) - 5.14(d)] at $U/W = 1$, $\lambda = 0.6$, and $\beta = 29.4/W$, where a gap is clearly observed. The spectral function is similar to the CDW case shown in Fig. 5.14, however, the origin of the gap is not CDW correlations since $\chi^c_{\gamma,\gamma'}(q)$ (not shown) is small in this state. Also, the double occupation $D_\gamma \approx -\frac{1}{9} < 0$ (see Fig. 2), indicating the Coulomb interaction is the dominant interaction in this phase.

The nature of this OC phase sketched on the left side of Fig. 5.15. It consists of one site where all three orbitals are fully occupied and two neighboring sites that are half-filled and in a high-spin state. This electronic configuration is consistent with the observed occupations and the value of the double occupation $D_\gamma = -\frac{1}{9}$.

In the HH model, the intra- and interorbital Hubbard interactions U_{eff} and U'_{eff} are renormalized by the e-ph interaction, and the ground state can change based on the value of these effective Hubbard interactions. Figures 5.15(a) and 5.15(b) show two types of charge fluctuations that are possible within the proposed OC state The potential energy costs of these fluctuations are $PE \sim U_{\text{eff}} + J$ and $PE \sim -2(U'_{\text{eff}} - J)$, respectively. To estimate the magnitude of these energies, I performed an exact diagonalization calculation in the atomic limit and compared the ground state energies of the shown atomic configurations. For $U/W = 1$ and $\lambda = 0.6$, I find that these two potential energies are 1.305 eV and 0.815 eV, respectively. When the orbital hybridization is introduced, the total potential energy cost is compensated for by a kinetic energy gain of $KE \approx t_{11} = 0.5$ eV. However, the ratio $\frac{PE}{KE} > 1$ in both cases, suggesting that charge fluctuations are suppressed, and the system will be insulating. The conditions for forming the OC insulating state are then $U'_{\text{eff}} - J < 0$ and $U_{\text{eff}} + J > 0$, which in turn requires that the e-ph coupling strength is not too strong; otherwise, the CDW phase is formed. (Note that a larger Hund's coupling favors satisfying these two conditions.) In the OC insulating state, the fully occupied site and two half-occupied sites can be arranged randomly in a long chain as the energy cost will not change. Therefore, short-range orbital correlations would be sufficient to produce insulating behavior at finite temperature.
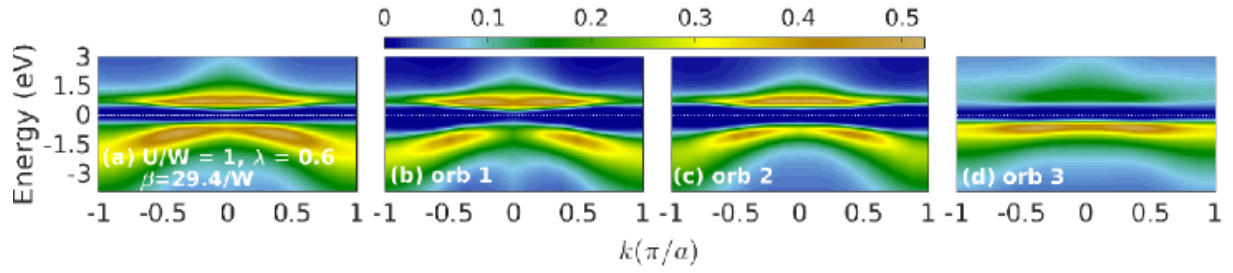
Figure 5.14: (color online) Spectral functions for $U/W = 1$ and $\lambda = 0.6$. Panels (b), (c), and (d) are the orbitals 1, 2, and 3 components of the spectral function in (a). The inverse temperature is $\beta = 29.4/W$. The white dot line is the Fermi surface.
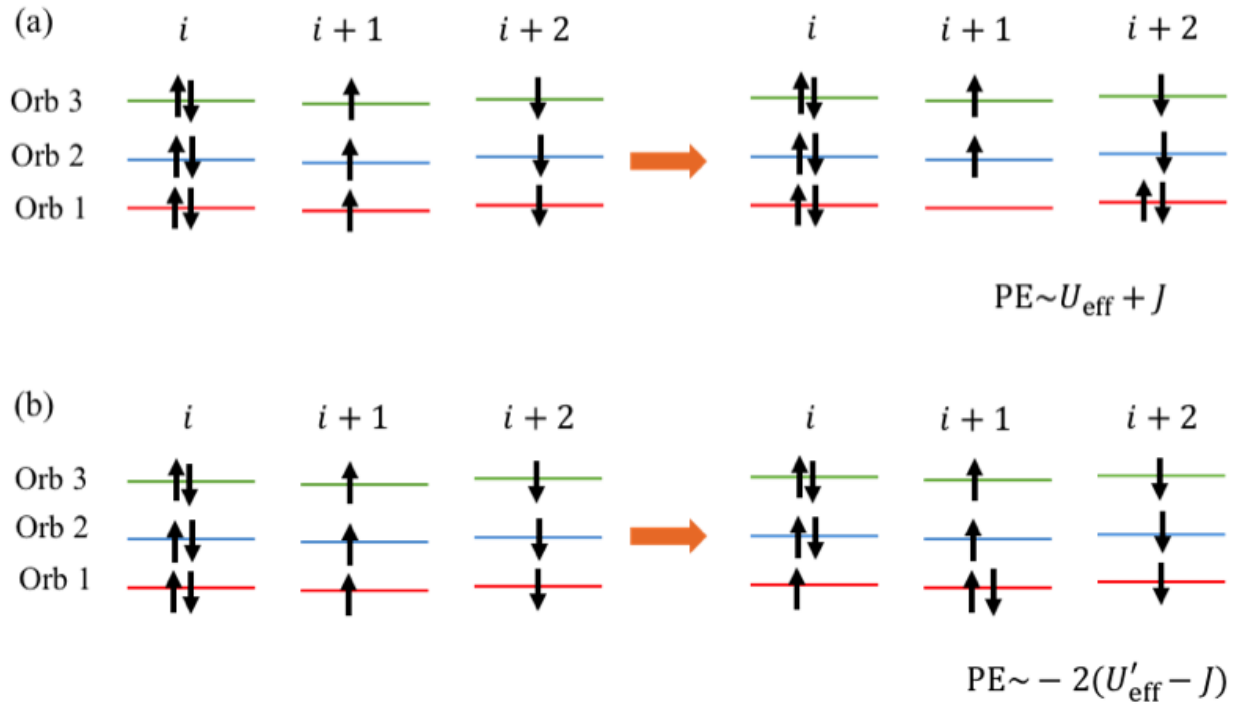
Figure 5.15: (color online) Cartoon sketch of the relevant charge fluctuation processes leading to the orbital ordered insulating state when $U/W = 1$ and $\lambda = 0.6$.

I can confirm the presence of OC by examining the equaltime orbital correlation function

$$T_{\gamma\gamma'}(d) = \frac{1}{N} \sum_i \langle (\hat{n}_{i+d,\gamma} - \hat{n}_{i+d,\gamma'})(\hat{n}_{i,\gamma} - \hat{n}_{i,\gamma'}) \rangle. \tag{5.7}$$

The charge configuration expected for the OC shown in Fig. 5.15 would produce an orbital correlation function $T'_{\gamma\gamma}(d) = 0$. Figure 5.16 (b) shows the variation of the on-site orbital correlations $T_{\gamma,\gamma'}(0)$ in the phase transition from the OSMP to the OC state. In general, the correlation function for $d = 0$ is larger than that for $d \neq 0$. Thus, the on-site correlation is a good indicator for when $T_{\gamma\gamma'}(d) \to 0$ and can be used to trace the forming of the orbital correlations. In the OSMP region, $T_{\gamma,\gamma'}(0)$ is greater than 0.1. For example, at $\lambda = 0$, $T_{1,2}(0)$, $T_{1,3}(0)$, and $T_{2,3}(0)$ are 0.16, 0.14, and 0.125, respectively. $T_{\gamma,\gamma'}(0)$ decreases slowly initial as the e-ph coupling strength is enhanced. Conversely, near the phase transition, $T_{\gamma,\gamma'}(0)$ decreases very quickly; at $\lambda = 0.6$, $T_{1,2}(0)$, $T_{1,3}(0)$, and $T_{2,3}(0)$ are 0.056, 0.061, and 0.057, respectively. The nonzero value at $\lambda = 0.6$ is likely due to the elevated temperature. I find that $T_{1,2}(0)$, $T_{1,3}(0)$, and $T_{2,3}(0)$ are decreased to 0.038, 0.03, and 0.029, respectively, as the inverse temperature is decreased to $29.4/W$. I expect that the correlation function tends towards zero as $T \to 0$, and a sharp phase transition from the OSMP to the OC state would occur.

I traced the phase transition from the OSMP to the OC in figure 5.16 (a), which shows the variation of orbital occupations in the phase transition from the OSMP to the OC phase at $U/W = 1$ and $\beta = 14.7/W$. Here, the chain size is $N = 12$. The critical e-ph coupling value λ_c of the phase transition from the Mott phase to the OC state is about 0.43, where $n_3 > 1$. As $U/W = 1$ and $\lambda = 0.6$, orbital occupations for three orbitals are 1.4, 1.38, and 1.22 at $\beta = 14.7/W$, respectively. Those occupations are changed to 1.346, 1.344, 1.31 at $\beta = 29.4/W$, implying the OC state supports the same occupation on each orbital, consistent with the electron configuration shown in Fig. 5.15.

5.2.4 Phase diagram

I have performed a study of a three-orbital Hubbard-Holstein model on an extended one-dimensional chain using non-perturbative DQMC. The phase diagram of the one-dimensional
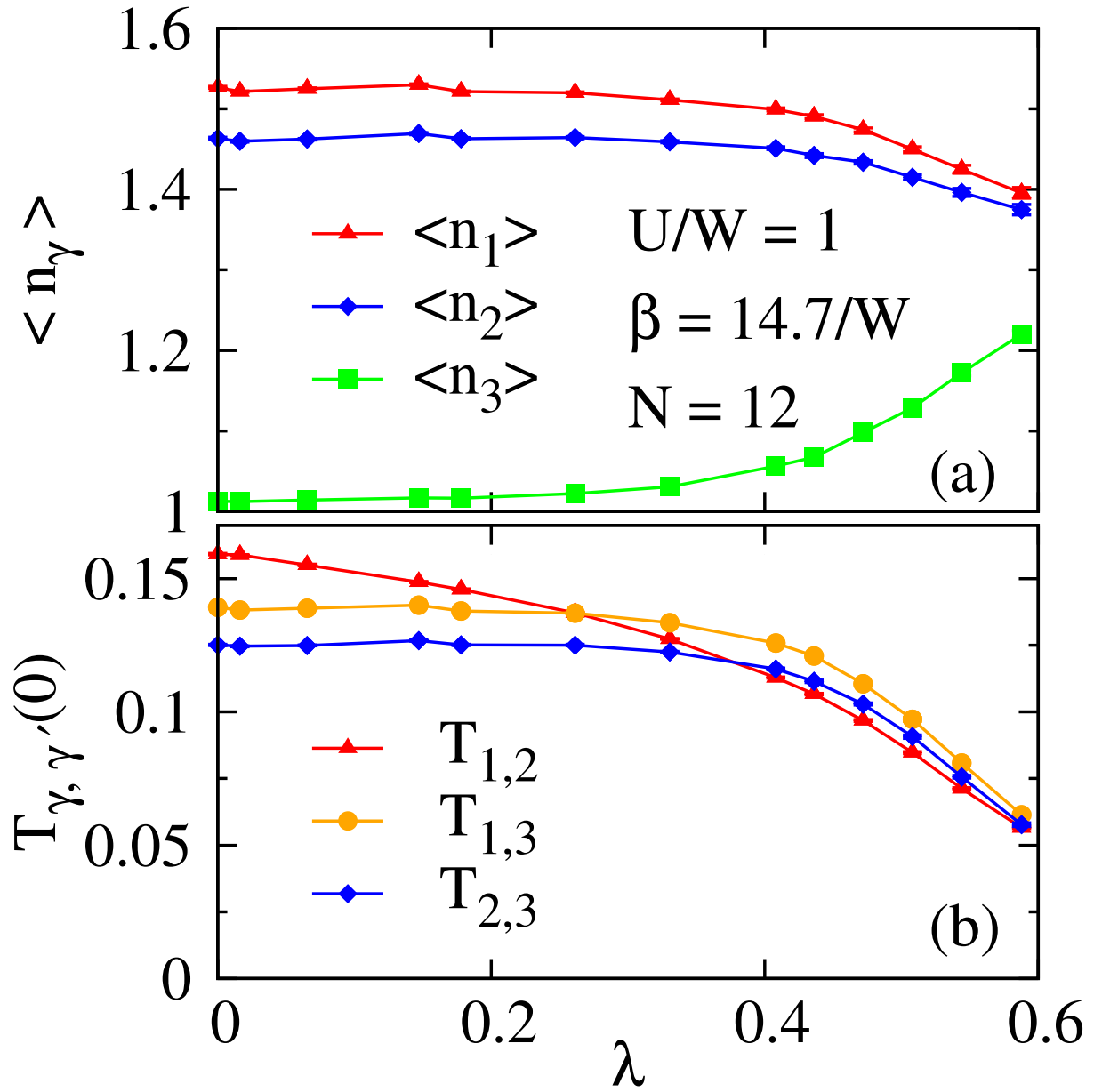
Figure 5.16: (color online) (a) The electronic occupations $\langle \hat{n}_\gamma \rangle$ of orbital γ as a function of the e-ph coupling strength λ. (b) The on-site orbital correlations $T_{\gamma\gamma'}$ between orbital γ and γ' as a function of λ. These results were obtained on an $N = 12$ site chain. In each panel, error bars smaller than the marker size have been suppressed for clarity.

model for $\beta = 14.7/W$ and $n = 4$, shown in Fig. 5.17, shares many similarities to the one found for an infinite-dimensional degenerate two-orbital HH model with inequivalent bandwidths [149], containing a metallic phase (M), a CDW phase, and an OSMP. The metallic phase is most prominent in small values of U and λ but penetrates into the region of intermediate interaction strengths separating the CDW and OSMP when $U/W \sim 2\lambda$. The critical e-ph coupling needed for the CDW phase transition at $U = 0$ in the model is $\lambda_c \sim 0.15$. The nonzero value of λ_c is consistent with results for the single band Holstein model [96, 90].

At strong couplings, I found evidence for an orbital correlation state in the phase diagram, which was not found in the previous DMFT study. I argue that this difference stems from the filling used in the model ($\langle \hat{n} \rangle = \frac{4}{3}$ here versus $\langle \hat{n} \rangle = 1$ in Ref. [149]) and the use of an extended cluster here [148]. The OC state resides between the CDW phase and OSMP and tends to extend to large Hubbard U. This region of the phase diagram is the same one where the OSMP disappears, and an anti-ferro-orbital correlation was found in the $\lambda = 0$ case [148]. I expect that a phase transition occurs between the anti-ferro-orbital order and the OC state at $U/W = 2$. These results show that the phase diagram of multiorbital HH models can exhibit remarkably rich physics as a function of interaction strengths, doping, and other parameters.

5.3   Summary

I have studied the interplay between the e-e and e-ph interactions in three- and two-orbital Hubbard-Holstein model in one- and infinite-dimension, respectively. In both cases, I find a competition between the onsite e-e and e-ph interactions leads to many competing phases. In the 1D case, the competition occurs between the OSMP and CDW at small coupling, while this competition occurs between the OSMP and OSPI in the infinite-dimension. I also find that the Hund's coupling J has nontrivial effects on the phases driven by the e-ph interactions. Importantly, these results demonstrate that weak to intermediate e-ph interaction strengths can have a significant impact on the phase diagram of this model. As
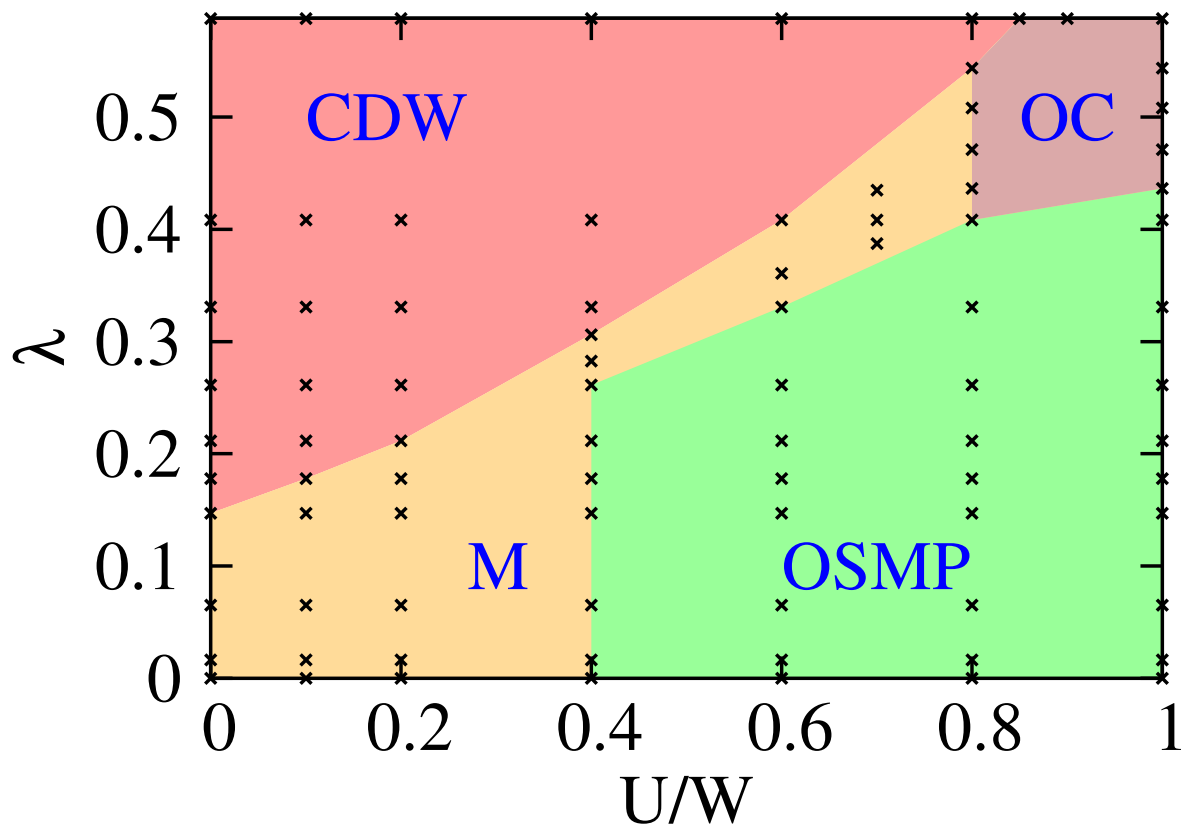
Figure 5.17: (color online) The phase diagram of the three-orbital Hubbard-Holstein model for $\beta = 14.7/W$ and $\hat{n} = 4$. The different phases are labeled as follows: metal (M), charge-density-wave order (CDW), orbital selective Mott phase (OSMP), and orbital correlation(OC).

such, one cannot rule out an important role for phonons *a priori* in multi-orbital systems, when multiple electronic interactions are already competing with one another.

In the past, the e-ph interaction has not been widely studied in the FeSCs in that an early *ab initio* calculation shows this interaction strength λ in the FeSCs is too small and only about 0.21 [26]. However, I find the electronic intrinsic characteristics could have a significant change under such a small e-ph coupling in both my one- and infinite-dimension models. These results suggest that one needs to be cautious of the e-ph interaction when studying FeSCs.

I close with a short note and some speculation. Ref. [241] has also used the term OSPI in the context of a two-orbital dimer model, where superexchange is stronger between a particular subset of orbitals, creating a preferential dimerization. An entirely different mechanism drives the OSPI, where I start from a metallic state and obtain the OSPI through the e-ph interaction. To the best of my the knowledge, this is the first time that theoretical calculations have produced such a mechanism. As with OSMP, the OSPI, in this case, is induced by the different bandwidths for the two orbitals. Finally, although the OSPI discovered here was derived from a Holstein coupling, I believe bond-stretching phonons that modulate interatomic hopping integrals could induce a similar phenomenon. In such cases, these interactions could have a significant impact on nematic phases observed in some FeSCs [244, 42].

Chapter 6

Three-orbital Su-Schrieffer-Heeger model in two dimensions

6.1 Introduction

Model Hamiltonians have played a vital role in shaping our understanding of e-ph interactions in materials. These models can be broadly divided into two categories based on whether the e-ph coupling is diagonal or off-diagonal in the orbital space. Diagonal e-ph interactions (*e.g.*, in the Holstein [100] or Fröhlich [75] models) couple the atomic displacements directly to the charge density at each site, modulating the carrier's potential energy. Conversely, off-diagonal e-ph couplings (*e.g.*, the Su-Schrieffer-Heeger [SSH] [242] model in one-dimension) occurs when the atomic motion modulates the overlap integrals between neighboring atoms, generating off-diagonal terms in orbital space.

Diagonal e-ph interactions have received the most attention to date and many techniques have been employed to study their properties [227, 163, 14, 15, 196, 188, 149, 19]. In the strong coupling limit, these interactions produce polaronic quasiparticles with large effective masses m^* [27, 129, 88, 221, 150], which are prone to forming insulating charge-density-wave phases [37, 27, 210, 19]. Far fewer studies have been carried out for off-diagonal interactions, and most of these have been restricted to one-dimension (1D) using either approximate [242, 146, 171, 239] or quantum Monte Carlo methods [234, 97, 46]. Few studies of SSH-type

models in two-dimensions (2D) exist [223, 254, 292, 145], and many of these employ the frozen phonon approximation [223, 145].

The lack of studies addressing off-diagonal e-ph interactions represents a significant gap in the communities' knowledge. These interactions are believed to be the dominant e-ph interactions in many materials, including the organic charge-transfer solids [242, 146, 45] and many perovskites systems like the rare-earth nickelates [176, 236, 112], and the high T_c superconducting cuprates [136, 263] and bismuthates [122]. More importantly, recent studies in the single- and two-particle limit have shown that the physics of off-diagonal e-ph interactions differs substantially from that of the more commonly studied diagonal one. For example, strong off-diagonal interactions can produce highly mobile polarons with light effective masses [239], generate robust phonon-mediated pairing, and even stabilize and control the location of a type-II Dirac point [186]. It is, therefore, imperative to study the off-diagonal e-ph interactions in higher dimensions and for arbitrary fillings, as one's intuition gained from the standard diagonal models may not serve us well.

In this chapter, I present a combined exact diagonalization (ED) and determinant quantum Monte Carlo (DQMC) study of a two-dimensional, multi-orbital sp-model defined on the Lieb lattice (see Fig. 6.1) with off-diagonal SSH-type e-ph interactions. My approach treats the problem in a numerically exact manner and does not suffer from a Fermion sign problem in the absence of a Hubbard interaction. Here, I focus on the so-called "negative charge transfer" regime [73, 207, 122], where the holes preferentially occupy the oxygen sublattice. This choice is motivated by the fact that this parameter regime is believed to be relevant to several perovskite systems with off-diagonal e-ph coupling, including the high-T_c superconducting bismuthates $Ba_{1-x}K_xBiO_3$ [73, 207] and the rare-earth nickelates $RNiO_3$ [112, 200, 23]. Since I neglect the Hubbard interaction, my model can be viewed as a 2D analog of the model describing the bismuthates. At half-filling, corresponding to one hole per unit cell, I find that the system is an insulator with a distorted structure, where the ligand O atoms (the p orbitals) have collapsed and expanded about alternating Bi (the s orbitals) sites. Upon hole doping, the insulating phase is suppressed giving way to a metallic phase characterized by holes that are locally bound to fluctuating local structural distortions. My results provide strong support for the polaronic view often adopted when describing

the bismuthates [73, 207], as well as the one recently proposed for the related rare-earth nickelates [236]. Finally, at low temperatures, I find s-wave superconducting tendencies that form primarily on the oxygen sublattice.

6.2 Model Hamiltonian

I study a three-orbital model defined on a Lieb lattice, as shown in Fig. 6.1(a). The orbital basis consists of a Bi $6s$ atom (red circle) and two O $2p$ orbitals (blue lobes) situated halfway between each of the Bi atoms. In what follows, I freeze the heavier Bi atoms into place and restrict lighter O atoms to move along the bond directions. The full Hamiltonian is $H = H_0 + H_{\text{lat}} + H_{\text{e−ph}}$, where

$$
\begin{aligned}
H_0 &= -t_{sp} \sum_{\langle \mathbf{r}, \delta \rangle, \sigma} \left(P_\delta s^\dagger_{\mathbf{r},\sigma} p_{\mathbf{r},\delta,\sigma} + h.c. \right) + t_{pp} \sum_{\langle \mathbf{r}, \delta, \delta' \rangle, \sigma} P_{\delta,\delta'} p^\dagger_{\mathbf{r},\delta,\sigma} p_{\mathbf{r},\delta',\sigma} + \\
&\quad \sum_{\mathbf{r},\sigma} \left[(\epsilon_s - \mu) \hat{n}^s_{\mathbf{r},\sigma} + (\epsilon_p - \mu)(\hat{n}^{p_x}_{\mathbf{r},\sigma} + \hat{n}^{p_y}_{\mathbf{r},\sigma}) \right], \\
H_{\text{lat}} &= \sum_{\mathbf{r}} \left(\frac{\hat{P}^2_{\mathbf{r},x}}{2M} + K\hat{X}^2_{\mathbf{r}} + \frac{\hat{P}^2_{\mathbf{r},y}}{2M} + K\hat{Y}^2_{\mathbf{r}} \right) \\
H_{\text{e−ph}} &= \alpha t_{sp} \sum_{\langle \mathbf{r}, \delta \rangle, \sigma} \left(\hat{u}_{\mathbf{r},\delta} s^\dagger_{\mathbf{r},\sigma} p_{\mathbf{r},\delta,\sigma} + h.c. \right).
\end{aligned}
$$

Here, $\langle \dots \rangle$ denotes a sum over nearest neighbor atoms, $\delta, \delta' = \pm x, \pm y$ index the oxygen atoms surrounding the Bi sites and the operators $s^\dagger_{\mathbf{r},\sigma}$, and $(s_{\mathbf{r},\sigma})$ and $p^\dagger_{\mathbf{r},\delta,\sigma}$ $(p_{\mathbf{r},\delta,\sigma})$ are the creation (annihilation) operators for spin σ holes on the Bi $6s$ and O $2p_\delta$ orbitals, respectively. The unit cells are indexed by $\mathbf{r} = n_x\mathbf{a} + n_y\mathbf{b}$, where $(n_x, n_y) \in \mathbb{Z}$, $\mathbf{a} = (a, 0)$, $\mathbf{b} = (0, a)$ are the primitive lattice vectors along x- and y-directions, respectively, and a is the Bi-Bi bond length in the undistorted structure (and also the unit of length). To simplify the notation, I have introduced the shorthand notation $p_{\mathbf{r},-x,\sigma} = p_{\mathbf{r}-\mathbf{a},x,\sigma}$ and $p_{\mathbf{r},-y,\sigma} = p_{\mathbf{r}-\mathbf{b},y,\sigma}$. The operators $\hat{n}^s_{\mathbf{r},\sigma} = s^\dagger_{\mathbf{r},\sigma} s_{\mathbf{r},\sigma}$ and $\hat{n}^{p_\alpha}_{\mathbf{r},\sigma} = p^\dagger_{\mathbf{r},\alpha,\sigma} p_{\mathbf{r},\alpha,\sigma}$ are the number operators for s and p_α $(\alpha = x, y)$ orbitals, respectively; ϵ_s and ϵ_p are the onsite energies; μ is the chemical potential; t_{sp} and t_{pp} are the nearest neighbor Bi-O and O-O hopping integrals in the undistorted crystal; and α is the e-ph coupling constant. The phase factors are $P_{x(y)} = -P_{-x(-y)} = 1$, and
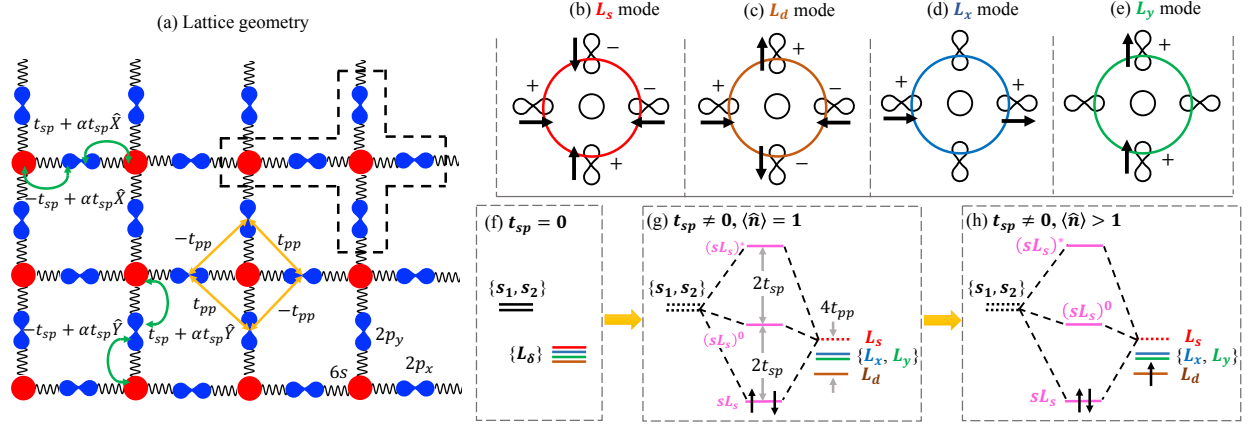
Figure 6.1: (a) The lattice structure of the three-orbital model. Panels (b) - (e) show four oxygen vibration modes and its related molecule orbitals. Panel (f) shows the energy of four oxygen molecule orbitals and Bi $6s$ orbital when there is no hybridization between $6s$ and $2p_{x(y)}$ orbitals. Panel (f) and (h) show the hole occupation on each orbital for $\langle \hat{n} \rangle = 1$ and $\langle \hat{n} \rangle > 1$, respectively, as $6s$ and $2p_{x(y)}$ orbitals are hybridized.

$P_{\pm x, \pm y} = P_{\pm y, \pm x} = -P_{\pm x, \mp y} = -P_{\mp y, \pm x} = 1$. The motion of the lattice is described by the atomic displacement (momentum) operators $\hat{X}_{\mathbf{r}, \alpha}$ ($\hat{P}_{\mathbf{r}, \alpha}$). M is the oxygen mass and K is the coefficient of elasticity between each Bi and O atom, and each O atom is linked by two springs to the neighboring Bi atoms. Thus, the bare phonon frequency is $\Omega = \sqrt{2K/M}$. Finally, the displacement of the O atoms modulate the hopping integral as $t_{sp}(1 + \alpha \hat{u}_{\mathbf{r}, \delta})$, where I have introduced shorthand for the displacement operators $\hat{u}_{\mathbf{r}, x} = \hat{X}_{\mathbf{r}}$, $\hat{u}_{\mathbf{r}, -x} = \hat{X}_{\mathbf{r} - \mathbf{a}}$, $\hat{u}_{\mathbf{r}, y} = \hat{Y}_{\mathbf{r}}$, and $\hat{u}_{\mathbf{r}, -y} = \hat{Y}_{\mathbf{r} - \mathbf{b}}$.

Throughout, I adopt parameters motivated by a recent DFT study of BaBiO$_3$ [122] with $t_{sp} = 2.08$, $t_{pp} = 0.056$, $\epsilon_s = 6.42$, and $\epsilon_p = 2.42$ (all in units of eV). As mentioned, these parameters place us in the negative charge transfer regime, where holes primarily reside on the O sublattice. For example, at half filling $\langle \hat{n} \rangle = 1$, I find $\langle \sum_{\alpha, \sigma} \hat{n}_{\mathbf{r}, \sigma}^{p_\alpha} \rangle = 0.685$ in the absence of the e-ph coupling. The oxygen holes reside in a molecular orbital defined by the A_{1g} combination of the the ligand oxygen orbitals surrounding the Bi atom (see below) [122]. Finally, I adopt the e-ph coupling strength $\alpha = 4a^{-1}$.

6.3   A molecular orbital viewpoint

Before I proceed to the DQMC simulations of the model, I present a simplified molecular orbital analysis of a Bi$_2$O$_4$ cluster, which provides a more transparent view of the physics. I first expand the simple square unit cell to allow for two distinct Bi $6s$ orbitals and four O $2p$ orbitals, as indicated by the black dashed frame in Fig. 6.1(a). This expanded cell defines the cluster after I apply periodic boundary conditions. The two Bi $6s$ orbitals as denoted as s_1 and s_2. Next, I transform the four ligand oxygen orbitals into a molecular orbital basis using

$$
\begin{aligned}
L_{\mathbf{r}, s, \sigma} &= \frac{1}{2}(p_{\mathbf{r}, x, \sigma} + p_{\mathbf{r}, y, \sigma} - p_{\mathbf{r}, -x, \sigma} - p_{\mathbf{r}, -y, \sigma}) \\
L_{\mathbf{r}, d, \sigma} &= \frac{1}{2}(p_{\mathbf{r}, x, \sigma} - p_{\mathbf{r}, y, \sigma} - p_{\mathbf{r}, -x, \sigma} + p_{\mathbf{r}, -y, \sigma}) \\
L_{\mathbf{r}, x, \sigma} &= \frac{1}{\sqrt{2}}(p_{\mathbf{r}, x, \sigma} + p_{\mathbf{r}, -x, \sigma}) \\
L_{\mathbf{r}, y, \sigma} &= \frac{1}{\sqrt{2}}(p_{\mathbf{r}, y, \sigma} + p_{\mathbf{r}, -y, \sigma}).
\end{aligned}
$$

Similarily, I can introduce new phonon operators

$$
\begin{aligned}
\hat{x}_{\mathbf{r},L_s} &= \frac{1}{2}(\hat{u}_{\mathbf{r},x} + \hat{u}_{\mathbf{r},y} - \hat{u}_{\mathbf{r},-x} - \hat{u}_{\mathbf{r},-y}) \\
\hat{x}_{\mathbf{r},L_d} &= \frac{1}{2}(\hat{u}_{\mathbf{r},x} + \hat{u}_{\mathbf{r},y} - \hat{u}_{\mathbf{r},-x} - \hat{u}_{\mathbf{r},-y}) \\
\hat{x}_{\mathbf{r},L_x} &= \frac{1}{\sqrt{2}}(\hat{u}_{\mathbf{r},x} + \hat{u}_{\mathbf{r},-x}) \\
\hat{x}_{\mathbf{r},L_y} &= \frac{1}{\sqrt{2}}(\hat{u}_{\mathbf{r},y} + \hat{u}_{\mathbf{r},-y}),
\end{aligned}
$$

with an analogous definitions for the momentum operators. Figs. 6.1(b)-6.1(e) sketch the phases factors of the ligand $2p_\delta$ orbitals using $\pm$ signs, and the displacement patterns of the new eigenmodes are indicated by the black arrows. Note that in this representation, the dimerized structure that forms in the insulating state of the 3D bismuthates and nickelates corresponds to a coherent state of the optical $x_{\mathbf{r},L_s}$ phonon modes. The $x_{\mathbf{r},L_x}$ and $x_{\mathbf{r},L_y}$ modes form the basis for the acoustic phonon branches.

After introducing the new basis, the Hamiltonian H^M for the Bi$_2$O$_4$ cluster is

$$
\begin{aligned}
H_0^M &= -2t_{sp}\sum_\sigma \left(s_{1,\sigma}^\dagger L_{s,\sigma} - s_{2,\sigma}^\dagger L_{s,\sigma} + h.c. \right) + \\
&\quad (\epsilon_s - \mu)\sum_\sigma (\hat{n}_\sigma^{s_1} + \hat{n}_\sigma^{s_2}) + (\epsilon_p - \mu)\sum_{\sigma,\alpha=x,y} \hat{n}_\sigma^{L_\alpha} \\
&\quad + (\epsilon_p + 2t_{pp})\sum_\sigma \hat{n}_\sigma^{L_s} + (\epsilon_p - 2t_{pp})\sum_\sigma \hat{n}_\sigma^{L_d} \\
H_{\text{lat}}^M &= \sum_\gamma \left(\frac{1}{2M}\hat{p}_{L_\gamma}^2 + K\hat{x}_{L_\gamma}^2 \right) \\
H_{e-ph}^M &= \alpha t_{sp}\sum_{\gamma,\sigma} \hat{x}_{L_\gamma} \left(s_{1,\sigma}^\dagger L_{\gamma,\sigma} + s_{2,\sigma}^\dagger L_{\gamma,\sigma} + h.c. \right).
\end{aligned}
$$

Here, the sums on γ are taken over $\gamma = s, d, x, y$.

Several insights into the problem at hand can be gleamed from this cluster model. In the atomic limit ($t_{sp} = 0$ and $t_{pp} = 0$) and in the negative charge transfer regime ($\epsilon_p < \epsilon_s$, in hole language), the four molecular orbitals are degenerate, as shown in Fig. 6.1(f). This degeneracy is lifted when the atomic overlaps are reintroduced. A nonzero t_{pp} raises (lowers) the onsite energy of the L_s (L_d) molecular orbital, while a nonzero t_{sp} hybridizes the two Bi

s orbitals with the L_s molecular orbital to form new bonding (sL_s), nonbonding $(sL_S)^0$, and antibonding $(sL_s)^*$ states. Here, the bonding state's energy is lowered by $2t_{sp}$ relative to the atomic energies, such that the two holes at half filling completely fill this state, as shown in Fig. 6.1(g). This ground state charge distribution is analogous to the one inferred for 3D bismuthates in *ab initio* calculations [73] and ARPES measurements [207].

The impact of the e-ph coupling is also evident from this form of the Hamiltonian; holes occupying the L_γ molecular orbital couple directly to the phonon eigenmode with the same symmetry. As such, the holes in the bonding (sL_s) state will excite the breathing motion of the surrounding oxygen atoms. In an extensive system, this coupling can lead to a coherent state of x_{L_s} modes, and a static breathing distortion of the lattice. In this case, a spontaneous symmetry breaking occurs that selects one of the Bi sites as the center of the compressed plaquette. From this analysis, it is also clear that additional doped holes will generally enter the L_d and $L_{x,y}$ orbitals, where they will excite the other phonon modes. Since the total displacement of the oxygen atoms is determined by the sum of the individual modes, the breathing distortion will begin to relax as the other phonon modes are excited. This is the fundamental mechanism behind the weakening of the static breathing distortion observed in the doped bismuthates.

To confirm this physical picture, I diagonalized the Hamiltonian H^M on a Bi_2O_4 cluster and evaluated several observables in the grand canonical ensemble where $\beta = 14.56/t_{sp}$, $\Omega = t_{sp}$, and μ was adjusted to set the particle number. When diagonalizing the model, I included up to $N_{ph} = 5$ quanta for each phonon mode, which was sufficient to obtain converged results for my choice of parameters.

Figure 6.2 summarizes the results of the ED calculations. Panel 6.2(a) and 6.2(b) show the evolution of the hole density $\langle \hat{n}^\gamma \rangle$ on each molecular orbital, and the fluctuation in the atomic displacement $\delta(x_\gamma) = \langle \hat{x}_\gamma^2 \rangle - \langle \hat{x}_\gamma \rangle^2$, respectively, for each phonon mode as a function of the total hole occupation of the cluster. At half-filling, the holes occupy the L_s orbital (the missing weight is on the Bi sites and is not shown for clarity) and no holes occupy the L_d, L_x, and L_d orbitals. At the same time, the displacement of the x_{L_s} mode fluctuates significantly, while the x_{L_d}, x_{L_x}, and x_{L_y} modes all have fluctuations consistent with zero point motion, indicating that they are in their ground state.
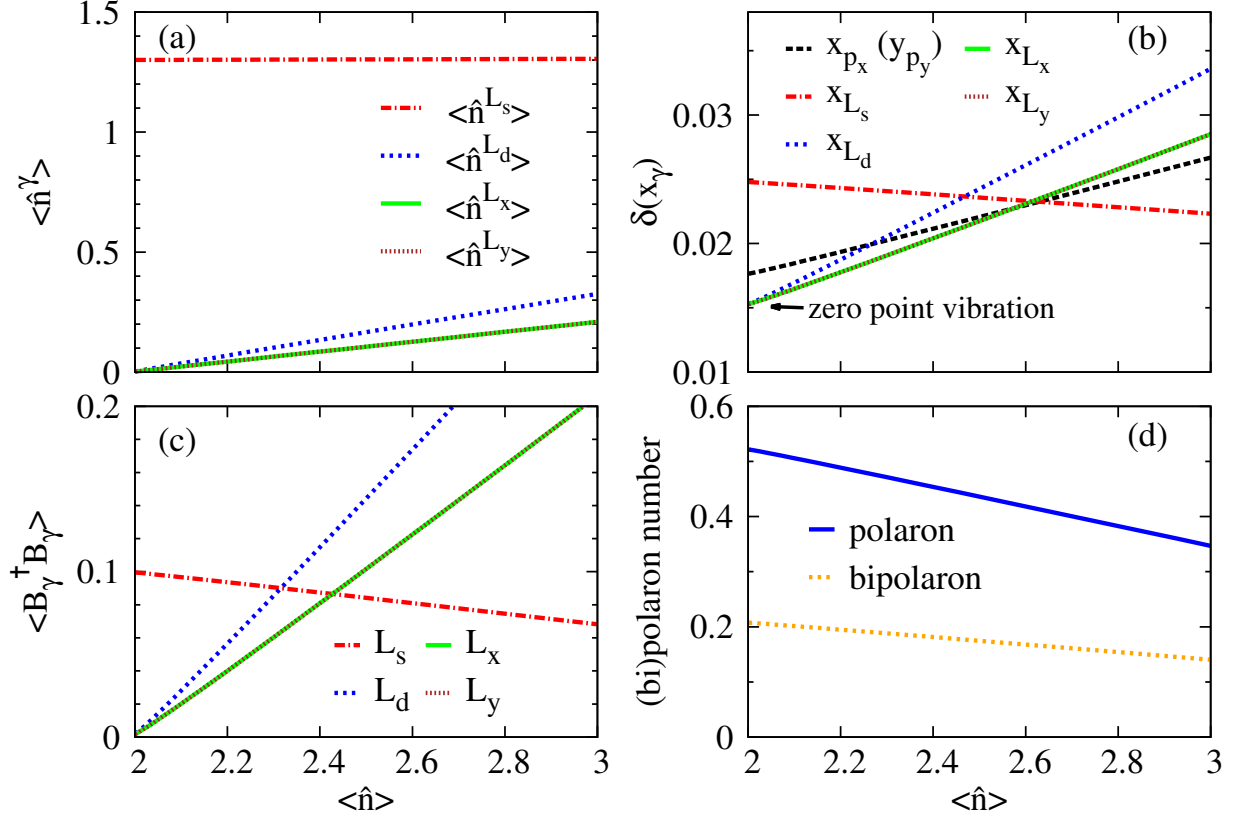
Figure 6.2: Exact diagonalization results for the Bi_2O_4 cluster as a function of the total filling and at a temperature of $\beta = 14.56/t_{sp}$. (a) The hole density on each molecule orbital as a function of doping. The missing hole weight is located equally on the Bi orbitals and is not shown. (b) The average fluctuation of the atomic displacement associated with each of the four eigenmodes shown in Fig. 1. (c) The average of phonon quanta in the cluster. (d) The expectation value of the polaron and bipolaron operator (see the main text).

Upon increasing total hole number, $\langle \hat{n}^{L_s} \rangle$ does not change while the occupation on the other molecular orbitals increases linearly, as expected based on the level diagram shown in Fig. 6.1(h). In this case, the L_d orbital has a larger hole occupation due to the finite value of t_{pp}. At the same time, $\delta(x_{L_d})$, $\delta(x_{L_x})$, and $\delta(x_{L_d})$ also increase linearly. The fluctuations of the four phonon modes are comparable for hole doping $\langle \hat{n} \rangle = 2.4 - 2.6$. The excitation of x_{L_d}, x_{L_x}, and x_{L_y} phonon modes could also be observed by the phonon number $\langle B_\gamma^\dagger B_\gamma \rangle$ of each mode, which is shown in Fig. 6.2(c). In the hole doping region $\langle \hat{n} \rangle = 2.4 - 2.6$, I find that $\langle B_{L_d}^\dagger B_{L_d} \rangle$, $\langle B_{L_x}^\dagger B_{L_x} \rangle$, and $\langle B_{L_y}^\dagger B_{L_y} \rangle$ are larger than $\langle B_{L_s}^\dagger B_{L_s} \rangle$, indicating the excitation of x_{L_d}, x_{L_x}, and x_{L_y} phonons is more prominent than that of x_{L_s} phonon. Hence, at this level of doping, I expect that the dimerized structure would be completely washed out by the sum of the phonon fluctuations.

To test for the presence of polaron-like objects, I also computed the expectation value of

$$
\begin{aligned}
\langle P \rangle &= \langle (\hat{n}^{s_1} + \hat{n}^{L_s}) \hat{x}_{L_s} - (\hat{n}^{s_2} + \hat{n}^{L_s}) \hat{x}_{L_s} \rangle \\
\langle BP \rangle &= \langle (\hat{n}_\uparrow^{s_1} + \hat{n}_\uparrow^{L_s})(\hat{n}_\downarrow^{s_1} + \hat{n}_\downarrow^{L_s}) \hat{x}_{L_s} - (\hat{n}_\uparrow^{s_2} + \hat{n}_\uparrow^{L_s}) \times (\hat{n}_\downarrow^{s_2} + \hat{n}_\downarrow^{L_s}) \hat{x}_{L_s} \rangle.
\end{aligned}
$$

These two quantities represent the number of polaron and bipolaron, respectively, which are shown in Fig. 6.2(d). With increasing hole dopng, both $\langle P \rangle$ and $\langle BP \rangle$ decrease, implying that the breathing distortion is suppressed. Throughout whole doping region, I find both $\langle P \rangle$ and $\langle BP \rangle$ are larger than zero, indicating polarons and bipolarons always exist on the cluster.

6.4 DQMC simulations of an extended lattice

The molecular orbital picture presented in the previous section provides an intuitive way of understanding the physics of the model. With this in mind, I now turn to detailed DQMC simulations for the model, defined on an extended cluster with $N = 4 \times 4$ Bi atoms (48 orbitals in total) and with $\Omega = \sqrt{2} t_{sp}$. Here, I am restricted to larger values of the phonon energy by the long autocorrelation times that develop in DQMC simulations with smaller values of Ω. All of the remaining parameters are identical to those used in the previous section. With these values, the DQMC calculations give $\langle X \rangle = \langle Y \rangle = 0$ and $\langle X^2 \rangle = \langle Y^2 \rangle = 0.57(a/4)^2$ at

half-filling. These values show that the oxygen atoms do not cross the bismuth atoms during the DQMC sampling, and these parameters are in a physically reasonable region.

I study the three-orbital model using DQMC, which can exactly treat the nonlocal e-ph coupling at finite temperature. The detailed algorithm as applied to the model is provided in Appx. C.

I first examine the dimerized insulating phase that forms at $\langle \hat{n} \rangle = 1$. Figures 6.3(b)-6.3(d) show the lattice displacement correlation functions $\langle \hat{X}(\mathbf{r})\hat{X}(0)\rangle$, $\langle \hat{Y}(\mathbf{r})\hat{Y}(0)\rangle$, and $\langle \hat{Y}(\mathbf{r})\hat{X}(0)\rangle$, as a function of position at temperature $1/\beta t_{sp} = 0.1$, which shows evidence of a static dimerized structure. For example, both $\langle \hat{X}(\mathbf{r})\hat{X}(0)\rangle$ and $\langle \hat{Y}(\mathbf{r})\hat{Y}(0)\rangle$ alternate in sign following a checkerboard pattern while $\langle \hat{Y}(\mathbf{r})\hat{X}(0)\rangle$ alternates in sign along x- and y-directions but is constant along the diagonal. These results are consistent with the breathing distortion pattern sketched in Fig. 6.3(a), as well as the observed lattice distortion that appears in the insulating phase of the bismuthates [50, 217, 123].

Remaining at $\langle \hat{n} \rangle = 1$, I now examine the temperature evolution of this phase. Figure 6.4(a) plots the direct current (dc) conductivity σ_{dc} and orbital-resolved spectral weight as a function of temperature $1/\beta t_{sp}$. The dc conductivity is defined as $\sigma_{\mathrm{dc}} = \frac{\beta^2}{\pi}\Lambda_{xx}(\mathbf{q} = 0, \tau = \beta/2)$ [249], where $\Lambda_{xx}(\mathbf{q}, \tau) = \sum_{\mathbf{r}}\langle \hat{j}_x(\mathbf{r}, \tau)\hat{j}_x(0,0)\rangle e^{i\mathbf{q}\cdot\mathbf{r}}$ is the current-current correlation function and

$$\hat{j}_x(\mathbf{r}, \tau) = -\mathrm{i}t_{sp}\sum_{\delta,\sigma}\left(P_\delta - \alpha\hat{u}_{\mathbf{r},\delta}\right)\left(s_{\mathbf{r},\sigma}^\dagger p_{\mathbf{r},\delta,\sigma} - h.c.\right) + \mathrm{i}t_{pp}\sum_{\delta,\delta',\sigma}Q_{\delta,\delta'}p_{\mathbf{r},\delta,\sigma}^\dagger p_{\mathbf{r},\delta',\sigma},$$

where $Q_{\pm x,\pm y} = -Q_{\pm y,\pm x} = -Q_{\pm x,\mp y} = Q_{\mp y,\pm x} = 1$. At high-temperature σ_{dc} (black dots) initially rises with decreasing temperature until reaching a maximum at $1/\beta t_{sp} \approx 0.2$, when it rapidly falls off signaling the formation of an insulating state. The orbital-resolved spectral weight $\beta G_{\gamma,\gamma}(\mathbf{r} = 0, \tau = \beta/2)$, where γ is the orbital index also reflects this behavior. Above the transition temperature, $\beta G_{s,s}(\mathbf{r} = 0, \beta/2)$ increases as temperature decreases while $\beta G_{p_{x/y},p_{x/y}}(\mathbf{r} = 0, \beta/2)$ remains relatively flat. Below the transition temperature, however, the spectral weights of all three orbitals decrease rapidly as the insulating state forms, signaling the removal of spectral weight from the Fermi level. The dc conductivity is proportional to the product of the mobility and concentration of carriers in a metal. My
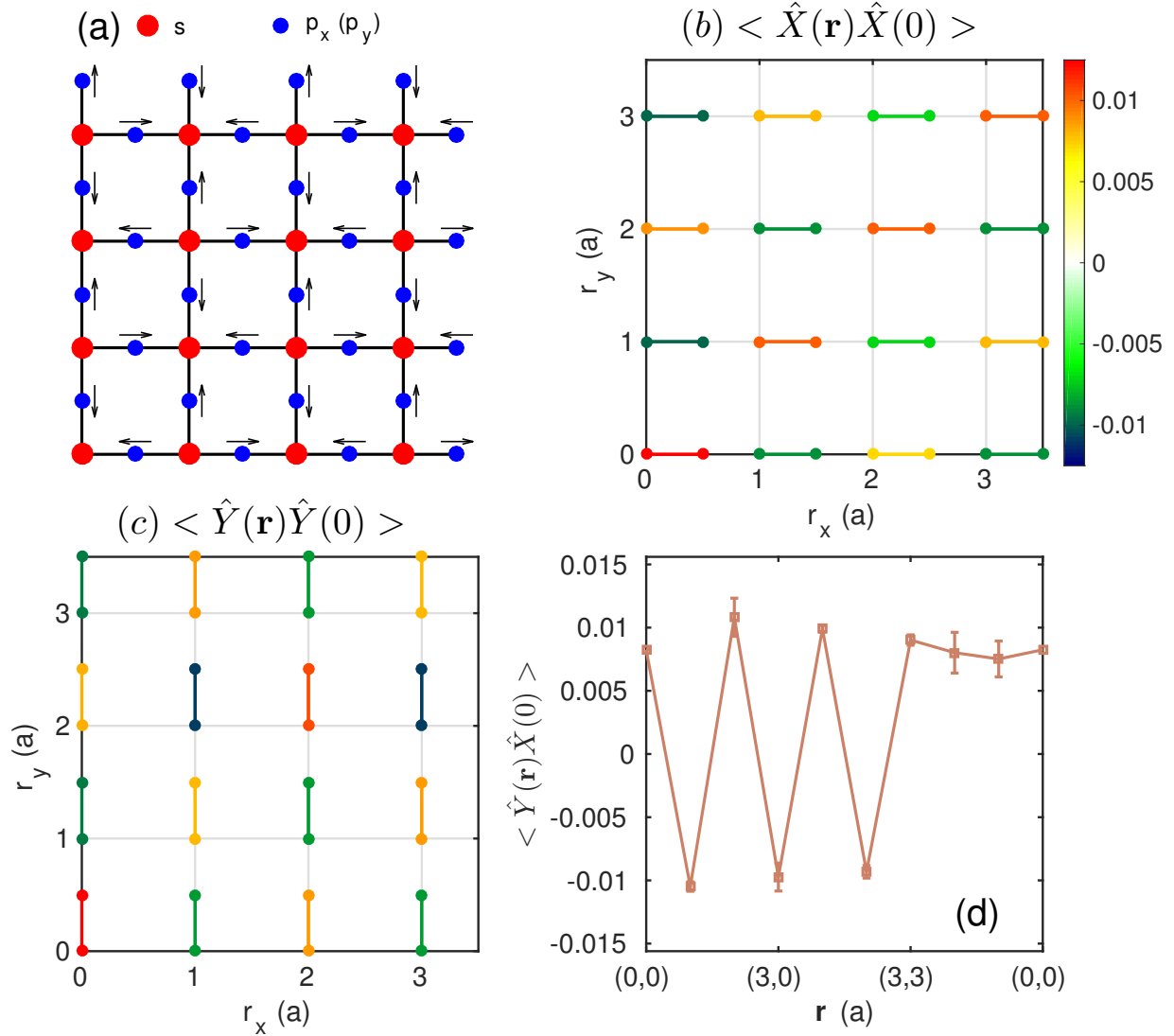
Figure 6.3: (a) A sketch of dimerized geometry. The red and blue dots indicate the *s* and $p_{x,y}$ orbitals, respectively, while the black arrow indicate the displacement pattern of each oxygen atom in the dimerized structure. Panels (b) and (c) plot the lattice displacement correlation functions $\langle \hat{X}(\mathbf{r})\hat{X}(0)\rangle$ and $\langle \hat{Y}(\mathbf{r})\hat{Y}(0)\rangle$ as a function of distance $\mathbf{r} = n_x\mathbf{a} + n_y\mathbf{b}$, respectively. Here, $\mathbf{a}$ and $\mathbf{b}$ are the primitive vectors along x- and y-directions, respectively. Panel (d) plots the real-space displacement correlation function $\langle \hat{Y}(\mathbf{r})\hat{X}(0)\rangle$ indicating the two-sublattice structure of the dimerized state. The distance between two nearest Bi atom in the undistorted square structure is *a*.
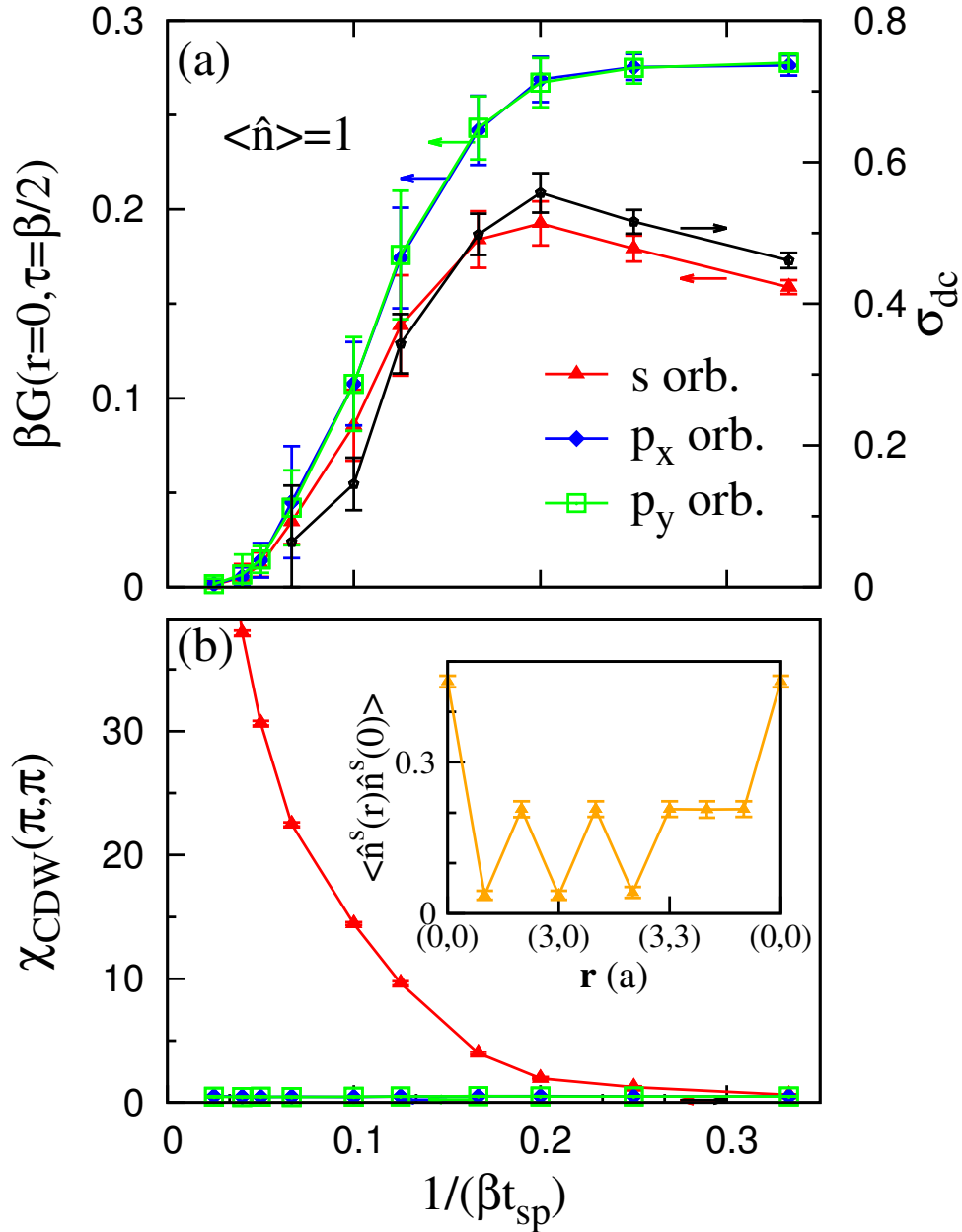
Figure 6.4: (a) The temperature dependence of the spectral weight at the Fermi level $\beta G(r = 0, \tau = \beta/2)$ and the direct current (dc) conductivity σ_{dc}. (b) The temperature dependence of the charge-density-wave susceptibility $\chi_{\mathrm{CDW}}(\pi, \pi)$. In both panels, the average filling is $\langle n \rangle = 1$ corresponding to the "half-filled" case with one hole per unit cell. Error bars smaller than the marker size have been suppressed for clarity.

results show that changes in σ_{dc} are correlated with the changes in the concentration of free carriers.

The formation of charge order in the insulating phase can also be observed in the charge susceptibility $\chi^{\mathrm{C}}_{\gamma,\gamma}(\mathbf{q}) = \frac{1}{N}\int_0^\beta d\tau \langle \hat{n}_{\mathbf{q},\gamma}(\tau)\hat{n}_{\mathbf{q},\gamma}(0)\rangle$. Here, $\mathbf{q}$ is the momentum, τ is the imaginary time, $\hat{n}_{\mathbf{q},\gamma} = \sum_{i,\sigma} e^{i\mathbf{q}\cdot\mathbf{r}_i}\hat{n}_{\mathbf{r}_i,\gamma,\sigma}$, and $\mathbf{r}_i$ is the lattice vector. Figure 6.4(b) plots the temperature evolution of $\chi^C_{\gamma,\gamma}(\mathbf{q})$ at $\mathbf{q} = (\pi,\pi)$, corresponding to the real space ordering inferred from Fig. 6.3. Below $1/\beta t_{ps} = 0.2$, the charge correlations rapidly increase on the s orbital, while there is little change in the signal on the p orbitals.

The behavior observed in Fig. 6.4 implies that the average density on the O sublattice remains uniform above and below the metal-to-insulator transition (MIT) while a density modulation forms on the Bi sites. This view is confirmed in the inset of Fig. 6.4(b), which plots the equal time Bi-Bi charge density correlation along the high symmetry directions of the cluster, where a clear (π,π)-ordering is observed. The fact that the charge order signal appears in the Bi orbital component can be understood once one recognizes that all of the oxygen orbitals in the system are equivalent, even in the insulating dimerized structure. In this case, the effect of the breathing distortion is to increase the hybridization between the L_s orbital and one of the Bi s orbitals at the expense of the other. The two holes are then shared between the L_s and compressed Bi s orbitals, while no hole occupies the s orbital of the expanded Bi site, thus accouting for the Bi charge density modulation.

Next, I study effects of hole doping on the MIT at fixed temperature $\beta t_{sp} = 0.1$. Figure 6.5(a) plots σ_{dc} as a function of filling, where it increases upon hole doping until saturating at $\langle \hat{n}\rangle \approx 1.4$, indicating metallic behavior. I also find evidence for the formation of mobile polarons in this region, where holes are bound to local breathing distortions of the oxygen sublattice. This behavior can be seen by examinng the polaron operator $\hat{p}(\mathbf{r}) = \hat{X}_{\mathbf{r},L_s}(\hat{n}^s_{\mathbf{r}} + \hat{n}^{L_s}_{\mathbf{r}})$. The composite operator $\hat{p}(\mathbf{r})$ measures the presence of a local breathing distortion centered at site $\mathbf{r}$ in combination with holes in the (sL_s) orbitals associated with that site.

Figure 6.5(b) plots the doping evolution of the number of polarons given by $\frac{1}{N}\sum_{\mathbf{r}}\langle \hat{p}(\mathbf{r})\rangle$. The polaron number is relatively constant in the insulating phase, and monotonically decreasing in the metallic phase but still nonzero, indicating that a finite number of polarons are present in the system at all dopings, consistent with the previous conclusion obtained
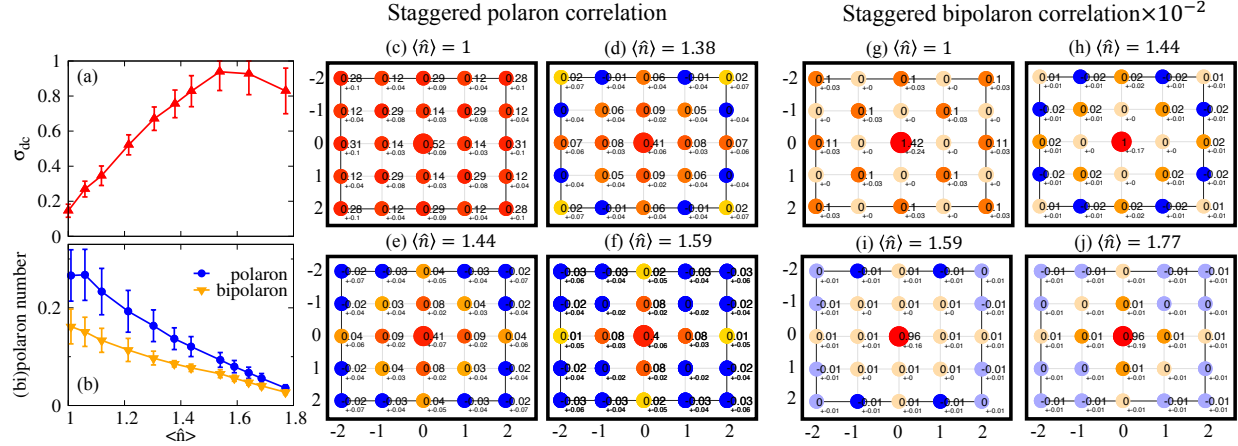
Figure 6.5: (a) The dc conductivity as a function of doping. (b) polaron and bipolaron number as a function of doping. (c)-(f) Staggered polaron correlation function $\langle P(\mathbf{r})\rangle$ and (h)-(j) staggered bipolaron correlation function $\langle BP(\mathbf{r})\rangle$ at different doping levels. The red (gray) color indicates values larger (smaller) than zero. The numerical value of the correlation function, along with the associated 1σ statistical error are indicated at each point. All results are for a temperature $1/(\beta t_{sp}) = 0.1$ and error bars smaller than the marker size have been suppressed for clarity.

from the small cluster. The real space correlations of the polarons can be extracted from the staggered polaron correlation function $\langle P(\mathbf{r}) \rangle = (-1)^{r_x+r_y} \langle \hat{p}(\mathbf{r})\hat{p}(0) \rangle$, which is plotted in Figs.6.5(c)-(f) for selected hole concentrations. At half filling, $\langle P(\mathbf{r}) \rangle$ is positive for any $\mathbf{r}$, indicating that the polaron correlations have frozen into a long-range two-sublattice order, consistent with the patterns inferred from Figs. 6.3. With increasing hole concentrations, $\langle P(\mathbf{r}) \rangle$ decreases at long range, indicating a relaxation of the ordered dimerized structure. In the high doping region, where the system is metallic (e.g. $\langle \hat{n} \rangle > 1.44$), the correlations are short-ranged. These observations are consistent with the proposal that the holes form mobile polarons at these dopings.

The mobile polarons can form polaron island or polaron liquid in the system. However, this study is limited in a 4×4 cluster, which is too small to distinguish the phase separation and the polaron liquid. To answer this question, one needs to study the three-orbital SSH on a larger cluster. Larger cluster sizes are currently not possible be done given our CPU resources. I expect this problem could be solved by employing self-learned DQMC technique [40].

Throughout, I have worked in the negative charge-transfer regime, where $\Delta = \epsilon_s - \epsilon_p > 0$ and the holes primarily reside on oxygen sublattice. My ED analysis showed that holes preferentially occupy the (sL_s) bonding states, which then couple to the local breathing distortion forming small lattice polarons and bipolarons. To explore this possibility, I examined the doping evolution of the bipolaron number given by $\frac{1}{N}\sum_{\mathbf{r}}\langle \hat{g}(\mathbf{r}) \rangle$ where $\hat{g}(\mathbf{r}) = \hat{X}_{\mathbf{r},L_s}(\hat{n}_{\mathbf{r},s,\uparrow} + \hat{n}_{\mathbf{r},L_s,\uparrow})(\hat{n}_{\mathbf{r},s,\downarrow} + \hat{n}_{\mathbf{r},L_s,\downarrow})$. I also examined the staggered bipolaron correlation function $\langle BP(\mathbf{r}) \rangle = (-1)^{r_x+r_y}\langle \hat{g}(\mathbf{r})\hat{g}(0) \rangle$. When computing the latter quantity, I only considered the signal on the Bi site by keeping only those terms proportional to $\hat{n}_{\mathbf{r},s,\uparrow}\hat{n}_{\mathbf{r},s,\downarrow}$. This simplification was necessary due to the enormous number of terms generated by the Wick contraction of the product of $\hat{g}(\mathbf{r})$ operators. It is also justified by the fact that I can clearly see excess charge density on the Bi sites when a local breathing distortion forms.

The doping evolution of the bipolaron number operator is plotted in Fig. 6.5(b). As with the polaron number, it is largest near half-filling and decays slowly with doping. However, at high dopings it is still finite, suggesting that a significant fraction of the carriers have a

162

bipolaron character. The staggered bipolaron correlation function is plotted in Figs. 6.5(g)-
(j). At $\langle \hat{n} \rangle = 1$, the bipolaron correlations are clear and long-ranged. This result lends to
the interpretation that the insulating phase can be thought of as a static bipolaron lattice.
As the hole concentration is increased, however, I find that the bipolaron correlations are
entirely suppressed at all length scales, while a finite number of bipolarons are present in
the system, as indicated in Fig. 4b. These results support the notion that mobile bipolarons
exist in the metallic phase.

This scenario raises questions regarding possible superconductivity. I therefore computed
the pair field susceptibility $\chi_{sc}^{\gamma} = \frac{1}{N} \int_0^{\beta} d\tau \langle \Delta_{\gamma}(\tau) \Delta_{\gamma}^{\dagger}(0) \rangle$, where $\Delta_s = \sum_{\mathbf{r}} s_{\mathbf{r},\uparrow} s_{\mathbf{r},\downarrow}$ and $\Delta_{p_{\delta}} =$
$\sum_{\mathbf{r}} p_{\mathbf{r},\delta,\uparrow} p_{\mathbf{r},\delta,\downarrow}$. Since $\chi_{sc}^{p_x}$ and $\chi_{sc}^{p_y}$ are the same, I use χ_{sc}^{p} to denote pairing on the O atoms.
Figure 6.6 plots χ_{sc}^{γ} as a function of temperature at $\langle \hat{n} \rangle = 1.59$, and compares it against the
dominant charge correlations at this doping $\chi_{ss}^{C}(\pi, \pi/2)$. All three susceptibilities increase
with decreasing temperature, but χ_{sc}^{p} dominates below $1/\beta t_{sp} \approx 0.04$. Extrapolating $1/\chi^{sc}$ to
zero (as shown in the inset), yields a $T_c \approx 382$ K ($1/\beta t_{sp} \approx 0.0158$). This value is artificially
high, due to the large value of Ω used in the calculations. Nevertheless, these results provide
evidence that the bipolaronic rich metallic phase has a superconducting ground state.

6.5   Discussion and Summary

I have studied off-diagonal e-ph interactions in the 2D three-orbital model on a Lieb
lattice. At half filling, I find a MIT at low temperature, which is accompanied by a lattice
dimerization, consistent with the charge-ordered insulating state observed in the 3D barium
bismuthates. The insulating phase is suppressed upon hole doping, leading to a metallic
phase with evidence of delocalized polaronic carriers. I argue that the relaxation of the
breathing distortions with doping can be understood from the excitation of the other types
of phonon modes when holes are introduced to the unoccupied molecular orbitals in the
material. I again stress that in this picture the breathing distortion relaxes when a significant
number of additional phonon modes are excited by the doped holes entering the unoccupied
molecular orbitals. In other words, the breathing-type optical phonons are still present in
the doped system due to the significant number of holes that remain in the L_s molecular
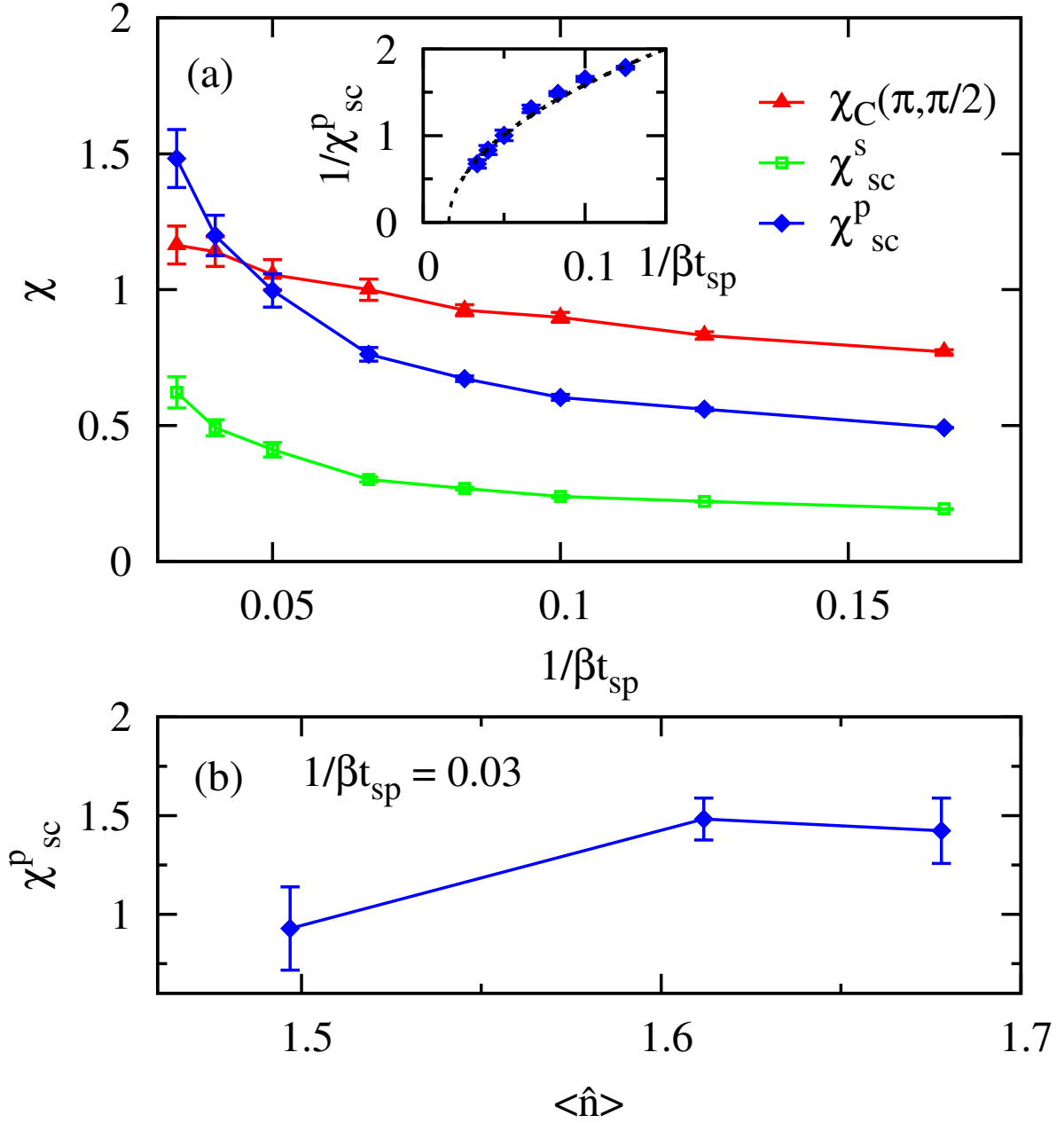
Figure 6.6: (a) The charge-density-wave $\chi_{CDW}(\pi,0)$ and pairing χ_{SC} susceptibilities as a function of temperature $1/(\beta t_{sp})$ at $\langle n \rangle = 1.59$. The inset plots $1/\chi_{sc}^{p}$ as a function of temperature $1/(\beta t_{sp})$. The black dashed line is the fitting result. (b) The doping dependence of χ_{SC} at a temperature of $1/(\beta t_{sp}) = 0.03$. Error bars smaller than the marker size have been suppressed for clarity.

orbital. Overall, my results are consistent with a picture where polarons create fluctuating local lattice distortions in the metallic phase but freeze into an ordered insulating phase below the MIT. Moreover, I find an *s*-wave superconducting state at finite doping, where the superconducting tendencies form on the oxygen sublattice as the system cools.

Finally, I stress that I have studied the off-diagonal *e*-ph interaction in a model that includes multiple orbitals. Previously, it has been proposed that this model can be downfolded onto an effective single band model with an attractive Hubbard interaction [217, 209, 168, 116, 281, 107, 22]. Since neither model suffers from a Fermion sign problem, it would be interesting to contrast the pictures created by these two scenarios to test the validity of this proposal.

Chapter 7

Summary and outlook

Although many studies claim that the fluctuations are essential to the high-T_C superconductors, including the cuprates and iron-based superconductors, there are many lines of evidence show that the phonon is not negligible as discussed in chapter 1. In general, there are two types of e-ph couplings used in theoretical models. The first one is the local e-ph coupling, which links the displacement of an atom to the total charge density in a given orbital. One typical model for the local e-ph coupling is the Holstein model. To understand the role of phonons in strongly correlated systems, the Holstein model has been extended to the Hubbard-Holstein (HH) model, which includes both e-e and e-ph coupling. To date, the single band HH model has been studied in various dimensions with different fillings [20, 44, 163, 90, 196, 14, 113, 131]. But the role of phonons in strongly correlated systems has not been fully understood. For example, the non-linear e-ph coupling, which cannot be captured by the Holstein model, has not been widely studied, although it is proposed that the non-linear e-ph coupling could suppress the electron-boson coupling in a cuprate superconductor [289]. This fact asks us to continuously explore the interplay between the e-e and e-ph interactions. Moreover, the correlated materials are not always captured by the single-band model. For example, the iron-based superconductors are multiorbital materials, which have five d orbitals near the Fermi surface [81]. In this case, one needs to extend the single-band HH model to a multiorbital HH model.

The second e-ph coupling is the nonlocal e-ph coupling, which links the displacement of an atom to both its nearest neighbors and itself. The typical model for the nonlocal e-ph

coupling is the Su-Schreiff-Heeger model [242]. This model has been extensively studied in the one-dimension and the single-band case [146, 234, 97, 46]. But many high-T_C superconductors are high-dimensional multiorbital materials. Then to study the role of the nonlocal e-ph coupling in those high-T_C superconductors, such as barium bismuthate and high-T_C cuprates, one needs to build the SSH model in a high-dimension with multiple orbitals.

In sum, the role of phonons in high-T_C superconductors has not been completely understood to date. In this dissertation, I continue to explore the role of phonons in high-T_C superconductors. My project included three parts: (1) the non-linear e-ph coupling, (2) the interplay between e-ph and e-e couplings in a multiorbital system, and (3) breathing phonons in a two-dimensional multiorbital model.

The first part of my research studied the non-linear e-ph coupling in a nonmagnetic system [147, 148]. It was found that a positive non-linear e-ph interaction could dramatically suppress the CDW correlations that dominate the linear Holstein model and a negative non-linear e-ph interaction has an opposite effect. Both the positive and negative non-linear e-ph interactions have a less pronounced effect for the superconducting correlations. These effects are attributed to a combined hardening of the phonon mode and weakening of the effective linear coupling by the positive non-linear terms, or softening of the phonon mode and enhancing of the effective linear coupling by the negative non-linear terms. I also found that the electronic and phononic properties of the non-linear Holstein model cannot be captured by an effective linear Holstein model simultaneously, indicating that one should be cautions of the strength of the e-ph interaction in pump-probed experiments. In this work, I didn't include the e-e interaction. To understand the role of non-linear e-ph interaction in a correlated materials, where e-e interactions is not negligible, I will study a modified HH model in the future, which includes both linear and non-linear e-ph coupling.

The second part of my research studies the interplay between the linear e-ph and e-e couplings in a multiorbital system [148]. In the single band HH model, the interplay between the e-e and e-ph interactions leads a competition between the CDW phase and MI phase [14, 196, 113]. But in the multiorbital Hubbard-Holstein model, the situatution is more complex due to an extra orbital degree of freedom. It was shown that the orbital

degree of freedom is essential to some new phases discovered in the multiorbital Hubbard model. One of the new phases is the OSMP, in which some orbitals are Mott insulators and the other orbitals remain metallic. When the Holstein phonon is included in the multiorbital Hubbard model, a phase transition from the OSMP phase to the CDW phase could be found. Moreover, when the ratio between bands is large enough, an OSPI appears. Both the OSMP and OSPI are the results of the orbital degree of freedom, which is absent in the single band HH model. In addition, it was found that the e-ph coupling strength for the phonon dominated phase in the multiorbital system is not necessary very large, indicating that the phonon in the multiorbital material, such as FeSC, could be more important than what people expect.

The third part of my research focuses on the breathing phonons in barium bismuthate. Here, I present a method for modeling the off-diagonal e-ph coupling in a three-orbital model using DQMC for the first time. The three-orbital SSH model includes Bi 6s and O $2\mathrm{p}_{x/y}$ orbitals, which is a 2D analog of the barium bismuthate high T_C superconductors. I find a metal-insulator transition with decreasing temperature at half filling and identify a dimerized structure in the insulating phase. At the same time, a charge-density-wave (CDW) appears on the Bi 6s orbital. With hole doping, the ordered polarons and bipolarons correlations disappear but the short-range correlations are present, implying that polarons and bipolarons preform in the metallic phase. At a finite doping, I observe that an s-wave superconducting fluctuation first appears on oxygen atoms as temperature decreases and becomes an ordered state at low temperature.

These are three studies I have done in this dissertation, but there are many more questions needed to be studied in the future. The first one is studying the interorbital scattering in a multiorbital HH model. In the single band model, phonons and electrons could be renormalized by intra-orbital scattering. In the multiorbital model, one might expect that the properties of both phonons and electrons could be modified by the extra scattering, namely inter-orbital scattering. But it is not clear how the inter-orbital scattering changes both properties. Comparing the CDW phase transition in the one-, two-, and three-orbital system can give us a direct clue how the orbital degree of freedoms reshapes both electronic and phononic properties. The second question concerns studying the phase diagram of the

three-orbital Hubbard-SSH model on a two-dimensional layer. This work directly relates to the cuprates. The thrid question is understanding the interplay between the holstein phonon and the breathing phonon. In a one dimension, the charge order induced by the holstein phonon is "2000" type at a quarter filling, while the charge order induced by the breathing phonon is "0110" type [46]. These two charge ordered states will compete with each other in a model including both the local e-ph and nonlocal e-ph interactions. Studying the phase diagram of the Holstein-SSH model is helpful to understand microscopic mechanism of quasi-one-dimensional organic superconductors, such as $(DMEDO - TTF)_2 X$, X = ClO_4 and BF_4 [175, 283, 285, 46, 125].

Throughout this work a number of aspects of e-ph coupling have been examined. The highlighted jobs are the e-ph coupling in the multiorbital correlated system and the nonlocal e-ph coupling project. My work first points out that the e-ph coupling strength for the phonon-mediated phenomenon in a multiorbital system is not necessary large. Previous DFT studies claim that the e-ph interaction strength in FeSCs is too small to change electronic properties [26]. My results alert the community to notice even a weak e-ph interaction is still important in a multiorbital system. The nonlocal e-ph coupling project paves a way to exactly study the SSH model in a high-dimension using DQMC. This is important since many nonlocal e-ph coupling problems are solved by classical methods or perturbation techniques [223, 254, 292, 145]. It is not clear how reliable results obtained from these perturbation theories are. Here, DQMC can be used to evaluate these perturbation theories. In summary, my research not only broadens the view of phonons in multiorbital systems but also lays a foundation for fully understanding the role of phonons in multiorbital systems.

Bibliography

[1] Adolphs, C. P. J. and Berciu, M. (2013). Going beyond the linear approximation in describing electron-phonon coupling: relevance for the Holstein model. *EPL.*, 102(4):47003. 52, 54, 55, 58, 59, 73, 76, 80, 84

[2] Adolphs, C. P. J. and Berciu, M. (2014a). Single-polaron properties for double-well electron-phonon coupling. *Phys. Rev. B*, 89(3):035122. 80

[3] Adolphs, C. P. J. and Berciu, M. (2014b). Strongly bound yet light bipolarons for double-well electron-phonon coupling. *Phys. Rev. B*, 90(8):085149. 52

[4] Akerlund, O., Forcrand, P. d., Georges, A., and Werner, P. (1999). Dynamical mean field approximation applied to quantum field theory. *Phys. Rev. D*, 88(12):125006. 95

[5] Anisimov, V. I., Nekrasov, I. A., Kondakov, D. E., Rice, T. M., and Sigrist, M. (2002). Orbital-selective Mott-insulator transition in $Ca_{2-x}Sr_xRuO_4$. *Eur. Phys. J. B*, 25(2):191. 85, 113

[6] Arsenault, L.-F., Sémon, P., and Tremblay, A.-M. S. (2012). Benchmark of a modified iterated perturbation theory approach on the fcc lattice at strong coupling. *Phys. Rev. B*, 86(8):085133. 62

[7] Aryanpour, K., Pickett, W. E., and Scalettar, R. T. (2006). Dynamical mean-field study of the Mott transition in the half-filled Hubbard model on a triangualr lattice. *Phys. Rev. B*, 74(8):085117. 14

[8] Awan, A. and Lancashire, R. J. (2016). Crystal field theory. https://chem.libretexts.org/Core/Inorganic_Chemistry/Crystal_Field_Theory/Crystal_Field_Theory. 8

[9] Bardeen, J., Cooper, L. N., and Schrieffer, J. R. (1957). Theory of superconductivity. *Phys. Rev.*, 108(5):1175. 1, 52

[10] Barišić, N., Chan, M. K., Li, Y., Yu, G., Zhao, X., Dressel, M., Smontara, A., and Greven, M. (2013). Universal sheet resistance and revised phase diagram of the cuprate high-temperature superconductors. *PNAS.*, 110(30):12235. 3

[11] Batlogg, B. (1984). Superconductivity in $Ba(Pb, Bi)O_3$. *Physica B*, 126(1-3):275. 12

[12] Batlogg, B., Cava, R. J., Jayaraman, A., Dover, R. B. v., Kourouklis, G. A., Sunshine, S., Murphy, D. W., Rupp, L. W., Chen, H. S., White, A., Short, K. T., Mujsce, A. M., and Rietman, E. A. (1987). Isotope effect in the high-T_C superconductors $Ba_2YCu_3O_7$ and $Ba_2EuCu_3O_7$. *Phys. Rev. Lett.*, 58(22):2333. 19

[13] Batlogg, B., Cava, R. J., Rupp, L. W., Mujsce, A. M., Krajewski, J. J., Pemeika, J. P., Peck, W. F., Cooper, A. S., and Espinosa, G. P. (1988). Density of states and isotope effect in BiO superconductors: evidence for nonphonon mechanism. *Phys. Rev. Lett.*, 61(14):1670. 22

[14] Bauer, J. (2010). Competing interactions and symmetry breaking in the Hubbard-Holstein model. *EPL*, 90(2):27002. 114, 117, 148, 166, 167

[15] Bauer, J. and Hewson, A. C. (2010). Competition between antiferromagnetic and charge order in the Hubbard-Holstein model. *Phys. Rev. B*, 81(23):235113. 114, 117, 120, 125, 148

[16] Beach, K. S. D. and Assaad, F. F. (2011). Orbital-selective Mott transition and heavy-fermion behavior in a bilayer Hubbard model for ^{3}He. *Phys. Rev. B*, 83(4):045103. 86

[17] Bednorz, J. G. and Mueller, K. A. (1986). Possible high T_C superconductivity in the Ba-La-Cu-O system. *Zeitschrift fur Physik*, 64(2):189–193. 2

[18] Beichi, I. and Sullivan, F. (2000). The metropolis algorithm. *Computing in Science and Engineering*, 2(1):65–69. 30

[19] Berciu, M. (2006). Green's function of a dressed particle. *Phys. Rev. Lett.*, 97:036402. 148

[20] Berger, E., Valásĕk, P., and Linden, W. v. d. (1995). Two-dimensional Hubbard-Holstein model. *Phys. Rev. B*, 52(7):4806. 114, 166

[21] Biermann, S., Medici, L. d., and Georges, A. (2005). Non-fermi-liquid behavior and double-exchange physics in orbital-selective Mott systems. *Phys. Rev. Lett.*, 95(20):206401. 86

[22] Bischofs, I. B., Allen, P. B., Kostur, V. N., and Bhargave, R. (2002). Topological doping of a three-dimensinal peierls system: Predicted structure of doped $BaBiO_3$. *Phys. Rev. B*, 66(17):174108. 165

[23] Bisogni, V., Catalano, S., Green, R. J., Gibert, M., Scherwitzl, R., Huang, Y., Strocov, V. N., Zubko, P., Balandeh, S., Triscone, J.-M., G., S., and Schmitt, T. (2016). Ground-state oxygen holes and the metalinsulator transition in the negative charge-transfer rare-earth nickelates. *Nature Communications*, 7:13017. 149

[24] Blankenbecler, R., Scalapino, D. J., and Sugar, R. L. (1981). Monte carlo calculations of coupled boson-fermion systems. I. *Phys. Rev. D*, 24(8):2278–2286. 27, 28

[25] Boeri, L., Calandra, M., Mazin, I. I., Dolgov, O. V., and Mauri, F. (2010). Effects of magnetism and doping on the electron-phonon coupling in $BaFe_2As_2$. *Phys. Rev. B*, 82(2):020506. 21, 114

[26] Boeri, L., Dolgov, O. V., and Golubov, A. A. (2008). Is $LaFeAsO_{1-x}F_x$ an electron-phonon superconductor? *Phys. Rev. Lett.*, 101(2):026403. 21, 114, 147, 169

[27] Bonča, J., Trugman, S. A., and Batistić, I. (1999). Holstein polaron. *Phys. Rev. B*, 60:1633–1642. 148

[28] Bouadim, K., Batrouni, G. G., Hébert, F., and Scalettar, R. T. (2008). Magnetic and transport properties of a coupled Hubbard bilayer with electron and hole doping. *Phys. Rev. B*, 77(14):144527. 89

[29] Bouadim, K., Batrouni, G. G., and Scalettar, R. T. (2009). Determinant quantum monte carlo study of the orbitally selective Mott transition. *Phys. Rev. Lett.*, 102(22):226402. 86

[30] Bourne, L. C., Crommie, M. F., Zettl, A., Loye, H.-C. z., Keller, S. W., Leary, K. L., Stacy, A. M., Chang, K. J., Cohen, M. L., and Morris, D. E. (1987). Search for isotope effect in superconducting $Y - Ba - Cu - O$. *Phys. Rev. Lett.*, 58(22):2337. 19

[31] Boyce, J. B., Bridges, F. G., Claeson, T., Geballe, T. H., and Remeika, J. M. (1990). X-ray absorption of $BaBiO_3$ and superconducting $BaBi_{0.25}Pb_{0.75}O_3$. *Phys. Rev. B*, 41(10):6306. 9

[32] Bryan, R. K. (1990). Maximum entropy analysis of oversampled data problems. *European Biophysics Journal*, 18(3):165–174. 48, 49

[33] Capone, M., Castellani, C., and Grilli, M. (2010). Electron-phonon interaction in strongly correlated systems. *Adv. Condens. Matter Phys.*, 2010(920860):1–18. 114

[34] Caron, J. M., Neilson, J. R., Miller, D. C., Arpino, K. ad Llobet, A., and McQueen, T. M. (2012). Orbital-selective magnetism in the spin-ladder iron selenides $Ba_{1-x}K_xFe_2Se_3$. *Phys. Rev. B*, 85(18):180405(R). 87

[35] Caron, J. M., Neilson, J. R., Miller, D. C., Llobet, A., and McQueen, T. M. (2011). Iron displacements and magnetoelastic coupling in the antiferromagnetic spin-ladder compound $BaFe_2Se_3$. *Phys. Rev. B*, 84(18):180409. 87

[36] Castellani, C., Castro, C. D., Feinberg, D., and Ranninger, J. (1979). New model hamiltonian for the metal-insulator transition. *Phys. Rev. Lett.*, 43(26):1957. 115, 127

[37] Chakraverty, B. K., Ranninger, J., and Feinberg, D. (1998). Experimental and theoretical constraints of bipolaronic superconductivity in high T_c materials: An impossibility. *Phys. Rev. Lett.*, 81:433–436. 148

[38] Chan, C.-K., Werner, P., and Millis, A. J. (2009). Magnetism and orbital ordering in an interacting three-band model: a dynamical mean-field study. *Phys. Rev. B*, 80(23):235114. 86, 106

[39] Chang, J., Eremin, I., and Thalmeier, P. (2009). Cooper-pair formation by anharmonic ratting modes in the β-pyrochlore superconductor KOS_2O_6. *New. J. Phys.*, 11(5):055068. 84

[40] Chen, C., Xu, X. Y., Liu, J., Batrouni, G., Scalettar, R., and Meng, Z. Y. (2018). Symmetry enforced self-learning monte carlo method applied to the holstein model. *arXiv:1802.06177*. 162

[41] Chi, S., Johnston, S., Levy, G., Grothe, S., Szedlak, R., Lubrook, B., Liang, R., Dosanjh, P., Burke, S. A., Damascelli, A., Bonn, D. A., Hardy, W. N., and Pennec, Y. (2014). Sign

inversion in the superconducting order parameter of LiFeAs inferred from Bogoliubov quasiparticle interference. *Phys. Rev. B*, 89(10):104522. 99

[42] Chu, J.-H., Kuo, H.-H., Analytis, J. G., and Fisher, I. R. (2012). Divergent nematic susceptibility in an iron arsenide superconductor. *Science*, 337(6095):710. 147

[43] Ciuchi, S. and Fratini, S. (2011). Band dispersion and electronic lifetimes in crystalline organic semiconductors. *Phys. Rev. Lett.*, 106(16):166403. 52

[44] Clay, R. T. and Hardikar, R. P. (2005). Intermediate phase of the one dimensional half-filled Hubbard-Holstein model. *Phys. Rev. Lett.*, 95(9):096401. 125, 166

[45] Clay, R. T. and Mazumdar, S. (2018). From charge- and spin-ordering to superconductivity in the organic charge-transfer solids. 149

[46] Clay, R. T., Ward, A. B., Gomes, N., and Mazumdar, S. (2017). Bond patterns and charge-order amplitude in quarter-filled charge-transfer solids. *Phys. Rev. B*, 95(2017):125114. 148, 167, 169

[47] Coh, S., Cohen, M. L., and Louie, S. G. (2015). Large electron-phonon interactions from FeSe phonons in a monolayer. *New J. Phys.*, 17(7):073027. 21, 114

[48] Coh, S., Cohen, M. L., and Louie, S. G. (2016). Antiferromagnetism enables electron-phonon coupling in iron-based superconductors. *Phys. Rev. B*, 94(10):104505. 21, 114

[49] Cooper, S. L., Reznik, D., Kotz, A., Kariow, M. A., Liu, R., Klein, M. V., Lee, W. C., Giapintzakis, J., Ginsberg, D. M., Veal, B. W., and Paulikas, A. P. (1993). Optical studies of the a-, b-, and c- axis charge dynamics in $YBa_2Cu_3O_{6+x}$. *Phys. Rev. B*, 47(13):8233. 14

[50] Cox, D. E. and Sleight, A. W. (1976). Crystal structure of $Ba_2Bi^{3+}Bi^{5+}O_6$. *Solid State Commun.*, 19(10):969. 9, 157

[51] Cox, D. E. and Sleight, A. W. (1979). Mxied valent $Ba_2Bi^{3+}Bi_{5+}O_6$: structure and properties vs. temperature. *Acta Cryst.*, B35:1. 9

[52] Creffield, C. E., Sangiovanni, G., and Capone, M. (2005). Phonon softening and dispersion in the 1D Holstein model of spinless fermions. *Eur. Phys. J. B*, 44(2):175. 52, 55

[53] Creutz, M. (1980). Monte carlo study of quantized SU(2) gauge theory. *Phys. Rev. D*, 21(8):2308. 30

[54] Cuk, T., Baumberger, F., Lu, D. H., Ingle, N., Zhou, X. J., Eisaki, H., Kaneko, N., Hussain, Z., Devereaux, T. P., Nagaosa, N., and Shen, Z.-X. (2004). Coupling of the B_{1g} phonon to the antinodal electronic states of $Bi_2Sr_2Ca_{0.92}Y_{0.08}Cu_2O_{8+\delta}$. *Phys. Rev. Lett.*, 93(11):117003. 19

[55] Daghofer, M., Nicholson, A., Moreo, A., and Dagotto, E. (2010). Three orbital model for the iron-based superconductors. *Phys. Rev. B*, 81(1):014511. 127

[56] Dagotto, E., Nazarenko, A., and Boninsegni, M. (1994). Flat quasiparticle despersion in the 2D $t - J$ model. *Phys. Rev. Lett.*, 73(5):728. 16

[57] Dai, P. C., Hu, J. P., and Dagotto, E. (2012). Magnetism and its microscopic origin in iron-based high-temperature superconductors. *Nat. Phys.*, 8(10):709. 85

[58] Damascelli, A., Hussain, Z., and Shen, Z.-X. (2003). Angle-resolved photoemission studies of the cuprate superconducors. *Rev. Mod. Phys.*, 75(2):473. 15

[59] Delft, D. v. (2008). Little cup of helium, big science. *Physics Today*, 61(3):36. 1

[60] Devereaux, T. P., Cuk, T., Shen, Z.-X., and Nagaosa, N. (2004). Anisotropic electron-phonon interaction in the cuprates. *Phys. Rev. Lett.*, 93(11):117004. 19, 20

[61] Devereaux, T. P., Virosztek, A., and Zawadowski, A. (1999). Neutron scattering and the B_{1g} phonon in the cuprates. *Phys. Rev. B*, 59(22):14618. 21

[62] Devreese, J. T. (1996). Polarons. *Encycl. Appl, Phys.*, 14:383. 51, 52

[63] Dong, S., Liu, J.-M., and Dagotto, E. (2014). $BaFe_2Se_3$: a high T_C magnetic multiferroic with large ferrielectric polarization. *Phys. Rev. Lett.*, 113(18):187204. 87

[64] Eckstein, M., Kollar, M., Byczuk, K., and Vollhardt, D. (2005). Hopping on the Bethe lattice: exact results for densities of states and dynamical mean-field theory. *Phys. Rev. B*, 71(23):235119. 35

[65] Egami, T. (2007). *Essential role of the lattice in the Mechanism of High Temperature Superconductivity.* Springer Berlin Heidelberg. 17

[66] Egami, T., Fine, B. V., Singh, D. J., Parshall, D., Cruz, C. d. l., and Dai, P. (2010). Spin-lattice coupling in iron-pnictide superconductors. *Physica C: superconductivity and its Applications*, 470:294–295. 21

[67] Emery, V. J. and Reiter, G. (1988). Mechanism for high-temperature superconductivity. *Phys. Rev. B*, 38(7):4547–4556. 14

[68] Engelsberg, S. and Schrieffer, J. R. (1963). Coupled electron-phonon system. *Phys. Rev.*, 131(3):993. 51

[69] Eschring, H. and Koepernik, K. (2009). Tight-binding models for the iron-based superconductors. *Phys. Rev. B*, 80(10):104503. 99

[70] Evtushinsky, D. V., Aichhorn, M., Sassa, Y., Liu, Z.-H., Maletz, J., Wolf, T., Yaresko, A. N., Biermann, S., V., B. S., and Büchner, B. (2016). Direct observation of dispersive lower Hubbard band in iron-based superconductor FeSe. *arXiv*, 1612.02313. 114

[71] Fanfarillo, L. and Bascones, E. (2015). Electronic correlations in Hund metals. *Phys. Rev. B*, 92(7):075136. 85, 113

[72] Ferrero, M., Becca, F., Fabrizio, M., and Capone, M. (2005). Dynamical behavior across the Mott transition of two bands with different bandwidths. *Phys. Rev. B*, 72(20):205126. 85

[73] Foyevtsova, K., Khazraie, A., Elfimov, I., and Swatzky, G. A. (2015). Hybridization effects and bond disproportionation in the bismuth perovskites. *Phys. Rev. B*, 91(12):121114(R). 12, 149, 150, 154

[74] Franchini, C., Sana, A., Marsman, M., and Kresse, G. (2010). Structural, vibrational, and quasiparticle properties of the Peierls semiconductor $BaBiO_3$: a hybrid function and self-consistent GW+vertex-corrections study. *Phys. Rev. B*, 81(8):085213. 19

[75] Fröhlich, H. (1954). Electrons in lattice fields. *Adv. Phys.*, 3:325. 148

[76] Fyer, R. M. and Scalettar, R. T. (1987). Calculation of specific heat and susceptibilities with the use of the Trotter approximation. *Phys. Rev. B*, 36(7):3833–3843. 27

[77] Gao, Y., Wagener, T. J., Weaver, J. H., Arko, A. J., Flandermeyer, B., and Capone, D. W. (1987). Inverse photoemession studies of the empty electronic states and surface stability of $La_{1.85}Sr_{0.15}CuO_4$. *Phys. Rev. B*, 36(7):3971(R). 14

[78] Georges, A., Kotliar, G., Krauth, W., and Rozenberg, M. J. (1996). Dynamical mean-field-theory of strongly correlated fermion systems and the limit of infinite dimensions. *Rev. Mod. Phys.*, 68(1):13. 26, 34, 86, 114, 115

[79] Georges, A., Medici, L. d., and Mravlje, J. (2013). Strong correlations from Hund's coupling. *Annu. Rev. Condens. Matter Phys.*, 4(4):137–178. 16, 85, 113

[80] Goodvin, G. L., Berciu, M., and Sawatzky, G. A. (2006). Green's function of the Holstein polaron. *Phys. Rev. B*, 74(24):245104. 52

[81] Graser, S., Maier, T. A., Hirschfeld, P. J., and Scalapino, D. J. (2009). Near-degeneracy of several pairing channels in multiorbital models for the Fe pnictides. *New J. Phys.*, 11(2):025016. 9, 166

[82] Greger, M., Kollar, M., and Vollhardt, D. (2013). Emergence of a common energy scale close to the orbital-selective Mott transition. *Phys. Rev. Lett.*, 110(4):046403. 86

[83] Grüner, G. (1988). The dynamics of charge-density waves. *Rev. Mod. Phys.*, 60(4):1129. 52

[84] Gull, E., Millis, A. J., Lichtenstein, A. I., Rubtsov, A. N., Troyer, M., and Werner, P. (2011). Continuous-time monte carlo methods for quantum impurity models. *Rev. Mod. Phys.*, 83(2):349. 34

[85] Gull, E., Werner, P., Wang, X., Troyer, M., and Millis, A. J. (2008). Local order and the gapped phase of the Hubbard model: a plaquette dynamical mean-field investigation. *EPL.*, 84(3):37009. 86

[86] Gull, S. F. (1989). *Developments in Maximum Entropy Data Analysis.* Springer Netherlands, Dordrecht. 49

[87] Gurvitvh, M. and Fiory, A. T. (1987). Resistivity of $La_{1.825}Sr_{0.175}CuO_4$ and $YBa_2Cu_3O_7$ to 1100 K: absence of saturation and its implications. *Phys. Rev. Lett.*, 59(12):1337. 19

[88] Hague, J. P., Kornilovitch, P. E., Alexandrov, A. S., and Samson, J. H. (2006). Effects of lattice geometry and interaction range on polaron dynamics. *Phys. Rev. B*, 73:054303. 148

[89] Hair, J. T. W. d. and Blasse, G. (1973). Determination of the valency state of bismuth in $BaBiO_3$ by infrared spectroscopy. *Solid State Commun.*, 12(7):727. 9

[90] Hardikar, R. P. and Clay, R. T. (2007). Phase diagram of the one-dimensional Hubbard-Holstein model at half and quarter filling. *Phys. Rev. B*, 75(8):245103. 131, 145, 166

[91] Hastings, W. K. (1970). Monte carlo sampling methods using markov chains and their applications. *Biometrika*, 57(1):97. 30

[92] Haule, K. and Kotliar, G. (2009). Coherence−incoherence crossover in the normal state of iron oxypnictides and importance of Hund's rule coupling. *New J. Phys.*, 11(2):025021. 113

[93] Held, K. and Vollhardt, D. (1998). Microscopic conditions favoring itinerant ferromagnetism: Hund's rule coupling and orbital degeneracy. *Eur. Phys. J. B*, 5(19):473. 106

[94] Hinks, D. G., Richards, D. R. nad Dabrowski, B., Marx, D. T., and Mitchell, A. W. (1988). The oxygen isotope effect in $Ba_{0.625}K_{0.375}BiO_3$. *Nature*, 335(6189):419. 22

[95] Hirsch, J. E. (1985). Two-dimensional Hubbard model: numerical simulation study. *Phys. Rev. B*, 31(7):4403–4419. 28, 32

[96] Hirsch, J. E. and Fradkin, E. (1982). Effect of quantum fluctuations on the Peierls instability: a monte carlo study. *Phys. Rev. Lett.*, 49(6):402. 145

[97] Hohenadler, M. (2016). Interplay of site and bond electron-phonon coupling in one dimension. *Phys. Rev. Lett.*, 117(20):206404. 148, 167

[98] Hohenadler, M., Evertz, H. G., and Linden, W. v. d. (2004). Quantum monte carlo and variational approaches to the Holstein model. *Phys. Rev. B*, 69(2):024301. 68

[99] Hohenadler, M., Neuber, D., Linden, W. v. d., Wellein, G., Loos, J., and Fehske, H. (2005). Photoemission spectra of many-polaron systems. *Phys. Rev. B*, 71(24):245111. 138

[100] Holstein, T. (1959). Studies of polaron motion: Part i. the molecular-crystal model. *Annals of Physics*, 8:325. 148

[101] Homes, C. C., Dai, Y. M., Schneeloch, J., Zhong, R. D., and Gu, G. D. (2016). Phonon anomalies in some iron telluride materials. *Phys. Rev. B*, 93(12):125135. 21

[102] Hsu, F.-C., Luo, J.-Y., Yeh, K.-W., Chen, T.-K., Huang, T.-W., Wu, P. M., Lee, Y.-C., Huang, Y.-L., Chu, Y.-Y., Yan, D.-C., and Wu, M.-K. (2008). Superconductivity in the PbO-type structure α-FeSe. *Proc. Natl. Acad. Sci.*, 105(38):14262–14264. 5, 21

[103] Huang, Q., Zasadzinski, J. F., Tralshawala, N., Gray, K. E., Hinks, D. G., Peng, J. L., and Greene, R. L. (1990). Tunnelling evedence for predominantly electron-phonon coupling in superconducting $Ba_{1-x}K_xBiO_3$ and $Nd_{2-x}Ce_xCuO_{4-y}$. *Nature*, 347(6291):369. 22

[104] Hubbard, J. (1963). Electron correlations in narrow energy bads. *Proc. Royal Soc. A*, 276(1365):238–257. 25

[105] Iglovikov, V. I., Khatami, E., and Scalettar, R. T. (2015). Geometry dependence of the sign problem in quantum monte carlo simulations. *Phys. Rev. B*, 92(4):045110. 33, 89

[106] Ishida, H. and Liebsch, A. (2010). Fermi-liquid, non-fermi-liquid, and Mott phases in iron pnictides and cuprates. *Phys. Rev. B*, 81(5):054513. 86

[107] Iwano, K. and Nasu, K. (1998). Four-step scenario for doping-induced phase changes in a three-dimensional charge-density-wave system. *Phys. Rev. B*, 57(12):6957. 165

[108] Jarrell, M. and Gubernatis, J. E. (1996). Bayesian inference and the analytic continuation of imaginary-time quantum monte carlo data. *Physics Report*, 269(3):133. 48, 49

[109] Jeon, G. S., Park, T.-H., Han, J. H., Lee, H. C., and Choi, H.-Y. (2004). Dynamical mean-field theory of the Hubbard-Holstein model at half filling: zero temperature metal-insulator and insulator-insulator transitions. *Phys. Rev. B*, 70(12):125114. 120

[110] Jiang, L., Levchenko, S. V., and Rappe, A. M. (2012). Rigorous definition of oxidation states of ion in solids. *Phys. Rev. Lett.*, 108(16):166403. 9

[111] Johnston, D. C. (2010). The puzzle of high temperature superconductivity in layered iron pnictides and chalcogenides. *Adv. Phys.*, 59(6):803. 85

[112] Johnston, S., Mukherjee, A., Elfimov, I., Berciu, M., and Sawatzky, G. A. (2014). Charge disproportionation without charge transfer in the rare-earth-element nickelates as a possible mechanism for the metal-insulator transition. *Phys. Rev. Lett.*, 112:106404. 149

[113] Johnston, S., Nowadnick, E. A., Kung, Y. F., Moritz, B., Scalettar, R. T., and Devereaux, T. P. (2013). Determinant quantum monte carlo study of the two-dimensional single-band Hubbard-Holstein model. *Phys. Rev. B*, 87(23):235133. 52, 55, 70, 166, 167

[114] Johnston, S., Vernay, F., Moritz, B., Shen, Z.-X., Nagaosa, N., Zaanen, J., and Devereaux, T. P. (2010). Systematic study of electron-phonon coupling to oxygen modes across the cuprates. *Phys. Rev. B*, 82(6):064513. 20

[115] Johnston, Steven Sinclair (2010). Electron-phonon coupling in quasi-two-dimensional correlated systems. http://hdl.handle.net/10012/5274. 30, 31

[116] Jurczek, E. (1987). Model study of the semiconductor-metal transition in $BaBi_{1-x}Pb_xO_3$ by use of a spatially inhomogeneous order-parameter approximation. *Phys. Rev. B*, 35(13):6997. 165

[117] Kamihara, Y., Hiramatsu, H., Hirano, M., Kawamura, R., Yanagi, H., Kamiya, T., and Hosono, H. (2006). Iron-based layered superconductor: LaOFeP. *J. Am. Chem. Soc.*, 128(31):10012–10013. 2

[118] Kaneko, U. F., Gomes, P. F., Garcí-Flores, A. F., Yan, J.-Q., Lograsso, T. A., Barberis, G. E., Vaknin, D., and Granado, E. (2017). Nematic fluctuations and phase transitions in LaFeAsO: a Raman scattering study. *Phys. Rev. B*, 96(1):014506. 9

[119] Kasahara, S., Shi, H. J., Hashimoto, K., Tonegawa, S., Mizukami, Y., Shibauchi, T., Sugimoto, K., Fukuda, T., Terashima, T., Nevidomskyy, A. H., and Matsuda, Y. (2012). Electronic nematicity above the structural and superconducting transition in $BaFe_2(As_{1-x}P_x)_2$. *Nature*, 486(7403):382. 9

[120] Kennes, D. M., Wilner, E. Y., Reichman, D. R., and Millis, A. J. (2016). Transient superconductivity from electronic squeezing of optically pumped phonons. *Nature Physics*, 13:479. 23

[121] Khatami, E., Macridin, A., and Jarrell, M. (2008). Effect of long-range hopping on T_C in a two-dimensional Hubbard-Holstein model of the cuprates. *Phys. Rev. B*, 78(6):060502. 114

[122] Khazraie, A., Foyevtsova, K., Elfimov, I., and Sawatzky, G. A. (2018). Oxygen holes and hybridization in the bismuthates. *Phys. Rev. B*, 97(7):075103. 149, 152

[123] Kim, G., Neumann, M., Kim, M., Le, M. D., Kang, T. D., and Noh, T. W. (2015). Suppression of three-dimensional charge density wave ordering via thickness control. *Phys. Rev. Lett.*, 115:226402. 157

[124] Kim, K. H., Jung, C. U., Noh, T. W., and Kim, S. C. (1997). Optical indirect transitions of semiconducting $BaPb_{1-x}BiO_3$. *Phys. Rev. B*, 55(23):15393. 19

[125] Kitou, S., Fujii, T., Kawamoto, T., Katayama, N., Maki, S., Nishibori, E., Sugimoto, K., Takata, M., Nakamura, T., and Sawa, H. (2017). Successive dimensional transition in $(TMTTF)_2PF_6$ revealed by synchrotron x-ray diffraction. *Phys. Rev. Lett.*, 119(6):065701. 169

[126] Knecht, C., Bl´umer, N., and Dongen, P. G. J. v. (2005). Orbital-selective Mott transitions in the anisotropic two-band Hubbard model at finite temperatures. *Phys. Rev. B*, 72(8):081103(R). 85, 86

[127] Koga, A., Kawakami, N., Rice, T. M., and Sigrist, M. (2004). Orbital-selective Mott transitions in the degenerate Hubbard model. *Phys. Rev. Lett.*, 92(21):216402. 113, 122

[128] Kontani, H. and Onari, S. (2010). Orbital-fluctuation-mediated superconductivity in iron pnictides: analysis of the five-orbital Hubbard-Holstein model. *Phys. Rev. Lett.*, 104(15):157001. 114

[129] Ku, L.-C., Trugman, S. A., and Bonča, J. (2002). Dimensionality effects on the holstein polaron. *Phys. Rev. B*, 65:174306. 148

[130] Kuentzler, R., Hornick, C., Dossman, Y., Wegner, S., Farsi, R. E., and Drillon, M. (1991). Superconductivity of Pb, K and Rb-doped $BaBiO_3$. *Physica C*, 184(4-6):316. 22

[131] Kurdestany, J. M. and Satpathy, S. (2017). Mott metal-insulator transition in the doped Hubbard-Holstein model. *Phys. Rev. B*, 96(8):085132. 166

[132] Kurmaev, E. Z., Wilks, R. G., Moewes, A., Skorikov, N. A., Izyumov, Y. A., Finkelstein, L. D., Li, R. H., and Chen, X. H. (2008). X-ray spectra and electronics structures o the iron arsenide superconductors $RFeAsO_{1-x}F_x$ (R = La, Sm). *Phys. Rev. B*, 78(78):220503. 2

[133] Lanatà, N., Strand, H., Giovannetti, G., Hellsing, B., Medici, L. d., and Capone, M. (2013). Orbital selectivity in Hund's metals: the iron chalcogenides. *Phys. Rev. B*, 87(4):045122. 85

[134] Lankau, A., Koepernik, K., Borisenko, S., Zabolotnyy, V., Büchner, B., Brink, J. v. d., and Eschrig, H. (2010). Absence of surface states for LiFeAs investigated using density functional calculations. *Phys. Rev. B*, 82(18):184518. 99

[135] Lanzara, A. (2008). Iron-based superconductor. http://research.physics.berkeley.edu /lanzara/research/pnictide.html. 6

[136] Lanzara, A., Bogdanov, P. V., Zhou, X. J., Keilar, S. A., Feng, D. L., Lu, E. D., Yoshida, T., Eisaki, H., Fujimori, A., Kishio, K., Shimoyama, J. I., Noda, T., Uchida, S., Hussain, Z., and Shen, Z. X. (2001a). Evidence for ubiquitous strong electron-phonon coupling in high-temperature superconductors. *Nature*, 412(6846):510. 19, 149

[137] Lanzara, A., Bogdanov, P. V., Zhou, X. J., Kellar, S. A., Feng, D. L., Lu, E. D., Yoshida, T., Eisaki, H., Fujimori, A., Kishio, K., Shimoyama, J.-I., Noda, T., Uchida, S., Hussain, Z., and Shen, Z.-X. (2001b). Evidence for ubiquitous strong electron-phonon coupling in high-temperature superconductors. *Nature*, 412(6846):510. 52

[138] Lee, D.-H. (2015). What makes the T_C of FeSe/SrTiO$_3$ so high? *Chin. Phys. B*, 24(11):117405. 21

[139] Lee, H., Zhang, Y.-Z., Jeschke, H. O., and Valentí, R. (2011). Orbital-selective phase transition induced by different magnetic states: a dynamical cluster approximation study. *Phys. Rev. B*, 84(2):020401. 86

[140] Lee, H., Zhang, Y.-Z., Jeschke, H. O., Valentí, R., and Monien, H. (2010). Dynamical cluster approximation study of the anisotropic two-orbital Hubbard model. *Phys. Rev. Lett.*, 104(2):026402. 86

[141] Lee, J. J., Schmitt, F. T., Moore, R. G., Johnston, S., Cui, Y.-T., Li, W., Yi, M., Liu, Z. K., Hashimoto, M., Zhang, Y., Lu, D. H., Devereaux, T. P., Lee, D.-H., and Shen, Z.-X. (2014). Interfacial mode coupling as the origin of the enhancement of T_C in FeSe films on SrTiO$_3$. *Nature*, 515(7526):245. 21, 114

[142] Lee, W. S., Johnston, S., Devereaux, T. P., and Shen, Z.-X. (2007). Aspects of electron-phonon self-energy revealed from angle resolved photoemission spectroscopy. *Phys. Rev. B*, 75(19):195116. 19

[143] Lee, W. S., Johnston, S., Moritz, B., Lee, J., Yi, M., Zhou, J., Schmitt, T., Patthey, L., Strocov, V., Kudo, K., Koike, Y., Brink, J. van den, D. T. P., and Shen, Z.-X. (2013). Role of lattice coupling in establishing electronic and magnetic properties in quasi-one-dimensional cuprates. *Phys. Rev. Lett.*, 110(26):265502. 52

[144] Leo, L. D., Civelli, M., and Kotliar, G. (2008). $T = 0$ heavy-fermion quantum critical point as an orbital-selective Mott transition. *Phys. Rev. Lett.*, 101(25):256404. 86

[145] Li, L., Xu, Z., and Chen, S. (2014). Topological phases of generalized Su-Schrieffer-Heeger models. *Phys. Rev. B*, 89(8):085111. 149, 169

[146] Li, S., Dong, X., Yi, D., and Xie, S. (2013). Theoretical investigation on magnetic field effect in organic devices with asymmetrical molecules. *Organics Electronics*, 14(9):2216. 20, 148, 149, 167

[147] Li, S. and Johnston, S. (2015). The effects of non-linear electron-phonon interactions on superconductivity and charge-density-wave correlations. *Europhys. Lett.*, 109(2):27007. 51, 54, 65, 68, 76, 167

[148] Li, S., Kaushal, N., Wang, Y., Tang, Y. Alvarez, G., Nocera, A., Maier, T. A., Dagotto, E., and Johnston, S. (2016). Nonlocal correlations in the orbital selective Mott phase of a one-dimensional multiorbital hubard model. *Phys. Rev. B*, 94(23):235126. 51, 85, 113, 127, 128, 136, 145, 167

[149] Li, S., Khatami, E., and Johnston, S. (2017). Competing phases and orbital-selective behaviors in the two-orbital Hubbard-Holstein model. *Phys. Rev.B*, 95(12):12112(R). 113, 136, 138, 145, 148

[150] Li, S., Nowadnick, E. A., and Johnston, S. (2015). Quasiparticle properties of the nonlinear holstein model at finite doping and temperature. *Phys. Rev. B*, 92:064301. 148

[151] Li, S., Tang, Y., Maier, T. A., and Johnston, S. (2018). Phase competition in a one-dimensional three-orbital hubbard-holstein model. *Phys. Rev. B*, 97:195116. 113

[152] Lieb, E. H. and Wu, F. Y. (1968). Absence of Mott transition in an exact solution of the short-range, one-band model in one dimension. *Phys. Rev. Lett.*, 20(25):1445. 12, 25

[153] Liebsch, A. (2004). Single Mott transition in the multiorbital Hubbard model. *Phys. Rev. B*, 70(16):165103. 85, 86, 87, 120

[154] Liebsch, A. (2005). Novel Mott transitions in a nonisotropic two-band Hubbard model. *Phys. Rev. Lett.*, 95(11):116402. 85, 86

[155] Liebsch, A. and Ishida, H. (2012). Temperature and bath size in exact diagonalization dynamical mean field theory. *J. Phys.: Condens. Matter*, 24(5):053201. 37

[156] Liu, G., Kaushal, N., Li, S., Bishop, C. B., Wang, Y., Johnston, S., Alvarez, G., Moreo, A., and Dagotto, E. (2016). Study of the orbital-selective Mott phases of a one-dimensional three-orbital Hubbard model using computational techniques. *Phys. Rev. E*, 93(6):063313. 86, 88, 89, 91, 94, 96, 99, 127, 128

[157] Loh, E. Y., Gubernatis, J. E., T., S. R., White, S. R., Scalapino, D. J., and L., S. R. (1990). Sign problem in the numerical simulation of many-electron systems. *Phys. Rev. B*, 41(13):9301–9307. 33, 54, 89, 127

[158] Loong, C.-K., Vashishta, P., Kalia, R. K., Jin, W., Degani, M. H., Hinks, D. G., Price, D. L., Jorgensen, J. D., Dabrowski, B., Mitchell, A. W., Richards, D. R., and Zheng, Y. (1992). Phonon density of states and oxygen-isotope effect in $Ba_{1-x}K_xBiO_3$. *Phys. Rev. B*, 45(14):8052. 22

[159] Luo, Q., Foyevtsova, K., Samolyuk, G. D., Reboredo, F., and Dagotto, E. (2014). Magnetic states of the five-orbital Hubbard model for one-dimensional iron-based superconductors. *Phys. Rev. B*, 90(3):035128. 87

[160] Luo, Q., Nicholson, A., Rincón, J., Liang, S., Riera, J., Alvarez, G., Wang, L., Ku, W., Samolyuk, G. D., Moreo, A., and Dagotto, E. (2013). Magnetic states of the two-leg-ladder alkali metal iron selenides AFe_2Se_3. *Phys. Rev. B*, 87(2):024404. 87

[161] Ma, F. and Lu, Z. (2008). Iron-based layered compound lafeaso is an antiferromagnetic semimetal. *Phys. Rev. B*, 78(3):033111. 5

[162] Machida, Y., Tomokuni, K., Isono, T., Izawa, K., Nakajima, Y., and Tamegai, T. (2009). Possible sign-reversing s-wave superconductivity in Co-doped $BaFe_2As_2$ proved by thermal transport measurements. *J. Phys. Soc. Jpn.*, 78(7):073705. 2

[163] Macridin, A., Moritz, B., Jarrell, M., and Maier, T. (2006). Synergistic polaron formation in the Hubbard-Holstein model at small doping. *Phys. Rev. Lett.*, 97(5):056402. 114, 148, 166

[164] Maeda, H., Tanaka, Y., Fukutomi, M., and Asano, T. (1988). A new high-T_C oxide superconductor without a rare earth element. *Jpn. J. Appl. Phys.*, 27(2):209. 1

[165] Mahan, G. D. (1990). *Many-particle Physics*. Springer US. 32

[166] Maier, T., Jarrell, M., Pruschke, T., and Hettler, M. H. (2005). Quantum cluster theories. *Rev. Mod. Phys.*, 77(3):1027. 26

[167] Mandal, S., Cohen, R. E., and Haule, K. (2014). Strong pressure-dependent electron-phonon coupling in FeSe. *Phys. Rev. Lett.*, 89(22):220502. 114

[168] Manh, D. N., Mayou, D., and Cyrot-Lackmann, F. (1986). Electronic strucutre and local charge density wave in $Ba_{1-x}K_xBiO_3$. *EPL*, 13(2):225. 165

[169] Mannella, N. (2014). The magnetic moment enigma in fe-based high temperature superconductors. *J. Phys.: Condens. Matter*, 26(47):473202. 85

[170] Mannella, N., Yang, W. L., Zhou, X. J., Zheng, H., Mitchell, J., Zaanen, J., Devereaux, T. P., Nagaosa, N., Hussain, Z., and Shen, Z.-X. (2005). Nodal quasiparticle in pseudogapped colossal magnetoresistive manganites. *Nature*, 438(7067):474. 52

[171] Marchand, D. J. J., De Filippis, G., Cataudella, V., Berciu, M., Nagaosa, N., Prokof'ev, N. V., Mishchenko, A. S., and Stamp, P. C. E. (2010). Sharp transition for single polarons in the one-dimensional su-schrieffer-heeger model. *Phys. Rev. Lett.*, 105:266605. 148

[172] Marsiglio, F. (1990). Pairing and charge-density-wave correlations in the Holstein model at half filling. *Phys. Rev. B*, 42(4):2416. 32, 33, 52, 55, 73

[173] Mattheiss, L. F., Gyorgy, E. M., and Johnson, D. W. (1998). Superconducting above 20 k in the Ba-K-Bi-O system. *Phys. Rev. B*, 37(7):3745–3746. 12

[174] Mazin, I. I. and Schmalian, J. (2009). Pairing symmetry and pairing state in ferropnictides: theoretical overview. *Physica C*, 469(9-12):614–627. 2

[175] Mazumdar, S. and Ramasesha, S. (1999). Theory of coexisting charge and spin-density waves in $(TMTTF)_2Br$, $(TMTSF)_2PF_6$, and $\alpha-(BEDT-TTF)_2MHg(SCN)_4$. *Phys. Rev. Lett.*, 82(7):1522. 169

[176] Medarde, M. L. (1997). Structural, magnetic and electronic properties of $RNiO_3$ perovskites (R = rare earth). *J. Phys. Condens. Matter*, 9(8):1679. 149

[177] Medici, L. d. (2011). Hunds coupling and its key role in tuning multiorbital correlations. *Phys. Rev. B*, 83(20):205112. 117

[178] Medici, L. d., Georges, A., and Biermann, S. (2005). Orbital-selective Mott transition in multiband systems: slave-spin representation and dynamical mean-field theory. *Phys. Rev. B*, 72(20):205124. 85, 86

[179] Medici, L. d., Giovannetti, G., and Capone, M. (2014). Selective Mott physics as a key to iron superconductors. *Phys. Rev. Lett.*, 112(17):177001. 85, 106, 113

[180] Medici, L. d., Hassan, S. R., Capone, M., and Dai, X. (2009). Orbital-selective Mott transition out of band degeneracy lifting. *Phys. Rev. Lett.*, 102(12):126401. 85, 86, 122

[181] Meissner, W. and Ochsenfeld, R. (1933). Ein neuer effekt bei eintritt der supraleitfahigkeit. *Naturwissenschaften*, 21(44):787–788. 1

[182] Menushenkov, A. P. and Klementev, K. V. (2000). Extended x-ray absorption fine-structure indication of a double-well potential for oxygen vibration in $Ba_{1-x}K_xBiO_3$. *J. Phys. Condens. Matter*, 12(16):3767. 9

[183] Meregalli, V. and Savrasov, S. Y. (1998). Electron-phonon coupling and properties of doped $BaBiO_3$. *Phys. Rev. B*, 57(22):14453. 17

[184] Meyer, D., Hewson, A. C., and Bulla, R. (2002). Gap formation and soft phonon mode in the Holstein model. *Phys. Rev. Lett.*, 89(19):196401. 120

[185] Mishchenko, A. S., Nagaoso, N., and Prokof'ev, N. (2014). Diagrammatic monte carlo method for many-polaron problems. *Phys. Rev. Lett*, 113(16):166402. 65

[186] Möller, M. M., Sawatzky, G. A., Franz, M., and Berciu, M. (2017). Type-ii dirac semimetal stabilized by electron-phonon coupling. *Nat. Commun.*, 8(1):2267. 149

[187] Mukherjee, A., Patel, N. D., Moreo, A., and Dahotto, E. (2016). Orbital selective directional conductor in the two-orbital Hubbard model. *Phys. Rev. B*, 93(8):085144. 85

[188] Murakami, Y., Werner, P., Tsuji, N., and Aoki, H. (2013). Ordered phases in the Holstein-Hubbard model: interplay of strong coulomb interaction and electron-phonon coupling. *Phys. Rev. B*, 88(12):125126. 114, 148

[189] Nagamatsu, J., Nakagawa, N., Muranaka, T., Zenitani, Y., and Akimitsu, J. (2001). Superconductivity at 39 K in magnesium diboride. *Nature*, 410(6824):63–64. 1

[190] Nakayama, K., Miyata, Y., Phan, G. N., Sato, T., Tanabe, Y., Urata, T., Tanigaki, K., and Takahashi, T. (2014). Reconstruction of band structure induced by electronic nematicity in an FeSe superconductor. *Phys. Rev. Lett.*, 113(23):237001. 9

[191] Namatame, H., Fujimori, A., Takagi, H., Uchida, S., Groot, F. M. d., and Fuggle, J. C. (1993). Electronic strutctue and the metal-semiconductor transition in $BaPb_{1-x}Bi_xO_3$ studied by photoemission and x-ray-absorption spectroscopy. *Phys. Rev. B*, 48(23):16917. 19

[192] Newns, D. M. and Tsuei, C. C. (2007). Fluctuation Cu-O-Cu bond model of high-temperature superconductivity. *Nat. Phys.*, 3(542):184. 84

[193] Nocera, A., Soltanieh-ha, M., Perroni, C. A., Cataudella, V., and Feiguin, A. E. (2014). Interplay of charge, spin, and lattice degrees of freedom in the spectral properties of the one-dimensional Hubbard-Holstein model. *Phys. Rev. B*, 90(19):195134. 114

[194] Nomura, Y., Sakai, S., and Arita, A. (2015). Nonlocal correlations induced by Hund's coupling: a cluster DMFT study. *Phys. Rev. B*, 91(23):235107. 86, 98

[195] Nowadnick, E. A., Johnston, S., Moritz, B., and Devereaux, T. P. (2015). Renormalizetion of spectra by phase competition in the half-filled Hubbard-Holstein model. *Phys. Rev. B*, 91(16):165127. 73

[196] Nowadnick, E. A., Johnston, S., Moritz, B., Scalettar, R. T., and Devereaux, T. P. (2012). Competition between antiferromagnetic and charge-density-wave order in the half-filled Hubbard-Holstein model. *Phys. Rev. Lett.*, 109(24):246404. 114, 117, 125, 148, 166, 167

[197] Oya, G. and Saur, E. J. (1979). Preparation of Nb_3Ge films by chemical transport reaction and their critical properties. *J. Low Temp. Phys.*, 34(5):569–583. 1

[198] Paglione, J. and Greene, R. L. (2010). High-temperature superconductivity in iron-based materials. *Nature Physics*, 6(9):645. 5, 7

[199] Park, H., Haule, K., and Kotliar, G. (2008a). Cluster dynamical mean field theory of the Mott transition. *Phys. Rev. Lett.*, 101(18):186403. 86, 87

[200] Park, H., Millis, A. J., and Marianetti, C. A. (2012). Site-selective Mott transition in rare-earth-element nickelates. *Phys. Rev. Lett.*, 109(15):156402. 149

[201] Park, S. R., Song, D. J., Leem, C. S., Kim, Chul, K. C., Kim, B. J., and Eisaki, H. (2008b). Angle-resolved photoemission spectroscopy of electron-doped cuprate supercodnctors: isotropic electron-phonon coupling. *Phys. Rev. Lett.*, 101(11):117006. 20

[202] Parlett, B. N. and Scott, D. S. (1979). The Lanczos algorithm with selective orthogonalization. *Mathematics of computation*, 33(145):217. 40

[203] Patel, N. D., Nocera, A., Alvarez, G., Arita, R., Moreo, A., and Dagotto, E. (2016). Magnetic properties and pairing tendencies of the iron-based superconducting ladder $BaFe_2S_3$: combined *ab initio* and density matrix renormalization group study. *Phys. Rev. B*, 94(7):075119. 87, 101

[204] Pei, S. and Jorgensen, J. D. (1990). Structural phase diagram of the $Ba_{1-x}K_xBiO_3$. *Phys. Rev. B*, 41(7):4126. 9

[205] Pickett, W. E. (1989). Electronic structure of the high-temperature oxide superconductors. *Rev. Mod. Phys.*, 61(2):433. 2

[206] Pintschovius, L. and Braden, M. (1999). Anomalous dispersion of LO phonons in $La_{1.85}Sr_{0.15}CuO_4$. *Phys. Rev. B*, 60(22):15039. 19

[207] Plumb, N. C., Gawryluk, D. J., Wang, Y., Ristić, Z., Park, J., Lv, B. Q., Wang, Z., Matt, C. E., Xu, N., Shang, T., Conder, K. Mesot, J., Johnston, S., Shi, M., and Radović, M. (2016). Momentum-resolved electronic structure of the high-T_C superconductor parent compound $BaBiO_3$. *Phys. Rev. Lett.*, 117(3):037002. 11, 12, 13, 19, 149, 150, 154

[208] Pomarico, E., Mitrano, M., Bromberger, H., Sentef, M. A., Al-Temimy, A., Coletti, C., StÖhr, A., Link, S., Starke, U., Cacho, C., Chapman, R., Springate, E., Cavalleri, A., and Gierz, I. (2017). Enhanced electron-phonon coupling in graphene with periodically distorted lattice. *Phys. Rev. B*, 95(2):024304. 23

[209] Prelovsek, P., Rice, T. M., and Zhang, F. C. (1987). Bi-polaron condensation induced by doping of charge-density-wave systems. *J. Phys. Rev. C: Solid State Phys.*, 20(13):L229. 165

[210] Prokof'ev, N. V. and Svistunov, B. V. (1998). Polaron problem by diagrammatic quantum monte carlo. *Phys. Rev. Lett.*, 81:2514–2517. 148

[211] Qazilbash, M. M., Hamlin, J. J., Baumbach, R. E., Zhang, L., Singh, D. J., Maple, M. B., and Basov, D. N. (2009). Electronic correlations in the iron pnictides. *Nature Physics*, 5(9):647–650. 16

[212] Rademaker, L., Johnston, S., Zaanen, J., and Brink, J. v. d. (2013). Determinant quantum monte carlo study of exciton condensation in the bilayer Hubbard model. *Phys. Rev. B*, 88(23):235115. 89

[213] Rademaker, L., Wang, Y., Berlijin, T., and Johnston, S. (2016). Enhanced superconductivity due to forward scattering in fese thin films on $SrTiO_3$ substrates. *New J. Phys.*, 18(2):022001. 21, 114

[214] Rahman, M. A., Rahaman, M. Z., and Samsuddoha, M. N. (2015). A review on cuprate based superconducting materials including characteristics and applications. *Am. J. Phys. Appl.*, 3(2):39. 2, 4

[215] Reznik, D., Pintschovius, L., Ito, M., Likubo, S., Sato, M., Goka, H., Fujita, M., Yamada, K., Gu, G. D., and Tranquada, J. M. (2006). Electron-phonon coupling reflecting dynamic charge inhomogeneity in copper oxide superconductors. *Nature*, 440(7088):1170. 20

[216] Reznik, D., Pintschovius, L., Tranquada, J. M., Arai, M., Endoh, Y., Masui, T., and Tajima, S. (2008). Temperature dependence of the bond-stretching phonon anomaly in $YBa_2Cu_3O_{0.95}$. *Phys. Rev. B*, 78(9):094507. 20

[217] Rice, T. M. and Sneddon, L. (1981). Real-space and $\vec{k}$-space electron pairing in $BaPb_{1-x}Bi_xO_3$. *Phys. Rev. Lett.*, 47(9):689. 9, 17, 157, 165

[218] Rincón, J., Moreo, A., Alvarez, G., and Dagotto, E. (2014a). Exotic magnetic order in the orbital-selective Mott regime of multiorbital systems. *Phys. Rev. Lett.*, 112(10):106405. 86, 87, 88, 89, 91, 94, 99, 109, 127, 128

[219] Rincón, J., Moreo, A., Alvarez, G., and Dagotto, E. (2014b). Quantum phase transition between orbital-selective Mott states in Hund's metals. *Phys. Rev. B*, 90(24):241105(R). 86, 87, 88, 89, 91, 94

[220] Roekeghem, A. v., Richard, P., Ding, H., and Biermann, S. (2016). Spectral properties of transition metal pnictides and chalcogenides: angle-resolved photoemission spectroscopy and dynamical mean field theory. *C. R. Phys.*, 17(1-2):140. 85, 86, 99

[221] Romero, A. H., Brown, D. W., and Lindenberg, K. (1999). Polaron effective mass, band distortion, and self-trapping in the holstein molecular-crystal model. *Phys. Rev. B*, 59:13728–13740. 148

[222] Rotter, M., Tegel, M., and Johrendt, D. (2008). Superconductivity at 38 K in the iron arsenide $(Ba_{1-x}K_x)Fe_2As_2$. *Phys. Rev. Lett.*, 101(10):107006. 5

[223] S., T. and Hirsch, J. E. (1988). Peierls instability in the two-dimensional half-filled Hubbard model. *Phys. Rev. B*, 37(16):9546. 149, 169

[224] S. Gerber, S. L. Yang, D. Z. H. S. J. A. S. S. R. J. J. L. T. J. b. M. C. J. A. G. Y. L. D. L. Y. Z. L. C. W. L. H. J. J. S. L. M. Y. G. L. D. S. S. J. M. G. S. N. K. W. K. Y. D. C. Z. H. R. G. M. T. P. D. W. S. L. P. S. K. Z. X. S. (2017). Femtosecond electron-phonon lock-in by potoemission and x-ray free-electron laser. *Science*, 357(6346):71–75. 21

[225] Saito, T., Onari, S., and Kontani, H. (2010). Orbital fluctuation theory in iron pnictides: effects of As-Fe-As bond angle, isotope substitution, and z^2-orbital pocket on superconductivity. *Phys. Rev. B*, 82(14):144510. 114

[226] Sakamoto, H., Momoi, T., and Kubo, K. (2002). Ferromagnetism in the one-dimensional Hubbard model with orbital degeneracy: from low to high electron density. *Phys. Rev. B*, 65(22):224403. 106

[227] Sangiovanni, G., Gunnarsson, O., Koch, E., Castellani, C., and Capone, M. (2006). Electron-phonon interaction and antiferromagnetic correlations. *Phys. Rev. Lett.*, 97(4):046404. 114, 148

[228] Scalapino, D. J. (1995). The case for $d_{x^2-y^2}$ pairing in the cuprate superconductors. *Physcs Reports*, 250(6):329. 2

[229] Scalapino, D. J. (2012). A common thread: the pairing interaction for unconventional superconductors. *Rev. Mod. Phys.*, 84(4):1383. 2

[230] Scalettar, R. T., E., B. N., and J., S. D. (1989). Competition of pairing and peierls-charge-density-wave correlations in a two-dimensional electron-phonon model. *Phys. Rev. B*, 40(1):197. 32, 33, 55, 62

[231] Scalettar, R. T., Scalapino, D. J., and Sugar, R. L. (1986). New algorithm for the numerical simulation of fermions. *Phys. Rev. B*, 34(1):7911–7917. 27, 52, 55

[232] Schilling, A., Cantoni, M., Guo, J. D., and Ott, H. R. (1993). Superconductivity above 130 K in the Hg-Ba-Ca-Cu-O system. *Nature*, 363(6426):56–58. 2

[233] Sémon, P., Haule, K., and Kotliar, G. (2017). Validity of the local approximation in iron pnictides and chalcogenides. *Phys. Rev. B*, 95(19):195115. 85, 86, 95

[234] Sengupta, P., Sandvik, A. W., and Campbell, D. K. (2003). One-dimensional extended Peierls-Hubbard model at half-filling. *Phys. Rev. B*, 67(24):245103. 148, 167

[235] Sentef, M. A. (2017). Light-enhanced electron-phonon coupling from nonlinear electron-phonon coupling. *Phys. Rev. B*, 95(20):105111. 23

[236] Shamblin, J., Heres, M., Zhou, H., Sangoro, J., Lang, M., Neuefeind, J., Alonso, J. A., and Johnston, S. (2018). Experimental evidence for bipolaron condensation as a mechanism for the metal-insulator transition in rare-earth nickelates. *Nat. Commun.*, 9:86. 149, 150

[237] Shen, Z.-X., Allen, J. W., Yeh, J. J., Kang, J. S., Ellis, W., Spicer, W., Lindau, I., Maple, M. B., Dalichaouch, Y. D., Torikachvili, M. S., SUn, J. Z., and Geballe, T. H. (1987). Anderson hamiltonian description of the experimental electronic structure and magnetic interactions of cooper oxide superconductors. *Phys. Rev. B*, 36(16):8414. 14

[238] Shirage, P. M., Kihou, K., Lee, C., Kito, H., Eisaki, H., and Iyo, A. (2011). Emergence of superconductivity in "32522" structure of $(Ca_3Al_2O_{5-y})(Fe_2Pn_2)$ (Pn=As and P). *J. Am. Chem. Soc.*, 133(25):9630–9633. 5

[239] Sous, J., Chakaraborty, M., Krems, R. V., and Berciu, M. (2018). Light bipolarons stabilized by peierls electron-phonon coupling. *arXiv:1805.06109*. 148, 149

[240] Stewart, G. R. (2011). Superconductivity in iron compounds. *Rev. Mod. Phys.*, 83(4):1589. 85

[241] Streltsov, S. V. and Khomskii, D. I. (2014). Orbital-dependent singlet dimers and orbital-selective peierls transitions in transition-metal compounds. *Phys. Rev. B*, (16):161112(R). 147

[242] Su, W. P., Schrieffer, J. R., and Heeger, A. J. (1979). Solitons in polyacetylene. *Phys. Rev. Lett.*, 42(25):1698. 148, 149, 167

[243] Su, W. P., Schrieffer, J. R., and Heeger, A. J. (1980). Soliton excitations in polyacetylene. *Phys. Rev. B*, 22(4):2099. 20

194

[244] Sun, J. P., Matsuura, K., Ye, G. Z., Mizukami, Y., Shimozawa, M., Matsubayashi, K., Yamashita, M., Watashige, T., Kasahara, S., Matsuda, Y., Yan, J.-Q., Sales, B. C., Uwatoko, Y., Cheng, J.-G., and Shibauchi, T. (2016). Dome-shaped magnetic order competing with high-temperature superconductivity at high pressures in FeSe. *Nature Commun.*, 7:12146. 147

[245] Tacon, M. L., Bosak, A., Souliou, S. M., Dellea, G., Loew, T., Heid, R., Bohnen, K.-P., Ghiringhelli, G., Krisch, M., and Keimer, B. (2014). Inelastic x-ray scattering in $YBa_2Cu_3O_{6.6}$ reveals giant phonon anomalies and elastic central peak due to charge-density-wave formation. *Nature Physics*, 10(1):52. 20

[246] Taraphder, A., Krishnamurthy, H. R., Pandit, R., and Ramakrishnan, T. V. (1993). Exotic physics in the negative-U, extended-Hubbard model for Barium Bismuthates? *EPL.*, 21(1):79. 17

[247] Taraphder, A., Krishnamurthy, H. R., Pandit, R., and Ramakrishnan, T. V. (1995). Negative-U extended Hubbard model for doped barium bismuthates. *Phys. Rev. B*, 52(21):1368. 17

[248] Trivedi, N. and Randeria, M. (1995). Deviations from fermi-liquid behavior above T_C in 2D short coherence length superconductors. *Phys. Rev. Lett.*, 75(2):312. 58, 96, 134

[249] Trivedi, N., Scalettar, R. T., and Randeria, M. (1996). Superconductor-insulator transition in a disordered electronic system. *Phys. Rev. B*, 54(6):3756(R). 157

[250] Uchida, S., Ido, T., Takagi, H., Arima, T., Tokura, Y., and Tajima, S. (1991). Optical spectra of $La_{2-x}Sr_xCuO_4$: effect of carrier doping on the electronic structure of the CuO_2 plane. *Phys. Rev. B*, 43(10):7942. 14

[251] Varma, C. M. (1988). Missing valence states, diamagnetic insulators, and superconductors. *Phys. Rev. Lett.*, 61(23):2713. 9, 14, 17

[252] Vekic, M. and White, S. R. (1993). Gap formation in the density of states for the Holstein model. *Phys. Rev. B*, 48(10):7643. 73

[253] Vielsack, G. and Weber, W. (1996). Search for negative U in the $Ba_{1-x}K_xBi_{1-y}Pb_yO_3$ system using constrained density-functional theory. *Phys. Rev. B*, 54(9):6614. 22

[254] Voo, K.-K. and Mou, C.-Y. (2004). Phases and density of states in a generalized Su-Schrieffer-Heeger model. *Phys. B*, 344(1-4):224. 149, 169

[255] Wang, Q., Shen, Y., Pan, B., Hao, Y., Ma, M., Zhou, F., Steffens, P., Schmalzl, K., Forrest, T. R., Abdel-Hafiez, M., Chen, X., Chareev, D. A., Vasiliev, A. N., Bourges, P., Sidis, Y., Cao, H., and Zhao, J. (2016a). Strong interplay between stripe spin fluctuations, nematicity and superconductivity in FeSe. *Nature Materials*, 15(2):159–163. 9

[256] Wang, Q. L., Zhi, L., Zhang, W.-H., Zhang, Z.-C., Zhang, J.-S., Li, W., Ding, H., Ou, Y.-B., Deng, P., and Chang, K. (2012). Interface-induced high-temperature superconductivity in single unit-cell FeSe films on $SrTiO_3$. *Chin. Phys. Lett.*, 29(3):037402. 114

[257] Wang, X. C., Liu, Q. Q., Lv, Y. X., Gao, W. B., Yang, L. X., Yu, R. C., Li, F. Y., and Jin, C. Q. (2008). The superconductivity at 18 K in LiFeAs system. *Solid State Commun,*, 148(11-12):538–540. 5

[258] Wang, Y., Linscheid, A., Berlijin, T., and Johnston, S. (2016b). *Ab initio* study of cross-interface electron-phonon couplings in FeSe thin films on $SrTiO_3$ and $BaTiO_3$. *Phys. Rev. B*, 93(13):134513. 21

[259] Wang, Y., Nakatsukasa, K., Rademaker, L., Berlijin, T., and Johnston, S. (2016c). Aspects of electron-phonon interactions with strong forward scattering in FeSe thin films on $SrTiO_3$ substrates. *Supercond. Sci. Technol.*, 29(5):054009. 21

[260] Watson, M. D., Backes, S., Haghighirad, A. A., Hoesch, M., Kim, T. K., Coldea, A. I., and Valenti, R. (2017). Formation of Hubbard-like bands as a fingerprint of strong electron-electron interactions in FeSe. *Phys. Rev. B*, 95(8):081106. 114

[261] Watson, M. D., Kim, T. K., Haghighirad, A. A., Davies, N. R., McCollam, A., Narayanan, A., Blake, S. F., Chen, Y. L., Ghannadzadeh, S., Schofield, A. J., Hoesch, M.,

Meinqast, C., Wolf, T., and Coldea, A. I. (2015). Emergence of the nematic electronic state in FeSe. *Phys. Rev. B*, 91(15):155106. 9

[262] Weber, M., Assaad, F. F., and Hohenadler, M. (2015). Phonon spectral function of the one-dimensional Holstein-Hubbard model. *Phys. Rev. B*, 91(23):235150. 73

[263] Weber, W. (1987). Electron-phonon interaction in the new superconductors $La_{2-x}(Ba, Sr)_x CuO_4$. *Phys. Rev. Lett.*, 58(13):1371. 149

[264] Werner, P. and Eckstein, M. (2013). Phonon-enhanced relaxation and excitation in the Holstein-Hubbard model. *Phys. Rev. B*, 88(16):125126. 114

[265] Werner, P., Emanuel, G., Troyer, M., and Millis, A. J. (2008). Spin freezing transition and non-fermi-liquid self-energy in a three-orbital model. *Phys. Rev. Lett.*, 101(16):166405. 16

[266] Werner, P. and Millis, A. J. (2007). High-spin to low-spin and orbital polarization transitions in multiorbital Mott systems. *Phys. Rev. Lett.*, 99(12):126405. 85, 86

[267] Wertheim, G. K., Remeika, J. P., and Buchanan, D. N. E. (1982). Electronic structure of $BaPb_{1-x}Bi_x O_3$. *Phys. Rev. B*, 26(4):2120. 9

[268] White, S. R., Scalapino, D. J., and Sugar, R. L. (1989a). Monte carlo calculation of dynamical properties of the two-dimensional Hubbard model. *Phys. Rev. Lett.*, 63(14):1523. 12

[269] White, S. R., Scalapino, D. J., Sugar, R. L., Loh, E. Y., Gubernatis, J. E., and Scalettar, R. T. (1989b). Numerical study of the two-dimensional Hubbard model. *Phys. Rev. B*, 40(1):506–516. 27, 29, 30, 32, 33, 54

[270] Wilson, S. D., Dai, P., Li, S., Chi, S., Kang, H. J., and Lynn, J. W. (2006). Resonance in the electron-doped high-transition-temperature superconductor $Pr_{0.88}LaCe_{0.12}CuO_{4-\delta}$. *Nature*, 442(7098):59. 20

[271] Xu, B., Dai, Y. M., Shen, B., Xiao, H., Ye, Z. R., Forget, A., Colson, D., Feng, D. L., Wen, H. H., and Homes, C. C. (2015). Anomalous phonon redshift in K-doped $BaFe_2As_2$ iron pnictides. *Phys. Rev. B*, 91(10):104510. 21

[272] Yamada, T., Ishizuka, J., and Ōno, Y. (2014). Metal-insulator transition and superconductivity in the two-orbital Hubbard-Holstein model for iron-based superconductors. *J. Phys. Soc. Jpn.*, 83(4):044711. 114

[273] Yang, W. L., Sorini, A. P., Chen, C. C., Moritz, B., Lee, W. S., Vernay, F., Olalde-Velasco, P., Denlinger, J. D., Delley, B., Chu, J. H., Analytis, J. G., Fisher, I. R., Ren, Z. A., Yang, J., Lu, W., Zhao, Z. X., Brink, J. v. d., Hussain, Z., Shen, Z. X., and Devereaux, T. P. (2009). Evidence for weak electronic correlations in iron pnictides. *Phys. Rev. B*, 80(1):014508. 16

[274] Yarmoff, J. A., Clarke, D. R., Drube, W., Karlsson, U. O., Taleb-Ibrahimi, A., and Himpsel, F. J. (1987). Valence of electronic structure of $Y_1Ba_2Cu_3O_7$. *Phys. Rev. B*, 36(7):3976. 14

[275] Yi, M., Liu, Z. K., Yu, R., Zhu, J. X., Lee, J. J., Moore, R. G., Schmitt, F. T., Li, W., Riggs, S. C., Chu, J. H., Lv, B., Hu, J., Hashimoto, M., Mo, S. K., Hussain, Z., Mao, Z. Q., Chu, C. W., Fisher, I. R., Shen, Z. X., and Lu, D. H. (2015). Observation of universal strong orbital-dependent correlation effects in iron chalcogenides. *Nature Communication*, 6(0):7777. 16, 17

[276] Yi, M., Lu, D. H., Yu, R., Riggs, S. C., Chu, J. H., Lv, B., Liu, Z. K., Lu, M., Cui, Y. T., Hashimoto, M., Mo, S. K., Hussain, Z., Chu, C. W., Fisher, I. R., Si, Q., and Shen, Z. X. (2013). Observation of temperature-induced crossover to an orbital-selective Mott phase in $A_xFe_{2-y}Se_2$ (A=K, Rb) superconductors. *Phys. Rev. Lett.*, 110(6):067003. 17, 111, 113

[277] Yildirim, T., Gülseren, O., Lynn, J. W., Brown, C. M., Udovic, T. J., Huang, Q., Rogado, N., Regan, K. A., Hayward, M. A., Slusky, J. S., He, T., Haas, M. K., Khalifah,

P., Inumaru, K., and Cava, R. J. (2001). Giant anharmonicity and nonlinear electron-phonon coupling in MgB_2: a combined first-rinciples calculation and neutron scattering study. *Phys. Rev. Lett.*, 87(3):037001. 22, 52, 84

[278] Yin, Z. P., Haule, K., and Kotliar, G. (2011). Kinetic frustration and the nature of the magnetic and paramagnetic states in iron pnictides and iron chalcogenides. *Nat. Mat.*, 10(12):932. 85

[279] Yin, Z. P., Kutepov, A., and Kotliar, G. (2013). Correlation-enhanced electron-phonon coupling: application of GW and screed hybrid functional to bismuthates, chloronitrides, and other high T_C superconductors. *Phys. Rev. X*, 3(2):021011. 19

[280] Yndurain, F. and Soler, J. M. (2009). Anomalous electron-phonon interaction in doped LaFeAsO: first-principles calculations. *Phys. Rev. B*, 79(13):134506. 21, 114

[281] Yu, J., Chen, X. Y., and Su, W. P. (1990). Doping of charge density wave in $Ba_{1-x}K_xBiO_3$. *Phys. Rev. B*, 41(1):344. 165

[282] Yu, R. and Si, Q. (2013). Orbital-selective Mott phase in multiorbital models for alkaline iron selenides $K_{1-x}Fe_{2-y}Se_2$. *Phys. Rev. Lett.*, 110(14):146402. 16, 17, 18, 85

[283] Yuan, Q. and Kopp, T. (2002). Coexistence of the bond-order wave and antiferromagnetism in a two-dimensional half-filled Peierls-Hubbard model. *Phys. Rev. B*, 65(8):085102. 169

[284] Zaanen, J., A., S. G., and Allen, J. W. (1985). Band gaps and electronic structure of transition-metal compounds. *Phys. Rev. Lett.*, 55(4):418–421. 14

[285] Zamborszky, F., Yu, W., Raas, W., Brown, S. E., Alavi, B., Merlic, C. A., and Baur, A. (2002). Competition and coexistence of bond and charge orders in $(TMTTF)_2AsF_6$. *Phys. Rev. B*, 66(8):081103(R). 169

[286] Zanoni, R., Chang, Y., Tang, M., Hwu, Y., Onellion, M., Margaritondo, G., Morris, P. A., Bonner, W. A., Tarascon, J. M., and Stoffel, N. G. (1988). Soft-x-ray photoemission study of the electronic structure of $Bi_4Ca_3Sr_3Ci_4O_{16+x}$. *Phys. Rev. B*, 38(16):11832. 14

[287] Zasadzinkski, J. F. and Tralshawala, N. (1989). Tunneling spectroscopy in superconducting $Ba_{1-x}K_xBiO_3$. *Physica C*, 158(3):519. 22

[288] Zhang, F. C. and Rice, T. M. (1988). Effectively hamiltonian for the superconducting Cu oxides. *Phys. Rev. B*, 37(7):3759. 14

[289] Zhang, W., Hwang, C., Smallwood, C. L., Miller, T. L., Affeldt, G., Kurashima, K., Jozwiak, C., Eisaki, H., Adachi, T., Koike, Y., Lee, D. H., and Lanzara, A. (2013). Ultrafast quenching of electron-boson interaction and superconducting gap in a cuprate superconductor. *Nat. Commun.*, 5(5959):1–6. 23, 166

[290] Zhang, Y., Chen, F., He, C., Zhou, B., Xie, B. P., Fang, C., Tsai, W, F., Chen, X. H., Hayashi, H., Jiang, J., Iwasawa, H., Shimada, K., Namatame, H., Taniguchi, M., Hu, J, P., and Feng, D. L. (2011). Orbital characters of band in the iron-based superconductor $BaFe_{1.85}Co_{0.15}As_2$. *Phys. Rev. B*, 83(5):054510. 9, 10

[291] Zhang, Y. Z., Lee, H., Lin, H. Q., Wu, C. Q., Jeschke, H. O., and Valentí, R. (2012). General mechanism for orbital selective phase transitions. *Phys. Rev. B*, 85(3):035123. 85

[292] Zoli, M. (2005). Path integral of the two-dimensional Su-Schrieffer-Heeger model. *Phys. Rev. B*, 71(20):205111. 149, 169

Appendices

Appendix A

Applications of the DQMC to a three-orbital Hubbard model

The three-orbital Hubbard Hamiltonian is given by

$$
\begin{aligned}
H &= H_0 + H_1 + H_2 + H_3 \\
H_0 &= -\sum_{i,\sigma,\gamma,\gamma'} t_{\gamma,\gamma'}(c^\dagger_{i,\gamma,\sigma} c_{i+1,\gamma',\sigma} + h.c.) + \sum_{i,\gamma,\sigma} \Delta_\gamma \hat{n}_{i,\gamma,\sigma} \\
H_1 &= U \sum_{i,\gamma} \hat{n}_{i,\gamma,\uparrow} \hat{n}_{i,\gamma,\downarrow} + U' \sum_{i,\gamma<\gamma',\sigma} \hat{n}_{i,\gamma,\sigma} \hat{n}_{i,\gamma',-\sigma} \\
H_2 &= (U' - J) \sum_{i,\gamma<\gamma',\sigma} \hat{n}_{i,\gamma,\sigma} \hat{n}_{i,\gamma',\sigma} \\
H_3 &= J \sum_{i,\gamma\neq\gamma'} (c^\dagger_{i,\gamma,\uparrow} c^\dagger_{i,\gamma',\downarrow} c_{i,\gamma,\downarrow} c_{i,\gamma',\uparrow} + c^\dagger_{i,\gamma,\uparrow} c^\dagger_{i,\gamma,\downarrow} c_{i,\gamma',\downarrow} c_{i,\gamma',\uparrow}).
\end{aligned}
$$

Here, $c^\dagger_{i,\gamma,\sigma}$ $(c_{i,\gamma,\sigma})$ creates (annihilates) spin σ electron in orbital $\gamma = 1, 2, 3$ on site i; $t_{\gamma,\gamma'}$ are the hopping integrals between orbital γ and γ'; Δ_γ are the onsite energies for each orbital; $\hat{n}_{i,\gamma,\sigma} = c^\dagger_{i,\gamma,\sigma} c_{i,\gamma,\sigma}$ is the particle number operator; U and U' are the onsite intra- and inter-orbital Coulomb repulsions; J is the Hund's interaction.

In the DQMC, I cannot calculate $e^{-\Delta\tau H}$ directly in that H_1, H_2, and H_3 have four operators' term. In order to calculate $e^{-\Delta\tau H}$ in the single electron basis, I need to use Hubbard-Stratonovich transformation to decouple those operators' term into two operators'

term. In the following, I will show two Hubbard-Stratonovich transformations to decouple H_3.

A   Discrete Hubbard-Stratonovich transformation

In the Trotter approximation, I write

$$e^{\Delta\tau H} \approx e^{-\Delta\tau H_3(2,3)}e^{-\Delta\tau H_2(2,3)}e^{-\Delta\tau H_3(1,3)}e^{-\Delta\tau H_2(1,3)}e^{-\Delta\tau H_3(1,2)}e^{-\Delta\tau H_2(1,2)}e^{-\Delta\tau H_1}e^{-\Delta\tau H_0},$$

in which

$$
\begin{aligned}
H_2(\gamma,\gamma') &= (U'-J)\sum_{i,\sigma}\hat{n}_{i,\gamma,\sigma}\hat{n}_{i,\gamma',\sigma} \\
H_3(\gamma,\gamma') &= J\sum_i(c^\dagger_{i,\gamma,\uparrow}c^\dagger_{i,\gamma',\downarrow}c_{i,\gamma,\downarrow}c_{i,\gamma',\uparrow} + c^\dagger_{i,\gamma,\uparrow}c^\dagger_{i,\gamma,\downarrow}c_{i,\gamma',\downarrow}c_{i,\gamma',\uparrow}) \\
&\quad + J\sum_i(c^\dagger_{i,\gamma',\uparrow}c^\dagger_{i,\gamma,\downarrow}c_{i,\gamma',\downarrow}c_{i,\gamma,\uparrow} + c^\dagger_{i,\gamma',\uparrow}c^\dagger_{i,\gamma',\downarrow}c_{i,\gamma,\downarrow}c_{i,\gamma,\uparrow}).
\end{aligned}
$$

The discrete Hubbard-Stratonovich (HS) transformation

$$e^{-a[n_\uparrow n_\downarrow - 1/2(n_\uparrow + n_\downarrow)]} = \begin{cases} \frac{1}{2}\sum_{s=\pm 1} e^{\lambda s(n_\uparrow - n_\downarrow)} & (a>0) \\ \frac{1}{2}\sum_{s=\pm 1} e^{\lambda s(n_\uparrow + n_\downarrow - 1) + \frac{a}{2}} & (a<0) \end{cases} \tag{A.1}$$

can be used to decouple H_1, which gives

$$
\begin{aligned}
e^{-\Delta\tau H_1} &= \frac{1}{8}\sum_{s_1,s_2,s_3} e^{\lambda_1 s_1(n_{1\uparrow}-n_{1\downarrow})}e^{\lambda_1 s_2(n_{2\uparrow}-n_{2\downarrow})}e^{\lambda_1 s_3(n_{3\uparrow}-n_{3\downarrow})} \times \\
&\quad \frac{1}{64}\sum_{s_4,s_5,s_6,s_7,s_8,s_9} e^{\lambda_2 s_4(n_{1\uparrow}-n_{2\downarrow})}e^{\lambda_2 s_5(n_{1\uparrow}-n_{3\downarrow})}e^{\lambda_2 s_6(n_{2\uparrow}-n_{3\downarrow})} \times \\
&\quad e^{\lambda_2 s_7(n_{1\downarrow}-n_{2\uparrow})}e^{\lambda_2 s_8(n_{1\downarrow}-n_{3\uparrow})}e^{\lambda_2 s_9(n_{2\downarrow}-n_{3\uparrow})} \\
&= \sum_{s_1,\cdots,s_9} \frac{1}{2^9}e^{(\lambda_1 s_1 + \lambda_2 s_4 + \lambda_2 s_5)n_{1\uparrow}}e^{(-\lambda_1 s_1 + \lambda_2 s_7 + \lambda_2 s_8)n_{1\downarrow}} \times \\
&\quad e^{(\lambda_1 s_2 + \lambda_2 s_6 - \lambda_2 s_7)n_{2\uparrow}}e^{(-\lambda_1 s_2 - \lambda_2 s_4 + \lambda_2 s_9)n_{2\uparrow}} \times \\
&\quad e^{(\lambda_1 s_3 - \lambda_2 s_8 - \lambda_2 s_9)n_{3\uparrow}}e^{(-\lambda_1 s_3 - \lambda_2 s_5 - \lambda_2 s_6)n_{3\uparrow}}
\end{aligned}
$$

in which $\lambda_1 = \ln(e^{|U\Delta\tau|/2} + \sqrt{e^{|U\Delta\tau|} - 1})$ and $\lambda_2 = \ln(e^{|U'\Delta\tau|/2} + \sqrt{e^{|U'\Delta\tau|} - 1})$.

To decouple H_3, a new discrete transformation will be used there. [See PRB **70**, 172504 (2004)]

$$e^{-\Delta\tau H_3(\gamma,\gamma')} = \frac{1}{2}\sum_{r=\pm 1} e^{\lambda_3 r(f_\uparrow(\lambda,\lambda') - f_\downarrow(\lambda,\lambda'))} e^{a(N_\uparrow(\lambda,\lambda') + N_\downarrow(\lambda,\lambda')) + bN_\uparrow(\lambda,\lambda')N_\downarrow(\lambda,\lambda')}, \qquad (A.2)$$

where

$$
\begin{aligned}
\lambda_3 &= \frac{1}{2}\ln(e^{|J\Delta\tau|/2} + \sqrt{e^{|J\Delta\tau|} - 1}), \\
b &= \ln(\cosh J\Delta\tau), \\
a &= -\ln(\cosh\lambda_3) = -\frac{1}{2}(J\Delta\tau + b), \\
f_\sigma(\gamma,\gamma') &= c_{\gamma,\sigma}^\dagger c_{\gamma',\sigma} + c_{\gamma',\sigma}^\dagger c_{\gamma,\sigma}, \\
N_\sigma(\gamma,\gamma') &= f_\sigma^2(\gamma,\gamma') = n_{\gamma,\sigma} + n_{\gamma',\sigma} - 2n_{\gamma,\sigma}n_{\gamma',\sigma}.
\end{aligned}
$$

The last term in Eq. A.2 can be further decoupled using Eq. A.1,

$$e^{a(N_\uparrow(\lambda,\lambda') + N_\downarrow(\lambda,\lambda')) + bN_\uparrow(\lambda,\lambda')N_\downarrow(\lambda,\lambda')} = \frac{1}{2}\sum_{s=\pm 1} e^{-cs - \frac{b}{2}} e^{(cs - \frac{J\Delta\tau}{2})(N_\uparrow(\gamma,\gamma') + N_\downarrow(\gamma,\gamma'))}, \qquad (A.3)$$

in which $c = \mathrm{arccosh}\sqrt{\cosh J\Delta\tau}$. Using eq. A.2 and .A.3, I can decouple $e^{-\Delta\tau H_3(\gamma,\gamma')}e^{-\Delta\tau H_2(\gamma,\gamma')}$ as

$$
\begin{aligned}
e^{-\Delta\tau H_3(\gamma,\gamma')}e^{-\Delta\tau H_2(\gamma,\gamma')} &= \frac{1}{2^2}\sum_{r,s} e^{\lambda_3 r(c_{\gamma\uparrow}^\dagger c_{\gamma'\uparrow} + c_{\gamma'\uparrow}^\dagger c_{\gamma\uparrow})} e^{-\lambda_3 r(c_{\gamma\downarrow}^\dagger c_{\gamma'\downarrow} + c_{\gamma'\downarrow}^\dagger c_{\gamma\downarrow})} \times \\
&\quad e^{-cs - \frac{b}{2}} e^{(cs + \Delta\tau\frac{U'-2J}{2})(n_{\gamma\uparrow} + n_{\gamma'\uparrow} - 2n_{\gamma\uparrow}n_{\gamma'\uparrow})} \times \\
&\quad e^{(cs + \Delta\tau\frac{U'-2J}{2})(n_{\gamma\downarrow} + n_{\gamma'\downarrow} - 2n_{\gamma\downarrow}n_{\gamma'\downarrow})} \\
&= \frac{1}{2^4}\sum_{r,s,s_1,s_2} e^{\lambda_3 r(c_{\gamma\uparrow}^\dagger c_{\gamma'\uparrow} + c_{\gamma'\uparrow}^\dagger c_{\gamma\uparrow})} e^{-\lambda_3 r(c_{\gamma\downarrow}^\dagger c_{\gamma'\downarrow} + c_{\gamma'\downarrow}^\dagger c_{\gamma\downarrow})} \times \\
&\quad \begin{cases} e^{-cs - \frac{b}{2}} e^{d(s)s_1(n_{\gamma\uparrow} - n_{\gamma'\uparrow})} e^{d(s)s_2(n_{\gamma\downarrow} - n_{\gamma'\downarrow})} \\ \qquad\qquad\qquad\text{as}\qquad cs + \frac{U'-2J}{2}\Delta\tau \geq 0 \\ e^{cs - \frac{b}{2} + (U'-2J)\Delta\tau} e^{d(s)s_1(n_{\gamma\uparrow} + n_{\gamma'\uparrow})} e^{d(s)s_2(n_{\gamma\downarrow} + n_{\gamma'\downarrow} - 1)} \\ \qquad\qquad\qquad\text{as}\qquad cs + \frac{U'-2J}{2}\Delta\tau < 0 \end{cases}
\end{aligned}
$$

204

where $d(s) = \text{arccosh}(e^{|cs + \frac{U'-2J}{2}\Delta\tau|})$. Finally, eq. A.1 can be written as

$$
\begin{aligned}
e^{-\Delta\tau H} &= \frac{1}{2^{21}} \sum_{s_1\cdots s_{21}} e^{\lambda_3 s_{21}(c^\dagger_{2,\uparrow}c_{3,\uparrow}+c^\dagger_{3,\uparrow}c_{2,\uparrow})} e^{-\lambda_3 s_{21}(c^\dagger_{2,\downarrow}c_{3,\downarrow}+c^\dagger_{3,\downarrow}c_{2,\downarrow})} \times \\
&\quad \begin{cases} e^{-cs_{16}-b/2} e^{d(s_{16})s_{17}(n_{2,\uparrow}-n_{3,\uparrow})} e^{d(s_{16})s_{18}(n_{2,\downarrow}-n_{3,\downarrow})} \\[6pt] e^{cs_{16}-b/2+(U'-2J)\Delta\tau} e^{d(s_{16})s_{17}(n_{2,\uparrow}+n_{3,\uparrow}-1)} e^{d(s_{16})s_{18}(n_{2,\downarrow}+n_{3,\downarrow}-1)} \end{cases} \\[6pt]
&\quad \times e^{\lambda_3 s_{20}(c^\dagger_{1,\uparrow}c_{3,\uparrow}+c^\dagger_{3,\uparrow}c_{1,\uparrow})} e^{-\lambda_3 s_{20}(c^\dagger_{1,\downarrow}c_{3,\downarrow}+c^\dagger_{3,\downarrow}c_{1,\downarrow})} \times \\[6pt]
&\quad \begin{cases} e^{-cs_{13}-b/2} e^{d(s_{13})s_{14}(n_{1,\uparrow}-n_{3,\uparrow})} e^{d(s_{13})s_{15}(n_{1,\downarrow}-n_{3,\downarrow})} \\[6pt] e^{cs_{13}-b/2+(U'-2J)\Delta\tau} e^{d(s_{13})s_{14}(n_{1,\uparrow}+n_{3,\uparrow}-1)} e^{d(s_{13})s_{15}(n_{1,\downarrow}+n_{3,\downarrow}-1)} \end{cases} \\[6pt]
&\quad \times e^{\lambda_3 s_{19}(c^\dagger_{1,\uparrow}c_{2,\uparrow}+c^\dagger_{2,\uparrow}c_{1,\uparrow})} e^{-\lambda_3 s_{19}(c^\dagger_{1,\downarrow}c_{2,\downarrow}+c^\dagger_{2,\downarrow}c_{1,\downarrow})} \times \\[6pt]
&\quad \begin{cases} e^{-cs_{10}-b/2} e^{d(s_{10})s_{11}(n_{1,\uparrow}-n_{2,\uparrow})} e^{d(s_{10})s_{12}(n_{1,\downarrow}-n_{2,\downarrow})} \\[6pt] e^{cs_{10}-b/2+(U'-2J)\Delta\tau} e^{d(s_{10})s_{11}(n_{1,\uparrow}+n_{2,\uparrow}-1)} e^{d(s_{10})s_{12}(n_{1,\downarrow}+n_{2,\downarrow}-1)} \end{cases} \\[6pt]
&\quad \times e^{(\lambda_1 s_1+\lambda_2 s_4+\lambda_2 s_5)n_{1\uparrow}} e^{(-\lambda_1 s_1+\lambda_2 s_7+\lambda_2 s_8)n_{1\downarrow}} \times \\[6pt]
&\quad e^{(\lambda_1 s_2+\lambda_2 s_6-\lambda_2 s_7)n_{2\uparrow}} e^{(-\lambda_1 s_2-\lambda_2 s_4+\lambda_2 s_9)n_{2\uparrow}} \times \\[6pt]
&\quad e^{(\lambda_1 s_3-\lambda_2 s_8-\lambda_2 s_9)n_{3\uparrow}} e^{(-\lambda_1 s_3-\lambda_2 s_5-\lambda_2 s_6)n_{3\uparrow}} \\[6pt]
&\quad \times e^{-\Delta\tau H_0} \\[6pt]
&= \frac{1}{2^{21}} \sum_{r_1,r_2,r_3} \sum_{s_1,\cdots,s_{12}} A(s_{16})A(s_{13})A(s_{10})e^{w_3}e^{v_3}e^{w_2}e^{v_2}e^{w_1}e^{v_1}e^{v_0}e^{k} \qquad (A.4)
\end{aligned}
$$

In the above equation, I have defined

$$
\begin{aligned}
e^{w_3} &= e^{\lambda_3 s_{21}(c^\dagger_{2,\uparrow}c_{3,\uparrow}+c^\dagger_{3,\uparrow}c_{2,\uparrow})} e^{-\lambda_3 s_{21}(c^\dagger_{2,\downarrow}c_{3,\downarrow}+c^\dagger_{3,\downarrow}c_{2,\downarrow})} \times \\[4pt]
e^{v_3} &= \begin{cases} e^{d(s_{16})s_{17}(n_{2,\uparrow}-n_{3,\uparrow})} e^{d(s_{16})s_{18}(n_{2,\downarrow}-n_{3,\downarrow})} \\[6pt] e^{d(s_{16})s_{17}(n_{2,\uparrow}+n_{3,\uparrow}-1)} e^{d(s_{16})s_{18}(n_{2,\downarrow}+n_{3,\downarrow}-1)} \end{cases} \\[6pt]
e^{w_2} &= e^{\lambda_3 s_{20}(c^\dagger_{1,\uparrow}c_{3,\uparrow}+c^\dagger_{3,\uparrow}c_{1,\uparrow})} e^{-\lambda_3 s_{20}(c^\dagger_{1,\downarrow}c_{3,\downarrow}+c^\dagger_{3,\downarrow}c_{1,\downarrow})} \times \\[4pt]
e^{v_2} &= \begin{cases} e^{d(s_{13})s_{14}(n_{1,\uparrow}-n_{3,\uparrow})} e^{d(s_{13})s_{15}(n_{1,\downarrow}-n_{3,\downarrow})} \\[6pt] e^{d(s_{13})s_{14}(n_{1,\uparrow}+n_{3,\uparrow}-1)} e^{d(s_{13})s_{15}(n_{1,\downarrow}+n_{3,\downarrow}-1)} \end{cases} \\[6pt]
e^{w_1} &= e^{\lambda_3 s_{19}(c^\dagger_{1,\uparrow}c_{2,\uparrow}+c^\dagger_{2,\uparrow}c_{1,\uparrow})} e^{-\lambda_3 s_{19}(c^\dagger_{1,\downarrow}c_{2,\downarrow}+c^\dagger_{2,\downarrow}c_{1,\downarrow})} \times \\[4pt]
e^{v_1} &= \begin{cases} e^{d(s_{10})s_{11}(n_{1,\uparrow}-n_{2,\uparrow})} e^{d(s_{10})s_{12}(n_{1,\downarrow}-n_{2,\downarrow})} \\[6pt] e^{d(s_{10})s_{11}(n_{1,\uparrow}+n_{2,\uparrow}-1)} e^{d(s_{10})s_{12}(n_{1,\downarrow}+n_{2,\downarrow}-1)} \end{cases} \\[6pt]
e^{v_0} &= e^{(\lambda_1 s_1+\lambda_2 s_4+\lambda_2 s_5)n_{1\uparrow}} e^{(-\lambda_1 s_1+\lambda_2 s_7+\lambda_2 s_8)n_{1\downarrow}} \times
\end{aligned}
$$

$$e^{(\lambda_1 s_2 + \lambda_2 s_6 - \lambda_2 s_7)n_{2\uparrow}} e^{(-\lambda_1 s_2 - \lambda_2 s_4 + \lambda_2 s_9)n_{2\uparrow}} \times$$

$$e^{(\lambda_1 s_3 - \lambda_2 s_8 - \lambda_2 s_9)n_{3\uparrow}} e^{(-\lambda_1 s_3 - \lambda_2 s_5 - \lambda_2 s_6)n_{3\uparrow}}$$

$$e^k = e^{-\Delta\tau H_0}$$

$$A(s) = \begin{cases} e^{-cs - \frac{b}{2}} & (cs + \frac{U' - 2J}{2}\Delta\tau \geq 0) \\ e^{cs - \frac{b}{2} + \Delta\tau(U' - 2J)} & (cs + \frac{U' - 2J}{2}\Delta\tau < 0) \end{cases}$$

A.1   The fast updating for v_0, v_1, v_2, and v_3

The processes of updating v_0, v_1, v_2, and v_3 are the same. In conenient, I only show the details for updating v_3. In the three-orbital model, The B_l matrix is defined as $B_l = e^{w_3} e^{v_3} e^{w_2} e^{v_2} e^{w_1} e^{v_1} e^{v_0} e^k$. Flipping the field s_{16}, s_{17}, or s_{18} on site i, e^{v_3} is changed to $e^{v_3'}$. The new B_l' matrix is

$$\begin{aligned} B_l' &= e^{w_3} e^{v_3'} e^{w_2} e^{v_2} e^{w_1} e^{v_1} e^{v_0} e^k \\ &= e^{w_3}(I + \Delta) e^{v_2} e^{w_2} e^{v_2} e^{w_1} e^{v_1} e^{v_0} e^k \\ &= R(I + \Delta)L \\ &= R(I + \Delta)R^{-1}B_l, \end{aligned}$$

where I is a unitary matix, $R = e^{w_3}$, and

$$\Delta = \begin{bmatrix} 0 & \cdots & 0 & \cdots & 0 & \cdots \\ \vdots & \vdots & \vdots & \vdots & \vdots & \vdots \\ 0 & \cdots & \Delta_{n,n} & \cdots & 0 & \cdots \\ \vdots & \vdots & \vdots & \vdots & \vdots & \vdots \\ 0 & \cdots & 0 & \cdots & \Delta_{m,m} & \cdots \\ \vdots & \vdots & \vdots & \vdots & \vdots & \vdots \end{bmatrix}$$

Then the new Green's function is given by

$$\begin{aligned} G_l' &= [I + R(I + \Delta)R^{-1}A_l]^{-1} \\ &= [I + R(I + \Delta)R^{-1}(G_l^{-1} - I)]^{-1} \end{aligned}$$

206

$$= G_l[R^{-1} + \Delta R^{-1}(I - G_l)]^{-1}R^{-1}$$

$$= G_l[R^{-1} + \Delta Q]^{-1}R^{-1},$$

where $Q = R^{-1}(I - G_l)$. Since there are only two non-zero elements in the Δ matrix, ΔQ equals

$$\Delta Q = \begin{pmatrix} 0 & 0 & \cdots \\ \vdots & \vdots & \vdots \\ \Delta_{n,n}Q_{n,1} & \Delta_{n,n}Q_{n,2} & \cdots \\ 0 & 0 & \cdots \\ \Delta_{m,m}Q_{m,1} & \Delta_{m,m}Q_{m,2} & \cdots \\ \vdots & \vdots & \vdots \end{pmatrix}$$

$$= \begin{pmatrix} 0 & 0 \\ \vdots & \vdots \\ \Delta_{n,n} & 0 \\ \vdots & \vdots \\ 0 & \Delta_{m,m} \\ \vdots & \vdots \end{pmatrix} \begin{pmatrix} Q_{n,1} & Q_{n,2} & \cdots \\ Q_{m,2} & Q_{m,2} & \cdots \end{pmatrix}$$

$$= uv.$$

Here u and v are $N \times 2$ and $2 \times N$ matrices. To do a fast calculation of the new Green's function, I use Woodbury matirxi identity here. The new Green's function is obtained via

$$G_l' = G_l[R^{-1} + uv]^{-1}R^{-1}$$

$$= G_l[R - Ru(I_2 + vRu)^{-1}vR]R^{-1}$$

$$= G_l[I - Ru(I_2 + vRu)^{-1}v]. \tag{A.5}$$

The updating acceptance probability is

$$r = \text{coeff} \times \det|R(R^{-1} + uv)|$$

$$= \text{coeff} \times \det|R| \times \det|R^{-1} + uv|$$

$$= \text{coeff} \times \det|R| \times \det|I_2 + vRu| \times \det|R^{-1}|$$

$$= \text{coeff} \times \det|I_2 + vRu|,$$

where $\text{coeff} = \frac{A(s'_{16})A(s'_{17})A(s'_{18})}{A(s_{16})A(s_{17})A(s_{18})}$.

A.2 The fast updating for w_1, w_2, and w_3

The processes of updating w_1, w_2, and w_3 are the same, here I just show how to update w_2.

w_2 matrix can be written as

$$w_2 = \begin{bmatrix} 0 & 0 & M \\ 0 & 0 & 0 \\ M & 0 & 0 \end{bmatrix}, \tag{A.6}$$

where M is a diagonal matrix. Then

$$e^{w_2} = \begin{bmatrix} \frac{e^M + e^{-M}}{2} & 0 & \frac{e^M - e^{-M}}{2} \\ 0 & 1 & 0 \\ \frac{e^M - e^{-M}}{2} & 0 & \frac{e^M + e^{-M}}{2} \end{bmatrix} \tag{A.7}$$

If I flip s_{20} on site i, the new B_l matrix is given by

$$B'_l = e^{w_3}e^{v_3}(I + \Delta)e^{w_2}e^{v_2}e^{w_1}e^{v_1}e^{v_0}e^k$$

$$= R(I + \Delta)R^{-1}B_l,$$

where $R = e^{w_3}e^{v_3}$ and

$$\Delta = \begin{bmatrix} x & & y \\ & & \\ y & & x \end{bmatrix}.$$

208

Here, $x = \left(\frac{e^{M'-M}+e^{-M'+M}}{2}\right)_{i,i} - 1$ and $y = \left(\frac{e^{M'-M}-e^{-M'+M}}{2}\right)_{i,i}$. The index of x and y in Δ matrix is labeled as (n,n) and (n,m). The new Green's function is

$$
\begin{aligned}
G'_l &= [I + R(I+\Delta)R^{-1}A_l]^{-1} \\
&= [I + R(I+\Delta)R^{-1}(G_l^{-1} - I)]^{-1} \\
&= G_l[I + R\Delta R^{-1}(I - G_l)]^{-1} \\
&= G_l[R^{-1} + \Delta R^{-1}(I - G_l)]^{-1}R^{-1} \\
&= G_l[R^{-1} + \Delta Q]^{-1}R^{-1},
\end{aligned}
$$

in which

$$
Q = R^{-1}(I - G_l)
$$

$$
\Delta Q = \begin{pmatrix}
0 & 0 & \cdots \\
xQ_{n,1} + yQ_{m,1} & xQ_{n,2} + yQ_{m,2} & \cdots \\
0 & 0 & \cdots \\
\vdots & \vdots & \vdots \\
yQ_{n,1} + xQ_{m,1} & yQ_{n,2} + xQ_{m,2} & \cdots \\
0 & 0 & \cdots \\
\vdots & \vdots & \vdots
\end{pmatrix} = \begin{pmatrix}
0 & 0 \\
\vdots & \vdots \\
x & y \\
\vdots & \vdots \\
y & x \\
\vdots & \vdots
\end{pmatrix} \begin{pmatrix}
Q_{n,1} & Q_{n,2} & \cdots \\
Q_{m,1} & Q_{m,2} & \cdots
\end{pmatrix}
$$

$$
= uv \tag{A.8}
$$

Applying the Woodbury matrix identity, the new Green's function is obtained via

$$
\begin{aligned}
G'_l &= G_l(R^{-1} + uI_2v)^{-1}R^{-1} \\
&= G_l[R - Ru(I_2 + vRu)^{-1}vR]R^{-1} \\
&= G_l[I - Ru(I_2 + vRu)^{-1}v],
\end{aligned}
$$

and the updating probability is

$$r = \det|R(R + uI_2v)|$$
$$= \det|I_2 + vRu|$$

B   Continuous Hubbard-Stratonovich transformation

The second way to decouple four operators in H_3 is the continuous Hubbard-Stratonovich transformation. [read PRB **33**, 3519]. Assuming $\hat{A}$ is an operator, then

$$e^{\hat{A}^2} = \int dx e^{-\pi x^2 + 2\sqrt{\pi}\hat{A}x}. \tag{A.9}$$

Eq. A.9 decouples $\hat{A}^2$ with additional field x. In order to decouple four operators in H_3, I need to write H_3 as

$$
\begin{aligned}
H_3 &= -\frac{J}{2}[c_{1\uparrow}^\dagger c_{2\uparrow} + c_{2\uparrow}^\dagger c_{1\uparrow} - c_{1\downarrow}^\dagger c_{2\downarrow} - c_{2\downarrow}^\dagger c_{1\downarrow}]^2 - J(n_{1\uparrow}n_{2\uparrow} + n_{2\downarrow}n_{1\downarrow}) \\
&\quad -\frac{J}{2}[c_{1\uparrow}^\dagger c_{3\uparrow} + c_{3\uparrow}^\dagger c_{1\uparrow} - c_{1\downarrow}^\dagger c_{3\downarrow} - c_{3\downarrow}^\dagger c_{1\downarrow}]^2 - J(n_{1\uparrow}n_{3\uparrow} + n_{3\downarrow}n_{1\downarrow}) \\
&\quad -\frac{J}{2}[c_{2\uparrow}^\dagger c_{3\uparrow} + c_{3\uparrow}^\dagger c_{2\uparrow} - c_{2\downarrow}^\dagger c_{3\downarrow} - c_{3\downarrow}^\dagger c_{2\downarrow}]^2 - J(n_{2\uparrow}n_{3\uparrow} + n_{3\downarrow}n_{2\downarrow}) \\
&\quad +J(n_{1\uparrow} + n_{2\uparrow} + n_{3\uparrow} + n_{1\downarrow} + n_{2\downarrow} + n_{3\downarrow}) \tag{A.10}
\end{aligned}
$$

The $[\ldots]^2$ terms in eq. A.10 can be decoupled using the continuous Hubbard-Stratonovich transformation, $n_{\gamma,\sigma}n_{\gamma',\sigma}$ in eq. A.10 can be decoupled using the discrete Hubbard-Strotonovich transformation. Then the total Hamiltonian is decoupled as

$$
\begin{aligned}
e^{-\Delta\tau H} &= \sum_{s_1\ldots s_{15}, x_1, x_2, x_3} e^{(\lambda_1 s_1 + \lambda_2 s_4 + \lambda_2 s_5 + \lambda_3 s_{10} + \lambda_3 s_{11})n_{1\uparrow}} e^{(-\lambda_1 s_1 + \lambda_2 s_7 + \lambda_2 s_8 + \lambda_3 s_{13} + \lambda_3 s_{14})n_{1\downarrow}} \times \\
&\quad e^{(\lambda_1 s_2 + \lambda_2 s_6 - \lambda_2 s_7 - \lambda_3 s_{10} + \lambda_3 s_{12})n_{2\uparrow}} e^{(-\lambda_1 s_2 - \lambda_2 s_4 + \lambda_2 s_9 - \lambda_3 s_{13} + \lambda_3 s_{15})n_{2\downarrow}} \times \\
&\quad e^{(\lambda_1 s_3 - \lambda_2 s_8 - \lambda_2 s_9 - \lambda_3 s_{11} - \lambda_3 s_{12})n_{3\uparrow}} e^{(-\lambda_1 s_3 - \lambda_2 s_5 - \lambda_2 s_6 - \lambda_3 s_{14} - \lambda_3 s_{15})n_{3\downarrow}} \times \\
&\quad e^{-\pi x_1^2} e^{\sqrt{2J\Delta\tau\pi}(c_{1\uparrow}^\dagger c_{2\uparrow} + c_{2\uparrow}^\dagger c_{1\uparrow} - c_{1\downarrow}^\dagger c_{2\downarrow} - c_{2\downarrow}^\dagger c_{1\downarrow})x_1} \times \\
&\quad e^{-\pi x_2^2} e^{\sqrt{J\Delta\tau\pi}(c_{1\uparrow}^\dagger c_{3\uparrow} + c_{3\uparrow}^\dagger c_{1\uparrow} - c_{1\downarrow}^\dagger c_{3\downarrow} - c_{3\downarrow}^\dagger c_{1\downarrow})x_2} \times \\
&\quad e^{-\pi x_3^2} e^{\sqrt{2J\Delta\tau\pi}(c_{2\uparrow}^\dagger c_{3\uparrow} + c_{3\uparrow}^\dagger c_{2\uparrow} - c_{2\downarrow}^\dagger c_{3\downarrow} - c_{3\downarrow}^\dagger c_{2\downarrow})x_3}
\end{aligned}
$$

$$= \sum_{s_1...s_{15},x_1,x_2,x_3} A(x_1)A(x_2)A(x_3)e^V e^{W_1} e^{W_2} e^{W_3} e^K,$$

in which $\cosh\lambda_1 = e^{U\Delta\tau/2}$, $\cosh\lambda_2 = e^{\Delta\tau U'/2}$, $\cosh\lambda_3 = e^{\Delta\tau(U'-2J)/2}$, $A(x) = e^{-\pi x^2}$, and

$$
\begin{aligned}
e^V &= e^{(\lambda_1 s_1 + \lambda_2 s_4 + \lambda_2 s_5 + \lambda_3 s_{10} + \lambda_3 s_{11})n_{1\uparrow}} e^{(-\lambda_1 s_1 + \lambda_2 s_7 + \lambda_2 s_8 + \lambda_3 s_{13} + \lambda_3 s_{14})n_{1\downarrow}} \times \\
&\quad e^{(\lambda_1 s_2 + \lambda_2 s_6 - \lambda_2 s_7 - \lambda_3 s_{10} + \lambda_3 s_{12})n_{2\uparrow}} e^{(-\lambda_1 s_2 - \lambda_2 s_4 + \lambda_2 s_9 - \lambda_3 s_{13} + \lambda_3 s_{15})n_{2\downarrow}} \times \\
&\quad e^{(\lambda_1 s_3 - \lambda_2 s_8 - \lambda_2 s_9 - \lambda_3 s_{11} - \lambda_3 s_{12})n_{3\uparrow}} e^{(-\lambda_1 s_3 - \lambda_2 s_5 - \lambda_2 s_6 - \lambda_3 s_{14} - \lambda_3 s_{15})n_{3\downarrow}} \\
e^{W_1} &= e^{\sqrt{2J\Delta\tau\pi}(c_{1\uparrow}^\dagger c_{2\uparrow} + c_{2\uparrow}^\dagger c_{1\uparrow} - c_{1\downarrow}^\dagger c_{2\downarrow} - c_{2\downarrow}^\dagger c_{1\downarrow})x_1} \\
e^{W_2} &= e^{\sqrt{J\Delta\tau\pi}(c_{1\uparrow}^\dagger c_{3\uparrow} + c_{3\uparrow}^\dagger c_{1\uparrow} - c_{1\downarrow}^\dagger c_{3\downarrow} - c_{3\downarrow}^\dagger c_{1\downarrow})x_2} \\
e^{W_3} &= e^{\sqrt{2J\Delta\tau\pi}(c_{2\uparrow}^\dagger c_{3\uparrow} + c_{3\uparrow}^\dagger c_{2\uparrow} - c_{2\downarrow}^\dagger c_{3\downarrow} - c_{3\downarrow}^\dagger c_{2\downarrow})x_3}
\end{aligned}
$$

B.1 The fast updating e^V

The e^V matrix is a diagonal matrix. If I flip a filed on site i, two diagonal elements in e^V will be changed. I define the new B'_l matrix after flipping as

$$
\begin{aligned}
B'_l &= e^{V'} e^{W_1} e^{W_2} e^{W_3} e^K \\
&= (I + \Delta)e^V e^{W_1} e^{W_2} e^{W_3} e^K \\
&= (I + \Delta)B_l,
\end{aligned}
$$

and the new Green's function as

$$
\begin{aligned}
G'_l &= [I + (I + \Delta A_l)]^{-1} \\
&= G_l[I + \Delta(I - G_l)]^{-1} \\
&= G_l[I - U(I_2 + VU)^{-1}V],
\end{aligned}
$$

in which

$$U = \begin{bmatrix} 0 & 0 \\ \vdots & \vdots \\ \Delta_{m,m} & 0 \\ \vdots & \vdots \\ 0 & \Delta_{n,n} \\ \vdots & \vdots \\ 0 & 0 \end{bmatrix} \tag{A.11}$$

$$V = \begin{bmatrix} -G_{m,1} & \dots & 1-G_{m,m} & \dots & -G_{m,n} & -G_{m,N} \\ -G_{n,1} & \dots & -G_{n,m} & \dots & 1-G_{n,n} & -G_{n,N} \end{bmatrix}. \tag{A.12}$$

The updating probability is obtained via $r = \det(I_2 + VU)$.

B.2 fast updating for e^{W_1}, e^{W_2}, and e^{W_3}

W_1, W_2, and W_3 are off-diagonal matrices. In generally, the W matrix is

$$W = \begin{bmatrix} & & M \\ & M & \end{bmatrix},$$

and

$$e^W = \begin{bmatrix} 1 & & & \\ & \frac{e^M+e^{-M}}{2} & \frac{e^M-e^{-M}}{2} & \\ & \frac{e^M-e^{-M}}{2} & \frac{e^M+e^{-M}}{2} & \\ & & & 1 \end{bmatrix},$$

where M is a diagonal matrix. If I change field x on site i, B_l becomes B_l' with $B_l' = R(I + \Delta)R^{-1}B_l$, where $R = e^V$ if x_1 is updated, $R = e^V e^{W_1}$ if x_2 is updated, and $R = e^V e^{W_1} e^{W_3}$ if

x_3 is updated. The Δ matrix has a following form,

$$
\Delta \;=\; \begin{bmatrix} \Delta_{m,m} & & \Delta_{m,n} \\ \\ \Delta n,m & & \Delta_{n,n} \end{bmatrix}, \tag{A.13}
$$

where m and n are the matrix indexs associated with the updated field on site i. Here, $\Delta_{m,m} = \Delta_{n,n} = x = \left(\frac{e^{M'-M}+e^{-M'+M}}{2}\right)_{i,i} - 1$ and $\Delta_{m,n} = \Delta n,m = y = \left(\frac{e^{M'-M}-e^{-M'+M}}{2}\right)_{i,i}$. The Green's function is obtained via

$$
\begin{aligned}
G'_l &= [I + R(I+\Delta)R^{-1}A_l]^{-1} \\
&= [I + R(I+\Delta)R^{-1}(G_l^{-1} - I)]^{-1} \\
&= G_l[I + R\Delta R^{-1}(I - G_l)]^{-1} \\
&= G_l[R^{-1} + \Delta R^{-1}(I - G_l)]^{-1}R^{-1} \\
&= G_l[R^{-1} + \Delta Q]^{-1}R^{-1} \\
Q &= R^{-1}(I - G_l) \\
\Delta Q &= \begin{bmatrix} 0 & 0 & \cdots \\ xQ_{m,1} + yQ_{n,1} & xQ_{m,2} + yQ_{n,2} & \cdots \\ 0 & 0 & \cdots \\ \vdots & \vdots & \vdots \\ yQ_{m,1} + xQ_{n,1} & yQ_{m,2} + xQ_{n,2} & \cdots \\ 0 & 0 & \cdots \\ \vdots & \vdots & \vdots \end{bmatrix}
\end{aligned}
$$

$$
\begin{aligned}
&= \begin{bmatrix} 0 & 0 \\ \vdots & \vdots \\ x & y \\ \vdots & \vdots \\ y & x \\ \vdots & \vdots \end{bmatrix} \begin{bmatrix} Q_{m,1} & Q_{m,2} & \cdots \\ Q_{n,1} & Q_{n,2} & \cdots \end{bmatrix} \\
&= UV
\end{aligned}
$$

Then

$$
\begin{aligned}
G'_l &= G_l(R^{-1} + UI_2V)^{-1}R^{-1} \\
&= G_l[R - RU(I_2 + VRU)^{-1}VR]R^{-1} \\
&= G_l[I - RU(I_2 + VRU)^{-1}V].
\end{aligned}
$$

The updating probability is

$$
\begin{aligned}
r &= \text{coeff} \times \det|R(R + UI_2V)| \\
&= \text{coeff} \times \det|I_2 + VRU,|
\end{aligned}
$$

where $\text{coeff} = \frac{e^{-\pi x'^2}}{e^{-\pi x^2}}$.

Appendix B

Applications of the Migdal theory to the three-orbital SSH model

Before applying the Migdal theory, I need to rewrite the Hamiltonian in the momentum space. First I do the Fourier transformation of operators,

$$s_{\mathbf{k},\sigma} \;=\; \frac{1}{\sqrt{N}} \sum_{\mathbf{r}} e^{-i\mathbf{k}\cdot\mathbf{r}} s_{\mathbf{r},\sigma} \tag{B.1}$$

$$p_{\mathbf{k},x,\sigma} \;=\; \frac{1}{\sqrt{N}} \sum_{\mathbf{r}} e^{-i\mathbf{k}\cdot(\mathbf{r}+\mathbf{a}/2)} p_{\mathbf{r},x,\sigma} \tag{B.2}$$

$$p_{\mathbf{k},y,\sigma} \;=\; \frac{1}{\sqrt{N}} \sum_{\mathbf{r}} e^{-i\mathbf{k}\cdot(\mathbf{r}+\mathbf{b}/2)} p_{\mathbf{r},y,\sigma} \tag{B.3}$$

$$a_{\mathbf{k}} \;=\; \frac{\Omega}{2\hbar} \sum_{\mathbf{r}} \left[\sqrt{\frac{M}{N}} \hat{X}_{\mathbf{r}+\frac{\mathbf{a}}{2}} e^{-i\mathbf{k}(\mathbf{r}+\frac{\mathbf{a}}{2})} - \frac{1}{\Omega\sqrt{NM}} \hat{P}_{\mathbf{r}+\frac{\mathbf{a}}{2},x} e^{-i\mathbf{k}(\mathbf{r}+\frac{\mathbf{a}}{2})} \right] \tag{B.4}$$

$$b_{\mathbf{k}} \;=\; \frac{\Omega}{2\hbar} \sum_{\mathbf{r}} \left[\sqrt{\frac{M}{N}} \hat{Y}_{\mathbf{r}+\frac{\mathbf{b}}{2}} e^{-i\mathbf{k}(\mathbf{r}+\frac{\mathbf{b}}{2})} - \frac{1}{\Omega\sqrt{NM}} \hat{P}_{\mathbf{r}+\frac{\mathbf{a}}{2},y} e^{-i\mathbf{k}(\mathbf{r}+\frac{\mathbf{b}}{2})} \right]. \tag{B.5}$$

Then I have $s_{\mathbf{k}+\mathbf{G},\sigma} = s_{\mathbf{k},\sigma}$, $p_{\mathbf{k}+\mathbf{G},x,\sigma} = e^{-i\mathbf{G}\cdot\mathbf{a}/2} p_{\mathbf{k},x,\sigma}$, $p_{\mathbf{k}+\mathbf{G},y,\sigma} = e^{-i\mathbf{G}\cdot\mathbf{b}/2} p_{\mathbf{k},y,\sigma}$, $a_{\mathbf{k}+\mathbf{G}} = e^{-i\mathbf{G}\cdot\mathbf{a}/2} a_{\mathbf{k}}$, and $b_{\mathbf{k}+\mathbf{G}} = e^{-i\mathbf{G}\cdot\mathbf{b}/2} b_{\mathbf{k}}$. Hence, $p_{\mathbf{k},x,\sigma}$, $p_{\mathbf{k},y,\sigma}$, $a_{\mathbf{k}}$, and $b_{\mathbf{k}}$ don't have translation symmetry. Here, $\mathbf{G}$ is the reciprocal lattice vector, $\mathbf{a}$ and $\mathbf{b}$ are the primitive vector along x- and y-directions, respectively. If I define the Green's function as

$$G_{\gamma\gamma'}(\mathbf{r}) \;=\; \frac{1}{N} \sum_{\mathbf{u}} \langle \gamma_{\mathbf{u}+\mathbf{r},\sigma} \gamma'^{\dagger}_{\mathbf{u},\sigma} \rangle \tag{B.6}$$

$$G_{\gamma\gamma'}(\mathbf{k}) = \sum_{\mathbf{r}} G_{\gamma\gamma'}(\mathbf{r}) e^{-i\mathbf{k}\cdot\mathbf{r}}, \tag{B.7}$$

$$g_{\gamma\gamma'}(\mathbf{k}) = \langle \gamma_{\mathbf{k},\sigma} \gamma'^{\dagger}_{\mathbf{k},\sigma} \rangle \tag{B.8}$$

then

$$G_{ss}(\mathbf{k}) = \langle s_{\mathbf{k},\sigma} s^{\dagger}_{\mathbf{k},\sigma} \rangle = g_{ss}(\mathbf{k}) \tag{B.9}$$

$$G_{sp_x}(\mathbf{k}) = e^{-i\mathbf{k}\cdot\mathbf{a}/2} \langle s_{\mathbf{k},\sigma} p^{\dagger}_{\mathbf{k},x,\sigma} \rangle = g_{sp_x}(\mathbf{k}) e^{-i\mathbf{k}\cdot\mathbf{a}/2} \tag{B.10}$$

$$G_{sp_y}(\mathbf{k}) = e^{-i\mathbf{k}\cdot\mathbf{b}/2} \langle s_{\mathbf{k},\sigma} p^{\dagger}_{\mathbf{k},y,\sigma} \rangle = g_{sp_y}(\mathbf{k}) e^{-i\mathbf{k}\cdot\mathbf{b}/2} \tag{B.11}$$

$$G_{p_x s}(\mathbf{k}) = e^{i\mathbf{k}\cdot\mathbf{a}/2} \langle p_{\mathbf{k},x,\sigma} s^{\dagger}_{\mathbf{k},\sigma} \rangle = g_{p_x s}(\mathbf{k}) e^{i\mathbf{k}\cdot\mathbf{a}/2} \tag{B.12}$$

$$G_{p_x p_x}(\mathbf{k}) = \langle p_{\mathbf{k},x,\sigma} p^{\dagger}_{\mathbf{k},x,\sigma} \rangle = g_{p_x p_x}(\mathbf{k}) \tag{B.13}$$

$$G_{p_x p_y}(\mathbf{k}) = e^{i\mathbf{k}\cdot(\mathbf{a}/2-\mathbf{b}/2)} \langle p_{\mathbf{k},x,\sigma} p^{\dagger}_{\mathbf{k},y,\sigma} \rangle = g_{p_x p_y}(\mathbf{k}) e^{i\mathbf{k}\cdot(\mathbf{a}/2-\mathbf{b}/2)} \tag{B.14}$$

$$G_{p_y s}(\mathbf{k}) = e^{i\mathbf{k}\cdot\mathbf{b}/2} \langle p_{\mathbf{k},y,\sigma} s^{\dagger}_{\mathbf{k},\sigma} \rangle = g_{p_y s}(\mathbf{k}) e^{i\mathbf{k}\cdot\mathbf{b}/2} \tag{B.15}$$

$$G_{p_y p_x}(\mathbf{k}) = e^{-i\mathbf{k}\cdot(\mathbf{a}/2-\mathbf{b}/2)} \langle p_{\mathbf{k},y,\sigma} p^{\dagger}_{\mathbf{k},x,\sigma} \rangle = g_{p_y p_x}(\mathbf{k}) e^{-i\mathbf{k}\cdot(\mathbf{a}/2-\mathbf{b}/2)} \tag{B.16}$$

$$G_{p_y p_y}(\mathbf{k}) = \langle p_{\mathbf{k},y,\sigma} p^{\dagger}_{\mathbf{k},y,\sigma} \rangle = g_{p_y p_y}(\mathbf{k}) \tag{B.17}$$

$$D_{aa}(\mathbf{q}) = d_{aa}(\mathbf{q}) \tag{B.18}$$

$$D_{ab}(\mathbf{q}) = d_{ab}(\mathbf{q}) e^{i\mathbf{q}\cdot(\mathbf{a}/2-\mathbf{b}/2)} \tag{B.19}$$

$$D_{ba}(\mathbf{q}) = d_{ba}(\mathbf{q}) e^{-i\mathbf{q}\cdot(\mathbf{a}/2-\mathbf{b}/2)} \tag{B.20}$$

$$D_{bb}(\mathbf{q}) = d_{bb}(\mathbf{q}) \tag{B.21}$$

$G_{\gamma\gamma'}(\mathbf{k})$ has a translation symmetry. For example,

$$\begin{aligned}
G_{sp_x}(\mathbf{k}) &= \sum_{\mathbf{r}} G_{sp_x}(\mathbf{r}) e^{-i\mathbf{k}\cdot\mathbf{r}} \\
&= \sum_{\mathbf{r}} \frac{1}{N} \sum_{\mathbf{u}} \langle s_{\mathbf{u}+\mathbf{r},\sigma} p^{\dagger}_{\mathbf{u}+\frac{\mathbf{a}}{2},x,\sigma} \rangle e^{-i\mathbf{k}\cdot\mathbf{r}} \\
&= \sum_{\mathbf{r}} \frac{1}{N} \sum_{\mathbf{u}} \sum_{\mathbf{k}_1,\mathbf{k}_2} \frac{1}{N} \langle s_{\mathbf{k},\sigma} p^{\dagger}_{\mathbf{k},x,\sigma} \rangle e^{i(\mathbf{k}_1-\mathbf{k}_2)\cdot\mathbf{u}} e^{i(\mathbf{k}_1-\mathbf{k})\cdot\mathbf{r}} e^{-i\mathbf{k}_2\cdot\frac{\mathbf{a}}{2}} \\
&= \langle s_{\mathbf{k},\sigma} p^{\dagger}_{\mathbf{k},x,\sigma} \rangle e^{-i\mathbf{k}\cdot\frac{\mathbf{a}}{2}} \tag{B.22} \\
G_{sp_x}(\mathbf{k}+\mathbf{G}) &= \langle s_{\mathbf{k}+\mathbf{G},\sigma} p^{\dagger}_{\mathbf{k}+\mathbf{G},x,\sigma} \rangle e^{-i(\mathbf{k}+\mathbf{G})\cdot\frac{\mathbf{a}}{2}} \\
&= \langle s_{\mathbf{k},\sigma} p^{\dagger}_{\mathbf{k},x,\sigma} \rangle e^{i\mathbf{G}\cdot\mathbf{a}/2} e^{-i(\mathbf{k}+\mathbf{G})\cdot\frac{\mathbf{a}}{2}}
\end{aligned}$$

$$= G_{sp_x}(\mathbf{k}) \tag{B.23}$$

In the momentum space, the Hamiltonian is

$$
\begin{aligned}
H_0 &= \sum_{\mathbf{k},\sigma} \mathrm{i}2t_{sp}^0 \left(\sin(\mathbf{k}\cdot\mathbf{a}/2) s_{\mathbf{k},\sigma}^\dagger p_{\mathbf{k},x,\sigma} + \sin(\mathbf{k}\cdot\mathbf{b}/2) s_{\mathbf{k},\sigma}^\dagger p_{\mathbf{k},y,\sigma} - h.c. \right) + \\
&\quad \sum_{\mathbf{k},\sigma} 4t_{pp}\sin(\mathbf{k}\cdot\mathbf{a}/2)\sin(\mathbf{k}\cdot\mathbf{b}/2) \left(p_{\mathbf{k},x,\sigma}^\dagger p_{\mathbf{k},y,\sigma} + h.c. \right) + \\
&\quad \sum_{\mathbf{k},\sigma} \left[(\Delta_s - \mu) s_{\mathbf{k},\sigma}^\dagger s_{\mathbf{k},\sigma} + (\Delta_p - \mu) \left(p_{\mathbf{k},x,\sigma}^\dagger p_{\mathbf{k},x,\sigma} + p_{\mathbf{k},y,\sigma}^\dagger p_{\mathbf{k},y,\sigma} \right) \right] \tag{B.24}
\end{aligned}
$$

$$
H_{\mathrm{ph}} = \hbar\Omega \sum_{\mathbf{q}} \left[a_{\mathbf{q}}^\dagger a_{\mathbf{q}} + b_{\mathbf{q}}^\dagger b_{\mathbf{q}} \right] \tag{B.25}
$$

$$
\begin{aligned}
H_{\mathrm{e-ph}} &= \alpha t_{sp} \sqrt{\frac{\hbar}{2NM\Omega}} \sum_{\mathbf{k}_1,\mathbf{k}_2,\sigma} \left(a_{\mathbf{k}_1-\mathbf{k}_2} + a_{\mathbf{k}_2-\mathbf{k}_1}^\dagger \right) \left[2\cos\left(\frac{\mathbf{k}_1\cdot\mathbf{a}}{2}\right) s_{\mathbf{k}_1,\sigma}^\dagger p_{\mathbf{k}_2,x,\sigma} + \right. \\
&\quad \left. 2\cos\left(\frac{\mathbf{k}_2\cdot\mathbf{a}}{2}\right) p_{\mathbf{k}_1,x,\sigma}^\dagger s_{\mathbf{k}_2,\sigma} \right] + \left(b_{\mathbf{k}_1-\mathbf{k}_2} + b_{\mathbf{k}_2-\mathbf{k}_1}^\dagger \right) \\
&\quad \left[2\cos\left(\frac{\mathbf{k}_1\cdot\mathbf{b}}{2}\right) s_{\mathbf{k}_1,\sigma}^\dagger p_{\mathbf{k}_2,y,\sigma} + 2\cos\left(\frac{\mathbf{k}_2\cdot\mathbf{b}}{2}\right) p_{\mathbf{k}_1,y,\sigma}^\dagger s_{\mathbf{k}_2,\sigma} \right], \tag{B.26}
\end{aligned}
$$

in which $\hbar\Omega = \sqrt{\frac{2K}{M}}$ and M is the oxygen mass. For conveince, I define $\tilde{\alpha}\sqrt{\frac{1}{2N\omega}} = \alpha t_{sp}\sqrt{\frac{\hbar}{2NM\Omega}}$, where $\tilde{\alpha} = \frac{\alpha t_{sp}\hbar}{\sqrt{M}}$ and $\omega = \hbar\Omega$. $H_{\mathrm{e-ph}}$ can be written in a matrix format as

$$
\begin{aligned}
H_{\mathrm{e-ph}} &= \frac{\tilde{\alpha}}{\sqrt{2\omega N}} \sum_{\mathbf{k}_1,\mathbf{k}_2,\sigma} \left(\begin{array}{ccc} s_{\mathbf{k}_1,\sigma}^\dagger & p_{\mathbf{k}_1,x,\sigma}^\dagger & p_{\mathbf{k}_1,y,\sigma}^\dagger \end{array} \right) \left\{ A_{\mathbf{k}_1-\mathbf{k}_2} \left[\begin{array}{ccc} 0 & 2\cos\left(\frac{\mathbf{k}_1\cdot\mathbf{a}}{2}\right) & 0 \\ 2\cos\left(\frac{\mathbf{k}_2\cdot\mathbf{a}}{2}\right) & 0 & 0 \\ 0 & 0 & 0 \end{array} \right] \right. \\
&\quad \left. + B_{\mathbf{k}_1-\mathbf{k}_2} \left[\begin{array}{ccc} 0 & 0 & 2\cos\left(\frac{\mathbf{k}_1\cdot\mathbf{b}}{2}\right) \\ 0 & 0 & 0 \\ 2\cos\left(\frac{\mathbf{k}_2\cdot\mathbf{b}}{2}\right) & 0 & 0 \end{array} \right] \right\} \left(\begin{array}{c} s_{\mathbf{k}_2,\sigma} \\ p_{\mathbf{k}_2,x,\sigma} \\ p_{\mathbf{k}_2,y,\sigma} \end{array} \right), \tag{B.27}
\end{aligned}
$$

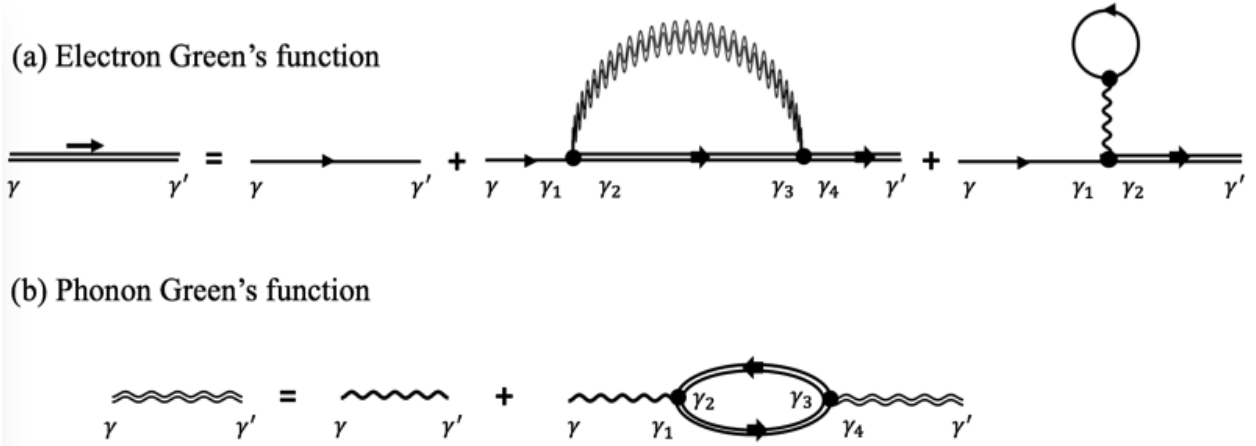where $A_{\mathbf{k}} = a_{\mathbf{k}} + a_{\mathbf{k}}^\dagger$ and $B_{\mathbf{k}} = b_{\mathbf{k}} + b_{\mathbf{k}}^\dagger$.

A   Self-energy

Feynman diagrams of the Migdal theory is show in Fig. B.1. The electron self-energy is given by

$$\Sigma(\mathbf{k}, i\omega_n) = -\frac{\tilde{\alpha}^2}{2N\beta\omega} \sum_{\mathbf{k}',m} d_{aa}(\mathbf{k} - \mathbf{k}', i\omega_n - i\omega_m) \times$$

$$\begin{bmatrix} 4\cos^2(k_x/2)g_{p_xp_x}(\mathbf{k}', i\omega_m) & 4\cos(k_x/2)\cos(k_x'/2)g_{p_xs}(\mathbf{k}', i\omega_m) & 0 \\ 4\cos(k_x/2)\cos(k_x'/2)g_{sp_x}(\mathbf{k}', i\omega_m) & 4\cos^2(k_x'/2)g_{ss}(\mathbf{k}', i\omega_m) & 0 \\ 0 & 0 & 0 \end{bmatrix}$$

$$+d_{ab}(\mathbf{k} - \mathbf{k}', i\omega_n - i\omega_m) \times$$

$$\begin{bmatrix} 4\cos(k_x/2)\cos(k_y/2)g_{p_xp_y}(\mathbf{k}', i\omega_m) & 0 & 4\cos(k_x/2)\cos(k_y'/2)g_{p_xs}(\mathbf{k}', i\omega_m) \\ 4\cos(k_y/2)\cos(k_x'/2)g_{sp_y}(\mathbf{k}', i\omega_m) & 0 & 4\cos(k_x'/2)\cos(k_y'/2)g_{ss}(\mathbf{k}', i\omega_m) \\ 0 & 0 & 0 \end{bmatrix}$$

$$+d_{ba}(\mathbf{k} - \mathbf{k}', i\omega_n - i\omega_m) \times$$

$$\begin{bmatrix} 4\cos(k_x/2)\cos(k_y/2)g_{p_yp_x}(\mathbf{k}', i\omega_m) & 4\cos(k_y/2)\cos(k_x'/2)g_{p_ys}(\mathbf{k}', i\omega_m) & 0 \\ 0 & 0 & 0 \\ 4\cos(k_x/2)\cos(k_y'/2)g_{sp_x}(\mathbf{k}', i\omega_m) & 4\cos(k_x'/2)\cos(k_y'/2)g_{ss}(\mathbf{k}', i\omega_m) & 0 \end{bmatrix}$$

$$+d_{bb}(\mathbf{k} - \mathbf{k}', i\omega_n - i\omega_m) \times$$

$$\begin{bmatrix} 4\cos^2(k_y/2)g_{p_yp_y}(\mathbf{k}', i\omega_m) & 0 & 4\cos(k_y/2)\cos(k_y'/2)g_{p_ys}(\mathbf{k}', i\omega_m) \\ 0 & 0 & 0 \\ 4\cos(k_y/2)\cos(k_y'/2)g_{sp_y}(\mathbf{k}', i\omega_m) & 0 & 4\cos^2(k_y'/2)g_{ss}(\mathbf{k}', i\omega_m) \end{bmatrix}$$

$$= -\frac{\tilde{\alpha}^2}{2N\beta\omega} \sum_{\mathbf{k}',m} \sum_{\mathbf{k}',m} D_{aa}(\mathbf{k} - \mathbf{k}', i\omega_n - i\omega_m) \times$$

$$\begin{bmatrix} 4\cos^2(k_x/2)G_{p_xp_x}(\mathbf{k}', i\omega_m) & 4\cos(k_x/2)\cos(k_x'/2)e^{-i\frac{k_x'}{2}}G_{p_xs}(\mathbf{k}', i\omega_m) & 0 \\ 4\cos(k_x/2)\cos(k_x'/2)e^{i\frac{k_x'}{2}}G_{sp_x}(\mathbf{k}', i\omega_m) & 4\cos^2(k_x'/2)G_{ss}(\mathbf{k}', i\omega_m) & 0 \\ 0 & 0 & 0 \end{bmatrix}$$

$$+D_{ab}(\mathbf{k} - \mathbf{k}', i\omega_n - i\omega_m)e^{-i\frac{k_x-k_y}{2}} \times$$

$$\begin{bmatrix} 4\cos(k_x/2)\cos(k_y/2)G_{p_xp_y}(\mathbf{k}', i\omega_m) & 0 & 4\cos(k_x/2)\cos(k_y'/2)e^{-i\frac{k_y'}{2}}G_{p_xs}(\mathbf{k}', i\omega_m) \\ 4\cos(k_y/2)\cos(k_x'/2)e^{i\frac{k_x'}{2}}G_{sp_y}(\mathbf{k}', i\omega_m) & 0 & 4\cos(k_x'/2)\cos(k_y'/2)e^{i\frac{k_x'-k_y'}{2}}G_{ss}(\mathbf{k}', i\omega_m) \\ 0 & 0 & 0 \end{bmatrix}$$

(a) Electron Green's function

(b) Phonon Green's function

Figure B.1: (color online) Feynman diagrams of the Migdal theory. γ, γ', γ_1, γ_2, γ_3, γ_4 are orbital indexs. The solid line indicates electron Green's function and the wave line indicates phonon Green's function. The single line and double line indicate bare and dressed Green's function, respectively.

$$+D_{ba}(\mathbf{k}-\mathbf{k}',\mathrm{i}\omega_n-\mathrm{i}\omega_m)e^{\mathrm{i}\frac{k_x-k_y}{2}}\times$$

$$\begin{bmatrix} 4\cos(k_x/2)\cos(k_y/2)G_{p_yp_x}(\mathbf{k}',\mathrm{i}\omega_m) & 4\cos(k_y/2)\cos(k_x'/2)e^{-\mathrm{i}\frac{k_x'}{2}}G_{p_ys}(\mathbf{k}',\mathrm{i}\omega_m) & 0 \\ 0 & 0 & 0 \\ 4\cos(k_x/2)\cos(k_y'/2)e^{\mathrm{i}\frac{k_y'}{2}}G_{sp_x}(\mathbf{k}',\mathrm{i}\omega_m) & 4\cos(k_x'/2)\cos(k_y'/2)e^{-\mathrm{i}\frac{k_x'-k_y'}{2}}G_{ss}(\mathbf{k}',\mathrm{i}\omega_m) & 0 \end{bmatrix}$$

$$+D_{bb}(\mathbf{k}-\mathbf{k}',\mathrm{i}\omega_n-\mathrm{i}\omega_m)\times$$

$$\begin{bmatrix} 4\cos^2(k_y/2)G_{p_yp_y}(\mathbf{k}',\mathrm{i}\omega_m) & 0 & 4\cos(k_y/2)\cos(k_y'/2)e^{-\mathrm{i}\frac{k_y'}{2}}G_{p_ys}(\mathbf{k}',\mathrm{i}\omega_m) \\ 0 & 0 & 0 \\ 4\cos(k_y/2)\cos(k_y'/2)e^{\mathrm{i}\frac{k_y'}{2}}G_{sp_y}(\mathbf{k}',\mathrm{i}\omega_m) & 0 & 4\cos^2(k_y'/2)G_{ss}(\mathbf{k}',\mathrm{i}\omega_m) \end{bmatrix}.$$

$$\text{(B.28)}$$

The Hartree term is given by

$$\Sigma^H(\mathbf{k},\mathrm{i}\omega_n) = \begin{bmatrix} 0 & \Sigma^H_{sp_x}(\mathbf{k},\mathrm{i}\omega_n) & \Sigma^H_{sp_y}(\mathbf{k},\mathrm{i}\omega_n) \\ \Sigma^H_{p_xs}(\mathbf{k},\mathrm{i}\omega_n), & 0 & 0 \\ \Sigma^H_{p_ys}(\mathbf{k},\mathrm{i}\omega_n) & 0 & 0 \end{bmatrix}, \quad \text{(B.29)}$$

where

$$\begin{aligned} \Sigma^H_{p_xs}(\mathbf{k},\mathrm{i}\omega_n) &= \Sigma^H_{sp_x}(\mathbf{k},\mathrm{i}\omega_n) \\ &= \frac{2\tilde{a}^2}{2N\omega\beta}D^0_{aa}(\mathbf{0},0)2\cos(\frac{k_x}{2})\sum_{\mathbf{k}',m}2\cos(\frac{k_x'}{2})\left[e^{\mathrm{i}\frac{k_x'}{2}}G_{sp_x}(\mathbf{k}',\mathrm{i}\omega_n)\right. \\ &\quad \left.+e^{-\mathrm{i}\frac{k_x'}{2}}G_{p_xs}(\mathbf{k}',\mathrm{i}\omega_n)\right], \end{aligned}$$

and

$$\begin{aligned} \Sigma^H_{p_ys}(\mathbf{k},\mathrm{i}\omega_n) &= \Sigma^H_{sp_y}(\mathbf{k},\mathrm{i}\omega_n) \\ &= \frac{2\tilde{a}^2}{2N\omega\beta}D^0_{bb}(\mathbf{0},0)2\cos(\frac{k_y}{2})\sum_{\mathbf{k}',m}2\cos(\frac{k_y'}{2})\left[e^{\mathrm{i}\frac{k_y'}{2}}G_{sp_y}(\mathbf{k}',\mathrm{i}\omega_n)\right. \\ &\quad \left.+e^{-\mathrm{i}\frac{k_y'}{2}}G_{p_ys}(\mathbf{k}',\mathrm{i}\omega_n)\right]. \end{aligned}$$

Here, $D^0_{aa}(\mathbf{k}, i\omega_n)$ and $D^0_{bb}(\mathbf{k}, iv_n)$ are the bare Green's functions for phonons a and b, respectively. $\omega_n = \frac{(2n+1)\pi}{\beta}$ and $v_n = \frac{2n\pi}{\beta}$ are the Matsubara frequency for fermions and bosons, respectively.

The phonon self-energy is given by

$$
\Pi(\mathbf{q}, iv_n) = \begin{bmatrix} \Pi_{aa}(\mathbf{q}, iv_n) & \Pi_{ab}(\mathbf{q}, iv_n) \\ \Pi_{ba}(\mathbf{q}, iv_n) & \Pi_{bb}(\mathbf{q}, iv_n) \end{bmatrix}
\tag{B.30}
$$

where

$$
\begin{aligned}
\Pi_{aa}(\mathbf{q}, iv_n) &= \frac{2\tilde{\alpha}^2}{2N\beta\omega} \sum_{\mathbf{k},m} \Bigg[2\cos(\frac{k_x}{2}) g_{p_x s}(\mathbf{k}, i\omega_m) 2\cos(\frac{k_x + q_x}{2}) g_{p_x s}(\mathbf{k}+\mathbf{q}, i\omega_m + iv_n) + \\
&\quad 2\cos(\frac{k_x}{2}) g_{s p_x}(\mathbf{k}, i\omega_m) 2\cos(\frac{k_x + q_x}{2}) g_{s p_x}(\mathbf{k}+\mathbf{q}, i\omega_m + iv_n) + \\
&\quad 4\cos^2(\frac{k_x}{2}) g_{ss}(\mathbf{k}, i\omega_m) g_{p_x p_x}(\mathbf{k}+\mathbf{q}, i\omega_m + iv_n) + \\
&\quad g_{p_x p_x}(\mathbf{k}, i\omega_m) 4\cos^2(\frac{k_x + q_x}{2}) g_{ss}(\mathbf{k}+\mathbf{q}, i\omega_m + iv_n) \Bigg] \\
&= \frac{2\tilde{\alpha}^2}{2N\beta\omega} \sum_{\mathbf{k},m} \Bigg[2\cos(\frac{k_x}{2}) e^{-i\frac{k_x}{2}} G_{p_x s}(\mathbf{k}, i\omega_m) 2\cos(\frac{k_x + q_x}{2}) e^{-i\frac{k_x + q_x}{2}} \times \\
&\quad G_{p_x s}(\mathbf{k}+\mathbf{q}, i\omega_m + iv_n) + 2\cos(\frac{k_x}{2}) e^{i\frac{k_x}{2}} G_{s p_x}(\mathbf{k}, i\omega_m) 2\cos(\frac{k_x + q_x}{2}) e^{i\frac{k_x + q_x}{2}} \times \\
&\quad G_{s p_x}(\mathbf{k}+\mathbf{q}, i\omega_m + iv_n) + 4\cos^2(\frac{k_x}{2}) G_{ss}(\mathbf{k}, i\omega_m) G_{p_x p_x}(\mathbf{k}+\mathbf{q}, i\omega_m + iv_n) + \\
&\quad G_{p_x p_x}(\mathbf{k}, i\omega_m) 4\cos^2(\frac{k_x + q_x}{2}) G_{ss}(\mathbf{k}+\mathbf{q}, i\omega_m + iv_n) \Bigg],
\end{aligned}
\tag{B.31}
$$

$$
\begin{aligned}
\Pi_{ab}(\mathbf{q}, iv_n) &= \frac{2\tilde{\alpha}^2}{2N\beta\omega} \sum_{\mathbf{k},m} \Bigg[2\cos(\frac{k_x}{2}) g_{p_y s}(\mathbf{k}, i\omega_m) 2\cos(\frac{k_y + q_y}{2}) g_{p_x s}(\mathbf{k}+\mathbf{q}, i\omega_m + iv_n) + \\
&\quad 2\cos(\frac{k_y}{2}) g_{s p_x}(\mathbf{k}, i\omega_m) 2\cos(\frac{k_x + q_x}{2}) g_{s p_y}(\mathbf{k}+\mathbf{q}, i\omega_m + iv_n) + \\
&\quad g_{p_y p_x}(\mathbf{k}, i\omega_m) 4\cos(\frac{k_x + q_x}{2})\cos(\frac{k_y + q_y}{2}) g_{ss}(\mathbf{k}+\mathbf{q}, i\omega_m + iv_n) + \\
&\quad 4\cos(\frac{k_x}{2})\cos(\frac{k_y}{2}) g_{ss}(\mathbf{k}, i\omega_m) g_{p_x p_y}(\mathbf{k}+\mathbf{q}, i\omega_m + iv_n) \Bigg] \\
&= \frac{2\tilde{\alpha}^2}{2N\beta\omega} e^{-i\frac{q_x - q_y}{2}} \sum_{\mathbf{k},m} \Bigg[2\cos(\frac{k_x}{2}) e^{-i\frac{k_x}{2}} G_{p_y s}(\mathbf{k}, i\omega_m) 2\cos(\frac{k_y + q_y}{2}) e^{-i\frac{k_y + q_y}{2}} \times
\end{aligned}
$$

$$G_{p_x s}(\mathbf{k} + \mathbf{q}, i\omega_m + i\nu_n) + 2\cos(\frac{k_y}{2})e^{i\frac{k_y}{2}}G_{s p_x}(\mathbf{k}, i\omega_m)2\cos(\frac{k_x + q_x}{2})e^{i\frac{k_x + q_x}{2}} \times$$

$$G_{s p_y}(\mathbf{k} + \mathbf{q}, i\omega_m + i\nu_n) + G_{p_y p_x}(\mathbf{k}, i\omega_m)4\cos(\frac{k_x + q_x}{2})e^{i\frac{k_x + q_x}{2}} \times$$

$$\cos(\frac{k_y + q_y}{2})e^{-i\frac{k+y+q_y}{2}}G_{ss}(\mathbf{k} + \mathbf{q}, i\omega_m + i\nu_n) + 4\cos(\frac{k_x}{2})e^{-i\frac{k_x}{2}}\cos(\frac{k_y}{2}) \times$$

$$e^{i\frac{k_y}{2}}G_{ss}(\mathbf{k}, i\omega_m)G_{p_x p_y}(\mathbf{k} + \mathbf{q}, i\omega_m + i\nu_n)\Big], \tag{B.32}$$

$$
\begin{aligned}
\Pi_{ba}(\mathbf{q}, i\nu_n) &= \frac{2\tilde{\alpha}^2}{2N\beta\omega}\sum_{\mathbf{k},m}\Big[2\cos(\frac{k_x}{2})g_{s p_y}(\mathbf{k}, i\omega_m)2\cos(\frac{k_y + q_y}{2})g_{s p_x}(\mathbf{k} + \mathbf{q}, i\omega_m + i\nu_n)+ \\
&\quad 2\cos(\frac{k_y}{2})g_{p_x s}(\mathbf{k}, ii\omega\omega_m)2\cos(\frac{k_x + q_x}{2})g_{p_y s}(\mathbf{k} + \mathbf{q}, i\omega_m + i\nu_n) + \\
&\quad g_{p_x p_y}(\mathbf{k}, i\omega_m)4\cos(\frac{k_x + q_x}{2})\cos(\frac{k_y + q_y}{2})g_{ss}(\mathbf{k} + \mathbf{q}, i\omega_m + i\nu_n) + \\
&\quad 4\cos(\frac{k_x}{2})\cos(\frac{k_y}{2})g_{ss}(\mathbf{k}, i\omega_m)g_{p_y p_x}(\mathbf{k} + \mathbf{q}, i\omega_m + i\nu_n)\Big] \\
&= \frac{2\tilde{\alpha}^2}{2N\beta\omega}e^{i\frac{q_x - q_y}{2}}\sum_{\mathbf{k},m}\Big[2\cos(\frac{k_x}{2})e^{i\frac{k_x}{2}}G_{s p_y}(\mathbf{k}, i\omega_m)2\cos(\frac{k_y + q_y}{2})e^{i\frac{k_y + q_y}{2}} \times \\
&\quad G_{s p_x}(\mathbf{k} + \mathbf{q}, i\omega_m + i\nu_n) + 2\cos(\frac{k_y}{2})e^{-i\frac{k_y}{2}}G_{p_x s}(\mathbf{k}, i\omega_m)2\cos(\frac{k_x + q_x}{2})e^{-i\frac{k_x + q_x}{2}} \times \\
&\quad G_{p_y s}(\mathbf{k} + \mathbf{q}, i\omega_m + i\nu_n) + G_{p_x p_y}(\mathbf{k}, i\omega_m)4\cos(\frac{k_x + q_x}{2})e^{-i\frac{k_x + q_x}{2}}\cos(\frac{k_y + q_y}{2}) \\
&\quad e^{i\frac{k+y+q_y}{2}}G_{ss}(\mathbf{k} + \mathbf{q}, i\omega_m + i\nu_n) + 4\cos(\frac{k_x}{2})e^{i\frac{k_x}{2}}\cos(\frac{k_y}{2})e^{-i\frac{k_y}{2}}G_{ss}(\mathbf{k}, i\omega_m) \times \\
&\quad G_{p_y p_x}(\mathbf{k} + \mathbf{q}, i\omega_m + i\nu_n)\Big], \tag{B.33}
\end{aligned}
$$

$$
\begin{aligned}
\Pi_{bb}(\mathbf{q}, i\nu_n) &= \frac{2\tilde{\alpha}^2}{2N\beta\omega}\sum_{\mathbf{k},m}\Big[2\cos(\frac{k_y}{2})g_{p_y s}(\mathbf{k}, i\omega_m)2\cos(\frac{k_y + q_y}{2})g_{p_y s}(\mathbf{k} + \mathbf{q}, i\omega_m + i\nu_n)+ \\
&\quad 2\cos(\frac{k_y}{2})g_{s p_y}(\mathbf{k}, i\omega_m)2\cos(\frac{k_y + q_y}{2})g_{s p_y}(\mathbf{k} + \mathbf{q}, i\omega_m + i\nu_n) + \\
&\quad 4\cos^2(\frac{k_y}{2})g_{ss}(\mathbf{k}, i\omega_m)g_{p_y p_y}(\mathbf{k} + \mathbf{q}, i\omega_m + i\nu_n) + \\
&\quad g_{p_y p_y}(\mathbf{k}, i\omega_m)4\cos^2(\frac{k_y + q_y}{2})g_{ss}(\mathbf{k} + \mathbf{q}, i\omega_m + i\nu_n)\Big] \\
&= \frac{2\tilde{\alpha}^2}{2N\beta\omega}\sum_{\mathbf{k},m}\Big[2\cos(\frac{k_y}{2})e^{-i\frac{k_y}{2}}G_{p_y s}(\mathbf{k}, i\omega_m)2\cos(\frac{k_y + q_y}{2})e^{-i\frac{k_y + q_y}{2}} \times \\
&\quad G_{p_y s}(\mathbf{k} + \mathbf{q}, i\omega_m + i\nu_n) + 2\cos(\frac{k_y}{2})e^{i\frac{k_y}{2}}G_{s p_y}(\mathbf{k}, i\omega_m)2\cos(\frac{k_y + q_y}{2})e^{i\frac{k_y + q_y}{2}} \times
\end{aligned}
$$

$$G_{sp_y}(\mathbf{k}+\mathbf{q}, i\omega_m + i\nu_n) + 4\cos^2(\frac{k_y}{2})G_{ss}(\mathbf{k}, i\omega_m)G_{p_yp_y}(\mathbf{k}+\mathbf{q}, i\omega_m + i\nu_n)$$

$$+ G_{p_yp_y}(\mathbf{k}, i\omega_m)4\cos^2(\frac{k_y+q_y}{2})G_{ss}(\mathbf{k}+\mathbf{q}, i\omega_m + i\nu_n)\Big]. \tag{B.34}$$

B Charge and superconducting susceptibility

The charge-density-wave susceptibility is defined as

$$\chi_{\alpha\beta}(\mathbf{q}) = \frac{1}{N} \sum_{\mathbf{r},\mathbf{r}',\sigma,\sigma'} e^{i\mathbf{q}\cdot(\mathbf{r}-\mathbf{r}')} \int_0^\beta d\tau \left[\langle \hat{n}_{\mathbf{r},\alpha,\sigma}(\tau)\hat{n}_{\mathbf{r}',\beta,\sigma'}(0) \rangle - \langle \hat{n}_{\mathbf{r},\alpha,\sigma}(\tau) \rangle \langle \hat{n}_{\mathbf{r}',\beta,\sigma'} \rangle \right], \tag{B.35}$$

in which α and β are orbital indexes. For the noninteracting Hamiltonian, $\chi_{\alpha\beta}(\mathbf{q}) = \frac{2}{N\beta} \sum_{\mathbf{k},n} G_{\alpha\beta}(\mathbf{k}+\mathbf{q}, i\omega_n)G_{\beta\alpha}(\mathbf{k}, i\omega_n)$. Since $G_{\alpha\beta}(\mathbf{k}, i\omega_n)$ has a translation symmetry, $\chi_{\alpha\beta}(\mathbf{q})$ has a translation symmetry as well. $\chi(q)$ is a 3×3 matrix, which could be written as

$$\chi(\mathbf{q}) = \begin{bmatrix} \tilde{\chi}_{ss}(\mathbf{q}) & e^{i\frac{q_x}{2}}\tilde{\chi}_{sp_x}(\mathbf{q}) & e^{i\frac{q_y}{2}}\tilde{\chi}_{sp_y}(\mathbf{q}) \\ e^{-i\frac{q_x}{2}}\tilde{\chi}_{p_xs}(\mathbf{q}) & \tilde{\chi}_{p_xp_x}(\mathbf{q}) & e^{-i\frac{q_x-q_y}{2}}\tilde{\chi}_{p_xp_y}(\mathbf{q}) \\ e^{-i\frac{q_y}{2}}\tilde{\chi}_{p_ys}(\mathbf{q}) & e^{i\frac{q_x-q_y}{2}}\tilde{\chi}_{p_yp_x}(\mathbf{q}) & \tilde{\chi}_{p_yp_y}(\mathbf{q}) \end{bmatrix}. \tag{B.36}$$

Here, $\tilde{\chi}_{\alpha\beta}(\mathbf{q}) = \frac{2}{N\beta} \sum_{\mathbf{k},n} g_{\alpha\beta}(\mathbf{k}+\mathbf{q}, i\omega_n)g_{\beta\alpha}(\mathbf{k}, i\omega_n)$ for the non-interacting system. $\tilde{\chi}_{\alpha\beta}(\mathbf{q})$ is introduced here in that I can obtain $\tilde{\chi}_{\alpha\beta}(\mathbf{q})$ directly from the Feynman diagram. With the Migdal theory,

$$\tilde{\chi}_{\alpha\beta}(\mathbf{q}) = \tilde{\chi}_{\alpha\beta}^0(\mathbf{q}) + R_\alpha(\mathbf{q}) \left[II - \Pi(\mathbf{q}, 0)D^0(\mathbf{q}, 0) \right]^{-1} Q_\beta(\mathbf{q}), \tag{B.37}$$

where $D^0(\mathbf{q}, 0)$ is the bare phonon Green's function and II is a 2×2 unit matrix. $R_\alpha(\mathbf{q})$ and $Q_\beta^T(\mathbf{q})$ are 1×2 vectors,

$$R_\alpha(\mathbf{q}) = \frac{2\tilde{\alpha}}{\sqrt{2N\beta\omega}N\beta} \left[D_{aa}^0(\mathbf{q}, 0)R_\alpha^1(\mathbf{q}) \quad D_{bb}^0(\mathbf{q}, 0)R_\alpha^2(\mathbf{q}) \right] \tag{B.38}$$

$$Q_\beta^T(\mathbf{q}) = -\frac{2\tilde{\alpha}}{\sqrt{2N\beta\omega}} \left[Q_\beta^1(\mathbf{q}) \quad Q_\beta^2(\mathbf{q}) \right]. \tag{B.39}$$

$$R_s^1(\mathbf{q}) = \sum_{\mathbf{k},m}\left[2\cos(\frac{k_x+q_x}{2})g_{ss}(\mathbf{k}+\mathbf{q},\mathrm{i}\omega_m)g_{p_x s}(\mathbf{k},\mathrm{i}\omega_m)\right.$$

$$\left.+2\cos(\frac{k_x}{2})g_{sp_x}(\mathbf{k}+\mathbf{q},\mathrm{i}\omega_m)g_{ss}(\mathbf{k},\mathrm{i}\omega_m)\right]$$

$$= e^{\mathrm{i}\frac{q_x}{2}}\sum_{\mathbf{k},m}\left[2\cos(\frac{k_x+q_x}{2})e^{-\mathrm{i}\frac{k_x+q_x}{2}}G_{ss}(\mathbf{k}+\mathbf{q},\mathrm{i}\omega_m)G_{p_x s}(\mathbf{k},\mathrm{i}\omega_m)+\right.$$

$$\left.G_{sp_x}(\mathbf{k}+\mathbf{q},\mathrm{i}\omega_m)2\cos(\frac{k_x}{2})e^{\mathrm{i}\frac{k_x}{2}}G_{ss}(\mathbf{k},\mathrm{i}\omega_m)\right]$$

$$R_s^2(\mathbf{q}) = \sum_{\mathbf{k},m}\left[2\cos(\frac{k_y+q_y}{2})g_{ss}(\mathbf{k}+\mathbf{q},\mathrm{i}\omega_m)g_{p_y s}(\mathbf{k},\mathrm{i}\omega_m)\right.$$

$$\left.+2\cos(\frac{k_y}{2})g_{sp_y}(\mathbf{k}+\mathbf{q},\mathrm{i}\omega_m)g_{ss}(\mathbf{k},\mathrm{i}\omega_m)\right]$$

$$= e^{\mathrm{i}\frac{q_y}{2}}\sum_{\mathbf{k},m}\left[2\cos(\frac{k_y+q_y}{2})e^{-\mathrm{i}\frac{k_y+q_y}{2}}G_{ss}(\mathbf{k}+\mathbf{q},\mathrm{i}\omega_m)G_{p_y s}(\mathbf{k},\mathrm{i}\omega_m)+\right.$$

$$\left.G_{sp_y}(\mathbf{k}+\mathbf{q},\mathrm{i}\omega_m)2\cos(\frac{k_y}{2})e^{\mathrm{i}\frac{k_y}{2}}G_{ss}(\mathbf{k},\mathrm{i}\omega_m)\right]$$

$$R_{p_x}^1(\mathbf{q}) = \sum_{\mathbf{k},m}\left[2\cos(\frac{k_x+q_x}{2})g_{p_x s}(\mathbf{k}+\mathbf{q},\mathrm{i}\omega_m)g_{p_x p_x}(\mathbf{k},\mathrm{i}\omega_m) + 2\cos(\frac{k_x}{2})g_{p_x p_x}(\mathbf{k}+\mathbf{q},\mathrm{i}\omega_m)\times\right.$$

$$\left.g_{sp_x}(\mathbf{k},\mathrm{i}\omega_m)\right]$$

$$= \sum_{\mathbf{k},m}\left[2\cos(\frac{k_x+q_x}{2})e^{-\mathrm{i}\frac{k_x+q_x}{2}}G_{p_x s}(\mathbf{k}+\mathbf{q},\mathrm{i}\omega_m)G_{p_x p_x}(\mathbf{k},\mathrm{i}\omega_m)+\right.$$

$$\left.G_{p_x p_x}(\mathbf{k}+\mathbf{q},\mathrm{i}\omega_m)2\cos(\frac{k_x}{2})e^{\mathrm{i}\frac{k_x}{2}}G_{sp_x}(\mathbf{k},\mathrm{i}\omega_m)\right]$$

$$R_{p_x}^2(\mathbf{q}) = \sum_{\mathbf{k},m}\left[2\cos(\frac{k_y+q_y}{2})g_{p_y s}(\mathbf{k}+\mathbf{q},\mathrm{i}\omega_m)g_{p_y p_x}(\mathbf{k},\mathrm{i}\omega_m) + 2\cos(\frac{k_y}{2})g_{p_x p_y}(\mathbf{k}+\mathbf{q},\mathrm{i}\omega_m)\times\right.$$

$$\left.g_{sp_x}(\mathbf{k},\mathrm{i}\omega_m)\right]$$

$$= e^{-\mathrm{i}\frac{q_x-q_y}{2}}\sum_{\mathbf{k},m}\left[2\cos(\frac{k_y+q_y}{2})e^{-\mathrm{i}\frac{k_y+q_y}{2}}G_{p_x s}(\mathbf{k}+\mathbf{q},\mathrm{i}\omega_m)G_{p_y p_x}(\mathbf{k},\mathrm{i}\omega_m)\right.$$

$$\left.+G_{p_x p_y}(\mathbf{k}+\mathbf{q},\mathrm{i}\omega_m)2\cos(\frac{k_y}{2})e^{\mathrm{i}\frac{k_y}{2}}G_{sp_x}(\mathbf{k},\mathrm{i}\omega_m)\right]$$

$$R_{p_y}^1(\mathbf{q}) = \sum_{\mathbf{k},m}\left[2\cos(\frac{k_x+q_x}{2})g_{p_y s}(\mathbf{k}+\mathbf{q},\mathrm{i}\omega_m)g_{p_x p_y}(\mathbf{k},\mathrm{i}\omega_m) + 2\cos(\frac{k_x}{2})g_{p_y p_x}(\mathbf{k}+\mathbf{q},\mathrm{i}\omega_m)\times\right.$$

$$\left.g_{sp_y}(\mathbf{k},\mathrm{i}\omega_m)\right]$$

$$= e^{\mathrm{i}\frac{q_x-q_y}{2}}\sum_{\mathbf{k},m}\left[2\cos(\frac{k_x+q_x}{2})e^{-\mathrm{i}\frac{k_x+q_x}{2}}G_{p_y s}(\mathbf{k}+\mathbf{q},\mathrm{i}\omega_m)G_{p_x p_y}(\mathbf{k},\mathrm{i}\omega_m)\right.$$

$$+G_{p_y p_x}(\mathbf{k}+\mathbf{q},i\omega_m)2\cos(\frac{k_x}{2})e^{i\frac{k_x}{2}}G_{sp_y}(\mathbf{k},i\omega_m)\Big]$$

$$R^2_{p_y} = \sum_{\mathbf{k},m}\Big[2\cos(\frac{k_y+q_y}{2})g_{p_y s}(\mathbf{k}+\mathbf{q},i\omega_m)g_{p_y p_y}(\mathbf{k},i\omega_m) + 2\cos(\frac{k_y}{2})g_{p_y p_y}(\mathbf{k}+\mathbf{q},i\omega_m)\times$$

$$g_{sp_y}(\mathbf{k},i\omega_m)\Big]$$

$$= \sum_{\mathbf{k},m}\Big[2\cos(\frac{k_y+q_y}{2})e^{-i\frac{k_y+q_y}{2}}G_{p_y s}(\mathbf{k}+\mathbf{q},i\omega_m)G_{p_y p_y}(\mathbf{k},i\omega_m)$$

$$+G_{p_y p_y}(\mathbf{k}+\mathbf{q},i\omega_m)2\cos(\frac{k_y}{2})e^{i\frac{k_y}{2}}G_{sp_y}(\mathbf{k},i\omega_m)\Big]$$

$$Q^1_s(\mathbf{q}) = \sum_{\mathbf{k},m}\Big[2\cos(\frac{k_x}{2})g_{p_x s}(\mathbf{k}+\mathbf{q},i\omega_m)g_{ss}(\mathbf{k},i\omega_m) + 2\cos(\frac{k_x+q_x}{2})g_{ss}(\mathbf{k}+\mathbf{q},i\omega_m)\times$$

$$g_{sp_x}(\mathbf{k},i\omega_m)\Big]$$

$$= e^{-i\frac{q_x}{2}}\sum_{\mathbf{k},m}\Big[G_{p_x s}(\mathbf{k}+\mathbf{q},i\omega_m)2\cos(\frac{k_x}{2})e^{-i\frac{k_x}{2}}G_{ss}(\mathbf{k},i\omega_m)+$$

$$2\cos(\frac{k_x+q_x}{2})e^{i\frac{k_x+q_x}{2}}G_{ss}(\mathbf{k}+\mathbf{q},i\omega_m)G_{sp_x}(\mathbf{k},i\omega_m)\Big]$$

$$Q^2_s(\mathbf{q}) = \sum_{\mathbf{k},m}\Big[2\cos(\frac{k_y}{2})g_{p_y s}(\mathbf{k}+\mathbf{q},i\omega_m)g_{ss}(\mathbf{k},i\omega_m) + 2\cos(\frac{k_y+q_y}{2})g_{ss}(\mathbf{k}+\mathbf{q},i\omega_m)\times$$

$$g_{sp_y}(\mathbf{k},i\omega_m)\Big]$$

$$= e^{-i\frac{q_y}{2}}\sum_{\mathbf{k},m}\Big[G_{p_y s}(\mathbf{k}+\mathbf{q},i\omega_m)2\cos(\frac{k_y}{2})e^{-i\frac{k_y}{2}}G_{ss}(\mathbf{k},i\omega_m)+$$

$$2\cos(\frac{k_y+q_y}{2})e^{i\frac{k_y+q_y}{2}}G_{ss}(\mathbf{k}+\mathbf{q},i\omega_m)G_{sp_y}(\mathbf{k},i\omega_m)\Big]$$

$$Q^1_{p_x}(\mathbf{q}) = \sum_{\mathbf{k},m}\Big[2\cos(\frac{k_x}{2})g_{p_x p_x}(\mathbf{k}+\mathbf{q},i\omega_m)g_{p_x s}(\mathbf{k},i\omega_m) + 2\cos(\frac{k_x+q_x}{2})g_{sp_x}(\mathbf{k}+\mathbf{q},i\omega_m)\times$$

$$g_{p_x p_x}(\mathbf{k},i\omega_m)\Big]$$

$$= \sum_{\mathbf{k},m}\Big[G_{p_x p_x}(\mathbf{k}+\mathbf{q},i\omega_m)2\cos(\frac{k_x}{2})e^{-i\frac{k_x}{2}}G_{p_x s}(\mathbf{k},i\omega_m)+$$

$$2\cos(\frac{k_x+q_x}{2})e^{i\frac{k_x+q_x}{2}}G_{sp_x}(\mathbf{k}+\mathbf{q},i\omega_m)G_{p_x p_x}(\mathbf{k},i\omega_m)\Big]$$

$$Q^2_{p_x}(\mathbf{q}) = \sum_{\mathbf{k},m}\Big[2\cos(\frac{k_y}{2})g_{p_y p_x}(\mathbf{k}+\mathbf{q},i\omega_m)g_{p_x s}(\mathbf{k},i\omega_m) + 2\cos(\frac{k_y+q_y}{2})g_{sp_x}(\mathbf{k}+\mathbf{q},i\omega_m)\times$$

$$g_{p_x p_y}(\mathbf{k},i\omega_m)\Big]$$

$$= e^{i\frac{q_x-q_y}{2}}\sum_{\mathbf{k},m}\Bigg[G_{p_yp_x}(\mathbf{k}+\mathbf{q},i\omega_m)2\cos(\frac{k_y}{2})e^{-i\frac{k_y}{2}}G_{p_xs}(\mathbf{k},i\omega_m)+$$

$$2\cos(\frac{k_y+q_y}{2})e^{i\frac{k_y+q_y}{2}}G_{sp_x}(\mathbf{k}+\mathbf{q},i\omega_m)G_{p_xp_y}(\mathbf{k},i\omega_m)\Bigg]$$

$$Q^1_{p_y}(\mathbf{q}) = \sum_{\mathbf{k},m}\Bigg[2\cos(\frac{k_x}{2})g_{p_xp_y}(\mathbf{k}+\mathbf{q},i\omega_m)g_{p_ys}(\mathbf{k},i\omega_m)+2\cos(\frac{k_x+q_x}{2})g_{sp_y}(\mathbf{k}+\mathbf{q},i\omega_m)\times$$

$$g_{p_yp_x}(\mathbf{k},i\omega_m)\Bigg]$$

$$= e^{-i\frac{q_x-q_y}{2}}\sum_{\mathbf{k},m}\Bigg[G_{p_xp_y}(\mathbf{k}+\mathbf{q},i\omega_m)2\cos(\frac{k_x}{2})e^{-i\frac{k_x}{2}}G_{p_ys}(\mathbf{k},i\omega_m)+$$

$$2\cos(\frac{k_x+q_x}{2})e^{i\frac{k_x+q_x}{2}}G_{sp_y}(\mathbf{k}+\mathbf{q},i\omega_m)G_{p_yp_x}(\mathbf{k},i\omega_m)\Bigg]$$

$$Q^2_{p_y}(\mathbf{q}) = \sum_{\mathbf{k},m}\Bigg[2\cos(\frac{k_y}{2})g_{p_yp_y}(\mathbf{k}+\mathbf{q},i\omega_m)g_{p_ys}(\mathbf{k},i\omega_m)+2\cos(\frac{k_y+q_y}{2})g_{sp_y}(\mathbf{k}+\mathbf{q},i\omega_m)\times$$

$$g_{p_yp_y}(\mathbf{k},i\omega_m)\Bigg]$$

$$= \sum_{\mathbf{k},m}\Bigg[G_{p_yp_y}(\mathbf{k}+\mathbf{q},i\omega_m)2\cos(\frac{k_y}{2})e^{-i\frac{k_y}{2}}G_{p_ys}(\mathbf{k},i\omega_m)+$$

$$2\cos(\frac{k_y+q_y}{2})e^{i\frac{k_y+q_y}{2}}G_{sp_y}(\mathbf{k}+\mathbf{q},i\omega_m)G_{p_yp_y}(\mathbf{k},i\omega_m)\Bigg]$$

The superconducting susceptibility is defined as

$$\chi^{sp}_{\alpha\beta} = \frac{1}{N}\int_0^\beta d\tau\sum_{\mathbf{r},\mathbf{r}'}\langle\alpha_{\mathbf{r},\uparrow}(\tau)\alpha_{\mathbf{r},\downarrow}(\tau)\beta^\dagger_{\mathbf{r}',\uparrow}(0)\beta^\dagger_{\mathbf{r}',\downarrow}(0)\rangle$$

$$= \frac{1}{N^3}\int_0^\beta d\tau\sum_{\mathbf{r},\mathbf{r}'}\sum_{\mathbf{k}_1,\mathbf{k}_2,\mathbf{k}_3,\mathbf{k}_4}\langle\alpha_{\mathbf{k}_1,\uparrow}(\tau)\alpha_{\mathbf{k}k_2,\downarrow}(\tau)\beta^\dagger_{\mathbf{k}_3,\uparrow}(0)\beta^\dagger_{\mathbf{k}_4,\downarrow}(0)\rangle e^{-i(\mathbf{k}_1+\mathbf{k}_2)\cdot\mathbf{r}}e^{-i(\mathbf{k}_3+\mathbf{k}_4)\cdot\mathbf{r}'}$$

$$= \frac{1}{N}\int_0^\beta d\tau\sum_{\mathbf{k}_1,\mathbf{k}_2}\langle\alpha_{\mathbf{k}_1,\uparrow}(\tau)\alpha_{-\mathbf{k}_1,\downarrow}(\tau)\beta^\dagger_{\mathbf{k}_2,\uparrow}(0)\beta^\dagger_{-\mathbf{k}_2,\downarrow}(0)\rangle$$

$$= \frac{1}{N}\int_0^\beta d\tau\sum_{\mathbf{k}}g_{\alpha\beta}(\mathbf{k},\tau)g_{\alpha\beta}(-\mathbf{k},\tau)$$

$$= \frac{1}{N\beta}\sum_{\mathbf{k},m}g_{\alpha\beta}(\mathbf{k},i\omega_m)g_{\alpha\beta}(-\mathbf{k},-i\omega_m)$$

$$= \frac{1}{N\beta}\sum_{\mathbf{k},m}G_{\alpha\beta}(\mathbf{k},i\omega_m)G_{\alpha\beta}(-\mathbf{k},-i\omega_m) \tag{B.40}$$

Within the Migdal theory, $\chi^{sp}_{\alpha\beta}$ is given by summing the infinite series of ladder diagrams. The result is

$$\chi^{sp}_{\alpha\beta} = \frac{1}{N\beta} \sum_{\mathbf{k},m} F_{\alpha\beta\alpha\beta}(\mathbf{k}, i\omega_m)\Lambda_{\alpha\beta\alpha\beta}(\mathbf{k}, i\omega_m), \tag{B.41}$$

where

$$F_{\tau_1\gamma_1\tau_2\gamma_2}(\mathbf{k}, i\omega_m) = G_{\tau_1\gamma_1}(\mathbf{k}, i\omega_m)G_{\tau_2\gamma_2}(-\mathbf{k}, -i\omega_m), \tag{B.42}$$

$$f_{\tau_1\gamma_1\tau_2\gamma_2}(\mathbf{k}, i\omega_m) = g_{\tau_1\gamma_1}(\mathbf{k}, i\omega_m)g_{\tau_2\gamma_2}(-\mathbf{k}, -i\omega_m). \tag{B.43}$$

$\Lambda_{\alpha\beta\alpha\beta}(\mathbf{k}, i\omega_m)$ is the solution of the vertex equation:

$$f_{\tau_1 s\tau_2 s}(\mathbf{k}, i\omega_m)\Lambda_{\tau_1 s\tau_2 s}(\mathbf{k}, i\omega_m) = f_{\tau_1 s\tau_2 s}(\mathbf{k}, i\omega_m) - \frac{\tilde{\alpha}^2}{2N\beta\omega}\sum_{\mathbf{k}',m'}\left\{D_{aa}(\mathbf{k}-\mathbf{k}', i\omega_m - i\omega_{m'}) \times\right.$$

$$\left[4\cos^2(\frac{k_x}{2})f_{\tau_1 s\tau_2 s}(\mathbf{k}, i\omega_m)F_{p_x sp_x s}(\mathbf{k}', i\omega_{m'})\Lambda_{p_x sp_x s}(\mathbf{k}', i\omega_{m'}) + \right.$$

$$f_{\tau_1 p_x\tau_2 p_x}(\mathbf{k}, i\omega_m)4\cos^2(\frac{k_x'}{2})F_{ssss}(\mathbf{k}', i\omega_{m'})\Lambda_{ssss}(\mathbf{k}', i\omega_{m'}) + $$

$$2\cos(\frac{k_x}{2})f_{\tau_1 s\tau_2 p_x}(\mathbf{k}, i\omega_m)2\cos(\frac{k_x'}{2})e^{-i\frac{k_x'}{2}}F_{p_x sss}(\mathbf{k}', i\omega_{m'})\Lambda_{p_x sss}(\mathbf{k}', i\omega_{m'}) + $$

$$\left.2\cos(\frac{kx}{2})f_{\tau_1 p_x\tau_2 s}(\mathbf{k}, i\omega_m)2\cos(\frac{k_x'}{2})e^{i\frac{k_x'}{2}}F_{ssp_x s}(\mathbf{k}', i\omega_{m'})\Lambda_{ssp_x s}(\mathbf{k}', i\omega_{m'})\right]$$

$$+D_{ab}(\mathbf{k}-\mathbf{k}', i\omega_m - i\omega_{m'})e^{-i\frac{k_x - k_y}{2}} \times$$

$$\left[4\cos(\frac{k_x}{2})\cos(\frac{k_y}{2})f_{\tau_1 s\tau_2 s}(\mathbf{k}, i\omega_m)F_{p_x sp_y s}(\mathbf{k}', i\omega_{m'})\Lambda_{p_x sp_y s}(\mathbf{k}', i\omega_{m'}) + \right.$$

$$f_{\tau_1 p_x\tau_2 p_y}(\mathbf{k}, i\omega_m)4\cos(\frac{k_x'}{2})\cos(\frac{k_y'}{2})e^{i\frac{k_x' - k_y'}{2}}F_{ssss}(\mathbf{k}', i\omega_{m'})\Lambda_{ssss}(\mathbf{k}', i\omega_{m'}) + $$

$$2\cos(\frac{k_x}{2})f_{\tau_1 s\tau_2 p_y}(\mathbf{k}, i\omega_m)2\cos(\frac{k_y'}{2})e^{-i\frac{k_y'}{2}}F_{p_x sss}(\mathbf{k}', i\omega_{m'})\Lambda_{p_x sss}(\mathbf{k}', i\omega_{m'}) + $$

$$\left.2\cos(\frac{k_y}{2})f_{\tau_1 p_x\tau_2 s}(\mathbf{k}, i\omega_m)2\cos(\frac{k_x'}{2})e^{i\frac{k_x'}{2}}F_{ssp_y s}(\mathbf{k}', i\omega_{m'})\Lambda_{ssp_y s}(\mathbf{k}', i\omega_{m'})\right]$$

$$+D_{ba}(\mathbf{k}-\mathbf{k}', i\omega_m - i\omega_{m'})e^{i\frac{k_x - k_y}{2}} \times$$

$$\left[4\cos(\frac{k_x}{2})\cos(\frac{k_y}{2})f_{\tau_1 s\tau_2 s}(\mathbf{k}, i\omega_m)F_{p_y sp_x s}(\mathbf{k}', i\omega_{m'})\Lambda_{p_y sp_x s}(\mathbf{k}', i\omega_{m'}) + \right.$$

$$f_{\tau_1 p_y\tau_2 p_x}(\mathbf{k}, i\omega_m)4\cos(\frac{k_x'}{2})\cos(\frac{k_y'}{2})e^{-i\frac{k_x' - k_y'}{2}}F_{ssss}(\mathbf{k}', i\omega_{m'})\Lambda_{ssss}(\mathbf{k}', i\omega_{m'}) + $$

$$2\cos(\frac{k_y}{2})f_{\tau_1 s \tau_2 p_x}(\mathbf{k}, \mathrm{i}\omega_m)2\cos(\frac{k'_x}{2})e^{-\mathrm{i}\frac{k'_x}{2}}F_{p_y sss}(\mathbf{k}', \mathrm{i}\omega_{m'})\Lambda_{p_y sss}(\mathbf{k}', \mathrm{i}\omega_{m'}) +$$

$$2\cos(\frac{k_x}{2})f_{\tau_1 p_y \tau_2 s}(\mathbf{k}, \mathrm{i}\omega_m)2\cos(\frac{k'_y}{2})e^{\mathrm{i}\frac{k'_y}{2}}F_{ssp_x s}(\mathbf{k}', \mathrm{i}\omega_{m'})\Lambda_{ssp_x s}(\mathbf{k}', \mathrm{i}\omega_{m'}) \Big]$$

$$+D_{bb}(\mathbf{k} - \mathbf{k}', \mathrm{i}\omega_m - \mathrm{i}\omega_{m'}) \times$$

$$\Big[4\cos^2(\frac{k_y}{2})f_{\tau_1 s \tau_2 s}(\mathbf{k}, \mathrm{i}\omega_m)F_{p_y s p_y s}(\mathbf{k}', \mathrm{i}\omega_{m'})\Lambda_{p_y s p_y s}(\mathbf{k}', \mathrm{i}\omega_{m'}) +$$

$$f_{\tau_1 p_y \tau_2 p_y}(\mathbf{k}, \mathrm{i}\omega_m)4\cos^2(\frac{k'_y}{2})F_{ssss}(\mathbf{k}', \mathrm{i}\omega_{m'})\Lambda_{ssss}(\mathbf{k}', \mathrm{i}\omega_{m'}) +$$

$$2\cos(\frac{k_y}{2})f_{\tau_1 s \tau_2 p_y}(\mathbf{k}, \mathrm{i}\omega_m)2\cos(\frac{k'_y}{2})e^{-\mathrm{i}\frac{k'_y}{2}}F_{p_y sss}(\mathbf{k}', \mathrm{i}\omega_{m'})\Lambda_{p_y sss}(\mathbf{k}', \mathrm{i}\omega_{m'}) +$$

$$2\cos(\frac{k_y}{2})f_{\tau_1 p_y \tau_2 s}(\mathbf{k}, \mathrm{i}\omega_m)2\cos(\frac{k'_y}{2})e^{\mathrm{i}\frac{k'_y}{2}}F_{ssp_y s}(\mathbf{k}', \mathrm{i}\omega_{m'})\Lambda_{ssp_y s}(\mathbf{k}', \mathrm{i}\omega_{m'}) \Big] \Big\}$$

$$f_{\tau_1 p_x \tau_2 p_x}(\mathbf{k}, \mathrm{i}\omega_m)\Lambda_{\tau_1 p_x \tau_2 p_x}(\mathbf{k}, \mathrm{i}\omega_m) = f_{\tau_1 p_x \tau_2 p_x}(\mathbf{k}, \mathrm{i}\omega_m)$$

$$-\frac{\tilde{\alpha}^2}{2N\beta\omega}\sum_{\mathbf{k}',m'}\Big\{ D_{aa}(\mathbf{k} - \mathbf{k}', \mathrm{i}\omega_m - \mathrm{i}\omega_{m'}) \times$$

$$\Big[4\cos^2(\frac{k_x}{2})f_{\tau_1 s \tau_2 s}(\mathbf{k}, \mathrm{i}\omega_m)F_{p_x p_x p_x p_x}(\mathbf{k}', \mathrm{i}\omega_{m'})\Lambda_{p_x p_x p_x p_x}(\mathbf{k}', \mathrm{i}\omega_{m'}) +$$

$$f_{\tau_1 p_x \tau_2 p_x}(\mathbf{k}, \mathrm{i}\omega_m)4\cos^2(\frac{k'_x}{2})F_{sp_x sp_x}(\mathbf{k}', \mathrm{i}\omega_{m'})\Lambda_{sp_x sp_x}(\mathbf{k}', \mathrm{i}\omega_{m'}) +$$

$$2\cos(\frac{k_x}{2})f_{\tau_1 s \tau_2 p_x}(\mathbf{k}, \mathrm{i}\omega_m)2\cos(\frac{k'_x}{2})e^{-\mathrm{i}\frac{k'_x}{2}}F_{p_x p_x sp_x}(\mathbf{k}', \mathrm{i}\omega_{m'})\Lambda_{p_x p_x sp_x}(\mathbf{k}', \mathrm{i}\omega_{m'}) +$$

$$2\cos(\frac{kx}{2})f_{\tau_1 p_x \tau_2 s}(\mathbf{k}, \mathrm{i}\omega_m)2\cos(\frac{k'_x}{2})e^{\mathrm{i}\frac{k'_x}{2}}F_{sp_x p_x p_x}(\mathbf{k}', \mathrm{i}\omega_{m'})\Lambda_{sp_x p_x p_x}(\mathbf{k}', \mathrm{i}\omega_{m'}) \Big]$$

$$+D_{ab}(\mathbf{k} - \mathbf{k}', \mathrm{i}\omega_m - \mathrm{i}\omega_{m'})e^{-\mathrm{i}\frac{k_x - k_y}{2}} \times$$

$$\Big[4\cos(\frac{k_x}{2})\cos(\frac{k_y}{2})f_{\tau_1 s \tau_2 s}(\mathbf{k}, \mathrm{i}\omega_m)F_{p_x p_x p_y p_x}(\mathbf{k}', \mathrm{i}\omega_{m'})\Lambda_{p_x p_x p_y p_x}(\mathbf{k}', \mathrm{i}\omega_{m'}) +$$

$$f_{\tau_1 p_x \tau_2 p_y}(\mathbf{k}, \mathrm{i}\omega_m)4\cos(\frac{k'_x}{2})\cos(\frac{k'_y}{2})e^{\mathrm{i}\frac{k'_x - k'_y}{2}}F_{sp_x sp_x}(\mathbf{k}', \mathrm{i}\omega_{m'})\Lambda_{sp_x sp_x}(\mathbf{k}', \mathrm{i}\omega_{m'}) +$$

$$2\cos(\frac{k_x}{2})f_{\tau_1 s \tau_2 p_y}(\mathbf{k}, \mathrm{i}\omega_m)2\cos(\frac{k'_y}{2})e^{-\mathrm{i}\frac{k'_y}{2}}F_{p_x p_x sp_x}(\mathbf{k}', \mathrm{i}\omega_{m'})\Lambda_{p_x p_x sp_x}(\mathbf{k}', \mathrm{i}\omega_{m'}) +$$

$$2\cos(\frac{k_y}{2})f_{\tau_1 p_x \tau_2 s}(\mathbf{k}, \mathrm{i}\omega_m)2\cos(\frac{k'_x}{2})e^{\mathrm{i}\frac{k'_x}{2}}F_{sp_x p_y p_x}(\mathbf{k}', \mathrm{i}\omega_{m'})\Lambda_{sp_x p_y p_x}(\mathbf{k}', \mathrm{i}\omega_{m'}) \Big]$$

$$+D_{ba}(\mathbf{k} - \mathbf{k}', \mathrm{i}\omega_m - \mathrm{i}\omega_{m'})e^{\mathrm{i}\frac{k_x - k_y}{2}} \times$$

$$\Big[4\cos(\frac{k_x}{2})\cos(\frac{k_y}{2})f_{\tau_1 s \tau_2 s}(\mathbf{k}, \mathrm{i}\omega_m)F_{p_y p_x p_x p_x}(\mathbf{k}', \mathrm{i}\omega_{m'})\Lambda_{p_y p_x p_x p_x}(\mathbf{k}', \mathrm{i}\omega_{m'})+$$

$$f_{\tau_1 p_y \tau_2 p_x}(\mathbf{k}, \mathrm{i}\omega_m)4\cos(\frac{k'_x}{2})\cos(\frac{k'_y}{2})e^{-\mathrm{i}\frac{k'_x - k'_y}{2}}F_{sp_x sp_x}(\mathbf{k}', \mathrm{i}\omega_{m'})\Lambda_{sp_x sp_x}(\mathbf{k}', \mathrm{i}\omega_{m'}) +$$

$$2\cos(\frac{k_y}{2})f_{\tau_1 s\tau_2 p_x}(\mathbf{k}, i\omega_m)2\cos(\frac{k'_x}{2})e^{-i\frac{k'_x}{2}}F_{p_y p_x s p_x}(\mathbf{k'}, i\omega_{m'})\Lambda_{p_y p_x s p_x}(\mathbf{k'}, i\omega_{m'}) +$$

$$2\cos(\frac{k_x}{2})f_{\tau_1 p_y \tau_2 s}(\mathbf{k}, i\omega_m)2\cos(\frac{k'_y}{2})e^{i\frac{k'_y}{2}}F_{s p_x p_x p_x}(\mathbf{k'}, i\omega_{m'})\Lambda_{s p_x p_x p_x}(\mathbf{k'}, i\omega_{m'})\Big]$$

$$+D_{bb}(\mathbf{k}-\mathbf{k'}, i\omega_m - i\omega_{m'}) \times$$

$$\Big[4\cos^2(\frac{k_y}{2})f_{\tau_1 s\tau_2 s}(\mathbf{k}, i\omega_m)F_{p_y p_x p_y p_x}(\mathbf{k'}, i\omega_{m'})\Lambda_{p_y p_x p_y p_x}(\mathbf{k'}, i\omega_{m'}) +$$

$$f_{\tau_1 p_y \tau_2 p_y}(\mathbf{k}, i\omega_m)4\cos^2(\frac{k'_y}{2})F_{s p_x s p_x}(\mathbf{k'}, i\omega_{m'})\Lambda_{s p_x s p_x}(\mathbf{k'}, i\omega_{m'}) +$$

$$2\cos(\frac{k_y}{2})f_{\tau_1 s\tau_2 p_y}(\mathbf{k}, i\omega_m)2\cos(\frac{k'_y}{2})e^{-i\frac{k'_y}{2}}F_{p_y p_x s p_x}(\mathbf{k'}, i\omega_{m'})\Lambda_{p_y p_x s p_x}(\mathbf{k'}, i\omega_{m'}) +$$

$$2\cos(\frac{k_y}{2})f_{\tau_1 p_y \tau_2 s}(\mathbf{k}, i\omega_m)2\cos(\frac{k'_y}{2})e^{i\frac{k'_y}{2}}F_{s p_x p_y p_x}(\mathbf{k'}, i\omega_{m'})\Lambda_{s p_x p_y p_x}(\mathbf{k'}, i\omega_{m'})\Big]\Big\}$$

C Fourier transformation

The Fourier transformation of the electron Green's function from the frequency space to the time space is

$$G(\mathbf{k}, \tau) = \frac{1}{\beta}\sum_{n=-\infty}^{+\infty} e^{-i\omega_n \tau}G(\mathbf{k}, i\omega_n) \tag{B.44}$$

In numerical calculation, we cannot reach $n = \pm\infty$, we always give a cut off Z. In order to keep accuracy,

$$
\begin{aligned}
G(\mathbf{k}, \tau) &= \frac{1}{\beta}\sum_{n=-\infty}^{+\infty} e^{-i\omega_n \tau}\left(G(\mathbf{k}, i\omega_n) - \frac{1}{i\omega_n - \xi} + \frac{1}{i\omega_n - \xi}\right) \\
&= \frac{1}{\beta}\sum_{n=-\infty}^{+\infty} e^{-i\omega_n \tau}\tilde{G}(\mathbf{k}, i\omega_n) + \frac{1}{\beta}\sum_{n=-\infty}^{+\infty} e^{-i\omega_n \tau}\frac{1}{i\omega_n - \xi} \\
&\approx \frac{1}{\beta}\sum_{n=-Z}^{Z-1} e^{-i\omega_n \tau}\tilde{G}(\mathbf{k}, i\omega_n) + \frac{1}{\beta}\sum_{n=-\infty}^{+\infty} e^{-i\omega_n \tau}\frac{1}{i\omega_n - \xi} \\
&= \frac{1}{\beta}\sum_{n=-Z}^{Z-1} e^{-i\omega_n \tau}\tilde{G}(\mathbf{k}, i\omega_n) + \begin{cases} -\frac{e^{(\beta-\tau)\xi}}{1+e^{\beta\xi}} & (\tau > 0) \\ n_F(\xi) - \frac{1}{2} & (\tau = 0) \\ \frac{e^{-\tau\xi}}{1+e^{\beta\xi}} & (\tau < 0) \end{cases} ,
\end{aligned}
\tag{B.45}
$$

where ξ is a constant number. The inverse Fourier transformation of the Green's function is

$$
\begin{aligned}
G(\mathbf{k}, i\omega_n) &= \int_0^\beta d\tau e^{i\omega_n \tau} G(\mathbf{k}, \tau) \\
&= \sum_{l=0}^{L-1} e^{i\omega_n \tau_l} \Delta W_n G(\mathbf{k}, \tau_l) - R_n e^{i\omega_n \beta} G(\mathbf{k}, \beta^-) + R_n G(\mathbf{k}, 0^+) \\
&= \sum_{l=0}^{L-1} e^{i\omega_n \tau_l} \Delta W_n G(\mathbf{k}, \tau_l) + R_n \left(G(\mathbf{k}, 0^+) + G(\mathbf{k}, \beta^-) \right) \\
&= \sum_{l=0}^{L-1} e^{i\omega_n \tau_l} \Delta W_n G(\mathbf{k}, \tau_l) + R_n \left(G(\mathbf{k}, 0^+) - G(\mathbf{k}, 0^-) \right),
\end{aligned} \tag{B.46}
$$

where $\Delta = \frac{\beta}{L}$, $W_n = 2\frac{1-\cos(\Delta \omega_n)}{\Delta^2 \omega_n^2}$, and $R_n = -\frac{1-i\Delta\omega_n - e^{-i\Delta\omega_n}}{\Delta \omega_n^2}$. Both formulas for the self-energy and the susceptibility have two summation loops, including adding momentum $\mathbf{k}$ and Matsubara frequency ω_n or ν_n. Doing this summation directly is not efficient. Instead, I can use the fast Fourier transformation to boost the computing speed. The first step to do the fast Fourier transformation is changing the equation format using the convolution theory. For example,

$$
\begin{aligned}
\sum_{\mathbf{k}',m'} D(\mathbf{k}-\mathbf{k}', i\omega_m - i\omega_{m'}) G(\mathbf{k}', i\omega_m) &= \sum_{\mathbf{k}',m'} \sum_{\mathbf{r}_2,\mathbf{r}_2} e^{-i(\mathbf{k}-\mathbf{k}')\cdot\mathbf{r}_1} e^{-i\mathbf{k}'\cdot\mathbf{r}_2} \\
&\quad \int_0^\beta d\tau_1 e^{i(\omega_m - \omega_{m'})} D(\mathbf{r}_1, \tau_1) \int_0^\beta d\tau_2 e^{i\omega_{m'}\tau_2} G(\mathbf{r}_2, \tau_2) \\
&= N\beta \sum_{\mathbf{r}} \int_0^\beta d\tau D(\mathbf{r}, \tau) G(\mathbf{r}, \tau) e^{i\omega_n \tau} e^{-i\mathbf{k}\cdot\mathbf{r}}
\end{aligned} \tag{B.47}
$$

Here, I use $\sum_{m'} e^{i\omega_{m'}(\tau_2 - \tau_1)} = \beta \delta(\tau_2 - \tau_1)$. Note

$$
\begin{aligned}
D(\mathbf{r}, \tau) &= \frac{1}{N} \sum_{\mathbf{k}} D(\mathbf{k}, \tau) e^{i\mathbf{k}\cdot\mathbf{r}} \\
D(\mathbf{k}, \tau) &= \frac{1}{\beta} \sum_{n=-Z}^{Z} e^{-i\nu_n \tau} D(\mathbf{k}, i\nu_n) \\
G(\mathbf{r}, \tau) &= \frac{1}{N} \sum_{\mathbf{k}} G(\mathbf{k}, \tau) e^{i\mathbf{k}\cdot\mathbf{r}} \\
G(\mathbf{k}, \tau) &= \frac{1}{\beta} \sum_{n=-Z}^{Z-1} e^{-i\omega_n \tau} G(\mathbf{k}, i\omega_n)
\end{aligned} \tag{B.48}
$$

Since $G(\mathbf{k}, 0^+) - G(\mathbf{k}, 0^-) = -1$, the integral of the imaginary time in Eq. B.47 can be evaluated by

$$\int_0^\beta d\tau D(\mathbf{r}, \tau) G(\mathbf{r}, \tau) e^{i\omega_n \tau} = W_n \Delta \sum_{l=0}^{L-1} e^{i\omega_n \tau_l} D(\mathbf{r}, \tau_l) G(\mathbf{r}, \tau_l) - R_n D(\mathbf{r}, 0) \delta(\mathbf{r} = \mathbf{0})$$

The summation in the above equation can be done using the fast Fourier transformation routine. When I calculate the superconducting susceptibility, there is another integral I need to consider. That is

$$\begin{aligned}
\int_0^\beta d\tau D(\mathbf{r}, \tau) f(\mathbf{r}, \tau) e^{i\omega_n \tau} &= W_n \Delta \sum_{l=0}^{L-1} e^{i\omega_n \tau_l} D(\mathbf{r}, \tau_l) f(\mathbf{r}, \tau_l) - R_n D(\mathbf{r}, 0) \\
&\quad [\delta(\mathbf{r} = (N_x - 1, 0)) + \delta(\mathbf{r} = (1, 0)) + 2\delta(\mathbf{r} = \mathbf{0})],
\end{aligned}$$

where $f(\mathbf{r}, \tau) = \frac{1}{N} \sum_{\mathbf{k}} 4\cos^2(\frac{k_x}{2}) G(\mathbf{k}, \tau) e^{i\mathbf{k}\cdot\mathbf{r}}$ When I calculate the phonon self-energy, the convolution theory is used as the following way,

$$\sum_{\mathbf{k},m} G(\mathbf{k}, i\omega_m) G(\mathbf{k}+\mathbf{q}, i\omega_m + i\nu_n) = -N\beta \sum_{\mathbf{r}} \int_0^\beta d\tau G(\mathbf{R}-\mathbf{r}, \beta-\tau) G(\mathbf{r}, \tau) e^{i\nu_n \tau} e^{-i\mathbf{q}\cdot\mathbf{r}},$$

where $\mathbf{R} = N_x \mathbf{a} + N_y \mathbf{b}$, $N = N_x \times N_y$, and

$$\begin{aligned}
G(\mathbf{R}-\mathbf{r}, \beta-\tau) &= \frac{1}{N} \sum_{\mathbf{k}} G(\mathbf{k}, \beta-\tau) e^{-i\mathbf{k}\cdot\mathbf{r}} \\
G(\mathbf{k}, \beta-\tau) &= \frac{1}{\beta} \sum_{n=-\infty}^{\infty} e^{-i\omega_n(\beta-\tau)} G(\mathbf{k}, i\omega_n) \\
&= -\frac{1}{\beta} \sum_{n=-Z}^{Z-1} e^{i\omega_n \tau} \tilde{G}(\mathbf{k}, i\omega_n) - \frac{e^{\tau\xi}}{1+e^{\beta\xi}} \\
G(\mathbf{r}, \tau) &= \frac{1}{N} \sum_{\mathbf{k}} G(\mathbf{k}, \tau) e^{i\mathbf{k}\cdot\mathbf{r}} \\
G(\mathbf{k}, \tau) &= \frac{1}{\beta} \sum_{n=-Z}^{Z-1} e^{-i\omega_n \tau} \tilde{G}(\mathbf{k}, i\omega_n) - \frac{e^{(\beta-\tau)\xi}}{1+e^{\beta\xi}}
\end{aligned}$$

Appendix C

Applications of DQMC to the three-orbital SSH model

A   Three-orbital SSH Model

The full Hamiltonian for the three-orbital Su-Schrieffer-Heeger (SSH) model is $H = H_0 + H_{\text{lat}} + H_{e-ph}$, where

$$
\begin{aligned}
H_0 &= -t_{sp} \sum_{\mathbf{r},\sigma} \left(s_{\mathbf{r},\sigma}^\dagger p_{\mathbf{r},x,\sigma} + s_{\mathbf{r},\sigma}^\dagger p_{\mathbf{r},y,\sigma} + h.c. \right) + t_{sp} \sum_{\mathbf{r},\sigma} \left(s_{\mathbf{r}+\mathbf{a},\sigma}^\dagger p_{\mathbf{r},x,\sigma} + s_{\mathbf{r}+\mathbf{b},\sigma}^\dagger p_{\mathbf{r},y,\sigma} + h.c. \right) \\
&\quad + t_{pp} \sum_{\mathbf{r},\sigma} \left(p_{\mathbf{r},y,\sigma}^\dagger p_{\mathbf{r},x,\sigma} - p_{\mathbf{r},y,\sigma}^\dagger p_{\mathbf{r}-\mathbf{a},x,\sigma} + p_{\mathbf{r}-\mathbf{b},y,\sigma}^\dagger p_{\mathbf{r}-\mathbf{a},x,\sigma} - p_{\mathbf{r}-\mathbf{b},y,\sigma}^\dagger p_{\mathbf{r},x,\sigma} + h.c. \right) \\
&\quad + \sum_{\mathbf{r},\sigma} \left[(\epsilon_s - \mu)\hat{n}_{\mathbf{r},s,\sigma} + (\epsilon_p - \mu)\hat{n}_{\mathbf{r},p_x,\sigma} + (\epsilon_p - \mu)\hat{n}_{\mathbf{r},p_y,\sigma} \right]
\end{aligned} \tag{C.1}
$$

contains the non-interacting electronic terms of H,

$$
H_{\text{lat}} = \sum_{\mathbf{r}} \left(\frac{\hat{P}_{\mathbf{r},x}^2}{2M} + MK^2\hat{X}_{\mathbf{r}}^2 + \frac{\hat{P}_{\mathbf{r},y}^2}{2M} + MK^2\hat{Y}_{\mathbf{r}}^2 \right) = \sum_{\mathbf{r}} \Omega \left(a_{\mathbf{r}}^\dagger a_{\mathbf{r}} + b_{\mathbf{r}}^\dagger b_{\mathbf{r}} + 1 \right) \tag{C.2}
$$

contains the noninteracting lattice terms, and

$$
H_{e-ph} = \alpha t_{sp}^0 \sum_{\mathbf{r},\sigma} \left(\hat{X}_{\mathbf{r}} s_{\mathbf{r},\sigma}^\dagger p_{\mathbf{r},x,\sigma} + \hat{Y}_{\mathbf{r}} s_{\mathbf{r},\sigma}^\dagger p_{\mathbf{r},y,\sigma} + \hat{X}_{\mathbf{r}} s_{\mathbf{r}+\mathbf{a},\sigma}^\dagger p_{\mathbf{r},x,\sigma} + \hat{Y}_{\mathbf{r}} s_{\mathbf{r}+\mathbf{b},\sigma}^\dagger p_{\mathbf{r},y,\sigma} + h.c. \right) \tag{C.3}
$$

contains the e-ph coupling terms. Here, $s_{\mathbf{r},\sigma}^\dagger$ $(s_{,\sigma})$, $p_{\mathbf{r},x,\sigma}^\dagger$ $(p_{,x,\sigma})$, $p_{\mathbf{r},y,\sigma}^\dagger$ $(p_{,y,\sigma})$ are the creation (annihilation) operators for electrons of spin σ on the Bi $6s$, O $2p_x$, and O $2p_y$ orbitals at a coordinate $\mathbf{r} = (r_x, r_y)$, respectively; $\hat{n}_{\mathbf{r},s,\sigma} = s_{\mathbf{r},\sigma}^\dagger s_{\mathbf{r},\sigma}$, $\hat{n}_{\mathbf{r},p_x,\sigma} = p_{\mathbf{r},x,\sigma}^\dagger p_{\mathbf{r},x,\sigma}$, and $\hat{n}_{\mathbf{r},p_y,\sigma} = p_{\mathbf{r},y,\sigma}^\dagger p_{\mathbf{r},y,\sigma}$ are the number operators for s, p_x, and p_y orbitals, respectively; ϵ_s and ϵ_p are the onsite energies for the $6s$ orbital and $2p$ orbital, respectively; μ is the chemical potential. t_{sp} is the hopping integral between the $6s$ orbital and $2p_\gamma$ ($\gamma = x$ or y) orbital in a uniform crystal structure. t_{pp} is the hopping integral between $2p_x$ and $2p_y$ orbitals. α is the e-ph coupling constant. The movement of the oxygen atoms distorts the uniform crystal structure and modulates the hopping integral t_{sp} by $\alpha t_{sp}\hat{X}_{\mathbf{r}}$ or $\alpha t_{sp}\hat{Y}_{\mathbf{r}}$. $\hat{P}_{\mathbf{r},x}$ $(\hat{P}_{\mathbf{r},y})$ and $\hat{X}_{\mathbf{r}}$ $(\hat{Y}_{\mathbf{r}})$ are the momentum and displacement operators of oxygen atoms. M is the oxygen mass and K is the coefficient of elasticity. The bare phonon frequency is defined as $\Omega = \sqrt{2K/M}$.

B   DQMC Procedure

B.1   DQMC algorithm

I use determinant quantum Monte Carlo (DQMC) to study the two-dimensional (2D) three-orbital SSH model. The details of the method will be discussed in this section. In general, the finite-temperature expectation value of an observable $\hat{O}$ is given by

$$\langle\hat{O}\rangle = \frac{\mathrm{Tr}\hat{O}e^{-\beta H}}{\mathrm{Tr}e^{-\beta H}}, \tag{C.4}$$

where the averaging is performed within the grand canonical ensemble. To evaluate $\langle\hat{O}\rangle$, the imaginary-time interval $[0, \beta]$ is divided into L discrete steps of length $\Delta\tau = \beta/L$. Then the partition function can be rewritten using the Trotter formula as

$$Z = \mathrm{Tr}\left(e^{-\Delta\tau L H}\right) \approx \mathrm{Tr}\left(e^{-\Delta\tau H_{e-ph}}e^{-\Delta\tau K}\right)^L, \tag{C.5}$$

where K contains the noninteracting terms $K = H_0 + H_{\mathrm{lat}}$. In the Trotter approximation, terms of order $t_{sp}^{0}{}^2\alpha(\Delta\tau)^2$ and higher have been neglected. This approximation is reasonable when $\Delta\tau$ is small.

The phonon operators can then be treated in the usual way by inserting a complete set of position and momentum eigenstates at each time slice. one then integrates out the phonon momenta. After doing so, the partition function depends on a trace over continuous lattice displacements $X_{\mathbf{r},l}$ and $Y_{\mathbf{r},l}$, and terms that are bilinear in the Fermion operators. The trace over the former can then be evaluated analytically and expressed as a product of matrix determinants. The final results is

Within the imaginary-time grid, the position operator $\hat{X}_{\mathbf{r}}$ ($\hat{Y}_{\mathbf{r}}$) is replaced with a set of continuous variables $X_{\mathbf{r},l}$ ($Y_{\mathbf{r},l}$). The momentum operators are replaced with a finite difference $P_{\mathbf{r},x,l} = \frac{M(X_{\mathbf{r},l+1} - X_{\mathbf{r},l})}{\Delta\tau}$ and $P_{\mathbf{r},y,l} = \frac{M(Y_{\mathbf{r},l+1} - Y_{\mathbf{r},l})}{\Delta\tau}$. The periodic boundary conditions are enforced on the interval $[0, \beta]$ such that $X_{\mathbf{r},L} = X_{\mathbf{r},0}$ and $Y_{\mathbf{r},L} = Y_{\mathbf{r},0}$. In this treatment, the bare phonon energy of the Hamiltonian H_{lat} is given by

$$Z = \int\int dX dY e^{-S_{ph}\Delta\tau} \det M^{\uparrow} \det M^{\downarrow}, \tag{C.6}$$

where $\int dX$ and $\int dY$ are shorthand for integrating over all of continuous phonon displacements $X_{\mathbf{r},l}$ and $Y_{\mathbf{r},l}$. $M^{\sigma} = I + B_L^{\sigma} B_{L-1}^{\sigma} \cdots B_1^{\sigma}$. Here, I is an $N \times N$ identity matrix and the B_l^{σ} matrices are defined as

$$B_l^{\uparrow(\downarrow)} = e^{-\Delta\tau H_{e-ph}} e^{-\Delta\tau H_0}. \tag{C.7}$$

The lattice term is defined as

$$S_{ph} = \frac{M}{2}\left(\frac{X_{\mathbf{r},l+1} - X_{\mathbf{r},l}}{\Delta\tau}\right)^2 + \frac{M}{2}\left(\frac{Y_{\mathbf{r},l+1} - Y_{\mathbf{r},l}}{\Delta\tau}\right)^2 + MK^2 X_{\mathbf{r},l}^2 + MK^2 Y_{\mathbf{r},l}^2. \tag{C.8}$$

The integrals over X and Y are evaluated using Metropolis Monte Carlo sample. Here, I include both single-site and block updates.

Most observables can be expressed in terms of the single particle Green's function $G^{\sigma}(\tau)$. For an electron propagating through field configurations $\{X_{\mathbf{r},l}\}$ and $\{Y_{\mathbf{r},l}\}$, the Green's function at time $\tau = l\Delta\tau$ is given by

$$[G^{\sigma}(l)]_{ij} = \langle \hat{T}_{\tau} c_{i,\sigma}(\tau) c_{j,\sigma}^{\dagger}(\tau)\rangle = [I + A_l^{\sigma}]_{ij}^{-1}, \tag{C.9}$$

where $A_l^\sigma = B_l^\sigma \cdots B_1^\sigma B_L^\sigma \cdots B_{l+1}^\sigma$ and $\hat{T}_\tau$ is the time ordering operator. The determinant of M^σ is independent of l and is related to the Green's function on any time slice $G^\sigma(l)$ by $\mathrm{M}^\sigma = \det G^\sigma(l)^{-1}$.

B.2 Efficient single-site updates

Equation C.9 shows that the next imaginary-time slice Green's function $G^\sigma(l+1)$ can be evaluated from the current Green's function via

$$G^\sigma(l+1) = B_{l+1}^\sigma G^\sigma(l) \left[B_{l+1}^\sigma \right]^{-1}. \tag{C.10}$$

This forms the basis for an efficient single-site update scheme. The Monte Carlo starts by computing the Green's function on the time slice $l = 0$ using Eq. C.9. A series of updates are then proposed for a phonon field at current imaginary-time slice while holding the other phonon field fixed. For example, one proposes updates $X_{\mathbf{r},l} \to X'_{\mathbf{r},l} = X_{\mathbf{r},l} + \Delta X_{\mathbf{r},l}$ while holding the configuration $\{Y_{\mathbf{r},l}\}$ fixed. Then the acceptance probability for this updates is given by

$$R = e^{-\Delta\tau\Delta E_{ph}} R^\uparrow R^\downarrow = e^{-\Delta\tau(E_{ph}[\{X'_{\mathbf{r},l}, Y_{\mathbf{r},l}\}] - E_{ph}[\{X_{\mathbf{r},l}, Y_{\mathbf{r},l}\}])} \frac{\det M^{\uparrow\prime}}{\det M^\uparrow} \times \frac{\det M^{\downarrow\prime}}{\det M^\downarrow}, \tag{C.11}$$

where $M^{\sigma\prime}$ and M^σ correspond to the phonon fields with and without the proposed updated, respectively.

After updating a field $X_{\mathbf{r},l}$, one has

$$B^\sigma(l) \to B^{\sigma\prime}(l) = e^{-\Delta\tau H'_{e-ph}} e^{-\Delta\tau H_0} = e^{-\Delta\tau(H_{e-ph}+V)} e^{-\Delta\tau H_0}, \tag{C.12}$$

where V is the variation of H_{e-ph} after changing a phonon field. Equation C.3 shows V is a symmetric matrix with only four non-zero elements and it can be written as

$$
V = \begin{bmatrix}
\ddots & \vdots & & \vdots & & \vdots & & \vdots & \\
\cdots & 0 & & \alpha t_{sp}^0 \Delta X_{\mathbf{r},l} & 0 & & & \cdots & \\
\cdots & \alpha t_{sp}^0 \Delta X_{\mathbf{r},l} & 0 & & & \alpha t_{sp}^0 \Delta X_{\mathbf{r},l} & & \cdots & \\
\cdots & 0 & & \alpha t_{sp}^0 \Delta X_{\mathbf{r},l} & 0 & & & \cdots & \\
\vdots & \vdots & & \vdots & & \vdots & & \ddots &
\end{bmatrix}.
\tag{C.13}
$$

To fast calculate the new $B_l^{\sigma\prime}$ matrix, I take an approximation as

$$
B_l^{\sigma\prime} \approx e^{-\Delta\tau V} B_l^\sigma.
\tag{C.14}
$$

This approximation is valid only when $\Delta\tau$ is small. Then $e^{-\Delta\tau V}$ is evaluated via $e^{-\Delta\tau V} = P e^{-\Delta\tau D} P^T$, where P is the eigenstate matrix of V and D is a diagonal matrix with only two non-zero elements, $D_{1,1} = -\sqrt{2}\alpha t_{sp}^0 \Delta X_{\mathbf{r},l}$ and $D_{N,N} = \sqrt{2}\alpha t_{sp}^0 \Delta X_{\mathbf{r},l}$. Then the new $B_l^{\sigma\prime}$ matrix can be written as

$$
B_l^{\sigma\prime} = P e^{-\Delta\tau D} P^T B_l^\sigma = P(I + \Delta) P^T B_l^\sigma,
\tag{C.15}
$$

where $\Delta = 0$ except $\Delta_{1,1} = e^{\sqrt{2}\alpha t_{sp}^0 \Delta X_{\mathbf{r},l}} - 1$ and $\Delta_{N,N} = e^{-\sqrt{2}\alpha t_{sp}^0 \Delta X_{\mathbf{r},l}} - 1$.

The new Green's function after changing a phonon field can be evaluated by

$$
G_l^{\sigma\prime} = [I + A_l^{\sigma\prime}]^{-1} = \left[I + P(I + \Delta) P^T A_l^\sigma\right]^{-1} = G_l^\sigma \left[P^T + \Delta Q\right]^{-1} P^T,
\tag{C.16}
$$

where $Q = P^T(I - G_l^\sigma)$. Due to the simplicity of the Δ matrix, ΔQ has only two non-zero rows,

$$
\begin{aligned}
\Delta Q &= \begin{bmatrix} \Delta_{1,1}Q_{1,1} & \Delta_{1,1}Q_{1,2} & \cdots & \Delta_{1,1}Q_{1,N} \\ 0 & 0 & \cdots & 0 \\ \vdots & \vdots & \vdots & \vdots \\ 0 & 0 & \cdots & 0 \\ \Delta_{N,N}Q_{N,1} & \Delta_{N,N}Q_{N,2} & \cdots & \Delta_{N,N}Q_{N,N} \end{bmatrix} \\
&= \begin{bmatrix} \Delta_{1,1} & 0 \\ \vdots & \vdots \\ 0 & \Delta_{N,N} \end{bmatrix} \times \begin{bmatrix} Q_{1,1} & Q_{1,2} & \cdots & Q_{1,N} \\ Q_{N,1} & Q_{N,2} & \cdots & Q_{N,N} \end{bmatrix} = uw, \qquad \text{(C.17)}
\end{aligned}
$$

where u and w are $N \times 2$ and $2 \times N$ matrices, respectively. Using the Woodbury matrix identity and Matrix determinant lemma, the new Green's function is calculated via

$$
G_l^{\sigma\prime} = G_l^\sigma \left[I - Pu(I_2 + vPw)^{-1}v \right], \qquad \text{(C.18)}
$$

and the acceptance ratio is given by

$$
R^\sigma = \det|I_2 + wPu|, \qquad \text{(C.19)}
$$

where I_2 is a 2×2 identity matrix. Once updates have been performed for all fields time time slice l, $G^\sigma(l)$ is advanced to $G^\sigma(l+1)$ using Eq. C.10 and the process repeated.

This update scheme is efficient although an approximation $B_l^{\sigma\prime} \approx e^{-\Delta\tau}B_l^\sigma$ is taken. In the Sec. B.4 I will compare results from this update with results from an update explicitly calculating $B_l^{\sigma\prime}$ to demonstrate that for a small $\Delta\tau$, our approximation can still produce an exact solution.

B.3 Block updates

In the block update scheme, the lattice displacement for a given site is updated simultaneously for imaginary-time slices l. That means the phonon field is updated as

$X_{\mathbf{r},l} \rightarrow X_{\mathbf{r},l} + \Delta X_{\mathbf{r}}$ or $Y_{\mathbf{r},l} \rightarrow Y_{\mathbf{r},l} + \Delta Y_{\mathbf{r}}$ for all $l \in [0, \beta]$. This type of update helps to efficiently move the phonon configurations out of false minima at lower temperatures. However, there is no fast updating formula for the block update and the Green's function is required to be calculated from Eq. C.9. Therefore the block update takes a lot of time in Monte Carlo calculations. To minimize the computing time, I set two to four block updates at randomly selected sites for every full set of single-site updates to $X_{\mathbf{r},l}$ and $Y_{\mathbf{r},l}$.

B.4   Reliability of the fast updates

To assess the reliability of the approximation made in Eq. C.14, I performed two DQMC calculations. In the first calculation, the updated Green's function follows each single-site update and the acceptance ratio is computed via Eq. C.9 and Eq. C.11, respectively. In this case, the approximation in Eq. C.14 is not taken. In the second calculation, this approximation is used, and the fast update formulas are used in each single-site update. In both calculations, the cluster size is set as 2×2 and the hole density is $\langle \hat{n} \rangle = 1$. The other parameters are the same as in chapter 6. Figure C.1 shows that the Green's functions for both calculations are the same, indicating $\Delta \tau = \beta/10$ is small enough to produce an exact solution.
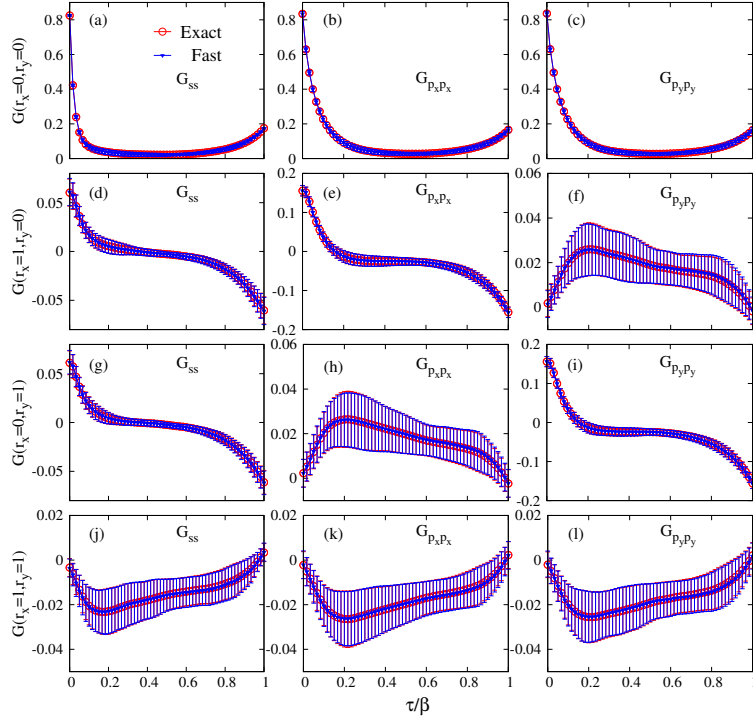
Figure C.1: (color online) Green's functions as a function of the imaginary time τ for different displacement $\mathbf{r} = r_x \mathbf{a} + r_y \mathbf{b}$. $\mathbf{a}$ and $\mathbf{b}$ are the primitive vectors along x- and y-directions, respectively. The first, second, third columns are the results of $G_{s,s}$, G_{p_x,p_x}, and G_{p_y,p_y}, respectively. The red circles and blue triangular points represents results from the exact update and the fast update, respectively. Error bars smaller than the marker size have been suppressed for clarity.

Vita

Shaozhi Li is a PH. D student in the department of Physics and Astronomy at the University of Tennessee. He works on condensed matter theoretical physics and his major research interests focus on strongly correlated systems and high-temperature superconductors.

He was born in Zhejiang province, China. He attended Zhejiang Normal University in 2006 in China. After graduation, he headed to the Shandong University for his master degree, where he started to work on condensed matter theoretical physics. He obtained his master degree from Shandong University in June, 2013 and went to the University of Tennessee for his PH. D degree in July. In 2014, he joined Dr. Steve's group, where he studied the effect of electron-phonon interactions on strongly correlated systems. As a PH. D student, Shaozhi Li made many achievements in academic including publishing seven papers. In 2017, he obtained Paul Stelson Fellowships for professional Promise and Allen Fellowship from the University of Tennessee. Besides, Shaozhi Li attended American Physical Society (APS) March meeting every year from 2014 to 2018, where he illustrated the importance of of electron-phonon interactions in high-temperature superconductors.